UNIVERSIDADE DE LISBOA

INSTITUTO SUPERIOR TÉCNICO

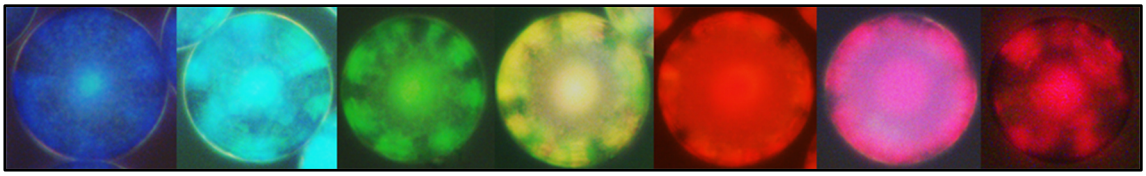

Self-assembled photonic pigments for non-iridescent structural color

Laurinda Rosa Pereira Areias

Supervisor: Doctor José Paulo Sequeira Farinha

Co-Supervisor: Doctor Ana Cristina Moreira Freire

Thesis approved in public session to obtain the PhD Degree in Chemistry

Jury final classification: Pass with Distinction

2021

TÉCNICO LISBOA

UNIVERSIDADE DE LISBOA

INSTITUTO SUPERIOR TÉCNICO

Self-assembled photonic pigments for non-iridescent structural color

Laurinda Rosa Pereira Areias

Supervisor: Doctor José Paulo Sequeira Farinha

Co-Supervisor: Doctor Ana Cristina Moreira Freire

Thesis approved in public session to obtain the PhD Degree in Chemistry

Jury final classification: Pass with Distinction

Jury

Chairperson: Doctor José Nuno Aguiar Canongia Lopes, Instituto Superior Técnico, Universidade de Lisboa

Members of Committee:

Doctor Tito da Silva Trindade, Universidade de Aveiro

Doctor Maria Helena Figueiredo Godinho, Faculdade de Ciências e Tecnologia, Universidade Nova de Lisboa

Doctor José Paulo Sequeira Farinha, Instituto Superior Técnico, Universidade de Lisboa

Doctor Ana Clara Lopes Marques, Instituto Superior Técnico, Universidade de Lisboa

Doctor Ermelinda Maria Sengo Maçôas, Instituto Superior Técnico, Universidade de Lisboa

Funding Institution: Fundação para a Ciência e a Tecnologia

2021

Resumo

Neste trabalho foram desenvolvidas novas estruturas fotónicas coloidais esféricas tendo em vista a sua aplicação como pigmentos com cor estrutural não iridescente, exibindo uma vasta gama de cores brilhantes e saturadas, desde o azul até ao vermelho. A cor estrutural em cristais fotónicos coloidais, resulta da reflexão seletiva de luz incidente, quando esta interage com uma estrutura que apresente uma variação periódica de índice de refração numa escala comparável com o comprimento de onda da luz visível.

Estes pigmentos fotónicos foram preparados por auto-organização de nanopartículas poliméricas, compostas por um núcleo de poli(estireno) e uma coroa de poli(metacrilato de metilo-*co*-ácido acrílico) com uma baixa dispersão de tamanhos. A carga presente na coroa destas nanopartículas direciona a sua auto-organização em estruturas cristalinas coloidais com empacotamento cúbico de faces centradas.

Para que a cor refletida não varie com o angulo de observação, ou seja, de maneira a obter uma cor não iridescente, a auto-organização destas nanopartículas é condicionada por confinamento esférico em pequenas gotas aquosas, recorrendo à tecnologia microfluídica. Nanopartículas com diâmetros compreendidos entre 173 nm e 331 nm, originam pigmentos que refletem cores em toda a gama de comprimentos de onda do visível, desde o violeta a 420 nm até ao infravermelho próximo a 800 nm. Foram obtidos pigmentos com diferentes graus de cristalinidade/desordem variando as condições de evaporação da água das microgotas.

Aumentando a temperatura do processo de auto-organização de 50°C para 65°C, aumenta a desordem estrutural, o que se traduz num alargamento da banda de refletividade e no aumento da dispersão difusa de luz. Curiosamente, a iridescência destes pigmentos esféricos depende pouco do grau de ordem/desordem da estrutura, sendo inferior a 10%, tanto para pigmentos com maior extensão de domínios policristalinos mas sem completa periodicidade, como para pigmentos amorfos com ordem de curto alcance e estrutura isotrópica.

Outra estratégia para obter pigmentos fotónicos esféricos exibindo cores mais saturadas e não iridescentes, passou pela adição de nanopartículas de

polidopamina, capazes de absorver uma ampla gama de comprimentos de onda. A distribuição homogénea destas nanopartículas nos pigmentos esféricos, contribuiu para a obtenção de estruturas isotrópicas com correlação de curto alcance, uma vez que condicionam o empacotamento das nanopartículas poliméricas e aumentaram a saturação da cor refletida através da absorção da dispersão difusa de luz. Após a adição destas nanopartículas absorventes é evidente a obtenção de pigmentos fotónicos com estrutura isotrópica, exibindo bandas de reflexão entre 0° e 75° com uma largura a meia altura constate. A cor destes pigmentos é mais uniforme e saturada, em comparação com a dos pigmentos sem adição destas nanopartículas, cuja cor apresenta um padrão mais brilhante e estriado.

De forma a obter filmes estruturalmente coloridos, estes pigmentos fotónicos esféricos foram adicionados a dispersões poliméricas aquosas, destinadas ao uso em revestimentos, como tintas e vernizes. A foto-estabilidade inerente a estes pigmentos confere maior durabilidade aos revestimentos resultantes, em comparação com os revestimentos à base de corantes tradicionais.

Estes novos pigmentos permitem obter revestimentos de base aquosa, não tóxicos e cuja cor não desvanece, com potencial para substituir corantes aromáticos e outros pigmentos tóxicos nas mais variadas aplicações.

Palavras-chave: nanopartículas poliméricas monodispersas; emulsificação por microfluídica; auto-organização confinada; pigmentos fotónicos esféricos; cor estrutural não-iridescente.

Abstract

We developed novel spherical colloidal photonic structures for application as non-iridescent structurally colored pigments, exhibiting bright and saturated colors, ranging from blue to red. Structural color in colloidal photonic crystals results from the selective reflection of incident light when it interacts with a structure with periodic variations in refractive index on a scale commensurate with the visible light range.

These photonic pigments were prepared by self-assembling polymeric nanoparticles composed of a poly(styrene) core and a poly(methyl methacrylate-co-acrylic acid) shell with very low size dispersity. The shell charge of the nanoparticles directs their self-assembling into colloidal crystal structures with face-centered cubic packing.

To obtain non-iridescent colors (i.e., that do not change upon changing the angle of observation), we constrain the self-assembly process of these nanoparticles through spherical confinement in small aqueous droplets by microfluidics technology, resulting in photonic pigments without full periodicity upon water evaporation. Different nanoparticles, with diameters ranging from 173 nm and 331 nm, originate pigments with bright and saturated colors throughout the entire visible spectrum, from the violet at 420 nm to near-infrared at 800 nm. Pigments with different degrees of crystallinity/disorder were obtained by changing the water evaporation conditions of the microdroplets.

By increasing the assembly temperature from 50°C to 65°C, disorder increases, resulting in spectral broadening of the reflectance bands, and increase of diffuse scattering. Interestingly, the iridescence of these spherical pigments shows low dependence on order/disorder structural degrees, being always lower than 10%, either for pigments with larger polycrystalline domains but no full periodicity, and for the ones with amorphous short-range correlations and isotropic structure.

In another approach to obtain non-iridescent pigments with saturated colors, broad-spectrum absorbers were introduced into our spherical photonic pigments, namely polydopamine nanoparticles (PDNPs). The homogeneously distributed PDNPs, enhance the saturation of the reflected colors by absorbing diffuse scattering, while at the same time hampers colloidal crystallization, contributing to short-range correlation and isotropic structures. Upon addition of these

nanoparticles, the obtained photonic structures clearly reveal an amorphous isotropic packing of polymer nanoparticles, exhibiting reflectance bands with a constant full width at half maximum for viewing angles from 0° to 75°. The color of these doped pigments is more uniform and saturated when compared to the one reflected by pigments without PDNPs, whose colors exhibited a brighter striated pattern.

In order to obtain structurally colored films, these spherical photonic pigments were added to aqueous polymer dispersions, intended for use in coatings, such as paints and varnishes. Due to the pigments inherent photostability the color of the coatings presents higher durability when compared to traditional dye-based colored coatings.

These new pigments provide fade-free, non-toxic, water-based coatings and have the potential to substitute aromatic dyes and other toxic pigments in different applications.

Keywords: monodispersed polymeric nanoparticles; microfluidic emulsification; confined self-assembly; spherical photonic pigments; non-iridescent structural color.

Acknowledgements

First, I would like to acknowledge my supervisor, Professor José Paulo S. Farinha, for the opportunity to develop this research project. For his trust and tireless encouraging along this exciting and winding learning journey.

I would also like to thank my co-supervisor Professor Ana Cristina Moreira Freire, that despite the distance and her full agenda was always available for me when I needed.

I would like to express my profound gratitude to Doctor Gema Marcelo, for all the assistance and knowledge sharing in the beginning of this project. It was a pleasure to work and learn with you.

I thank Professor Virginia Chu for receiving me at INESC.MN, where the development of the microfluidic circuits from soft-lithographic techniques was made, with the assistance of Virginia Soares and Catarina Caneira. I´m also thankful to Guilherme Andrade for his precious tips for designing the geometry of the microfluidic circuits with AutoCAD software.

I thank to all my laboratory colleagues, for creating a friendly and healthy environment to work and for the time spent at social coexistence. A special acknowledgement to Ines Mariz for the assistance in reflectance confocal microscopy and to Filipa Correia for providing me the carbon dots.

I´m very thankful to my friends and family, for all the support and motivation over these years. A special acknowledgment to my husband, Nuno Medina, for his patience, unconditional support, and belief in my research.

Abbreviations

AA	acrylic acid
ACF	autocorrelation function
Ca	capillary number
CAD	computer aided design
CCs	colloidal crystals
CCD	charge-coupled device
CIE	Commission Internationale de l'Éclairage
CMC	critical micellar concentration
CLSM	confocal laser scanning microscopy
CV	coefficient of variation
DLS	dynamic light scattering
DLVO theory	theory named after Derjaguin, Landau, Verwey and Overbeek
DSC	differential scanning calorimetry
DWL	direct write laser
fcc	face-centered cubic
FIB	focused ion beam
FF	form factor
FWHM	full width at half maximum
hcp	hexagonal close-packed
I_{max}	intensity at the wavelength of maximum reflectance
$I_{background}$	intensity of the scattering background
MMA	methyl methacrylate
NA	numerical aperture
NTA	nanoparticle tracking analysis
O/W	oil-in-water
PAA	polyacrylic acid
PBG	photonic bandgap
PDI	polydispersity index
PDMS	polydimethylsiloxane

PDNPs	polydopamine nanoparticles
PGMEA	propylene glycol methyl ether acetate
PhCs	photonic crystals
PhGs	photonic glasses
PMMA	poly(methyl methacrylate)
PNP	polymer nanoparticles
PS	polystyrene
RCM	reflectance confocal microscopy
rhcp	random hexagonally close-packed
Re	Reynolds number
$R(z)$	reflectance as a function of the depth of focus, z
SCPSs	spherical colloidal photonic structures
SPhCs	spherical photonic crystals
SPhGs	spherical photonic glasses
SDS	sodium dodecyl sulfate
SEM	scanning electron microscopy
SF	structure factor
sRGB	standard red-green-blue color gamut
St	styrene
TEM	transmission electron microscopy
Tg	glass transition temperature
UV	ultraviolet
W/O	water-in-oil
W/O/W	water-in-oil-in-water
Z	depth of focus in RCM
ZP	Zeta potential
1D (2D or 3D)	one (two or three)-dimensional
2D-FFT	two-dimensional fast Fourier transform
(111)	111 crystalline planes
[111]	111 crystalline direction
D	nanoparticles diameter

D_{PNP}	diameter of polymer nanoparticles
D_S	diameter of the photonic supraparticles
D_d	diameter of the aqueous emulsion droplets
d	interplanar spacing of the crystallographic planes
d_{111}	distance between (111) diffracting planes
m	diffraction order
n	refractive index
n_{eff}	effective refractive index
n_{PNP}	refractive index of the polymer nanoparticles
n_{voids}	refractive index of the interstitial regions
θ	incidence/observation angle
λ_{max}	wavelength of maximum reflectance
$\Delta\lambda$	width of the reflectance band at half maximum
$\emptyset$	volume fraction
$\emptyset_{PNP}$	PNPs volume fraction
γ	surface tension
μ_c	continuous phase viscosity
μ_d	dispersed phase viscosity
U_c	continuous phase average velocity
Q_c	continuous phase volumetric flow rate
w_c	width of the continuous phase microchannel
h	microchannels depth
φ	flow rates ratio of immiscible phases
Q_d	dispersed phase volumetric flow rate
λ	viscosity ratio of immiscible phases
σ	standard deviation of droplets size

Contents

Preface ..... **xv**

Outline of this thesis ..... **xvii**

1. General Introduction **1**

1.1. Structural color 2

1.1.1. Interference of thin films and multilayers 3

1.1.2. Diffraction grating effect 3

1.1.3. Photonic crystals 4

1.1.4. Scattering by amorphous photonic materials 7

1.2. Colloidal photonic crystals and glasses 8

1.2.1. Colloidal assembly 9

1.2.2. Assembly methods for colloidal photonic structures 12

1.2.3. Spherical colloidal photonic structures 13

1.3. Aims and Scope 15

1.4. References 15

2. Synthesis and characterization of polymer nanoparticles **27**

2.1. Polymer nanoparticles (PNP) 28

2.1.1. Heterogeneous polymerization techniques 28

2.1.2. Emulsion polymerization 29

2.2. Experimental part 32

2.2.1. Materials 32

2.2.2. PNP synthesis 32

2.2.3. Characterization techniques 33

2.3. Results 36

2.4. Conclusions 42

2.5. References 42

3. Emulsion droplet generation by microfluidics **47**

3.1. Introduction 48

3.1.1. Microfluidics 48

3.1.2. Droplet-based microfluidic devices and emulsification 50

3.1.3. Lithographic techniques for microfluidics 54
3.1.3.1. Photolithography 54
3.1.3.2. Soft lithography 56
3.2. Experimental methodology 57
3.2.1. Materials 57
3.2.2. Equipment 57
3.2.3. Microchannels design and hard mask fabrication 58
3.2.4. SU-8 mold and PDMS microfluidic devices fabrication 60
3.2.5. Emulsification procedure and droplet formation 62
3.3. Results and discussion 63
3.4. Conclusions 65
3.5. References 66

4. Polymer nanoparticle assembly inside emulsion droplets 71
4.1. Self-assembly in spherical confinement 73
4.1.1. Experimental procedure 73
4.1.2. Direct observation of the assembly process 74
4.2. Internal structure tunability 77
4.2.1. Effect of pH 78
4.2.2. Effect of temperature and drying time 80
4.3. Conclusions 84
4.4. References 85
4.5. Appendix 4 90

5. PNP arrangement in spherical photonic pigments probed by reflectance confocal microscopy 91
5.1. Techniques to probe the internal structure of colloidal photonic materials 93
5.2. Reflectance confocal microscopy 95
5.3. Experimental part 97
5.3.1. Instruments 97
5.3.2. Sample preparation 98
5.4. Results 98
5.5. Conclusions 107
5.6. References 108
5.7. Appendix 5 113

6. Variation of structural and optical properties with the assembly temperature 117

6.1. Experimental section 119

6.2. Temperature dependent size and structural color 121

6.3. Structural characterization of the PNP arrangement 124

6.3.1. SEM imaging 124

6.3.2. FIB-SEM analysis and thermal treatment 128

6.3.3. RCM imaging 130

6.4. Optical characterization of spherical photonic pigments 133

6.4.1. Scattering ratio 139

6.4.2. Gap to midgap ratio 140

6.4.3. Experimental determination of PNP volume fractions in the spherical pigments 141

6.5. Reflectance microscopy images 144

6.6. CIE color maps 145

6.7. Conclusions 146

6.8. References 147

6.9. Appendix 6 153

7. Increasing color saturation through disorder 165

7.1. Experimental section 166

7.1.1. Synthesis of polydopamine nanoparticles 166

7.1.2. Co-assembly of PDNPs and PNPs into photonic structures 167

7.1.3. Characterization techniques 168

7.2. Topological and internal order/disorder probed by SEM 168

7.3. FIB-SEM imaging of doped and undoped structures 172

7.4. Effect of PDNPs addition by RCM 173

7.5. Reflectance properties of doped *vs* undoped pigments 176

7.6. Color appearance 182

7.7. Further improving the saturation of red hues 185

7.8. Conclusions 186

7.9. References 187

7.10. Appendix 7 191

8. Water-born polymer coatings with non-iridescent structural color 197

8.1. Water-born polymer coatings 198
8.1.1. Introducing color into water-born polymer coatings 198
8.1.1.1. Dyes and pigments 198
8.1.1.2. Photonic pigments 200
8.1.2. Coloration of water-born polymer coatings with spherical photonic pigments 201
8.2. Experimental procedure 203
8.2.1. Different compositions of the photonic paints 203
8.2.2. Characterization techniques 205
8.3. Micro and macroscopic color appearance of the structurally colored coatings 205
8.4. Reflectance properties and color coordinates 207
8.5. Conclusions 211
8.6. References 211

9. Concluding remarks and future perspectives 215

Preface

Most colors in artificial materials such as paints, cosmetics, and coatings are based on light absorbing materials such as dyes and pigments, similarly to most biological chromophores. However, nature sometimes uses an alternative approach to create the most brilliant colors, as in bird feathers or butterfly wings. These bright and dazzling colors are not based in the absorption of light, but in the interactions of light with micro and nanostructures, resulting in interference, diffraction, and scattering. Structural colors arise from the interference of light scattered from inhomogeneities in the refractive index of the material, spaced at scales comparable to optical wavelengths. These materials create vivid structural colors that, by their operational principle, cannot bleach or suffer discoloration, unless the structure is destroyed. Structural colored materials are of interest for coloration in future devices and consumables as they can be achieved with biocompatible and environmentally friendly materials.

Compared to conventional pigments, the structural color materials unique properties, such as high photostability, low toxicity, brilliant colors with exotic appearance, color tunability, and energy efficiency, have attracted great attention for a variety of applications. Replacing pigment colors with artificial structural colors has drawn considerable interest due to tremendous environmental pressure and the easy fading of conventional pigments and dyes.

Inspired by nature’s marvelous structural colors, the artificial full-spectrum structural coloration with wide viewing angles is a tireless pursuit to achieve vivid colors for application in different fields. Structural colors can arise from ordered as well as disordered photonic structures. Periodically ordered photonic structures such as opals, where iridescent colors arise from Bragg diffraction are well established. Their colors are, however, strongly dependent on the angle of view because the periodicity of interparticle distance originates narrow diffraction maxima. For certain applications in reflective screens, coatings, paints, as well as cosmetics, this angular dependency can be undesirable. The disordered counterpart of photonic crystals (PhCs) are photonic glasses (PhGs), which are random assemblies of monodisperse spherical nanoparticles. The isotropic nature of their short-range ordered structure enables PhGs to have angle-independent structural colors, isotropic transport properties, reflectance, and

transmittance pseudo-photonic bandgaps. Although the preparation of PhGs is relatively well explored, a limited range of colors was produced so far by self-assembly of monodisperse nanoparticles.

The use of colloidal assembly is a common approach to prepare photonic crystals and glasses for the development of structural colors. The fact that they can either form crystalline lattices with long-range order or glassy structures with short-range order through self-assembly, provides the most economical way to develop structural colors, rendering it promising for practical applications due to their stable structures with high control over a relatively wide range of length scales that cover ultraviolet, visible, and infrared.

Bottom-up approaches based on colloidal self-assembly has significant advantages, offering the most facile way to create 2D and 3D photonic structures in a wide variety of possible shapes. It is cost-effective and can be applied on a large area. Most photonic crystals produced via colloidal assembly show brilliant and iridescent structural colors due to Bragg diffraction, which depends on the angle of observation. However, colloidal photonic materials with spherical macroscopic morphology have reflection spectra which are independent of rotation under illumination of the surface at a fixed incident angle of light, broadening the spectrum of their applications. Packing colloidal nanoparticles into a spherical shape exhibiting structural colors can be achieved with different arrangements: close-packed ordered or amorphous colloidal assemblies, non-close-packed colloidal assemblies, or inverse opals.

Spherical colloidal photonic structures were generated by evaporation-induced nanoparticle crystallization/agglomeration in an emulsion droplet, producing micron-sized supraparticles, where their natural curvature creates a uniform and angle-independent color. The size of the supraparticles is mainly determined by the initial droplet template size and the nanoparticle volume fraction in the initial droplet. Thus, to fabricate uniform spherical pigments, monodisperse droplets are required, which can be prepared using a microfluidic device. This strategy not only ensure size uniformity, but also increases the structural and functional diversity of the colloidal photonic structures, paving the way for the development of advanced systems that can have promising applications in optical devices such as colorimetric sensors, diffraction gratings or dispersible structural color pigments with high stability against degradation under environmental factors.

In the spherical confinement of emulsion droplets, assembly can be controlled in such a way that structures with different nanoparticle arrangement exhibits different optical properties when compared to their conventional film or bulk counterparts. This makes spherical photonic structures more promising to generate colored materials with low iridescence properties even for wide angles of observation, for applications in flexible electronic devices or coatings industry.

Outline of this thesis

The investigation of spherical colloidal photonic pigments and how different structures relates with the reflected colors, constitutes the focus of this thesis.

A general introduction about structural color, colloidal assembly and spherical templating is described in Chapter 1. In Chapter 2 we describe the synthesis and characterization of the polymer nanoparticles (PNPs) used as the building blocks for the assembly of photonic pigments. These were obtained by emulsion polymerization and have diameters increasing from 173 nm to 331 nm. To assemble these PNPs into microscopic spherical photonic pigments, or supraparticles, we resort to microfluidics technology based on soft lithography techniques, described in Chapter 3. Microfluidic emulsification produces stable and monodispersed emulsion droplets, which allows a precise control of the assembly process, guaranteeing reproducible optical properties.

Different assembly conditions are described in Chapter 4. The pH, temperature, stirring conditions and drying time were changed, thus resulting in photonic structures with different PNPs packing and optical properties. From this assembly studies, we selected temperature as the parameter that better allowed to finely tune the final structure and optical properties through the precise kinetic control of water evaporation.

In Chapter 5, we describe how confocal laser scanning microscopy (CLSM), can also be a major player in the characterization of photonic structures. When used in reflectance mode, this technique allows imaging different crystalline domains under illumination with wavelengths falling on the structure pseudo-bandgap. Moreover, by reconstructing the planes scanned at different depths, a complete 3D overview of the inner structure ordered/disordered domains can be obtained in a fast, easy, and non-destructive approach.

Chapter 6 describes the full characterization of the different photonic pigments, reflecting bright and vivid colors, covering the entire visible light range. By changing the temperature at which PNPs with different diameters were assembled, we obtain a palette of different colors and different color saturations within the same hue.

Chapter 7 describes the doping of the pigment structures with polydopamine nanoparticles (PDNPs) to increase the color saturation of pigments assembled at higher temperatures. The addition of PDNPs to the structure, not only increased color saturation by absorbing diffusely scattered light, but further contributed to a more disordered packing of PNPs, and consequently, to more homogeneous optical properties of the reflected colors with increasing the viewing angle.

Chapter 8 describes the incorporation of the spherical pigments into water-born polymer coatings. These photonic pigments are highly stable in the wet paint formulation and were able to maintain their optical properties when encapsulated in the polymer films, thus producing structurally colored coatings. This approach is an extraordinary alternative to the fade-prone conventional coloring solutions for water-born polymer coatings existing in the market.

1. General Introduction

In this chapter we briefly describe the mechanisms responsible for structural color generation in nature, with emphasis on colloidal-based systems. Special attention is dedicated to the self-organization of colloidal nanoparticles into photonic crystals and glasses, followed by an outline of the preparation methods available for their fabrication. The last section addresses the advantages of spherical confinement in colloidal assemblies, and their relation with the optical properties of photonic structures.

1.1. Structural color

Colors play an essential role in the evolution and survival of many animals, insects and plants, and it is somewhat inspiring that a large fraction of the color in the world around us, is produced from structures that are in fact small nanoscale assemblies which selectively reflect certain wavelengths of visible light through constructive interference.[1,2] This is called structural color, and unlike the colors of dyes and pigments that originate from the selective absorption or emission of light, and bioluminescence which is emitted by chemical reactions in the photophores of some organisms, it arises via diffraction effects from nanostructures with regular features on the length scale of the wavelength of visible light.[3-5]

Structural color has attracted much attention recently due to its potential for applications in technology, especially inspired in the colors of opals and butterfly wings which display a large diversity of structures, colors and visual effects.[6-8] These colors vary according to structural dimension and refractive index so that various colors can be obtained using a single set of materials, in addition, they never fade as long as the structures persist.

These features offer huge potential in several industries and applications, from paints and inks,[9,10] to anticounterfeiting patches,[11,12] colorimetric sensors and color-encoded microcarriers for bioassays,[13,14] reflective color displays[15,16] among many others.[3,17,18] Because they are not susceptible to photobleaching and can have a better environmental footprint there is a large drive in the field to generate rich and varied colors for use as photonic pigments for paints and coatings.[10,19-21]

Structural color can be categorized as either iridescent or non-iridescent. Broadly defined, surfaces of which the color changes with the angle of observation or illumination are called iridescent colors, while non-iridescent colors remain similar in appearance regardless of the angle of observation.[22,23] From the point of view of physical mechanisms, when light encounters boundaries between media that differ in refractive index, structural colors can be produced by interference, diffraction or scattering. Both interference and diffraction can produce iridescent colors, while some forms of scattering produce non-iridescent structural colors from structures with low regularity.[24-26]

Most of the structural colors present in nature are considered to originate from the physical mechanisms illustrated in Figure 1.1, and encompasses film interference, diffraction gratings, photonic crystals and scattering or their combinations, which are briefly discussed in the following sections.[17,20]

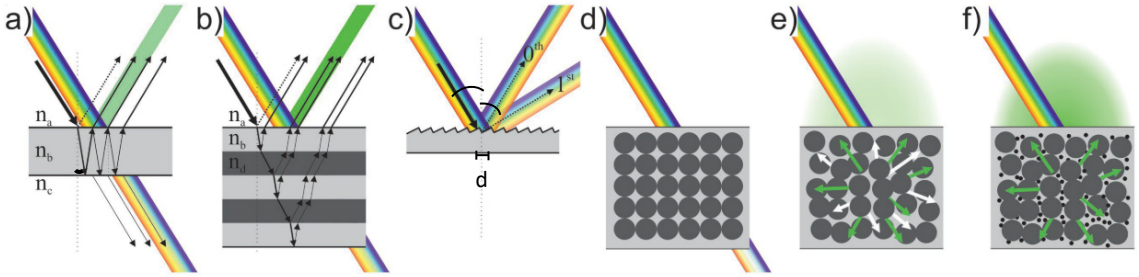

Figure 1.1: Structural coloration caused by the interaction of light with structured materials. **a)** thin film interference; **b)** multilayer interference; **c)** interference from grating diffraction; **d)** 3D colloidal photonic crystal, with a photonic bandgap in the green region; **e)** coherent scattering from colloidal glasses showing weak coloration without absorbing material; **f)** diffuse scattering absorption shields the coherent effect, leading to a more saturated structural color. n_{a-d} represents refractive indices of the different materials; d corresponds to the groove period; dotted arrows in c) indicates different diffraction orders. Adapted from Goerlitzer *et al*.[20]

1.1.1. Interference of thin-films and multilayers

Thin-film interference illustrated in Figure 1.1a, shows the reflectivity of a thin, non-absorbing layer with refractive index n_b, in between two media with refractive indices n_a and n_c. Light is either reflected or refracted at the interfaces in between the materials and can be subsequently internally reflected multiple times within the thin-film. The light reflected at the upper and lower boundaries of the film interact, creating constructive interference for a given angle and wavelength of incident light, as exemplified by the iridescent soap bubbles.[24,25]

Multi-film interference is qualitatively understood in terms of a pair of thin layers piling periodically. The addition of further layers to produce a periodic stack, results in multiple reflections at the interfaces and therefore further enhances interference effects as illustrated in Figure 1.1b. Compared to thin-film interference, colors produced by multi-film interference are brighter and more saturated.[1,27]

1.1.2. Diffraction grating effect

Grating diffraction mechanism makes use of a periodic lattice represented in Figure 1.1c. The basic physics of the grating is just the same as that involved in

a periodic multilayer stack, except for the orientation of the periodicity. Whereas in films the interfering waves arise from reflections at stacked layers, in gratings they arise from periodic patterns on a surface.[25]

When light interacts with a periodic surface consisting of a series of parallel grooves, with periodic spacing, d, can give rise to coloration because constructive interference for different wavelengths is fulfilled under different angles.[5,28] The grating produces a decomposition of white light into spectral components producing a rainbow of colors. The complete spectrum reflected nearest to the perpendicular (grating normal) correspond to the lowest diffraction order and is reflected over a smaller angle than higher-order spectrum, and the colors are more saturated and appear brighter. The resulting color is characterized by a pronounced color shift upon changing the observation angle and is commonly used in polychromatic security features of credit cards or banknotes.[5,20]

1.1.3. Photonic crystals

Photonic crystals (PhCs) are another important source of structural coloration illustrated in Figure 1.1.d. They are periodic structures that can control the propagation of photons in the same manner that atomic crystals control electrons.[29,30] As a consequence of the differing dielectric media and the subsequent refractive index contrast within the crystal, light is scattered and/or diffracted from the different surfaces, producing a band of forbidden frequencies, known as photonic bandgap (PBG), where light cannot propagate within the structure. Thus, the selectively reflected light endows materials with bright structural colors when the PBG is located in the visible light range.[31] The refractive index contrast and the lattice topology affects the existence of a full PBG (light propagation is prohibited in all directions regardless its polarization) but the wavelength range affected is determined by the length scale or lattice parameter of the crystal.[32] An incomplete PBG or pseudo-bandgap, also referred as a stop-band, is one that prohibits light from propagating only in specific directions. The potential presence of PBGs and the ability to tune its position to suit specific frequencies is one of the most attractive qualities of PhCs.[31,33,34]

PhCs are classified as one-dimensional (1D), two-dimensional (2D) or three-dimensional (3D) structures according to the periodic spatial modulation of refractive indices in either one, two or three directions, respectively (Figure 1.2).

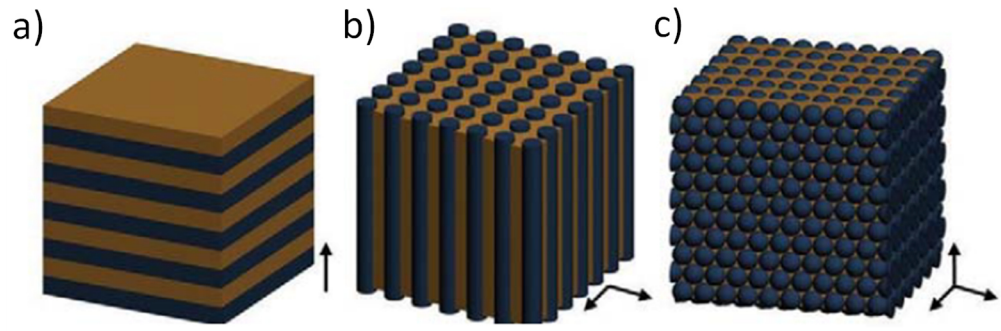

Figure 1.2: Schematics of **a)** one; **b)** two; and **c)** three-dimensional photonic crystals. The arrows to the right of the crystals show the direction in which a periodic modulation in refractive index exists. A 1D photonic crystal is merely a multilayer film of two media with different refractive index. Adapted from Paquet and Kumacheva.[30]

In a PhC, matching the wavelength of incident light to the periodic lattice spacing results in Bragg diffraction, so if one would like to manipulate the flow of visible light, which has a typical wavelength of 500 nm, photonic crystal building blocks should have a size comparable to 500 nm, which brings them into the realm of colloids. For photonic crystals composed of spherical polymer or silica nanoparticles, referred as artificial opals (Figure 1.3a), due to its intrinsically low value of refractive index contrast, Δn, a pseudo-bandgap exists in the [111] direction for a face-centered cubic (fcc) packing, and the wavelength of light that is reflected by the 3D structure can be related to the material periodicity, d, via an approximation of Bragg's and Snel's law according to equation 1.1:[27,35,36]

$$m\lambda = 2d\sqrt{n_{eff}^2 - sin^2\theta} \qquad (1.1)$$

where m is the diffraction order, d is the spacing between the layers of spheres or voids that make up the diffraction planes, n_{eff}, is the effective refractive index of the structure and θ is the angle of incidence of white light in the medium (relative to surface normal). As the angle of incidence increases, so the diffracted wavelength will decrease, that is, a red reflection at $\theta = 0^{\circ}$ will move towards green and blue, as observed for natural opals.[35]

The longest wavelength of the reflected color, λ, will occur at normal incidence for $m = 1$ due to diffraction from the (111) planes of spheres for close-packed fcc structures, which have the greatest value of interplanar spacing, d. Usually d, is replaced by the average distance between the sphere centers, D, described in terms of the cubic unit cell of the fcc structure (Figure 1.3b). The relation between

the interplanar spacing and the cubic lattice parameter, a, is given by equation 1.2:[27]

$$d = \frac{a}{\sqrt{h^2+k^2+l^2}} \tag{1.2}$$

where the sets of numbers designated by h, k and l called Miller indices correspond to crystalline planes and directions normal to them (note that not every plane in the structure will give rise to strongly diffracted colors).

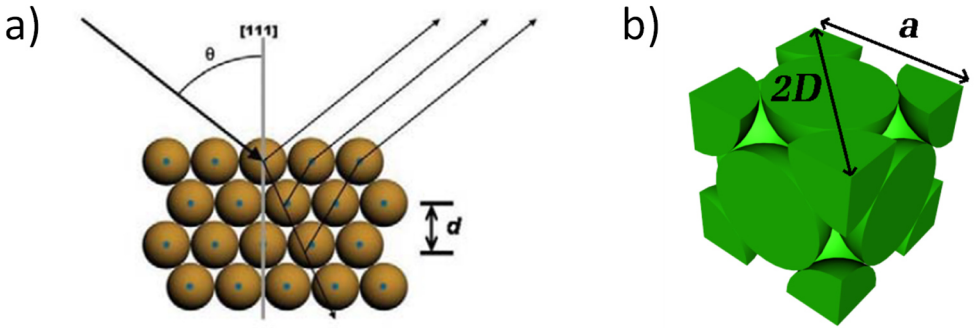

Figure 1.3: **a)** Incident light undergoes diffraction from the (111) panes when propagating through a colloidal photonic crystal (certain frequencies are reflected while others are transmitted). The wavelength of light that is coherently scattered, λ, can be estimated according to the angle of incidence, θ, the effective refractive index of the medium, n_{eff}, and the periodicity of the structure, d. Adapted from Paquet and Kumacheva.[30] **b)** Depiction of the cubic unit cell for 3D fcc latices where a is the lattice constant or lattice parameter and D is the nanoparticles diameter. Adapted from Tilley.[27]

The relation between the measured average distance between the sphere centers, D, and the cubic lattice parameter is given by $a = \sqrt{2}.D$, hence the distance between (111) diffracting planes is given by equation 1.3:

$$d_{(111)} = \sqrt{\frac{2}{3}} \times D \tag{1.3}$$

Rewriting Bragg-Snel's equation, the wavelength diffracted by the (111) planes is given by equation 1.4, and depends on nanoparticles diameter, D:

$$\lambda = 1.633D\left(n_{eff}^2 - sin^2\theta\right)^{1/2} \tag{1.4}$$

The effective refractive index can be related to the refractive indices of the components of the photonic structure and is usually determined from the volume fractions, $\emptyset$, occupied by the nanoparticles and the voids in between them: $n_{eff} = \emptyset_{part} n_{part} + (1 - \emptyset_{part}) n_{voids}$, where $\emptyset_{part}$ and n_{part} corresponds to the volume fraction and refractive index of nanoparticles inside the PhC structure, respectively, and n_{voids} corresponds to the refractive index of the material filling

the pores. For close-packed fcc structures the volume fraction occupied by particles can be calculated from Figure 1.3b, and according to the lowest energy principle corresponds to $\emptyset_{particles} \sim 0.74$.[31,33]

1.1.4. Scattering by amorphous photonic materials

Scattering of light by amorphous photonic materials is a source of structural color, which is completely different from the photonic crystal type, because it has an origin in the irregularity of the structure. Amorphous structures, known as photonic glasses (PhGs), appeared as an analogue to photonic crystals and describes the disordered arrangement of monodisperse spherical particles with only short-range order, which appears due to physical contact between the particles (Figure 1.1e).[37-40]

Unlike the iridescent colors from colloidal PhCs that originate from Bragg reflection as a result of long-range order, the short-range ordered and long-range random isotropic microstructure of PhGs, results in non-iridescent structural colors. This is because the spectral characteristics of PhGs under diffuse illumination are independent of the observation angle.

These type of structure is responsible for the coloration from many avian feather barbs, where the presence of different random arrangements within the disordered photonic structure controls the visual effect of structural color.[24,26,41]

The mechanisms proposed to explain the production of structural colors from those feather barbs fall into two classes of light scattering: coherent and incoherent scattering, according to the presence or absence of a phase relationship between the scattered waves from the disordered structure, respectively.[42-44]

The characteristics of light scattered by spherical particles are determined by the structure factor (SF), related to the particle-particle distance, and the form factor (FF), related to the intrinsic properties of the particles, such as, size and refractive index.[45] When the particles are assembled in a crystalline arrangement, the SF induces coherent scattering, that dominate the scattering properties of the structure, as previously explained by Bragg-Snel's law for photonic crystals. On the other hand, in an amorphous arrangement of particles the contribution of the SF to the reflected colors is rather weak due to low regularity of the microstructure, and thus, is easily compromised by incoherent light scattering

induced by the FF (consists of strong forward scattering and weak backscattering). Therefore, PhGs reflected colors are multidirectional, angle independent, and strongly affected by the refractive index and the size of the individual particles.[46,47]

Several explanations have been proposed for the origin of structural colors arising from a random distribution of spherical particles, accounting for both incoherent multiple scattering and constructive interference of coherently scattered light from the short-range correlations between particles,[42,48-51] nevertheless, so far the origin of angle-independent structural colors is not fully understood and the prediction of the exact range of accessible colors of PhGs have not yet been established.[39,51,52]

For submicron-sized low refractive index particles (refractive index < 2), such as the case of polymer or silica nanoparticles, the spectrum of light scattered by the FF is red shifted as the size of the particles in the microstructure increases (the backscattered light diffusively reflects a specific color according to the size of the scattering particles and the forward scattering scatters the entire visible light). As long as the FF-derived reflection are located in the UV range, it does not contribute to the color spectrum perceivable by the human eye. However, the FF of particles larger than a critical diameter reflect visible light and hence affect the structural color saturation, especially for colors at longer wavelengths, posing an obstacle for realizing full-color PhGs.[53-55]

These additional reflectance bands in the blue part of the spectrum that compromise the red hues by color mixing can be removed by introducing broadband or spectrally selective absorption materials, as illustrated in Figure 1.1f, where small black nanoparticles are co-assembled with the colloidal photonic glasses, or alternatively, the colloidal particles forming the structure can be absorbing themselves.[39,46,52,54,56,57]

1.2. Colloidal photonic crystals and glasses

Colloidal-like particles have long been used by nature to provide bright structural colors (Figure 1.4) either from ordered, disordered or stimuli-responsive structures, thus resulting in iridescent, angle-independent, or dynamic/reversible changing colors, respectively.

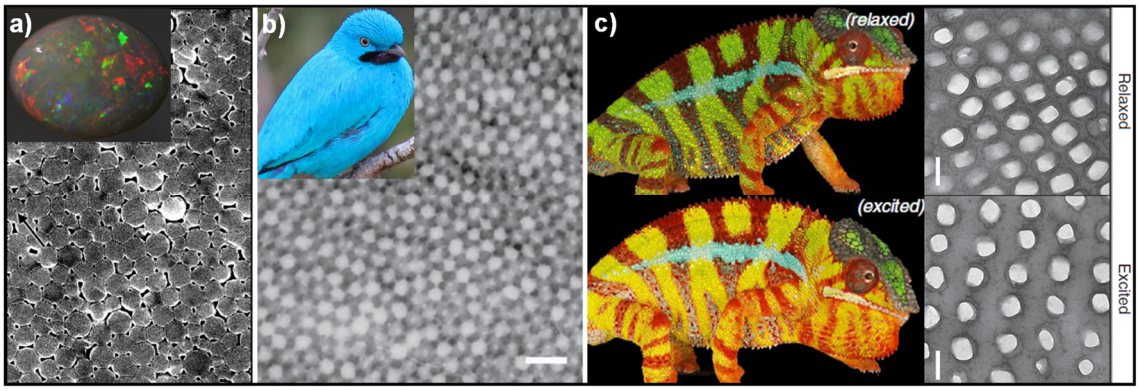

Figure 1.4: Examples of natural structural colors from colloidal type photonic structures. **a)** Photonic crystal type showing the iridescent structural colors from the Australian light gray opal consisting of silica spheres.[61] **b)** Photonic glass type exhibiting the non-iridescent structural colors of the male plum-throated cotinga (*Cotinga maynana*), due to the amorphous arrangement of β-keratin spheres and air from the feather barbs nanostructure.[62] **c)** Stimuli-responsive photonic crystal structure of panther chameleons showing a reversible color change from green to yellow/orange according to the lattice spacing of guanine nanocrystals in the skin S-iridophores.[63]

Because structurally colored materials are not susceptible to photobleaching are increasingly sought for a wide range of applications, and colloids are often used to build photonic materials due to their ease of fabrication and versatility.[58-60] While in some cases the iridescence of artificial colloidal photonic crystal materials is undesirable, the introduction of disorder into its photonic structures may solve this issue, by increasing their angular visibility. Hence, the angle-independent structural colors of artificial colloidal photonic glasses are highly desirable.[43,56,62,64-67]

For security applications, optical switches, sensing or color reflective displays, it is important to be able to reversibly switch the structural color either in an on/off configuration or by a measurable shift in the photonic stop-band location (caused by a change in either the periodicity of the structure or the refractive index of its constituents).[68-73]

Colloidal nanoparticles have extensively been used to explore biomimetic approaches for structural colors because of their easy size tunability and the simple, cost-effective and scalable bottom-up assembly method.[17,20,43,55,74]

1.2.1. Colloidal assembly

Colloids are small particles (1–1000 nm in diameter) that display Brownian motion in suspension.[75] Colloids can explore many different configurations and

reach thermodynamic equilibrium, which is one of the key properties of colloidal systems.[58,76,77] Thus, colloidal nanoparticles are able to spontaneously self-assemble into ordered structures that settles into a state of minimum of energy, known as colloidal crystals, providing that the polydispersity of the particles is small enough to facilitate the stacking.[33,78-81] With increasing colloidal concentration, the isotropic fluid will transform in a coexisting fluid and crystal phases and finally into a crystalline phase.[82-84]

The surface of particles synthesized by different methods are covered with functional groups, and thus, various types of interactions can take place simultaneously during the assembly process. Colloidal crystals and glasses results from a subtle balance of the different forces acting on the colloidally stable nanoparticles.[85,86] These forces can be divided into three main classes: 1) repulsive forces resulting from interparticle interactions between two and more particles (or with extended interfaces) that prevent a colloidal dispersion from spontaneous aggregation and flocculation; 2) attractive interparticle forces that can counteract repulsive forces and may yield specific assembly structures as a result of this (im)balance; and 3) external forces acting on individual particles or particle ensembles (Figure 1.5).[87-89]

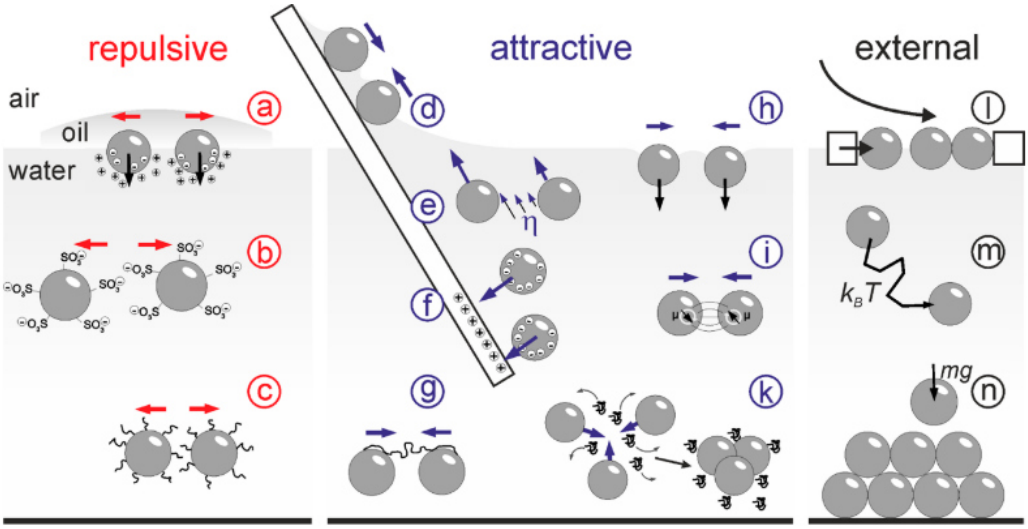

Figure 1.5: Schematic representation of various forces and interactions for colloidal particles occurring in three dimensions and at interfaces. Repulsive interparticle interactions (red): **a)** dipolar repulsion by partial ionic dissociation at interfaces; **b)** Coulomb repulsion; **c)** steric repulsion. Attractive interactions (blue): **d)** immersion capillary forces; **e)** hydrodynamic coupling/drag forces; **f)** Coulomb attraction to oppositely charged surfaces, **g)** bridging attraction/flocculation; **h)** flotation capillary forces; **i)** van der Waals (vdW) attraction; **k)** depletion attraction. External forces (black): **l)** barrier compression or forced convection (effectively resulting in particle aggregation); **m)** Brownian motion; **n)** gravitational sedimentation. Adapted from Vogel *et al*.[85]

In a bulk system the balance of forces to achieve attractive interactions can be introduced, for example, via changes in the electrostatic stabilization (i.e., by changing pH or ion concentration), the mixture of mutually attractive colloidal species (i.e., negatively and positively charged colloidal particles), or entropic interactions (typically based on depletion attraction).[88,90]

Contrarily to top-down approaches that often require complex and expensive lithographic equipment and clean-room facilities, bottom-up assembly of colloidal nanoparticles is an easier method to obtain photonic structures, comprising PhCs and PhGs.[91-93] The crystallization of silica or polymer nanoparticles into fcc colloidal crystals, known as synthetic opals, can also be used as templates to replicate their structure in the form of inverse opals.[94-98]

Although for self-assembled colloidal crystals of spherical nanoparticles the equilibrium structure is predicted to be face-centered cubic (fcc), planar stacking faults are often observed in the stacking sequences of the hexagonal close-packed (hcp) layers.[93,99-101] Therefore, a random hexagonal close-packed (rhcp) structure is obtained, because the energy difference between fcc and hcp is vanishingly small and stacking faults form easily (Figure 1.6).[102] Because of the small energy difference, self-assembly often results in a mixture of the two structures (fcc or hcp crystals that are heavily faulted on) and even crystals with mainly fcc structure still possess a significant degree of disorder, which affects their optical properties due to the contribution of diffuse scattering.[103-105]

In close-packed hexagonal layers of stacked spheres on top of each other, each layer can occupy one of three specific positions, A, B and C (Figure 1.6a). The two simplest periodic sequences are hcp with an ABAB… stacking and the fcc with ABCABC… stacking (Figure 1.6b). A random mixture of the two stacking sequences is observed, the so-called rhcp structure (Figure 1.6c) where hcp layers in between fcc layers are considered stacking defects. Other type of defects are also present in colloidal crystals of spheres, such as point and line defects (Figure 1.6d).[106-108]

The assembly process is often viewed only from the perspective of the arrangement into ordered structures like PhCs.[64,109] In this case the goal is optimizing the conditions to obtain a high quality crystal, minimizing the residual disorder. Obviously, the latter is never fully eliminated, and partial disorder is always present due to the numerous intrinsic defects present in the samples. On

the other hand, for disordered structures such as PhGs, elimination of the remnant order is equally important and hardly fully attained.[64,91,110,111]

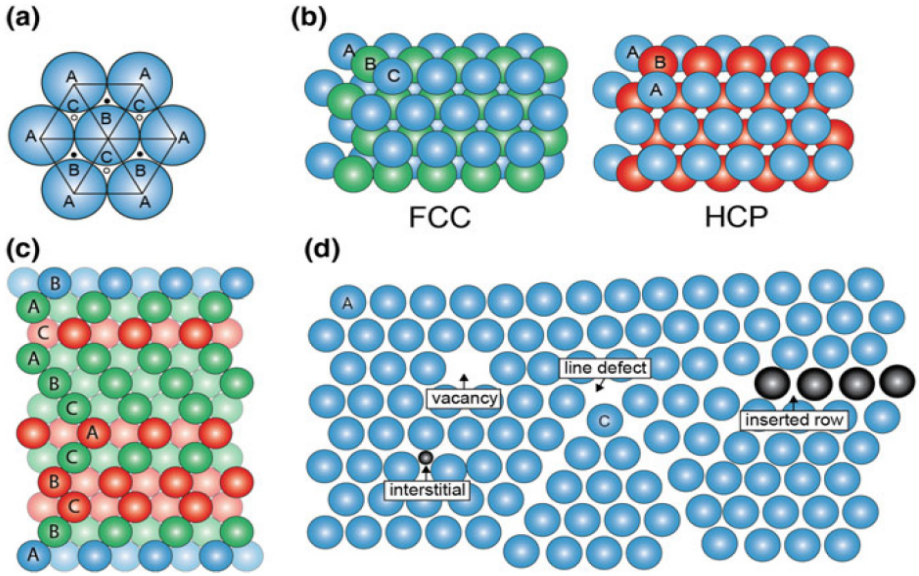

Figure 1.6: Schematic representation of synthetic opals structure. **a)** Top view of the A, B and C positions in a hexagonal close-packed layer (hcp) of colloidal nanoparticles. **b)** Top view of the stacking of 3 close-packed layers in fcc and hcp structures. **c)** Side view of an example of a random hexagonal close-packed (rhcp) stacking sequence ABCBCACB. The local environment changes back and forth from fcc (green) to hcp (red). The first and last layer are not assigned fcc or hcp because a top and bottom layer are needed for assignment. **d)** Several types of in-plane defects that can occur in colloidal crystals of spheres. Adapted from J.-M. Meijer.[106]

1.2.2. Assembly methods for colloidal photonic structures

Compared to the lithographic methods for the fabrication of nanostructured materials, colloidal assembly is rather inexpensive and has another additional advantage, that is, the structure, size and composition of the individual nanoparticles can be modified in order to tune their optical properties.[64,81,112]

Colloidal photonic crystals were first fabricated by assisted sedimentation of nanoparticles onto flat substrates resulting in a compact arrangement of spheres.[113,114] Crystallization under these conditions invariably involves crack formation, that appears due to shrinkage at a late stage of drying as the volume fraction approaches 0.74, and can barely be prevented when the lateral size of the sample is above a few tens of micrometers.[115] Drying involves a contraction that does not occur in the supporting substrate, and which can only be accommodated by the creation of cracks.

Although several techniques were used to develop colloidal photonic crystals in the search for defect-free samples, namely, Langmuir-Blodgett films,[116] vertical

(or convective) deposition,[117] 3D colloidal crystal grown by the layer-by-layer templating method,[118] or by constrained crystallization[119] the obtained structures are mainly restricted to planar geometries. Methods to develop photonic structures other than films include the use of expensive patterned substrates to direct the arrangement of colloidal particles, so that crystallization takes place according to the predefined geometry.[58,120-123]

1.2.3. Spherical colloidal photonic structures

One ingenious way to obtain 3D photonic structures was introduced by the Pine group.[124] They resorted to emulsion templating technique, taking advantage of the fact that droplets are highly deformable, and so, circumvent crack formation at a late stage of the assembly process. Further, the final spherical photonic structures are easily collected after templating.[112,125-127]

Typically, these can be created via evaporation of a solvent from a droplet containing colloidal nanoparticles, via microfluidics[128,129] or ink-jet printing.[130] Microfluidic devices offer the highest level of control over the emulsification procedure and allows the fabrication of highly uniform droplets, with precisely adjusted droplet size, and the design of more complex, multicompartment liquid architectures.[131-134] Furthermore, elastomer-based devices made from polydimethylsiloxane (PDMS) can be fabricated cheaply and rapidly from reusable, photolithographically designed masters.[135-137]

The low throughput of conventional droplet-based microfluidics, which typically limits droplet generation to the milliliter per hour range, has recently been addressed by microfluidics parallelization: the placing of many replicate devices that operate in parallel onto a single chip. This strategy successfully increased the throughput of microfluidics to an industrial relevant scale, required for economic commercial use.[138-141]

Colloidal assembly in the spherical confinement of emulsion droplet templates, produces 3D photonic supraparticles: hierarchical spherical agglomerates that consist of assembled particulate building blocks (although no uniform nomenclature exists to describe these spherical photonic structures).[112,142,143]

An evaporating droplet of a colloidal dispersion will lead to a continuous concentration increase of nanoparticles, until they are forced into direct contact and form a solid supraparticle.[85,100,101,144,145] So, precise manipulation of the

forces acting on the nanoparticles before emulsification, as well as the kinetics of the assembly process, are key parameters to control the structure morphology.[146] Slow evaporation rates provides time for the individual particles to minimize their free energy and foster the formation of more ordered and regular structures (spherical colloidal crystals ($Ø \sim 0.74$)). On the other hand, a stronger attractive component and a faster assembly process, accelerates the agglomeration behavior, fostering the production of glassy structures (spherical colloidal glasses ($Ø \sim 0.64$)).[85,131,147]

These spherical photonic structures besides originating dispersible structural pigments, have another great advantage: their spherical symmetry renders them angle-independent structural colors, via modification of the local geometry, where all viewing directions are normal to some portion of the supraparticles.[46] Thus, the pseudo-bandgaps of spherical colloidal PhCs are independent of rotation under illumination of the surface at a fixed incident angle of light, broadening the perspective of their applications. It should be noted that the structural color of these spherical photonic structures when viewed at an oblique angle to a strong lighting source, can reflect different colors.[147,148] Fortunately the assembly of short-range ordered colloidal supraparticles is expected to strongly reduce the angular-dependence of the reflected colors due to their isotropic structure.[142,149,150]

In perspective, the ability to produce photonic structures through assembly in spherical confinement allows a greater variety of optical properties, to achieve highly vibrant and shining non-iridescent structural colors, for applications in coatings or color reflective displays. It is evident that while a promising near future exists for photonic structures made by bottom-up assembly methods, several technological hurdles remain to be overcome before they can realize their full potential. Encouraged by recent developments as well as in our results, we believe that bottom-up colloidal photonic technologies could soon find their way to the marketplace for a myriad of colorful products, namely as dispersive pigments used as color agents in water-born polymer coatings. Such advances illuminate a bright future for the field!

1.3. Aims and Scope

Our main objective was to obtain non-fading and dispersible structurally colored spherical pigments reflecting colors in the entire range of visible light wavelengths, with high color saturation and low-iridescence, with the potential to replace traditional pigments in inks, paints, reflective screens, etc.

To this end, we successfully:

- Synthesized polymer nanoparticles (PNP) with different diameters and narrow size distributions by emulsion polymerization;
- Created monodispersed and stable emulsion droplets by microfluidic emulsification procedures, based on soft lithography technology;
- Understood and controlled the different factors affecting the assembly of PNP in spherical confinement, to ensure uniform optical properties;
- Tuned the macroscopic optical appearance of the spherical photonic pigments through the assembly process, by changing the rate of water evaporation, thus obtaining a palette of colors for the different hues;
- Understood the effect of structure doping with the broad-spectrum absorber polydopamine nanoparticles (PDNPs), not only on the color saturation but also in the packing of PNP;
- Evaluated the stability and color appearance of the photonic pigments when incorporated in water-born polymer coatings.

1.4. References

1. Kinoshita, S. & Yoshioka, S. Structural colors in nature: The role of regularity and irregularity in the structure. *Chem. Phys. Chem.* **6**, 1442–1459 (2005).
2. Burg, S. L. & Parnell, A. J. Self-assembling structural colour in nature. *J. Phys. Condens. Matter* **30**, 4130001 (2018).
3. Dumanli, G. A. & Savin, T. Recent advances in the biomimicry of structural colours. *Chem. Soc. Rev.* **45**, 6698–6724 (2016).
4. Nassau, K. *The Physics and Chemistry of Color - The Fifteen Causes of Color. Wiley*. (1983).
5. Parker, A. R. 515 million years of structural colour. *J. Opt. A Pure Appl. Opt.* **2**, R15–R28 (2000).
6. Marlow, F., Sharifi, P., Muldarisnur., Brinkmann, R. & Mendive, C. Opals Opals: Status and Prospects. *Angew. Chem. Int. Ed.* **48**, 6212–6233 (2009).

7. Rodrígues, R. E., Agarwal, S. P., An, S., Kazyak, E., Das, D., Shang, W., Skye, R., Deng, T. & Dasgupta, N. P. Biotemplated Morpho Butterfly Wings for Tunable Structurally Colored Photocatalysts. *ACS Appl. Mater. Interfaces* **10**, 4614–4621 (2018).

8. Smith, G. S. Structural color of Morpho butterflies. *Am. J. Phys.* **77**, 1010–1019 (2009).

9. Belmonte, A., Bus, T., Broer, D. J. & Schenning, A. P. H. J. Patterned Full-Color Reflective Coatings Based on Photonic Cholesteric Liquid-Crystalline Particles. *ACS Appl. Mater. Interfaces* **11**, 14376–14382 (2019).

10. Clough, J. M., Guimard, E., Rivet, C., Sprakel, J. & Kodger, T. E. Photonic Paints: Structural Pigments Combined with Water-Based Polymeric Film-Formers for Structurally Colored Coatings. *Adv. Opt. Mater.* **7**, 1900218 (2019).

11. Pan, M., Wang, L., Dou, S., Zhao, J., Xu, H., Wang, B., Zhang, L., Li, X., Pan, L. & Li, Y. Recent Advances in Colloidal Photonic Crystal-Based Anti-counterfeiting materials. *Crystals* **9**, 417 (2019).

12. Chen, K., Zhang, Y. & Ge, J. Highly Invisible Photonic Crystal Patterns Encrypted in Inverse Opaline Macroporous Polyurethane Film for Anti-counterfeiting Applications. *ACS Appl. Mater. Interfaces* **11**, 45256–45264 (2019).

13. Wang, H., Liu, Y., Chen, Z., Sun, L. & Zhao, Y. Anisotropic structural color particles from colloidal phase separation. *Sci. Adv.* **6**, eaay1438 (2020).

14. Fenzl, C., Hirsch, T. & Wolfbeis, O. S. Photonic Crystals for Chemical Sensing and Biosensing. *Angew. Chem. Int. Ed.* **53**, 3318–3335 (2014).

15. Park, J., Yoon, S., Heo, N. & Lee, W. Electrochromic inverse opal photonic gel containing charged hydrogel in aqueous media for full color reflective display. *J. Ind. Eng. Chem.* **88**, 117–126 (2020).

16. Liu, H., Yang, H., Li, Y., Song, B., Wang, Y., Liu, Z., Peng, L., Lim, H., Yoon, J. & Wu, W. Switchable All-Dielectric Metasurfaces for Full-Color Reflective Display. *Adv. Opt. Mater.* **7**, 1801639 (2019).

17. Fu, Y., Tippets, C. A., Donev, E. U. & Lopez, R. Structural colors from natural to artificial systems. *WIREs Nanomed. Nanobiotechnol.* **8**, 758–75 (2016).

18. Takeoka, Y. Environment and human friendly colored materials prepared using black and white components. *Chem. Commun.* **54**, 4905–4914 (2018).

19. Kim, J. Bin, Lee, S. Y., Lee, J. M. & Kim, S. Designing Structural-Color Patterns Composed of Colloidal Arrays. *ACS Appl. Mater. Interfaces* **11**, 14485–14509 (2019).

20. Goerlitzer, E. S. A., Taylor, R. N. K. & Vogel, N. Bioinspired Photonic Pigments from Colloidal Self-Assembly. *Adv. Mater.* **30**, 1706654 (2018).

21. Sakai, M., Seki, T. & Takeoka, Y. Colorful Photonic Pigments Prepared by Using Safe Black and White Materials. *ACS Sustain. Chem. Eng.* **7**, 14933–14940 (2019).

22. Doucet, M. & Meadows, M. G. Iridescence: a functional perspective. *J. R. Soc. Interface* **6**, S115–S132 (2009).

23. Shawkey, M. D., Morehouse, N. I. & Vukusic, P. A protean palette: colour materials and mixing in birds and butterflies. *J. R. Soc. Interface* **6**, S221-S-231 (2009).

24. Kinoshita, S., Yoshioka, S. & Miyazaki, J. Physics of structural colors. *Rep. Prog. Phys.* **71**, 076401 (2008).

25. Sun, J., Bhushan, B. & Tong, J. Structural coloration in nature. *RSC Adv.* **3**, 14862–14889 (2013).

26. Vigneron, J. & Simonis, P. Structural Colours. *Adv. In Insect Phys.* **38**, 181–218 (2010).

27. Tilley, R. J. D. *Colour and the Optical Properties of Materials. Wiley, Second edition*. (2011).

28. Parker, A. R. Natural photonics for industrial inspiration. *Phil. Trans. R. Soc. A* **364**, 1759–1782 (2009).

29. Biró, L. P. & Vigneron, J.-P. Photonic nanoarchitectures in butterflies and beetles valuable sources for bioinspiration. *Laser Photonics Rev* **5**, 27–51 (2011).

30. Paquet, C. & Kumacheva, E. Nanostructured polymers for photonics. *Mater. Today* **11**, 48–56 (2008).

31. Joannopoulos, J. D., Johnson, S. G., Winn, J. N. & Meade, R. D. *Photonic Crystals: Molding the flow of light. Princeton University Press, Second edition*. (2008).

32. Yablonovitch, E. Inhibited Spontaneous Emission in Solid-State Physics and Electronics. *Phys. Rev. Lett.* **58**, 2059–2062 (1987).

33. Prather, D. W., Shi, S., Sharkawy, A., Murakowski, J. & Schneider, G. J. *Photonic crystals: Theory, application, and fabrication*. *Wiley series in Pure and Applied Optics* (2009).

34. López, B. C. Materials Aspects of Photonic Crystals. *Adv. Mater.* **20**, 1679–1704 (2003).

35. Armstrong, E. & Dwyer, C. O. Artificial opal photonic crystals and inverse opal structures – fundamentals and applications from optics to energy storage. *J. Mater. Chem. C* **3**, 6109–6143 (2015).

36. Waterhouse, G. I. N. & Waterland, M. R. Opal and inverse opal photonic crystals: Fabrication and characterization. *Polyhedron* **26**, 356–368 (2007).

37. Ballato, J., Dimaio, J., James, A. & Gulliver, E. Photonic band engineering through tailored microstructural order. *Appl. Phys. Lett.* **75**, 1497 (1999).

38. García, P. D., Sapienza, R., Blanco, Á. & López, C. Photonic Glass: A Novel Random Material for Light. *Adv. Mater.* **19**, 2597–2602 (2007).

39. Shang, G., Eich, M. & Petrov, A. Photonic glass based structural color. *APL Photonics* **5**, 060901 (2020).

40. Reufer, M., Rojas-ochoa, L. F., Eiden, S., Sáenz, J. J. & Scheffold, F. Transport of light in amorphous photonic materials. *Appl. Phys. Lett.* **91**, 171904 (2007).

41. Saranathan, V., Forster, J. D., Noh, H., Liew, S.-F., Mochrie, S. G. J., Cao, H., Dufresne, E. R. & Prum, R. O. Structure and optical function of amorphous photonic nanostructures from avian feather barbs: a comparative small angle X-ray scattering (SAXS) analysis of 230 bird species. *J. R. Soc. Interface* **9**, 2563–2580 (2012).

42. Richard O. Prum, Torres, R. H., Williamson, S. & Dyck, J. Coherent light scattering by blue feather barbs. *Nature* **396**, 28 (1998).

43. Forster, J. D., Noh, H., Liew, S.-F. Saranathan, V., Schreck, C. F., Yang, L., Park, J.-G. & Prum, R. O., Mochrie, S. G. J., Hern, C. S. O., Cao, H., Dufresne, E. R. Biomimetic Isotropic Nanostructures for Structural Coloration. *Adv. Mater.* **22**, 2939–2944 (2010).

44. Finger, E. Visible and UV Coloration in Birds : Mie Scattering as the Basis of Color in Many Bird Feathers. *Naturwissenschaften* **82**, 570–573 (1995).

45. Conley, G. M., Burresi, M., Pratesi, F., Vynck, K. & Wiersma, D. S. Light Transport and Localization in Two-Dimensional Correlated Disorder. *Phys. Rev. Lett.* **112**, 143901 (2014).

46. Aguirre, C., Reguera, E. & Stein, A. Colloidal Photonic Crystal Pigments with Low Angle Dependence. *ACS Appl. Mater. interfaces* **2**, 3257–3262 (2010).

47. Lee, S., Kumar, S., Woo, J. & Lee, J. Coloration of colloidal polymer particles through selective extraction of Mie backscattering for cation-responsible colorimetric sensors. *J. Colloid Interface Sci.* **560**, 894–901 (2020).

48. Noh, H., Liew, S.-F., Saranathan, V., Mochrie, S. G. J., Prum, R. O., Dufresne, E. R. & Cao, H. How Noniridescent Colors Are Generated by Quasi-ordered Structures of Bird Feathers. *Adv. Mater.* **22**, 2871–2880 (2010).

49. Noh, H., Liew, S.-F., Saranathan, V., Prum, R. O., Mochrie, S. G. J., Dufresne, E. R. & Cao, H. Contribution of double scattering to structural coloration in quasiordered nanostructures of bird feathers. *Phys. Rev. E* **81**, 051923 (2010).

50. Noh, H., Liew, S.-F., Saranathan, V., Prum, R. O., Mochrie, S. G. J., Dufresne, E. R. & Cao, H. Double scattering of light from Biophotonic Nanostructures with short-range order. *Opt. Express* **18**, 11942–11948 (2010).

51. Hwang, V., Stephenson, A. B., Magkiriadou, S., Park, J. & Manoharan, V. N. Effects of multiple scattering on angle-independent structural color in disordered colloidal materials. *Phys. Rev. E* **101**, 012614 (2020).

52. Schertel, L., Siedentop, L., Meijer, J.-M., Keim, P., Aegerter, C. M., Aubry, G. J. & Maret, G. The Structural Colors of Photonic Glasses. *Adv. Opt. Mater.* **7**, 1900442 (2019).

53. Magkiriadou, S., Park, J., Kim, Y. & Manoharan, V. N. Absence of red structural color in photonic glasses, bird feathers, and certain beetles. *Phys. Rev. E* **90**, 062302 (2014).

54. Lee, S., Kumar, S., Choi, J. W., Kim, V. Y. & Lee, J. Copolymer Particles with Incorporated Gold and Silver Nanoparticles to Absorb Short-Wavelength Scattering in Full-Color Photonic Glasses. *Part. Part. Syst. Charact.* **36**, 1900167 (2019).

55. Liu, P., Bai, L., Yang, J., Gu, H., Zhong, Q., Xie, Z. & Gu, Z. Self-assembled colloidal arrays for structural color. *Nanoscale Adv.* **1**, 1672–1685 (2019).

56. Takeoka, Y., Yoshioka, S., Takano, A., Arai, S., Nueangnoraj, K., Nishihara, H., Teshima, M., Ohtsuka, Y. & Seki, T. Production of Colored Pigments with Amorphous Arrays of Black and White Colloidal Particles. *Angew. Chem.* **125**, 7402–7406 (2013).

57. Josephson, D. P., Eric J. Popczun & Stein, A. Effects of Integrated Carbon as a Light Absorber on the Coloration of Photonic Crystal-Based Pigments. *J. Phys. Chem. C* **117**, 13585–13592 (2013).

58. Velev, O. D. & Gupta, S. Materials Fabricated by Micro- and Nanoparticle Assembly – The Challenging Path from Science to Engineering. *Adv. Mater.* **21**, 1897–1905 (2009).

59. Bishop, K. J. M., Wilmer, C. E., Soh, S. & Grzybowski, B. A. Nanoscale Forces and Their Uses in Self-Assembly. *Small* **5**, 1600–1630 (2009).

60. Phillips, K. R., England, G. T., Sunny, S., Shirman, E., Shirman, T., De, Vogel, N. & Aizenberg, J. A colloidoscope of colloid-based porous materials and their uses. *Chem. Soc. Rev.* **45**, 281–322 (2016).

61. Gaillou, E., Fritsch, E., Aguilar-Reyes, B., Rondeau, B., Post, J., Barreau, A. & Ostroumov, M. Common gem opal: An investigation of micro- to nano-structure. *Am. Mineral.* **93**, 1865–1873 (2008).

62. Dufresne, E. R., Noh, H., Saranathan, V., Mochrie, S. G. J. & Prum, R. O. Self-assembly of amorphous biophotonic nanostructures by phase separation. *Soft Matter,* **5**, 1792–1795 (2009).

63. Saenko, S., Saenko, S. V., Marel, D. Van Der & Milinkovitch, M. Photonic crystals cause active colour change in chameleons. *Nat. Commun.* **6**, 6368 (2015).

64. Galisteo-lópez, J. F., Ibisate, M., Sapienza, R. & Froufe-Pérez, L. S. Self-Assembled Photonic Structures. *Adv. Mater.* **23**, 30–69 (2011).

65. Magkiriadou, S., Park, J., Kim, Y. & Manoharan, V. N. Disordered packings of core-shell particles with angle-independent structural colors. *Opt. Mater. Express* **2**, 1343–1352 (2012).

66. Yoshioka, S. & Takeoka, Y. Production of Colourful Pigments Consisting of Amorphous Arrays of Silica Particles. *ChemPhysChem* **15**, 2209–2215 (2014).

67. Park, J.-G., Kim, S.-H., Magkiriadou, S., Choi, T. M., Kim, Y.-S. & Manoharan, V. N. Full-Spectrum Photonic Pigments with Non-iridescent Structural Colors through Colloidal Assembly. *Angew. Chem. Int. Ed.* **53**, 2899–2903 (2014).

68. Haibo Hu, Zhong, H. & Chen, Q. Magnetically responsive photonic watermarks on banknotes. *J. Mater. Chem. C* **2**, 3695–3702 (2014).

69. Finlayson, C. E. & Baumberg, J. J. Polymer opals as novel photonic materials. *Polym Int.* **62**, 1403–1407 (2013).

70. Smolin, D. A., Hellmann, G. P. & Gallei, M. Fully Reversible Shape Transition of Soft Spheres in Elastomeric Polymer Opal Films. *Langmuir* **29**, 11275–11283 (2013).

71. Wang, J., Hu, Y., Deng, R., Liang, R., Li, W., Liu, S. & Zhu, J. Multiresponsive Hydrogel Photonic Crystal Microparticles with Inverse-Opal Structure. *Langmuir* **29**, 8825–8834 (2013).

72. Marcelo, G., Areias, L. R. P., Maçôas, E., Mendicuti, F., Valiente, M., Martinho, J. M. G. & Farinha, J. P. S. Structural color and rheology of self-assembled poly(N-isopropylacrylamide-methacrylic acid) microgels in water. *Eur. Polym. J.* **113**, 349–356 (2019).

73. Qi, F., Meng, Z., Xue, M. & Qiu, L. Recent advances in self-assemblies and sensing applications of colloidal photonic crystals. *Anal. Chim. Acta* **1123**, 91–112 (2020).

74. Li, L., Kolle, S., Weaver, J. C., Ortiz, C., Aizenberg, J., Kolle, M. A highly conspicuous mineralized composite photonic architecture in the translucent shell of the blue-rayed limpet. *Nat. Commun.* **6**, 6322 (2015).

75. Lekkerkerker, H. N. W. & Tuinier, R. *Colloids and the Depletion Interaction. Lectures notes in physics, Springer*. (2011).

76. Pusey, P. N. & Megen, W. Van. Phase behaviour of concentrated suspensions of nearly hard colloidal spheres. *Nature* **320**, 340–342 (1986).

77. Poon, W. Colloids as Big Atoms. *Science* **304**, 830–831 (2004).

78. Pusey, P. N. The effect of polydispersity on the crystallization of hard spherical colloids. *J. Phys.* **48**, 709–712 (1987).

79. Koh, Y. K., Yip, C. H., Chiang, Y. & Wong, C. C. Kinetic Stages of Single-Component Colloidal Crystallization. *Langmuir* **24**, 5245–5248 (2008).

80. Jeong, B. U., Wang, Y., Ibisate, M. & Xia, Y. Some New Developments in the Synthesis , Functionalization , and Utilization of Monodisperse Colloidal Spheres. *Adv. Funct. Mater.* **15**, 1907–1921 (2005).

81. Li, F., Josephson, D. P. & Stein, A. Colloidal Assembly: The Road from Particles to Colloidal Molecules and Crystals Angewandte. *Angew. Chem. Int. Ed.* **50**, 360–388 (2011).

82. Poon, W. C. K., Weeks, R. & Royall, C. P. On measuring colloidal volume fractions. *Soft Matter* **8**, 21–30 (2012).

83. Russel, W. B. & Haig, D. Tunable colloidal crystals. *Nature* **421**, 490–491 (2003).

84. Yethiraj, A. & Blaaderen, A. Van. A colloidal model system with an interaction tunable from hard sphere to soft and dipolar. *Nature* **421**, 513–517 (2003).

85. Vogel, N., Retsch, M., Fustin, C., Campo, A. & Jonas, U. Advances in Colloidal Assembly: The Design of Structure and Hierarchy in Two and Three Dimensions. *Chem. Rev.* **115**, 6265–6311 (2015).

86. Hernandez, E. C., Guerrero, J., Fernandez-Nieves, A. & Gordillo, J. M. Drop generation in controlled fluid flows. in *Fluids, Colloids and Soft Materials: An Introduction to Soft Matter Physics,* John Wiley & Sons, Hoboken (2016).

87. Li, Q., Jonas, U., Zhao, X. S. & Kappl, M. The forces at work in colloidal self-assembly: a review on fundamental interactions between colloidal particles. *Asia-Pac. J. Chem. Eng.* **3**, 255–268 (2008).

88. Israelachvili, J. N. *Intermolecular and Surface Forces. Third Edition, Elsevier*. (2011).

89. Yethiraj, A. Tunable colloids: control of colloidal phase transitions with tunable interactions. *Soft Matter* **3**, 1099–1115 (2007).

90. Wasan, D., Nikolov, A. & Moudgil, B. Colloidal dispersions: Structure, stability and geometric confinement. *Powder Technol.* **153**, 135–141 (2005).

91. Garcia, P. D., Sapienza, R. & López, C. Photonic Glasses: A Step Beyond White Paint. *Adv. Mater.* **22**, 12–19 (2010).

92. Meseguer, F. Colloidal crystals as photonic crystals. *Colloids Surfaces A Physicochem. Eng. Asp.* **270**–**271**, 1–7 (2005).

93. Freymann, G. von, Kitaev, V., Lotsch, B. V. & Ozin, G. A. Bottom-up assembly of photonic crystals. *Chem Soc Rev* **42**, 2528–2554 (2013).

94. Busch, K. & John, S. Photonic band gap formation in certain self-organizing systems. *Phys. Rev. E* **58**, 3896–3908 (1998).

95. Stober, W. & Fink, A. Controlled Growth of Monodisperse Silica Spheres in the Micron Size Range. *J. Colloid Interface Sci.* **26**, 62–69 (1968).

96. Arshady, R. Suspension, emulsion, and dispersion polymerization: A methodological survey. *Colloid Polym. Sci.* **270**, 717–732 (1992).

97. Mittal, V. *Advanced Polymer Nanoparticles, Synthesis and Surface Modifications. CRC Press*. (2011).

98. Gaillot, D. P. & Summers, C. J. Inverse Opal Photonics. in *Atomic Layer Deposition of Nanostructured Materials, First Edition, Wiley-VCH.* 345–375 (2012).

99. Lozano, G. S., Dorado, L. A., Depine, R. A. & Míguez, H. Towards a full understanding of the growth dynamics and optical response of self-assembled photonic colloidal crystal films. *J. Mater. Chem. C* **19**, 185–190 (2009).

100. Nijs, B. D., Dussi, S., Smallenburg, F., Meeldijk, J. D., Groenendijk, D. J., Filion, L., Imhof, A., Blaaderen, A. V. & Dijkstra, M. Entropy-driven formation of large icosahedral colloidal clusters by spherical confinement. *Nat. Mater.* **14**, 56–60 (2015).

101. Vinothan N. Manoharan. Colloidal matter: Packing, geometry, and entropy. *Science* **349**, 1253751 (2015).

102. Mau, S. & Huse, D. A. Stacking entropy of hard-sphere crystals. *Phys. Rev. E* **59**, 4396–4401 (1999).

103. Schu, S., Roller, J., Kick, A., Meijer, J. & Zumbusch, A. Real-space imaging of translational and rotational dynamics of hard spheres from the fluid to the crystal. *Soft Matter* **13**, 8240–8249 (2017).

104. Alsayed, A. M., Islam, M. F., Zhang, J., Collings, P. J. & Yodh, A. G. Premelting at defects within bulk colloidall crystals. *Science* **309**, 1207–1211 (2005).

105. Blaaderen, A. Van & Wiltzius, P. Real-Space Structure of Colloidal Hard-Shere Glasses. *Science* **270**, 1177–1179 (1995).

106. Janne-Mieke Meijer. Colloidal Crystals of Spheres and Cubes in Real and Reciprocal Space. Springer Theses. (2014).

107. Dolbnya, I. P., Petukhov, A. V, Aarts, D. G. A. L., Vroege, G. J. & Lekkerkerker, H. N. W. Coexistence of rhcp and fcc phases in hard-sphere colloidal crystals. *Eur. Lett.* **72**, 962–968 (2005).

108. Bolhuis, P. G., Frenkel, D., Mau, S.-C. & Huse, D. A. Entropy difference between crystal phases. *Nature* **388**, 235–237 (1997).

109. Xia, B. Y., Gates, B., Yin, Y. & Lu, Y. Monodispersed Colloidal Spheres: Old Materials with New Applications. *Adv. Mater.* **12**, 693–713 (2000).

110. Ledermann, A., Cademartiri, L., Hermatschweiler, M., Toninelli, C., Ozin, G. A., Wiersma, D. S., Wegener, M. & Freymann, G. V. Three-dimensional silicon inverse photonic quasicrystals for infrared wavelengths. *Nat. Mater.* **5**, 942–945 (2006).

111. Arsenault, A., Fleischhaker, F., Freymann, G. V., Kitaev, V., Miguez, H., Mihi, A., Tétreault, N., Vekris, E., Manners, I., Aitchison, S., Perovic, D. & Ozin, G. A. Perfecting Imperfection — Designer Defects in Colloidal Photonic Crystals. *Adv. Mater.* **18**, 2779–2785 (2006).

112. Wintzheimer, S., Granath, T., Oppmann, M., Kister, T., Thai, T., Kraus, T., Vogel, N. & Mandel, K. Supraparticles: Functionality from Uniform Structural Motifs. *ACS Nano* **12**, 5093–5120 (2018).

113. Míguez, H., Meseguer, F., López, C., Mifsud, A., Moya, J. S. & Vázques, L. Evidence of FCC Crystallization of SiO_2 Nanospheres. *Langmuir* **13**, 6009–6011 (1997).

114. Míguez, H., López, C., Meseguer, F., Blanco, A., Vázquez, L., Mayoral, R., Ocaña, M., Fornés, V. & Mifsud, A. Photonic crystal properties of packed submicrometric SiO_2 spheres. *Appl. Phys. Lett.* **71**, 1148–1150 (1997).

115. Vlasov, Y. A., Astratov, V. N., Baryshev, A. V., Kaplyanskii, A. A., Karimov, O. Z. & Limonov, M. F. Manifestation of intrinsic defects in optical properties of self-organized opal photonic crystals. *Phys. Rev. E* **61**, 5784–5793 (2000).

116. Bardosova, M., Pemble, M. E., Povey, I. M., R. H. Tredgold, A. & Whitehead, D. E. Enhanced Bragg reflections from size-matched heterostructure photonic crystal thin films prepared by the Langmuir-Blodgett method. *Appl. Phys. Lett.* **89**, 093116 (2006).

117. Jiang, P., Bertone, J. F., Hwang, K. S. & Colvin, V. L. Single-Crystal Colloidal Multilayers of Controlled Thickness. *Chem. Mater.* **11**, 2132–2140 (1999).

118. Krassimir P. Velikov, Christova, C. G., Dullens, R. P. A. & Blaaderen, A. van. Layer-by-Layer Growth of Binary Colloidal Crystals. *Science.* **296**, 106–110 (2002).

119. Park, S. H., Qin, D. & Xia, Y. Crystallization of Mesoscale Particles over Large Areas. *Adv. Mater* **10**, 1028–1032 (1998).

120. Hou, J., Li, M. & Song, Y. Patterned Colloidal Photonic Crystals. *Angew. Chem. Int. Ed.* **57**, 2544–2553 (2018).

121. Khanh, N. N. & Yoon, K. B. Facile Organization of Colloidal Particles into Large , Perfect One- and Two-Dimensional Arrays by Dry Manual Assembly on Patterned Substrates. *J. Am. Chem. Soc.* **131**, 14228–14230 (2009).

122. Blaaderen, A. Van, Ruelt, R. & Wiltziust, P. Template-directed colloidal crystallization. *Nature* **385**, 321–324 (1997).

123. Yang, S. M. & Ozin, G. A. Opal chips: vectorial growth of colloidal crystal patterns inside silicon wafers. *Chem. Commun.* 2507–2508 (2000).

124. Imhof, A. & Pine, D. J. Ordered macroporous materials by emulsion templating. *Nature* **389**, 948–951 (1997).

125. Manoharan, V. N., Imhof, A., Thorne, J. D. & Pine, D. J. Photonic Crystals from Emulsion Templates. *Adv. Mater.* **13**, 447–450 (2001).

126. Egen, M. & Zentel, R. Tuning the Properties of Photonic Films from Polymer Beads by Chemistry. *Chem. Mater.* **14**, 2176–2183 (2002).

127. Griesebock, B., Egen, M. & Zentel, R. Large Photonic Films by Crystallization on Fluid Substrates. *Chem. Mater.* **14**, 4023–4025 (2002).

128. Zhou, L., Liu, G., Wu, Y., Fan, Q. & Sha, J. The Synthesis of Core-shell Monodisperse P(St-MAA) Microspheres and Fabrication of Photonic Crystals Structure with Tunable Colors on Polyester Fabrics. *Fibers Polym.* **15**, 1112–1122 (2014).

129. Yeo, S. J., Tu, F., Kim, S.-H., Yi, G.-R. Yoo, P. J. & Lee, D. Angle- and strain-independent coloured free-standing films incorporating non-spherical colloidal photonic crystals. *Soft Matter* **11**, 1582–1588 (2015).

130. Sowade, E., Blaudeck, T. & Baumann, R. R. Inkjet Printing of Colloidal Nanospheres: Engineering the Evaporation-Driven Self-Assembly Process to Form Defined Layer Morphologies. *Nanoscale Res. Lett.* **10**, 362 (2015).

131. Brugarolas, T., Tu, F. & Lee, D. Directed assembly of particles using microfluidic droplets and bubbles. *Soft Matter* **9**, 9046–9058 (2013).

132. Dendukuri, B. D. & Doyle, P. S. The Synthesis and Assembly of Polymeric Microparticles Using Microfluidics. *Adv. Mater.* **21**, 4071–4086 (2009).

133. Utada, A. S., Chu, L., Link, D. R., Holtze, C. & Weitz, D. A. Dripping, Jetting, Drops, and Wetting: The Magic of Microfluidics. *MRS Bull.* **32**, 702–708 (2007).

134. Wang, J., Wang, J. & Han, J. Fabrication of Advanced Particles and Particle-Based Materials Assisted by Droplet-Based Microfluidics. *Small* **13**, 1728–1754 (2011).

135. Xia, Y. & Whitesides, G. M. Soft Lithography. *Angew. Chem. Int. Ed.* **37**, 550–575 (1998).

136. Anna, S. L., Bontoux, N. & Stone, H. A. Formation of dispersions using 'flow focusing' in microchannels. *Appl. Phys. Lett.* **82**, 364–366 (2003).

137. Abate, A. R. & Weitz, D. A. High-Order Multiple Emulsions Formed in Poly (dimethylsiloxane) Microfluidics. *Small* **5**, 2030–2032 (2009).

138. Amstad, E., Chemama, M., Eggersdorfer, M., Arriaga, L. R., Brenner, M. P. & Weitz, D. A. Robust scalable high throughput production of monodisperse drops. *Lab Chip* **16**, 4163–4172 (2016).

139. Nawar, S., Stolaroff, J. K., Ye, C., Wu, H., Nguyen, D. T., Xin, F. & Weitz, D. A. Parallelizable microfluidic dropmakers with multilayer geometry for the generation of double emulsions. *Lab Chip* **20**, 147–154 (2020).

140. Yadavali, S., Lee, D. & Issadore, D. Robust Microfabrication of Highly Parallelized Three-Dimensional Microfluidics on Silicon. *Sci. Rep.* **9**, 1123 (2019).

141. Stolovicki, E., Ziblat, R. & Weitz, D. A. Throughput enhancement of parallel step emulsifier devices by shear-free and efficient nozzle clearance. *Lab Chip* **18**, 132–138 (2018).

142. Rastogi, V., Melle, S., Calderón, O. G., García, A. A., Marquez, M. & Velev, O. D. Synthesis of Light-Diffracting Assemblies from Microspheres and Nanoparticles in Droplets on a Superhydrophobic Surface. *Adv. Mater.* **20**, 4263–4268 (2008).

143. Cho, Y., Kim, S., Yi, G. & Yang, S. Self-organization of colloidal nanospheres inside emulsion droplets: Higher-order clusters, supraparticles, and supraballs. *Colloids Surfaces A Physicochem. Eng. Asp.* **345**, 237–245 (2009).

144. Manoharan, V. N. Colloidal spheres confined by liquid droplets: Geometry, physics, and physical chemistry. *Solid State Commun.* **139**, 557–561 (2006).

145. Boles, M. A., Engel, M. & Talapin, D. V. Self-Assembly of Colloidal Nanocrystals: From Intricate Structures to Functional Materials. *Chem. Rev.* **116**, 11220–11289 (2016).

146. Bhardwaj, R., Fang, X., Somasundaran, P. & Attinger, D. Self-Assembly of Colloidal Particles from Evaporating Droplets: Role of DLVO Interactions and Proposition of a Phase Diagram. *Langmuir* **26**, 7833–7842 (2010).

147. Zhao, Y., Shang, L., Cheng, Y. & Gu, Z. Spherical Colloidal Photonic Crystals. *Acc. Chem. Res.* **47**, 3632–3642 (2014).

148. Vogel, N., Utech, S., England, G. T., Shirman, T., Phillips, K. R., Koay, N., Burgessd, I. B., Kolle, M., Weitz, D. A. & Aizenberg, J. Color from hierarchy: Diverse optical properties of micron-sized spherical colloidal assemblies. *PNAS* **112**, 10845–10850 (2015).

149. Takeoka, Y., Yoshioka, S., Takano, A., Arai, S., Nueangnoraj, K., Nishihara, H., Teshima, M., Ohtsuka, Y. & Seki, T. Production of Colored Pigments with Amorphous Arrays of Black and White Colloidal Particles. *Angew. Chem. Int. Ed.* **52**, 7261–7265 (2013).

150. Ding, T., Long, Y., Zhong, K., Song, K. & Tung, C. Modifying the symmetry of colloidal photonic crystals: a way towards complete photonic bandgap. *J. Mater. Chem. C* **2**, 4100–4111 (2014).

2. Synthesis and characterization of polymer nanoparticles

In this chapter we describe the preparation and characterization of polymer nanoparticles (PNP) for the assembling of colloidal photonic structures. A general description of the heterogeneous polymerization techniques is introduced, followed by the synthesis of PNP, through batch emulsion polymerization. These PNP are composed of a polystyrene core and a thin shell of poly(methyl methacrylate-co-acrylic acid) (P(St-MMA-AA)) in the size range from ~170 nm to 335 nm in mean diameter, with narrow size distributions.

2.1. Polymer nanoparticles

Polymer nanoparticles (PNP) are a very important class of polymeric materials, used for many applications, like coatings, adhesives, paints, etc. The size and the particle size distribution of PNP, controlled by the synthetic procedure, are of great importance because they determine key properties such as viscosity, surface area, and packing density.[1,2]

2.1.1. Heterogeneous polymerization techniques

There are three major types of heterogeneous polymerization processes: precipitation, suspension, and emulsion.[3,4] Particle forming polymerization techniques are distinguished based on four criteria, namely, the initial state of the polymerization mixture; the kinetics of the polymerization; the mechanism of particle formation; and on the shape and size of the final polymer particles. Although different synthesis methods could be used for heterogeneous polymerization procedures, all the systems are characterized by a continuous phase (polymerization medium) containing dispersed phases.[5,6] Adjusting the experimental conditions and selecting appropriate reaction type, spherical polymer particles can be produced within relatively narrow size ranges from about 30 nm to 1−2 mm.[7] Approximate particle sizes that can be prepared from various heterogeneous polymerization techniques are schematically depicted in Figure 2.1.

Precipitation polymerization refers to processes in which the initial reaction medium is a homogeneous solution, but the synthesized polymer precipitates during the course of the polymerization.[6] Precipitation polymerization leading to the formation of polymer particles of colloidal dimensions is called dispersion polymerization.

In the dispersion polymerization process, the monomer and initiator are soluble in the continuous phase. The polymer particles, which precipitate as they are produced, are stabilized against coagulation.[8,9] This polymerization yields polymer particles with 0.1−15 μm diameter, often with low size dispersity. Dispersion polymerization covers the particle size gap between emulsion and suspension polymerizations.

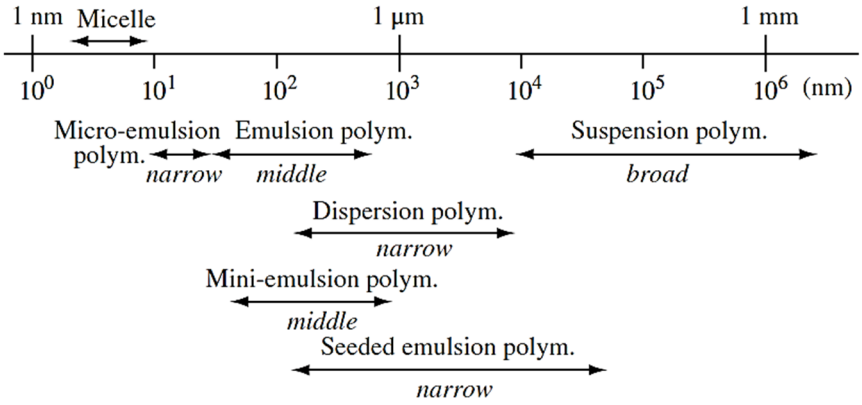

Figure 2.1: Approximate particle size range and distribution width (narrow, broad, middle) that can be prepared from the various heterogeneous polymerization techniques. Adapted from Tobita and Hamielec.[5]

Suspension polymerization can be used to prepare polymer particles with larger sizes, and is carried out by suspending monomer droplets, between 50−500 μm in diameter, in a aqueous continuous phase (that is nonsolvent for both monomer and formed polymer). The monomer droplets (subsequently converted to polymer particles) are prevented from coalescing by stirring and by surface active stabilizing agents.[10,11] In suspension polymerization, the initiator is located mainly in the monomer droplets. As the polymerization progresses the droplets are transformed into sticky, viscous monomer-polymer particles which finally become rigid, spherical polymer particles with sizes from 50−500 μm.[5] The control of particle size distribution is in general complex and so is the scaling-up of the process.[12]

Because we were particularly interested in obtaining polymer nanoparticles within the size range comparable to the wavelengths of visible light, emulsion polymerization was our method of choice.

2.1.2. Emulsion polymerization

Emulsion polymerization involves emulsification of monomers (dispersed phase) in a continuous aqueous phase forming an oil-in-water (O/W) emulsion (inverse emulsion (W/O) polymerization is also possible). Emulsion polymerization differs from suspension polymerization in two important aspects: the initiator is located in the aqueous phase, and the polymer particles produced are orders of magnitude smaller than in suspension polymerization. At the end of emulsion polymerization, a colloidal dispersion of polymer nanoparticles whose diameter is about several tens to a few hundred nanometers, is obtained.[13,14]

Emulsion polymerization is the most common method used to produce a wide range of PNP. Based on the utilization of surfactant, it can be classified as conventional and surfactant-free emulsion polymerization.[15] A conventional emulsion polymerization formulation usually comprises monomer(s), water, surfactant, and a water-soluble initiator. The reaction system is characterized by large monomer droplets (ca. 1−10 μm in diameter) dispersed in the continuous aqueous phase with the aid of a surfactant. Monomer-swollen micelles (ca. 5−10 nm in diameter) may also exist in the reaction medium provided that the concentration of surfactant in the aqueous phase is above its critical micelle concentration (CMC). Only a small fraction of the relatively hydrophobic monomer(s) is present in the micelles (if present) or dissolved in the aqueous phase. Most of the monomer is stored in the emulsified monomer droplets that acts as monomer reservoirs. When the surfactant concentration is below the CMC or in surfactant-free emulsion polymerizations usually a small amount of functional hydrophilic comonomers (such as acrylic or methacrylic acids) and ionizable initiators (such as potassium persulfate) are commonly used to improve the colloidal stability during polymerization.[16]

Emulsion polymerization starts when water-borne initiator radicals generated by the decomposition of the initiator molecules, grow in size via the propagation reaction with monomer molecules dissolved in the aqueous phase. Different mechanisms of particle nucleation, namely micellar or homogeneous, have been proposed for the formation of stable particles, which are the primary sites of the polymerization.[17-20]

Micellar nucleation mechanism comprises particle formation by the entry of radicals, generated in the aqueous phase, into the monomer-swollen micelles. Water-borne free radicals first polymerize with monomer molecules dissolved in the continuous aqueous phase, increasing thus, the hydrophobicity of the oligomeric radicals. When a critical chain length is achieved, these oligomeric radicals become so hydrophobic that they show a strong tendency to enter the monomer-swollen micelles and then continue to propagate by reacting with the monomer molecules therein, originating a particle nuclei. To guarantee adequate colloidal stability of the growing particle nuclei, micelles that do not contribute to particle nucleation disband to supply the increasing demand for surfactant. In addition, the surfactant molecules adsorbed on monomer droplets may also

desorbs out of the droplet surface, diffuse across the continuous aqueous phase and then adsorb on the expanding particle surface.[21,22]

In the case of homogeneous nucleation, the initiator radicals reacts with the small amount of monomer in the aqueous phase, and the propagation continues beyond a critical chain length before the growing oligomer is no longer soluble in the aqueous phase, and undergoes a coil-to-globule transition. This transition excludes water, forming a precursor particle that can become swollen with monomer. These precursor particles either grow via propagation or coagulation with other precursor particles to form a stable particle.[23] Coagulation occurs until reaching a critical surface potential to prevent further coagulation. As particles coagulate, the surface-to-volume ratio decreases, which causes an increase in surface potential. When the particles become sufficiently large, coagulation ceases due to an insufficient kinetic energy to overcome the bi-particle surface repulsion.[1,19]

The relative importance of micellar and homogeneous nucleation mechanisms depends strongly on the water solubility of the monomers and surfactant concentration in the aqueous phase. High surfactant concentrations and less water-soluble monomers will favor micellar nucleation. Homogenous particle nucleation is attributed to systems where either the amount of surfactant is below its CMC, no surfactant is used during the polymerization, or the monomer is significantly water soluble.[21,22]

When nucleation is completed, the number of polymer particles per unit volume of water remains relatively constant toward the end of the polymerization. After this stage, the newly formed radicals are absorbed by the growing polymer particles, which are the main loci of polymerization and growth. The monomer concentration inside the polymer particles is kept constant by diffusion of monomer from the monomer reservoirs (monomer droplets) through the aqueous phase into the polymer particles. At a certain conversion, the monomer reservoirs are consumed and disappear, decreasing the monomer concentration in the reaction loci towards the end of the polymerization. The size of the particles produced is usually confined in the range of 30−500 nm.[22,24,25]

From a mechanistic point of view, radical compartmentalization is likely the most distinctive feature of emulsion polymerization. This refers to the fact that the radicals are distributed among the different particles, and hence radicals in

different particles cannot terminate between them. This allows the simultaneous achievement of high polymerization rates and higher molecular weight polymers than in bulk or suspension systems. Both the polymerization rate and the molecular weight depend on the average number of radicals per particle.[23,26]

Larger particle sizes can be produced using a relatively low surfactant concentration in the particle nucleation stage. In addition, a narrow particle size distribution will be achieved. This is simply because a shorter particle nucleation period, results in narrower particle size distributions.[21] Particle nucleation controls the particle size and particle size distribution. The use of salts is common in emulsion polymerization, controlling the viscosity and ionic strength of the medium, both of which influence the course of the nucleation process.[7,15,24]

The term emulsion polymerization does not mean polymerization occurs in the droplets of a monomer, with the exception of mini-emulsion polymerization.[27] The droplets surface area in these systems is very large due to their small size (10−500 nm diameter) and most of the surfactant is adsorbed at the monomer droplet surface, stabilizing them.[28] Droplet nucleation in mini-emulsion polymerizations make it suitable for synthesizing particles containing additives (e.g. dyes) or for co-polymerizing highly water insoluble monomers that are difficult to polymerize in emulsion because of their limited transport rate through the aqueous phase.

2.2. Experimental part

2.2.1. Materials

Deionized water from a Millipore system Milli-Q ≥ 18 MΩ cm (with a Millipak membrane filter 0.22 μm) was used. Styrene (St, Sigma-Aldrich, ≥ 99%) and acrylic acid (AA, Aldrich, 99%) were used after passing through a column of aluminum oxide (Sigma Aldrich, activated, basic, 58 Å pore size) to remove the inhibitors. Methyl methacrylate (MMA, Aldrich, 99%), sodium dodecyl sulfate (SDS, 99%, Alfa Aesar), sodium hidrogenocarbonate (99.7%, Aldrich) and potassium peroxydisulfate (KPS, 99.99%, Alfa Aesar) were used as received.

2.2.2. Polymer nanoparticles synthesis

Polymer nanoparticles were synthesized by batch emulsion polymerization using a jacketed cylindrical reaction vessel (Verre-Labo Mula), equipped with a reflux

condenser, and a PTFE blade powered by a high-torque mechanical stirrer (Heidolph RZR 2040). The temperature was maintained through the jacket with the use of a circulating temperature bath (Lauda ecoline 003). A typical sample was prepared as follows: the reaction vessel was charged with 120 mL of mili-Q water containing $NaHCO_3$ (0.8 g) and SDS (0.05 g). To this aqueous solution was added a mixture of previously deinhibited monomers, consisting of 25 mL of styrene (St), methyl methacrylate (MMA) and acrylic acid (AA) (St/MMA/AA (90:5:5 v/v/v). Table 2.1 summarizes the quantity of monomers, surfactant, initiator, continuous phase, and salt for the PNP synthesis.

A nitrogen atmosphere and a stirring rate of 400 rpm were maintained throughout the reaction. The emulsion was deoxygenated by bubbling with nitrogen at room temperature for 30 min, and then a gradual increase in temperature was performed until 70°C. After 20 min at 70°C, the initiator (0.4g) was added. The reaction proceeded for 5h, and was followed by DLS, to monitor the size and size dispersity of the PNP. Upon completion of the reaction and after cooling, the colloidal dispersions were filtered through glass wool and stored.

Table 2.1: Reagents amount for the synthesis of PNP with different diameters.

Sample	**Monomers (g)**			**Surfactant (mg)**	**Initiator (g)**	**Continuous phase (mL)**	**Buffering agent (g)**
	St	MMA	AA	SDS	KPS	H_2O	$NaHCO_3$
1	20.5	1.2	1.3	48	0.4	120	0.8
2				40			
3				35			
4				30			
5				25			
6				21			
7				15			
8				12			
9				10			

2.2.3. Characterization methods

pH measurements: pH was measured using a VWR pHenomenal pH 1000 L pH meter equipped with a VWR pHenomenal MIC 220 microelectrode and a VWR pHenomenal PT1000 1 M temperature sensor.

Dynamic light scattering (DLS): hydrodynamic diameter determination was performed on diluted dispersions of nanoparticles in MilliQ water at 20°C. Measurements were carried with a Malvern Zetasizer Nano ZS series apparatus

(equipped with BI-200SM goniometer, BI-APD avalanche photodiode detector, and BI-9000AT autocorrelator; Spectra Physics (Santa Clara, CA, USA) He-Ne laser with 35 mW at 632.8 nm). The principle of dynamic light scattering is that fine particles and molecules that are in constant random thermal motion (Brownian motion), diffuse at a speed related to their size, smaller particles diffusing faster than larger particles. The scattering intensity will fluctuate with time and this is detected using a sensitive avalanche photodiode detector (APD). The intensity changes are analyzed with a digital autocorrelator which generates a correlation function. This curve can be analyzed to give the size and the size distribution. Z-average was calculated from the analysis of the autocorrelation functions from ten measurements for each sample. The polydispersity index (PDI) in DLS typically depicts the intensity of light scattered by nanoparticles in different fractions of the same sample and is calculated by $(\text{width/mean})^2$ of the peak. We only consider PDI of ≤ 0.06 to be sufficiently monodisperse samples.

Nanoparticle Tracking Analysis (NTA): hydrodynamic diameter determination was also performed with a digital microscope LM20 System (NanoSight, Salisbury, UK). The diluted samples were injected with syringes into the sample chamber equipped with a 405 nm diode laser. Camera settings were adapted to different samples due to different scattering power of the particles. Videos of scattering particles undergoing Brownian motion, were captured, and analyzed with NanoSight NTA 2.3 Analytical Software. Samples were measured in the single shutter and gain mode for 60 seconds with manual brightness and threshold adjustments at 20°C. Five measurements of each, always newly injected, sample were performed. The mean size and size distributions were obtained by the NTA software.

Scanning electron microscopy (SEM): images were obtained on a JEOL scanning electron microscope (Model JSM7001F, JEOL, Tokyo, Japan), with an accelerating voltage of 15 kV. A field emission gun (FEG) was used as electron source giving a more coherent beam and higher brightness than the tungsten filament, leading to greatly improved image quality and resolution. One drop of diluted particles dispersions in water was dried directly on the SEM stub before coating with gold using a turbo-pumped sputter coater from Quorum Technology (model Q150T ES, Quorum Technology, Ashford, UK) for 1 min; Au/Pd spin coated layer ≤ 5 nm. SEM images were processed with ImageJ® software

(http://rsbweb.nih.gov/ij/), to obtain information on mean size, standard deviation and overall estimation of size PDI (PDI is given by the ratio of the standard deviation by the mean diameter value of at least 100 nanoparticles).

Differential scanning calorimetry (DSC): calorimetric experiments were carried out in a DSC Q2000 from TA Instruments Inc. (TzeroTM DSC technology) operating in the Heat FlowT4P option. Measurements were performed under anhydrous high purity nitrogen at a flow rate of 50 mL/min. The sample cell is an aluminum pan in which few milligrams (between 3 to 5 mg) of a dry powder of PNP is placed. The reference cell is an empty aluminum pan. Both sample and reference cell are heated/cooled with a constant rate of 10°C/min, from 0°C to 160°C. The glass transition temperature (Tg) was determined for two PNP samples. To guarantee a precise determination of the Tg, nanoparticles dispersions were thoroughly washed with water by 3 cycles of centrifugation/redispersion and cleaned with ionic exchange resin before DSC measurements.

Size exclusion chromatography (SEC-MALS): molecular weights of the PNP chains and their size dispersity were determined by size exclusion chromatography in tandem with multi-angle static light-scattering (SEC-MALS). The system was a Shimadzu Prominence consisting of a LC-20AD peristaltic pump, a DGU-20A3R degassing unit, a Rheodyne 7725i injector (injection volume of 20 µL). Three detectors in series were used: a Shimadzu Prominence RF-20 A fluorimetric detector; a multi-angle static light-scattering Wyatt MiniDawn Treos detector; and a Shimadzu RID-10 A refractive index detector (internal temperature 40°C). Data acquisition and analysis were made with Astra 5.3.2.1 software from Wyatt. The chromatography column was a Phenomenex Phenogel analytical columns (30 cm x 7.8 mm, pore size 10^4 Å) and a Phenogel linear precolumn from Phenomenex using dry THF as mobile phase at a flow rate of 0.8 mL min^{-1}, with the columns thermostat at 23°C in a Shimadzu CTO-20 AC columns oven. We measure the molecular weight of the polymer chains for four different PNP samples, after destroying the nanoparticles by dissolution in THF. Prior to PNP dissolution, the colloidal dispersions were thoroughly washed with water by centrifugation/redispersion cycles, cleaned with ionic exchange resin and dried.

2.3. Results

Highly monodispersed PNP were prepared in one step synthesis via batch emulsion polymerization, where the surfactant concentration was always under its CMC ($CMC_{SDS} = 8.20\,x\,10^{-3}\,M$) and was the only parameter changed, to obtain the different PNP sizes. Changing the SDS quantity, the primary determinant for the particle diameter, nanoparticles with sizes ranging from 173 nm to 331 nm in diameter were synthesized (Table 2.2). PNP diameter increased as the surfactant amount deceased from 48 mg to 10 mg. Lower surfactant concentrations results in the formation of fewer stable particle nuclei by an homogeneous nucleation mechanism, resulting in larger particles.[29-31]

The main polymerization parameter affecting the morphology of the nanoparticles is the hydrophilicity of the co-monomers in aqueous media, leading to different compositions of the interior and outermost layer (Figure 2.2a). Thus, the final morphology of the nanoparticles is expected to be a core-shell structure composed of a polystyrene core and a thin shell with a highly charged surface composed of poly(methyl methacrylate-*co*-acrylic acid), enriched with polar groups that contributes to the stability of the obtained colloidal dispersions.[32,33]

Complete monomer conversion is assumed from the mass balance, with only few aggregates at the end of the reaction being filtered. The solid content of each colloidal dispersion was ~15%. Based on the molar percentages of each of the co-monomers, 87% of St, 5% of MMA and 8% of AA, we expect the polymer in the PNP to have the same molar composition, as the monomer mixture before polymerization (Figure 2.2b). Accordingly, the density of the PNP corresponds to 1.066 g/cm^3.

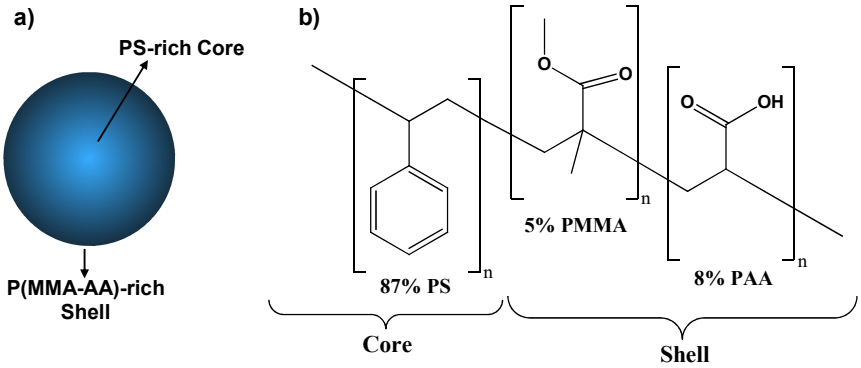

Figure 2.2: a) Schematic illustration of the core-shell PNP structure, where the center is enriched in polystyrene and the outer layer is enriched with poly(methyl methacrylate) and polyacrylic acid segments. **b)** Structure representation of polymer chains molar composition.

Perfectly spherical and highly monodispersed PNP were imaged by SEM (Figure 2.3). The SEM histograms in Figure 2.4 correspond to at least 100 nanoparticles for each diameter.

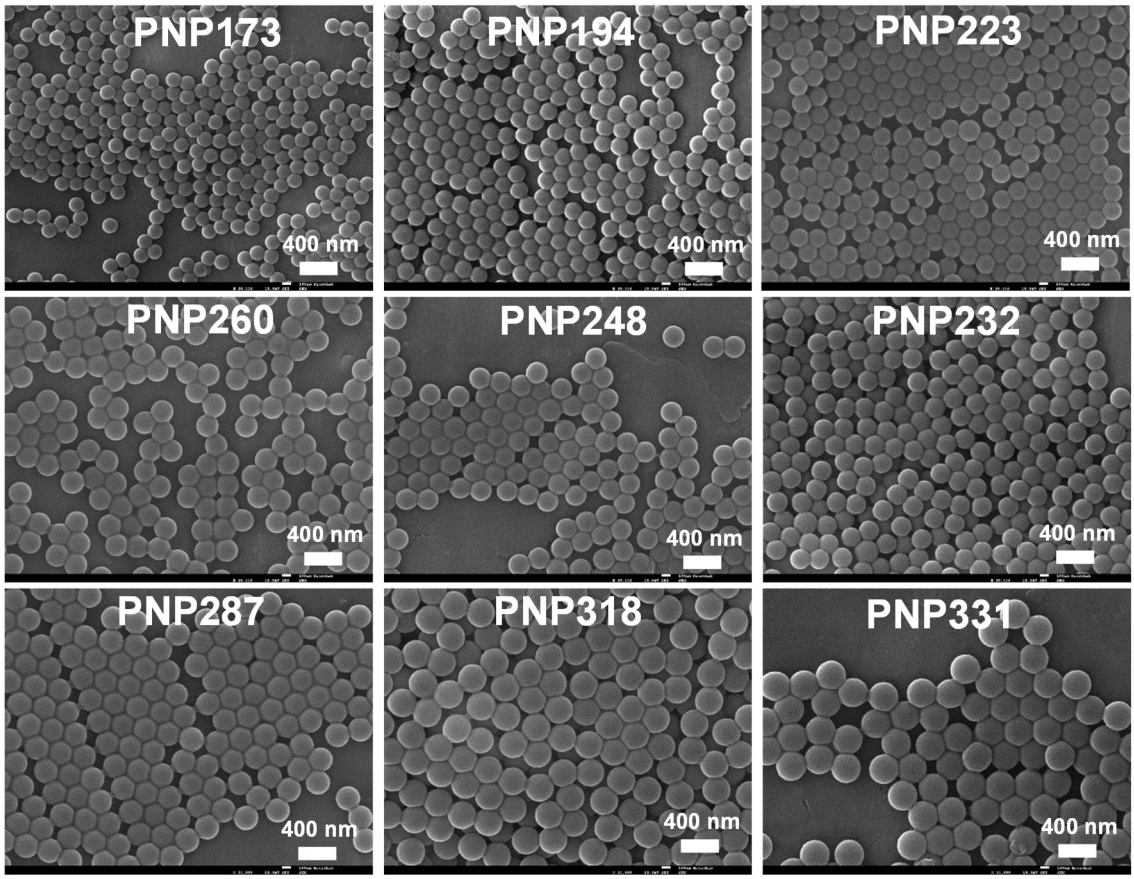

Figure 2.3: SEM images of the synthesized polymer nanoparticles. The PNP diameter increased from 173 nm to 331 nm in mean diameter, with the gradual decrease from 48 mg to 10 mg of SDS in the reaction medium.

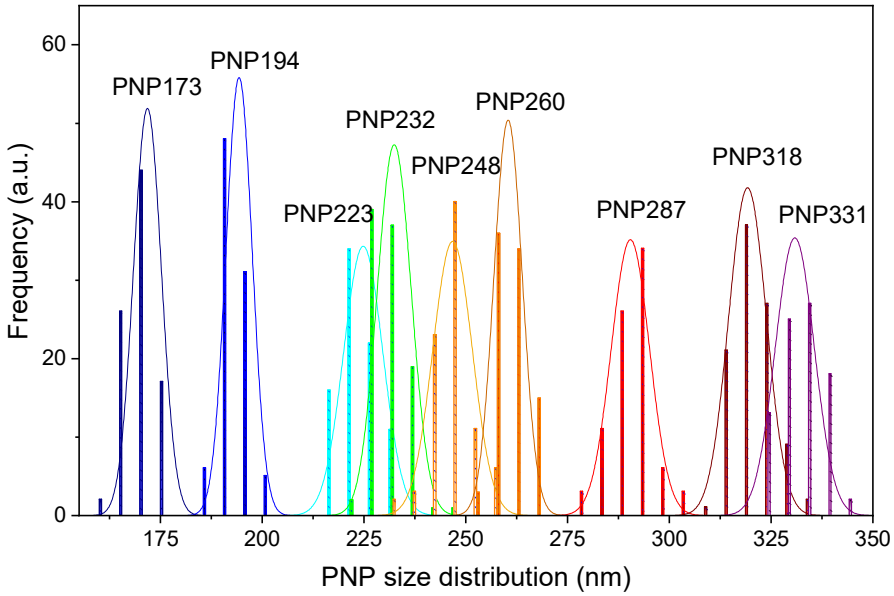

Figure 2.4: SEM histogram of PNP size distribution obtained by analyzing at least 100 nanoparticles for each sample.

PNP size and size distributions were also obtained by DLS and NTA. Both these techniques determine the particle size from the hydrodynamic diameter using the Stokes-Einstein equation.[34,35] Figures 2.5 and 2.6 shows the size distributions obtained by DLS and NTA for each PNP sample, respectively.

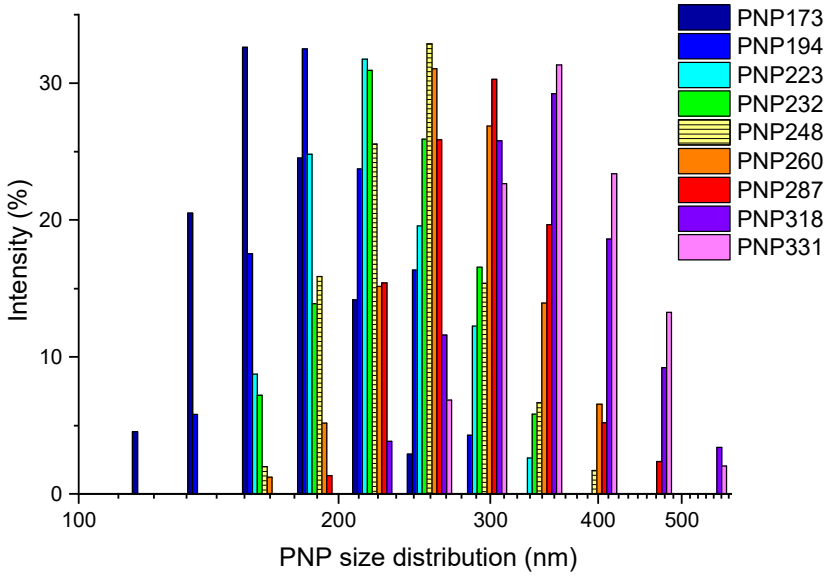

Figure 2.5: Intensity histogram of PNP size distribution from DLS measurements. The size distribution obtained is a plot of the relative intensity of light scattered by the particles in various size classes.

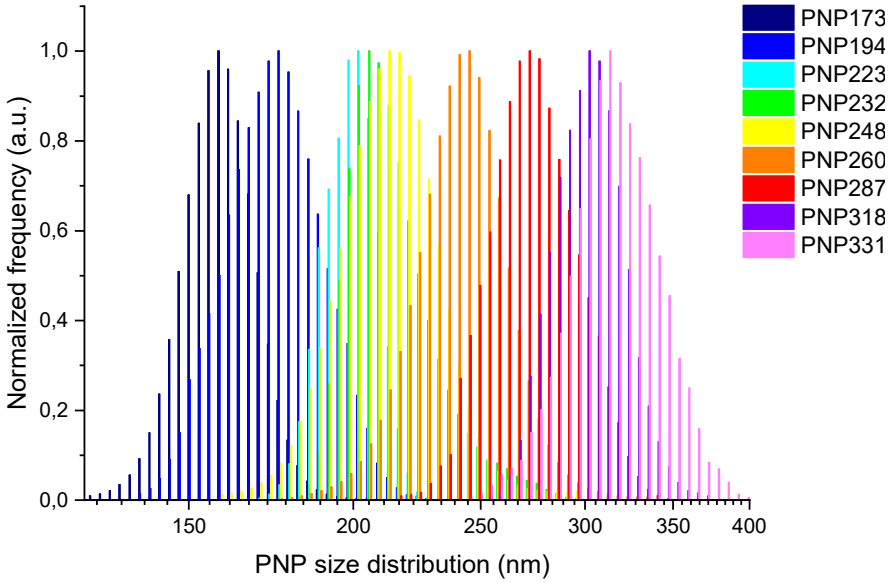

Figure 2.6: Histogram of PNP size distribution from NTA measurements. Narrow size distributions were obtained for all the samples.

DLS sensitivity for larger particles gives a measure of the colloidal stability, due to its excellent diagnostic capability to detect aggregation. However, its resolution for polydisperse samples is rather low, because even a small number of larger nanoparticles can obscure the contribution from smaller ones. On the other hand, the

particle by particle analysis of NTA, offers an important advantage in comparison with DLS, is that it is not biased towards larger nanoparticles or aggregates.[35-37] Table 2.2 summarizes the PNP diameter obtained from the different techniques. The SEM polydispersity indices (PDI) were obtained by dividing the standard deviation by the mean diameter. PDI values lower than 5% were obtained for all the samples (Table 2.2). From the SEM diameters and the mass balance, the thickness of the PNP shell would correspond to less than 10% of the total volume occupied by them, regardless their diameter.

Table 2.2: Comparison of the PNP diameter obtained from DLS, NTA and SEM. The corresponding SEM size polydispersity index (PDI) for each of the samples is also shown. [a,b]Hydrodynamic diameter; [c] PDI from SEM measurements.

Sample	PNP Code	[SDS]/M	PNP Diameter (nm)			PDI[c] (%)
			DLS[a]	NTA[b]	SEM	
1	PNP173	$1.39x10^{-3}$	172	157	173	2.5
2	PNP194	$1.16x10^{-3}$	203	178	194	3.2
3	PNP223	$1.01x10^{-3}$	220	207	223	1.9
4	PNP232	$8.67x10^{-4}$	241	209	232	2.0
5	PNP248	$7.22x10^{-4}$	245	216	248	2.8
6	PNP260	$6.10x10^{-4}$	270	241	260	2.5
7	PNP287	$4.45x10^{-4}$	275	249	287	3.1
8	PNP318	$3.61x10^{-4}$	334	300	318	3.3
9	PNP331	$3.09x10^{-4}$	352	305	331	2.1

The average PNP diameter obtained by NTA are slightly smaller than the ones obtained by DLS. While DLS and NTA samples are solvated, SEM works on dry samples under ultrahigh vacuum conditions.[38] Based on this, usually bigger diameters are expected from DLS and NTA measurements when compared to SEM. Nevertheless, we do not obtain significant differences (this might be due to the coating layer of conductive material). An advantage of DLS and NTA is the capability to sample a much larger number of particles than SEM, providing therefore, more robust data on size distributions.

The highly charged PNP surface contributes to the stability of the obtained colloidal dispersions. The potential at the particle-fluid interface, the Zeta potential (ZP), reflects the potential difference between the electric double layer (EDL) of the mobile particles and the layer of dispersant around them. The composition of this diffuse layer is dynamic and depends on a variety of factors

such as pH, ionic strength, surfactants, etc.[34] Although the ZP does provide indications on colloid stability (values of ζ $\pm$ 0−10 mV, $\pm$ 10−20 mV, $\pm$ 20−30 mV and > $\pm$ 30 mV are classified as highly unstable, relatively stable, moderately stable and highly stable, respectively), it does not reflect the entire picture. While ZP provides information on the electrostatic repulsive forces it does not provide any insight on the attractive van der Waals forces.[39] We measure the zeta potential of the aqueous dispersion of PNP248 at pH 5.2, $\zeta = -38$ mV. Before using these nanoparticles for the assembling of photonic structures, the pH of the dispersion is increased to 6.2 and the zeta potential increases to −46 mV (further increasing PNP dispersion pH to 9 did not show significant difference on the zeta potential, $\zeta = -40$ mV). On the other hand, decreasing the pH to 4 results in a decrease of the ZP to −27 mV, decreasing the stability of the nanoparticles dispersion.

The thermal behavior of the core-shell PNP was also evaluated. The glass transition temperature, Tg, was determined by differential scanning calorimetry (DSC) measurements for two PNP samples with a large diameter difference, PNP194 and PNP331. We intended to evaluate if the Tg was affected by the nanoparticles diameter (as it happens in the case of polymer chains where higher molecular weights results in higher Tg values).[40-43] The Tg values are very similar, with no significant differences observed within this size range: for PNP194 correspond to 106°C, whereas for PNP331 is 104°C (Figure 2.7).

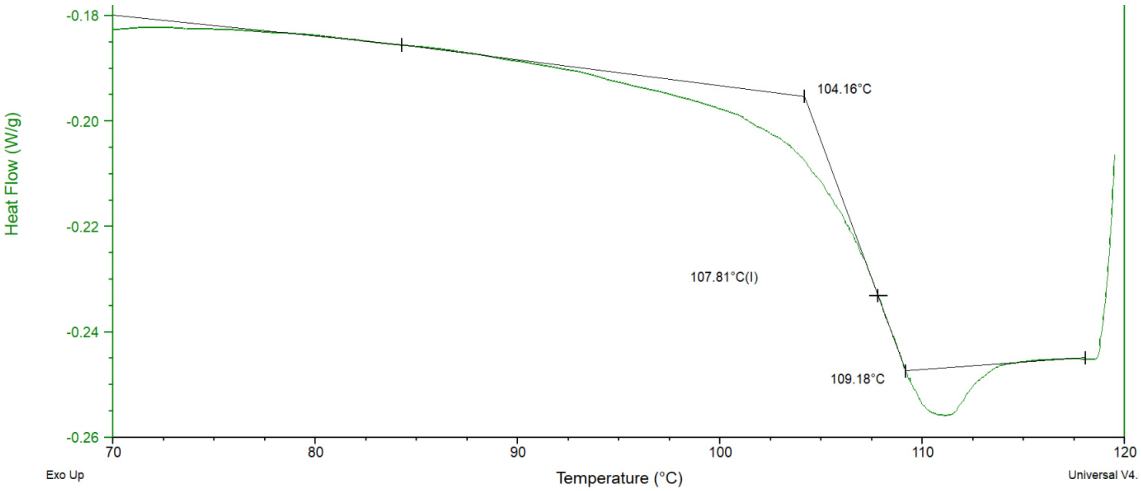

Figure 2.7: DSC measurement of the glass transition temperature of PNP331, at a heating rate of 10°C/min. The onset Tg corresponds to 104°C.

It is important to notice that we do not observe different glass transition temperatures for the core and shell regions. Because PNP were synthesized by batch emulsion polymerization the core and shell regions are not segregated and in addition, the shell thickness is very small.[44]

The molecular weight of the polymer chains for different PNP was determined by gel permeation chromatography after destroying the particles by dissolving them in THF.[45-47] Although the PNP diameter increased from 173 nm to 331 nm, the average molecular weight of the polymer chains shows no significant differences for the different PNP (Figure 2.8 and Table 2.3).

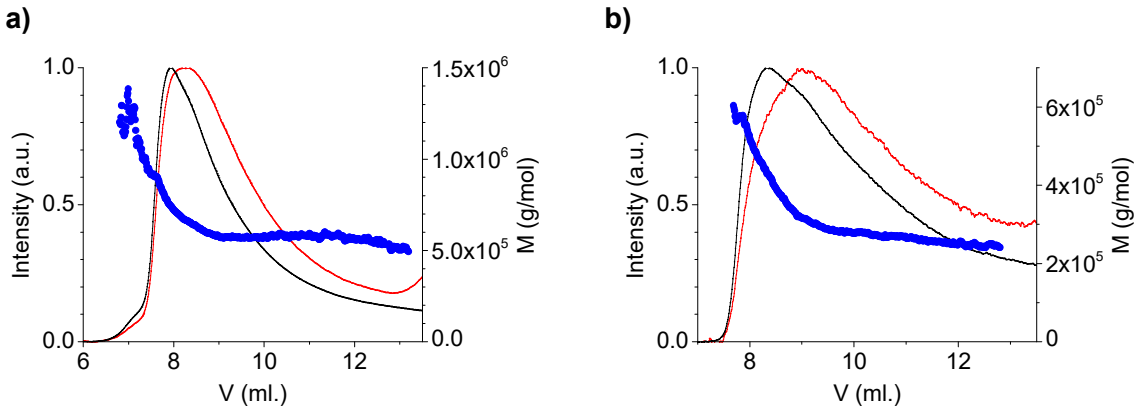

Figure 2.8: GPC chromatogram of the P(St-MMA-AA) polymer chains from **a)** PNP194 and **b)** PNP331. Molecular weight calculated for each elution volume (blue dots). Refractive index (RI) signal (red line, in arbitrary units) and multiangle light scattering (MALS) signal at 90° (black line, in arbitrary units) *vs.* elution volume.

Knowing the PNP diameter, we determine the number of PNP obtained in each synthesis and estimated the particle volume fraction, ∅, for the different PNP dispersions, according to equation 2.1:[48]

$$\emptyset = \frac{4}{3}\pi r^3 \left(\frac{N}{V}\right) \qquad (2.1)$$

where, ∅, corresponds to the fraction of the total volume, V, that is filled by N spheres, each of radius, r. Table 2.3 summarizes the results obtained. By decreasing the amount of surfactant in the polymerization medium, the number of nucleated polymer nanoparticles decreased, resulting in larger diameters, but interestingly the size of the polymer chains remains nearly the same (although synthesized by free-radical emulsion polymerization).

Table 2.3: Comparison of the number of particles, the polymer chains molecular weight and the glass transition temperature for different PNP. [a]weight average molecular weight; [b]absolute number average molecular weight; size dispersity index < 1.3 ($PDI = Mw/Mn$).

PNP code	Number of particles	Dispersion ∅	Mw^a (g/mol)	Mn^b (g/mol)	Tg (°C)
PNP173	7.86 x10^{15}	0.19	4.00 x10^5	3.25 x10^5	-
PNP194	5.58 x10^{15}	0.17	6.38 x10^5	6.23 x10^5	106
PNP223	3.67 x10^{15}	0.20	-	-	-
PNP232	3.26 x10^{15}	0.18	-	-	-
PNP248	2.67 x10^{15}	0.19	3.76 x10^5	3.51 x10^5	-
PNP260	2.32 x10^{15}	0.18	-	-	-
PNP287	1.72 x10^{15}	0.19	-	-	-
PNP318	1.27 x10^{15}	0.19	3.20 x10^5	2.90 x10^5	-
PNP331	1.12 x10^{15}	0.18	7.03 x10^5	5.55 x10^5	104

2.4. Conclusions

We successfully synthesized highly monodispersed PNP with diameters ranging from 173 nm to 331 nm, by batch emulsion polymerization, tuning only the concentration of surfactant in the reaction medium.

Decreasing the amount of SDS, increases the diameter but decreases the number of PNP, maintaining thus, a constant volume fraction of PNP for the different colloidal dispersions.

Within the synthesized size range, the glass transition temperature of the PNP and the molecular weight of the polymer chains shows no dependence on the diameter of the PNP.

The charged shell of the PNP, due to the presence of ionizable carboxylic acid groups at their surface, will drive the assembly into photonic structures.

2.5. References

1. Mittal, V. *Advanced Polymer Nanoparticles, Synthesis and Surface Modifications. CRC Press*. (2011).
2. Rao, J. P. & Geckeler, K. E. Polymer nanoparticles: Preparation techniques and size-control parameters. *Prog. Polym. Sci.* **36**, 887–913 (2011).
3. Odian, G. *Principles of Polymerization. Fourth Edition, Wiley-Interscience: Hoboken, N. J.* (2004).
4. Kiparissides, C. Polymerization reactor modeling: A review of recent developments and future directions. *Chem. Eng. Sci.* **51**, 1637–1659 (1996).

5. Tobita, H. & Hamiliec, A. E. Polymerization Processes 2. Modeling of Processes and Reactors. in *Ullmann's Encyclopedia of Industrial Chemistry. Wiley-VCH,* 1–50 (2015).

6. Slomkowski, S., Alemán, J. V., Gilbert, R. G., Hess, M., Horie, K., Jones, R. G., Kubisa, P., Meisel, I., Mormann, W., Penczek, S. & Stepto, R. F. T. Terminology of polymers and polymerization processes in dispersed systems (IUPAC Recommendations 2011). *Pure Appl. Chem.* **83**, 2229–2259 (2011).

7. Arshady, R. Suspension, emulsion, and dispersion polymerization: A methodological survey. *Colloid Polym. Sci.* **270**, 717–732 (1992).

8. Kawaguchi, S. & Ito, K. Dispersion Polymerization. *Adv. Polym. Sci.* **175**, 299–328 (2005).

9. Rudin, A. & Choi, P. Dispersion and Emulsion Polymerizations, Chapter 10. in *The Elements of Polymer Science & Engineering, Third Edition, Elsevier* 427–447 (2013).

10. Brooks, B. W. Suspension Polymerization Processes. *Chem. Eng. Technol.* **33**, 1737–1744 (2010).

11. Chaudhary, V. & Sharma, S. Suspension polymerization technique: parameters affecting polymer properties and application in oxidation reactions. *J. Polym. Res.* **26**, 102 (2019).

12. Rudin, A. & Choi, P. Polymer Reaction Engineering, Chapter 12. in *The Elements of Polymer Science & Engineering (Third Edition)* 495–520 (2013).

13. Vanderhoff, J. W. Mechanism of emulsion polymerization. *J. Polym. Sci. Polym. Symp.* **72**, 161–198 (1985).

14. Zimehl, R., Lagaly, G. & Ahrens, J. Some aspects of polymer colloids I. Preparation and properties of different types of latex particles. *Colloid Polym. Sci.* **268**, 924–933 (1990).

15. Ugelstad, J. & Hansen, F. K. Kinetics and Mechanism of Emulsion Polymerization. *Rubber Chem. Technol.* **49**, 536–609 (1976).

16. Aslamazova, T. R. Emulsifier-free latexes and polymers on their base. *Prog. Org. Coatings* **25**, 109–167 (1995).

17. Lichti, G., Gilbert, R. G. & Donald, H. The Mechanisms of Latex Particle Formation and Growth in the Emulsion Polymerization of Styrene Using the Surfactant Sodium Dodecyl Sulfate. *J. Polym. Sci. Polym. Chem. Ed.* **21**, 269–291 (1983).

18. Nazaran, P. & Tauer, K. Nucleation in Emulsion Polymerization: Another Step towards Non-Micellar Nucleation Theory. *Macromol. Symp.* **259**, 264–273 (2007).

19. Zhenxing, H., Xiaowei, Y., Junliang, L., Yuping, Y., Ling, W. & Yanwei, Z. An investigation of the effect of sodium dodecyl sulfate on quasi-emulsifier-free emulsion polymerization for highly monodisperse polystyrene nanospheres. *Eur. Polym. J.* **47**, 24–30 (2011).

20. Goodall, A. R., Wilkinson, M. C. & Hearn, J. Mechanism of Emulsion Polymerization of Styrene in Soap-Free Systems. *J. Polym. Sci. Polym. Chem. Ed.* **15**, 2193–2218 (1977).

21. Chern, C. S. Emulsion polymerization mechanisms and kinetics. *Prog. Polym. Sci.* **31**, 443–486 (2006).

22. Sood, A. Modeling of the Particle Size Distribution in Emulsion Polymerization. *J. Appl. Polym. Sci.* **109**, 1403–1419 (2008).

23. Thickett, S. C. & Gilbert, R. G. Emulsion polymerization: State of the art in kinetics and mechanisms. *Polymer.* **48**, 6965–6991 (2007).

24. Harkins, W. D. General Theory of Mechanism of Emulsion polymerization. II. *J. Polym. Sci.* **V**, 217–251 (1949).

25. Wang, Q., Fu, S. & Yu, T. Emulsion polymerization. *Prog. Polym. Sci.* **19**, 703–753 (1994).

26. Asua, J. M. Emulsion Polymerization: From Fundamental Mechanisms to Process Developments. *J. Polym. Sci. Part A Polym. Chem.* **42**, 1025–1041 (2004).

27. Asua, J. M. Miniemulsion polymerization. *Prog. Polym. Sci.* **27**, 1283–1346 (2002).

28. Schork, F. J., Luo. Y., Smulders, W., Russum, J. P., Butté, A. & Fontenot, K. Miniemulsion Polymerization. *Adv Polym Sci* **175**, 129–255 (2005).

29. Reese, C. E., Guerrero, C. D., Weissman, J. M., Lee, K. & Asher, S. A. Synthesis of Highly Charged , Monodisperse Polystyrene Colloidal Particles for the Fabrication of Photonic Crystals. *J. Colloid Interface Sci.* **232**, 76–80 (2000).

30. Cong, H. & Cao, W. Thin Film Interference of Colloidal Thin Films. *Langmuir* **20**, 8049–8053 (2004).

31. Hansen, F. K. & Ugelstad, J. Particle Nucleation in Emulsion Polymerization. I. A Theory for Homogeneous Nucleation. *J. Polym. Sci. Polym. Chem. Ed.* **16**, 1953–1979 (1978).

32. Hoshino, F., Kawaguchu, H. & 0htsuka, Y. N-Substituted Acrylamide-Styrene Copolymer Latices III. Morphology of Latex Particles. *Polym. J.* **19**, 1157–1164 (1987).

33. Wang, J., Wen, Y., Ge, H., Sun, Z., Zheng, Y., Song, Y. & Jiang, L. Simple Fabrication of Full Color Colloidal Crystal Films with Tough Mechanical Strength. *Macromol. Chem. Phys.* **207**, 596–604 (2006).

34. Bhattacharjee, S. DLS and zeta potential – What they are and what they are not? *J. Control. Release* **235**, 337–351 (2016).

35. Hole, P., Sillence, K., Hannell, C. & Manus, C. Interlaboratory comparison of size measurements on nanoparticles using nanoparticle tracking analysis (NTA). *J. Nanopart. Res.* **15**, 2101 (2013).

36. Troiber, C., Kasper, J. C., Milani, S., Scheible, M., Martin, I., Schaubhut, F., Küchler, S., Rädler, J., Simmel, F. C., Friess, W. & Wagner, E. Comparison of four different particle sizing methods for siRNA polyplex characterization. *Eur. J. Pharm. Biopharm.* **84**, 255–264 (2013).

37. Pol, E. Van Der, Coumans, F. A. W., Sturk, A., Nieuwland, R. & Leeuwen, T. G. Van. Refractive Index Determination of Nanoparticles in Suspension Using Nanoparticle Tracking Analysis. *Nano Lett.* **14**, 6159–6201 (2014).

38. Mourdikoudis, S., Pallares, R. M. & Thanh, N. T. K. Characterization techniques for nanoparticles: comparison and complementarity upon studying. *Nanoscale* **10**, 12871–12934 (2018).

39. Missana, T. On the Applicability of DLVO Theory to the Prediction of Clay Colloids Stability. *J. Colloid Interface Sci.* **230**, 150–156 (2000).

40. Aras, L. & Richardson, M. J. The glass transition behaviour and thermodynamic properties of amorphous polystyrene. *Polymer.* **30**, 2246–2252 (1989).

41. Claudy, R., Létoffé, J. M., Camberlain, Y. & Pascault, J. R. Glass Transition of Polystyrene Versus Molecular Weight. *Polym. Bull.* **9**, 208–215 (1983).

42. Zhang, C., Guo, Y. & Priestley, R. D. Confined Glassy Properties of Polymer Nanoparticles. *J. Polym. Sci., Part B Polym. Phys.* **51**, 574–586 (2013).

43. Zhang, C., Guo, Y. & Priestley, R. D. Glass Transition Temperature of Polymer Nanoparticles under Soft and Hard Confinement. *Macromolecules* **44**, 4001–4006 (2011).

44. Mathlouthi, C., Hugenell, F., Delpech, F. & Rharbi, Y. Heat Capacity of Confined Polystyrene in Close-Packed Particles. *Macromolecules* **50**, 472–481 (2017).

45. Smirnova, N. N., Kolyakina, E. V., Kulagina, T. G. & Grishin, D. F. Influence of the molecular weight of polystyrene on its thermodynamic properties. *Russ.Chem.Bull., Int.Ed.* **62**, 2251–2257 (2013).

46. Mourey, T. H. SEC Molecular-Weight-Sensitive Detection. *International Journal of Polymer Analysis and Characterization* **9**, 97–135 (2004).

47. Sciucca, S. Della, Penco, M. & Sartore, L. Effect of Molecular Weight on Enthalpy Relaxation in Syndiotactic Poly(Methyl-Methacrylate). *Macromol. Symp.* **247**, 35–42 (2007).

48. Poon, W. C. K., Weeks, R. & Royall, C. P. On measuring colloidal volume fractions. *Soft Matter* **8**, 21–30 (2012).

3. Emulsion droplet generation by microfluidics

This chapter describes the microfluidic technology for the production of stable and monodispersed emulsion droplets, that will serve as templates for the assembling of PNP into spherical colloidal photonic structures. After a brief introduction on droplet formation mechanisms, we describe the design and manufacture of PDMS microfluidic devices from soft lithography techniques. We show that the emulsification of a dispersed aqueous phase containing the PNP, into a continuous oil phase, produces stable emulsions with highly uniform droplet size.

3.1. Introduction

Bottom-up, evaporation-induced, self-organization of colloids from aqueous droplet templates, originates spherical photonic structures that diffract light with properties different from those generated in bulk.[1-6] Monodisperse emulsion droplets supply the geometrical confinement to synthesize 3D colloidal spherical photonic materials with homogeneous and reproducible optical properties.[7-10]

Emulsion droplets can be produced by several techniques. For example, high-energy methods such as atomization, sprays, or high-shear mixing, yields droplets with broad size distributions.[11] In pore-based methods such as membrane emulsification, the two immiscible liquids are forced together through a filter or a microfabricated array of pores.[12] Here, droplet size distribution can be significantly narrower, but the pore size distribution limits the uniformity of the resulting emulsions. Inkjet printing, a microtechnology in which droplets fragment from a liquid jet emitted from a capillary or a nozzle, allows the formation of very uniform streams, although secondary satellite droplets must be controlled.[13,14]

Among the techniques developed to produce emulsions with a low size dispersity, microfluidics has incomparable advantages due to the fine coupling of precise flow patterns and shears control of the immiscible fluids.[15-17] In comparison with conventional methods, microfluidic technologies for droplet formation yields considerably more uniform droplet sizes, increasing thus, emulsions stability.

The production of highly monodispersed and stable emulsion droplets by microfluidics originates 3D colloidal assemblies with controlled shapes, uniform structures and specific optical properties.[1,7,8,10,18,19]

To obtain spherical photonic pigments with homogeneous and reproducible optical properties we must be able to control all stages of its fabrication. The creation of small, highly monodispersed, and stable emulsion droplets, avoiding coalescence and/or break-up, is the first and one of the most important steps in the fabrication process. Here, this issue was addressed by means of droplet microfluidic technology aided by soft lithography.

3.1.1. Microfluidics

Microfluidics is a multidisciplinary subject involving physics, chemistry, biology, and engineering. It is the science and technology of systems that process or

manipulate small (10^{-9} to 10^{-18} L) amounts of fluids, constrained in microchannels of cross-sectional dimensions on the order of 10 to 100 μm.[20]

Droplet-based microfluidics generates and manipulates discrete droplets with precisely controlled volume through shearing between immiscible phases in microchannels, generally dominated by surface tension and/or fluid dynamic forces such as pressure, inertial and viscous forces.[21] Microfluidic physics is quite rich due to its small dimensions, producing a wide variety of physical phenomena, that are expressed by dimensionless numbers, that give a sense of their relative importance against competing phenomena.[21-23]

In microfluidic devices, the Reynolds number, Re, expressing the ratio between inertial and viscous forces acting on a small element of fluid, are typically small enough for inertial effects to be irrelevant in comparison with viscous forces. Small geometric length scales of microfluidics, displaying long and narrow microchannels with dimensions on the order of 50 μm, typically lead to $Re << 1$, and so, microfluidic flows generally fall safely within the laminar flow regime (predominantly uniaxial and incompressible), enabling a higher degree of control on the injection process.[22-26]

Due to the large surface-to-volume ratio of microfluidic scales, the flow between two immiscible fluids is usually surface tension dominated. Shearing by interfacial tension on a micrometer scale occurs because the effects of surface forces are significantly larger than those of other forces, such as gravitational, inertial and viscous forces.[22,25,26]

In microfluidic flows between immiscible fluids, for example when injecting water into a stream of oil at a T-junction, surface tension, γ, affects the dynamics of the free surface: instead of forming emulsion droplets, the two streams would flow alongside one other, if there were no interfacial tension between water and oil.[27,28]

Competing stresses drive the interface: surface tension acts to reduce the interfacial area, and viscous stresses act to extend and drag the interface downstream. These stresses destabilize the interface and cause droplets formation. In microfluidic droplet formation, the capillary number, Ca, is the most important dimensionless parameter, characterizing the relative importance of viscous stresses and capillary pressure and can be define in terms of the continuous phase flow field that acts to deform the droplet, where μ_c and U_c

corresponds to the viscosity and the average velocity of the continuous phase, respectively (equation 3.1).[21,29]

$$Ca = \frac{\mu_c U_c}{\gamma} = \frac{\mu_c Q_c}{\gamma w_c h} \quad (3.1)$$

Here, Q_c and w_c, represents the volumetric flow rate and width of the continuous phase microchannel, respectively; h is the channel depth. In microfluidic droplet formation, the capillary numbers typically range from $Ca \sim 10^{-3}$ to 10^{1} for flow rates accessible using syringe pumps.[21,30]

An additional dimensionless parameter that is important in microfluidic droplet formation is the ratio of the dispersed and continuous volumetric flow rates, φ, given by $\varphi = Q_d/Q_c$, where Q_d corresponds to the volumetric flow rate of the dispersed phase. In the limit of $\varphi \to 0$, the dispersed phase liquid remains stationary.

In contrast to droplet formation, droplet break-up is governed by the viscosity ratio of the two immiscible phases, given by $\lambda = \mu_d/\mu_c$, where μ_d and μ_c corresponds to the viscosity of the dispersed and continuous phases, respectively.[27] Other dimensionless parameters in the microfluidics physics, don't play a significant role in microfluidics droplet formation.[23]

3.1.2. Droplet-based microfluidic devices and emulsification

The design of common droplet-based microfluidic devices is extremely diverse, however, the mechanisms of emulsifications in those devices are quite similar. That is, under the action of shear forces by the immiscible dispersed and continuous phases, the liquid threads of the dispersed phase are broken up into droplets. In addition to single emulsions, double emulsions and emulsions with more complex internal structures have been generated.[31] In general, the fluid phase to be dispersed is driven into a microchannel via a pressure-driven flow, in which either the volume flow rate or the applied pressure are controlled. A second immiscible liquid is driven into a separate microchannel via an independently controlled flow. The two streams meet at a junction, at which the dispersed phase liquid extends to form a finger or jet. The geometry of the junction and the volumetric flow rates of the two fluids determine the local flow field, which deforms the interface and droplets form after dispersed phase break-up (Figure 3.1).

Steady flows of the two liquids yields periodic formation of equal sized droplets in a continuous stream.

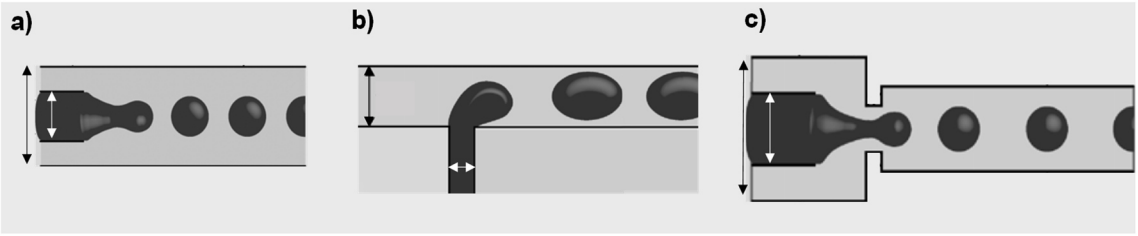

Figure 3.1: Illustration of the main microfluidic geometries used for droplet formation. **a)** co-flowing streams, **b)** cross-flowing streams in T-shaped junction and **c)** elongated flow in a flow-focusing geometry. Droplet sizes depend on the volumetric flow rates or pressure imposed in each liquid phase to drive the flow and on the characteristic dimensions of the microchannels width, denoted by the black arrows for the continuous phase and by the white arrows for the dispersed phase. Adapted from Christopher and Anna.[25]

Examining the mechanisms for droplet formation and break-up in each of the geometries in Figure 3.1, several common features emerge. In all cases, droplet formation appears to occur in a two-stage process. Initially, fluid stresses around the emerging droplet interface act to stretch and deform the interface. Later the neck of the droplet begins to thin. During thinning, the droplet continues to fill with dispersed phase liquid. Generically, droplet break-up can be characterized by the competition between local fluid stresses acting to deform the liquid interface and capillary pressure acting to resist deformation. In the case of cross-flowing streams in T-shaped junction geometries, experimental data shows that, for a given continuous phase flow rate, if the flow of the dispersed phase is increased, the flow pattern changes from droplets at T-junction to droplets in channel.[32] This indicates that, for a given Ca, when the ratio of volumetric flow rates, φ, is increased a regime change happens. With further increasing the φ, the flow regime changes to parallel flow.

The final size of the droplets depends not only on the specific geometry considered but also on the volume of liquid that was able to enter the droplet prior to the neck breaking. Droplet diameter decreases continuously with increasing capillary number, due to increased viscous stresses acting to deform the droplet. On the other hand, droplet diameter increases as the flow rate ratio increases, since the emerging droplet can be filled at a relatively higher rate.[25,33,34] Significantly smaller droplets can be formed using flow-focusing devices, either

by increasing shear gradients or by drawing the stream into a thin jet that break-up by the Rayleigh-Plateau instability.[21,30,35]

In the microfluidic T-junction device geometry, orthogonally flowing continuous and dispersed phases meet to produce droplets, three distinct regimes of droplet formation and break-up can be identified: the squeezing, the dripping, and the jetting regimes (Figure 3.2).

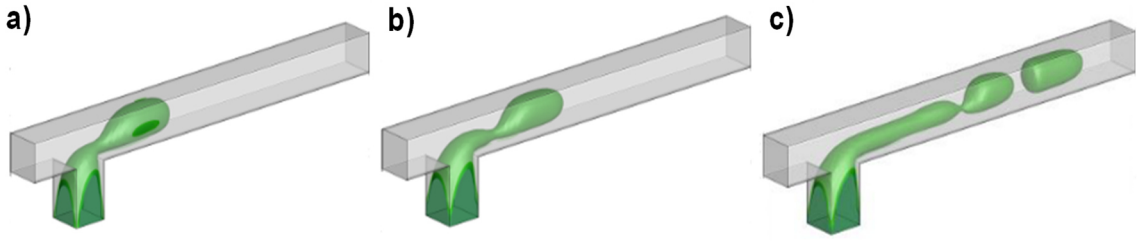

Figure 3.2: Representative images showing the modes of droplet formation and break-up at a microfluidic T-junction. **a)** Squeezing regime; **b)** Dripping regime; **c)** Jetting regime. Adapted from Nekouei and Vanapalli.[36]

The squeezing regime corresponds to a confined break-up process. This mechanism occurs when the emerging droplet grows large enough to completely obstruct the continuous phase channel (apart from a thin film of the continuous phase wetting the walls surrounding the emerging droplet). Droplets created under this regime are often referred to as plugs, because the droplet fills the channel cross-section, and its length in the flow direction is greater than its width. Due to the obstruction of the continuous phase channel by the plugs, the upstream pressure in the continuous phase liquid increases, resulting in an additional force exerted on the interface that promotes break-up.

In the unconfined dripping regime, droplets do not disrupt the continuous phase flow significantly, and thus their size is primarily controlled by the local shear stress. Droplet break-up in the dripping regime is a mixture of capillary instabilities, combined with viscous drag on the emerging droplet from the outer liquid, which stretches and thins the necked region behind the droplet.[37,38]

Finally, in the jetting regime the droplets are formed by elongational flows that efficiently from jets (contrarily to the previous methods where droplets are formed within predominantly shearing flows). It is exclusive of very high flow rates, or low interfacial tension, i.e. higher values of the capillary number, Ca. The jet interface exhibits undulations that grow until discrete droplets pinch-off (like pendant

droplets that break-up of the jetting front). The resulting droplets are larger than in the dripping mode, and less uniform.[39]

The dispersion of a fluid into another, is a system out of thermodynamic equilibrium: the total energetic cost for the formation of the interfacial area is unfavorable and the minimum energy of the system is a configuration where the two liquids are separated in two phases. The driving force acting towards the homogenization of the system is balanced by the action of surfactants. In microfluidic droplet-based technology, surfactant molecules play an ubiquitous role, because they are driven to the interface, and hence, are used to stabilize droplets and prevent coalescence by lowering the interfacial tension between the two immiscible phases.[40]

The decrease of the surface tension is related to the number of surfactant molecules adsorbed at the interface. As surfactant adsorbs to the interface, the interface rigidifies. This rigidification origin is the so-called Marangoni effect: as the droplet moves, surfactant distribution is non-uniform, with an excess of surfactant molecules at the rear of the droplet, leading to a surface tension gradient (surface tension is decreased at the rear of the droplet). Surfactants modify not only the behavior of interfaces but also the behavior of the whole liquid emulsion through the coupling with the flow around the interface.[41] The motion of surfactant at the interface, its exchange properties with the bulk phase, and the response of surfactant layer to deformations of the interface are dynamic processes.

Surfactants provides an energy barrier and stabilize emulsions against droplet coalescence by two mechanism: droplets stabilization by steric repulsion of surfactant molecules and/or by surfactant gradients at the droplet interface induced by the drainage of a continuous film between two droplets that results in a force acting against the drainage, according to the Marangoni effect (Figure 3.3). Whether droplets coalesce or separate depends on whether the fluid film between them drains to a minimum thickness that is within the range of the attractive van der Waals force.[41]

Besides droplet coalescence, aging mechanism such as Ostwald ripening, also leads to emulsion coarsening because small emulsion droplets, which have higher Laplace pressure, tend to dissolve in larger ones leading to an increase of

droplet size with time and coarsening of the emulsions.[43,44] This is possible when the dispersed phase is even slightly soluble in the continuous phase.

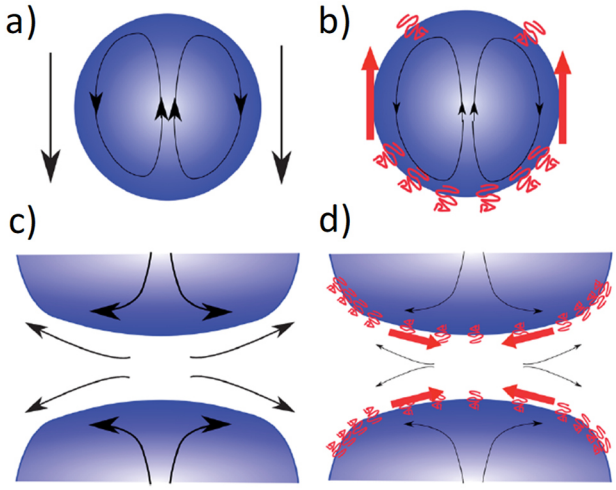

Figure 3.3: Marangoni effects in the presence of surfactant. **a)** The flow pattern in the absence of surfactant for a droplet moving in a surrounding fluid is given by the black arrows (in the reference frame of the droplet). **b)** In the presence of surfactant, the flow induces a heterogeneous surfactant distribution causing a Marangoni stress opposing to the flow (red arrows): the viscous drag is then modified by the presence of surfactant which rigidifies the interface. **c)** Upon collision of droplets, the continuous phase has to be drained before droplets coalesce. **d)** In the presence of surfactants, the gradient of surfactant density at the surface generates a Marangoni stress (red arrows) which counteracts the film drainage, increasing thus drainage time and therefore stabilizing the droplets against coalescence. Adapted from Baret.[42]

Emulsions with polydisperse size droplets are more prone to the destabilization mechanisms, and therefore monodisperse emulsion droplets generation and stabilization is of most importance before water evaporation, in order to obtain monodispersed and reproducible spherical photonic structures.

3.1.3. Lithographic techniques for microfluidics

The standard methods for fabricating microfluidic devices were inherited from the microelectronics industry. Patterns of etched resists are defined on rigid, planar substrates such as silicon and glass with photolithography or electron-beam lithography, and relief structures are then created by reactive-ion or wet etching.

3.1.3.1. Photolithography

Photolithography is the most widely used form of lithography, where a pattern is transferred to a photosensitive polymer (a photoresist) by exposure to ultraviolet light shone through an optical mask, which consists of opaque patterns (iron oxide or aluminium) on a transparent support (quartz or glass) used to define

features on a Si wafer. The pattern in the photoresist is then further transferred to the underlying substrate (light alters the structure of the resist, and the areas of the resist exposed to light can be washed away with chemicals, leaving just the pattern of the mask on the surface) by subtractive (etching) or additive (deposition) techniques, illustrated in Figure 3.4.

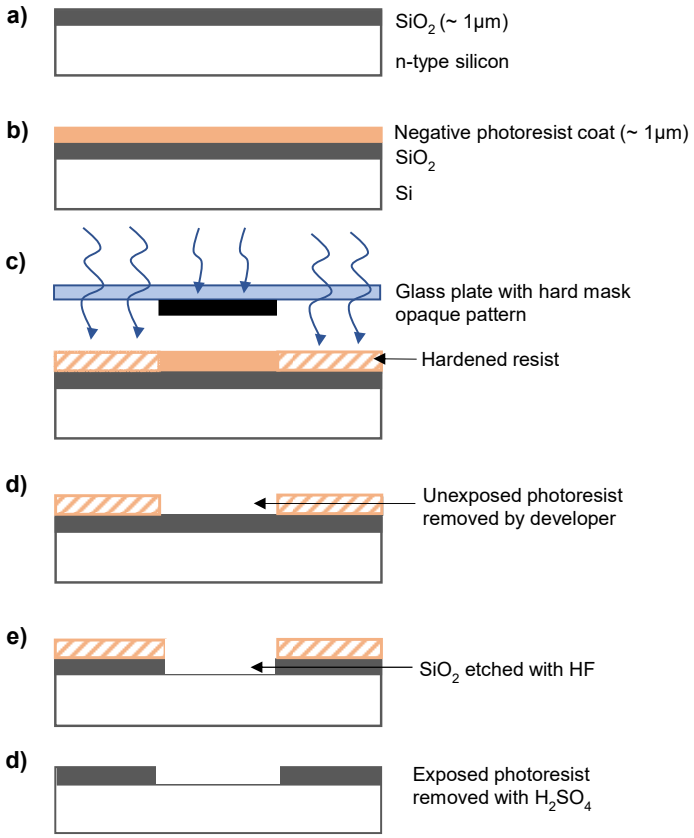

Figure 3.4: Process flow of basic photolithography exemplifying a pattern transfer from a mask to a layer of silicon dioxide. **a)** oxidized silicon wafer; **b)** coating with photoresist; **c)** exposure of hard mask pattern, **d)** development of unexposed photoresist leaves the negative image of the hard mask pattern; **e)** oxide etching and **f)** photoresist stripping. Adapted from Zaouk *et al*.[45]

The advantages of this methodology are the high spatial resolution and parallel processing: photolithography and etching create all features in a single step.[46] Photolithography, however, has disadvantages for the fabrication of microfluidic devices. Besides being expensive, the microchannels sealing and the sample introduction or collection are not an easy task. Nonetheless, is the most general way to prepare masters for soft lithography. Photolithography can easily generate relief patterns of photoresist, obtained by direct writing laser (DWL) of a computer aided design (CAD) program in two or three dimensions, that can serve as templates for molding a prepolymer.[47]

3.1.3.2. Soft lithography

One of the most common methods for generating microfluidic circuits is soft lithography, taking advantage of the outstanding properties of the silicone elastomer polydimethylsiloxane (PDMS).[48] Organic polymers offer an alternative technology for the fabrication of microfluidic devices, specifically addressing rapid prototyping and replica molding.[49] These techniques are called soft lithography due to the elasticity of the polymers they are made with.[50] PDMS properties (Table 3.1) make it suitable as a material for prototyping of microfluidic devices for a wide range of applications.

Table 3.1: Physical and chemical properties of PDMS. Adapted from Sindy and Whitesides.[47]

Property	Characteristics	Consequence
Optical	Transparent; UV cut-off 240 nm	Optical detection from 240 to 1100 nm
Electrical	Insulating	Allows embedded circuits
Mechanical	Elastomeric	Conforms to surfaces; allows actuation by reversible deformation
Thermal	Insulating; stable up to 300°C	Can be used to insulate heated solutions
Interfacial	Low surface free energy	Replicas release easily from molds; not wetted by water unless oxidized
Permeability	Low permeability to water; permeable to gases and nonpolar organic solvents	Channels contains aqueous solutions; Incompatible with few organic solvents
Reactivity	Inert towards most reagents; can be oxidized by plasma	Can be modified to be hydrophilic and reactive toward silanes
Toxicity	Nontoxic	Can be implanted in vivo

Besides its low cost, its versatile surface chemistry and the mechanical flexibility and durability, are very important features because the microchannels sealing can be achieved by oxidizing the PDMS surface without resorting to adhesives. With a single structure defined in a photoresist by photolithography, it is possible to generate many replicas in PDMS by molding. Soft lithography is therefore a replication technique: it provides a cheap way of reproducing structures that would otherwise need to be formed with expensive techniques.[51]

Soft lithography starts with the production of a PDMS replica of a master (or mold).[48] The liquid PDMS pre-polymer conforms to the shape of the master and replicates its features with high fidelity. The low surface free energy and elasticity of PDMS allow it to release from the masters without damaging the master or itself.

One advantage of PDMS is that it can seal to itself, or to other surfaces, reversibly or irreversibly and without distortion of the channels. Sealing of PDMS channels is substantially simpler than sealing channels in glass, silicon, or thermoplastics. A reversible sealing provided by simple van der Waals contact is watertight but cannot withstand pressures greater than ~5 psi. For an irreversible sealing, PDMS is exposed to an air plasma for 1 min. It is believed that this treatment generates silanol groups (Si-OH) on the surface of the PDMS by the oxidation of methyl groups. For sealing, the two surfaces must be brought into contact quickly (<1 min) after oxidation, because the surface of the oxidized PDMS reconstructs in air.[48]

3.2. Experimental methodology

PDMS microfluidic devices developed by soft lithography were fabricated at INESC-MN.

3.2.1. Materials

Alconox solution (Alconox Inc); Sylgard 184 poly(dimethyl)siloxane (Dow Corning); Blunt syringes needle (LS22 and LS20 Gauge, Instech Laboratories, Inc); Polyethylene tubing (BTPE-50, 0.58x0.97 mm, Instech Laboratories, Inc.); Metal couplers (SC22/15, Instech Laboratories, Inc.); SU-8 50 photoresist (Microchem Corp.); Propylene glycol methyl ether acetate (PGMEA, 99.5%, Sigma-Aldrich); Isopropyl Alcohol (IPA, 99.9%, LabChem Inc.); Photoresist PFR 7790G (JSR); Photoresist developer TMA238WA (JSR); Silicon wafer (150 mm diameter, University Wafer); TechniEtch Al80 Aluminium etchant (Microchemicals); Hexadecane (99%, Alfa Aesar); Span® 80, (viscosity 1000-2000 mPa.s at 20°C, Sigma-Aldrich); Aqueous dispersion of monodispersed PNP and Ion-exchange resin (AG®501-X8 and Bio-Rex® MSZ 501 (D) Mix Bed Resin, 20-50 mesh, Bio Rad), were used.

3.2.2. Equipment

Automatic Dicing Saw DAD-321; Class 10/100 clean room; Nordiko 7000 magnetron sputtering system (Nordiko Technical Services Ltd); SVG Resist coater and developer track (Silicon Valley Group Inc.); Heidelberg DWLii direct write laser lithograph (Heidelberg Instruments); Vertical laminar airflow cabinet (Faster-BSC-EN); UVO Cleaner 1444AX-220 (Jelight Company, Inc.); Spin

coater(Laurell Technologies Corp.); Digital hotplate; Stuart UV Light (254 nm, 400 W, UV Light Technology Limited); Stereo microscope (AmScope); Vacuum desiccator (Bel-Art Products); Oven loading model 100–800 (70°C, Memmert); Expanded oxygen plasma cleaner PDC-002-CE (200 W, Harrick Plasma); Pump 33 syringe pumps (Harvard Apparatus); Digital shaking drybath (Thermo Scientific); Metallurgical microscope OKM-1 (Kern optics); Digital microscope camera ODC 832 (Kern optics).

3.2.3. Microchannels design and hard mask fabrication

The design and shape of the emulsification microfluidic circuits were developed in AutoCAD (Autodesk® AutoCAD 2016 student version). Regardless previously reported experiments,[28,47,52,53] the design of a microchannel architecture that best suited our purpose was, either way, a trial and error experience.

For W/O emulsion droplets generation, circuits with T-junction geometry were drawn with different microchannel widths: 50×50 μm; 100×50 μm and 100×100 μm for the continuous×dispersed phases, respectively. Flow-focusing devices coupled with T-junction architecture were also drawn for the generation of W/O/W emulsions, where the inner T-shaped microchannels width was either 50×50 μm or 100×100 μm for the continuous×dispersed phases, respectively, and the outer flow-focusing microchannels width was design with 100 or 200 μm (Figure 3.5). Collecting chambers to evaluate droplet size distribution were also drawn, with supporting pillars to avoid chambers collapse upon sealing.

AutoCAD drawings with different circuit geometries were transferred to a high-resolution photomask for the fabrication of the microfluidic devices by soft lithography. An efficiently large number of microfluidic circuits were transferred to the hard mask, saving time and money. The fabrication of the aluminium hard mask (Figure 3.6), is based in clean room procedures, with the exception of the substrate cutting and cleaning where corning glass is cutted in squares of 5×5 cm in a dicing saw and thoroughly clean with alconox solution under ultrasound. A layer of aluminium with 2000 Å thickness is deposited on the glass surface with N7000 magnetron sputtering and subsequently a layer of positive photoresist (coater 6/2) is deposit on top of the aluminium layer, using the SVG track. Alignment marks are followed (AMSION map with dimensions: X: 40000; Y: 41000 μm) for transferring the AutoCAD drawings to the photoresist by direct

write laser (DWL). Laser exposed photoresist is then developed for 1 minute at 110°C. Aluminium etching is performed in the wet bench with the isotropic and selective TechniEtch Al 80 etchant, for 5 minutes at ambient temperature and manual agitation. Rinsing with acetone removes the photoresist and the hard mask is obtained.

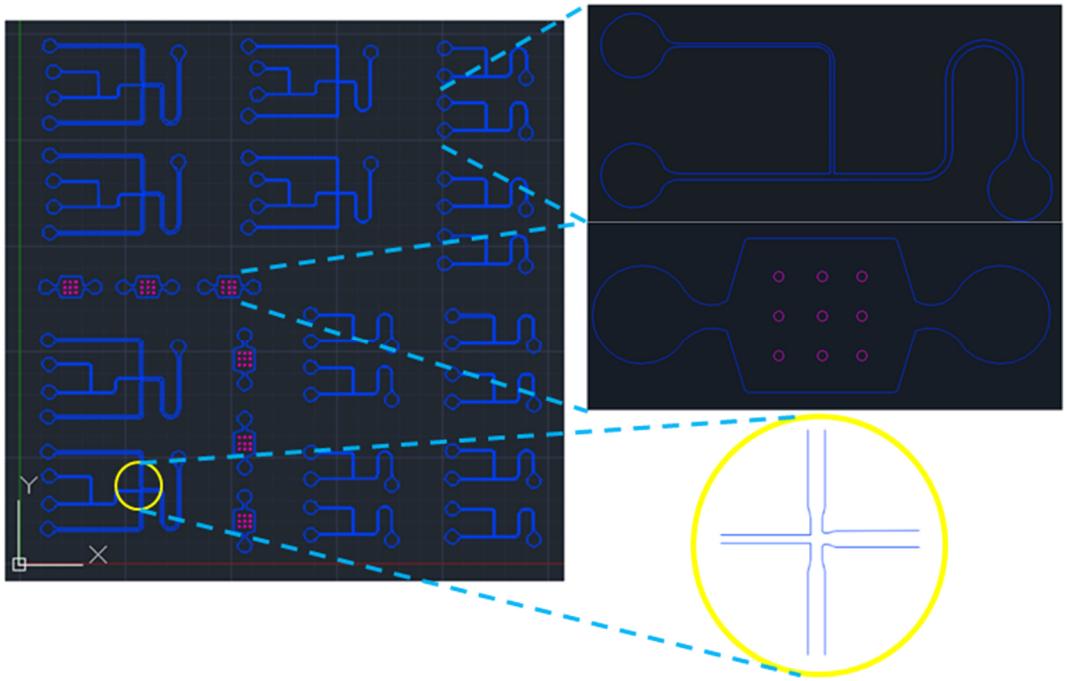

Figure 3.5: AutoCAD drawings of the microchannel architecture for the microfluidic devices. T-junction geometries; collecting chambers; and flow-focusing geometry.

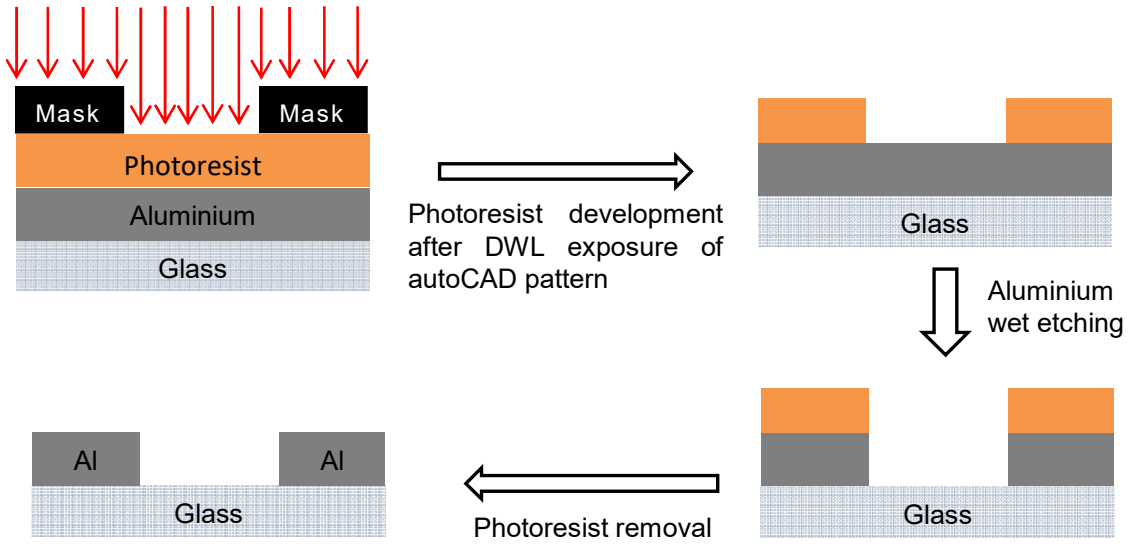

Figure 3.6: Schematics of the aluminium (Al) hard mask fabrication, by direct writing laser of an AutoCAD design in a positive photoresist followed by the wet etching of Al. On this mask, Al should be everywhere except where the pattern is (subtractive lithography).

3.2.4. SU-8 mold and PDMS microfluidic devices fabrication

The fabrication of an SU-8 mold with 50 µm height,[54] used for the replication of PDMS microfluidic circuits, is based on additive photolithography of the negative photoresist SU-8 (Figure 3.7). Its fabrication does not require clean room facilities and starts by thoroughly cleaning 4×4 cm silicone substrates (cutted from silicon wafers) with alconox solution in an ultrasonication bath at 65°C, for 45 min. When necessary, a plasma treatment was performed to the substrate surface to improve adhesion of the SU-8 layer.

A layer of SU-8 is spincoated onto the Si substrate in two steps: 500 rpms for 10 s at 100 rpm/s acceleration to spread the SU-8 photoresist and 1900 rpm for 30 s at 300 rpm/s acceleration to define the intended 50 µm height of the SU-8 layer. After the coating, a pre-baking is performed in a hot plate during 6 minutes at 65°C plus 20 min at 95°C.

The hard mask is aligned over the pre-baked SU-8 layer with the aluminium surface facing down and exposed to ultraviolet light for 40 s. A post-exposure bake is performed during 1min at 65°C plus 5 min at 95°C, and after, the non-exposed photoresist is developed by submerging the SU-8 substrate in propylene glycol methyl ether acetate (PGMEA) under manual agitation. A final hard bake is performed at 150°C for 15 min.

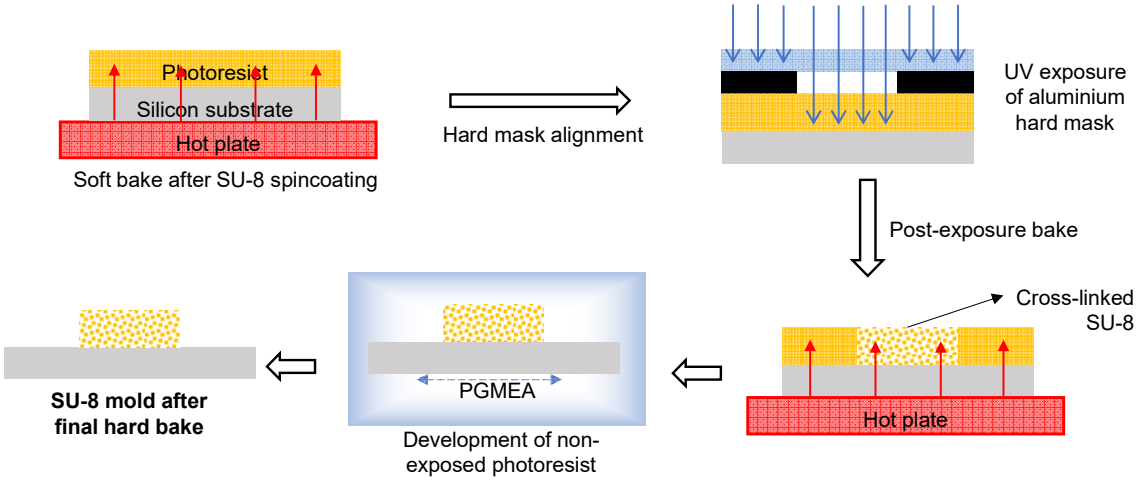

Figure 3.7: Schematics of the SU-8 mold fabrication, by photolithography of the hard mask onto the negative photoresist SU-8 (additive photolithography). The final height of the mold was measured with a profilometer and corresponds to 54 µm.

The replication of the SU-8 mold into PDMS microfluidic structures, start by placing and fixing the mold on the bottom of a petri dish, with the patterned surface facing up. To produce a replica (Figure 3.8), a 10:1 wt ratio of PDMS

base to curing agent is mixed (Sylgard 184), degassed for 30 min and poured on top of the patterned surface of the SU-8 mold place inside the petri dish, and is then left to cure in the oven for 90 min at 70°C. PDMS elastomer is also used to fabricate 500 µm height PDMS slabs for sealing the microfluidic devices. These slabs are produced by spin coating the PDMS mixture on top of a silicon wafer at 250 rpm for 25 s with an acceleration of 100 rpm/s. Cured PDMS is peeled off from the SU-8 mold and access holes are punched for inlets and outlet with 20 gauge luer stubs.

Irreversible surface bonding is achieved by sealing the PDMS structures against the PDMS slabs by first oxidizing both sides using an oxygen plasma cleaner at the medium power setting for 60 s. Immediately after the plasma treatment membranes are placed in contact with the PDMS structures. For an efficient sealing of the microfluidic devices after the plasma treatment, the circuits must be stored for at least 24 hours before being used. This would allow the hydrophobic recovery and stabilization by diffusion of the unreacted siloxane groups, because PDMS becomes relatively hydrophilic for a few hours after the sealing step.

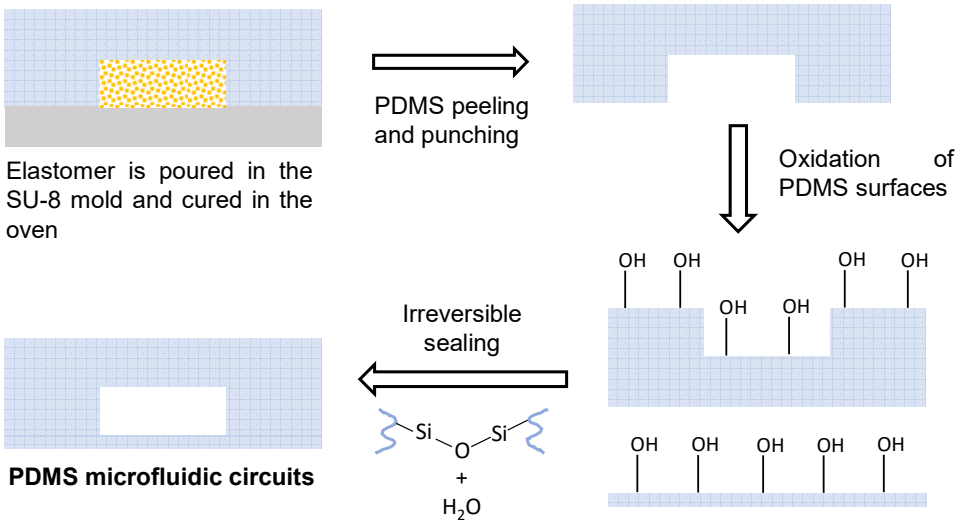

Figure 3.8: Schematics of the PDMS microfluidic devices fabrication from the SU-8 mold. After plasma treatment, PDMS slabs are readily sealed to the molded PDMS structures (before oxidized PDMS reconstructs in air), and microfluidic devices for the emulsion droplets generation are obtained.

To further extend the lifetime of the SU-8 mold, it was replicated in epoxy resin. Permabond epoxy resin was poured onto the first PDMS replica of the SU-8 mold. After degassing for 48 h, the resin is placed in an oven at 80°C where temperature increases at 2-degree steps until reaching 120°C. Once stabilized at this

temperature the resin is cured for 30 min and the epoxy mold is pealed of and stored for further PDMS microfluidic circuits replication.[55]

3.2.5. Emulsification procedure and droplet formation

The emulsification process in PDMS microfluidic devices with T-shaped microchannels is based in a dispersed phase, composed of an aqueous dispersion of polymer nanoparticles (PNP) with a volume fraction of ~0.2, and a continuous oil phase composed of hexadecane with 5 wt% SPAN 80 surfactant. The formation of W/O droplets in microfluidic channels was followed by microscopy and recorded with CCD digital color camera coupled to an optical microscope.

The experimental procedure for droplet formation is summarized in Figure 3.9. Dispersed and continuous phases are injected into the microfluidic device through syringe with a blunt needle, connected to polyethylene tubing via a metal coupler into the inlets access holes. It is very important that syringes and polyethylene tubes remain free of air gaps to avoid rapid pressure differences that results in irregular flows. Therefore, the syringes should be appropriately purged until the liquid reaches the tip of the metal coupler before inserting the coupler into the access holes.

Volumetric flow rates for each phase are imposed and controlled by syringe pumps. The outlet is connected through a metal coupler to polyethylene tubing with its tip submerged in a petri dish filled with the continuous phase, where emulsion droplets are collected.

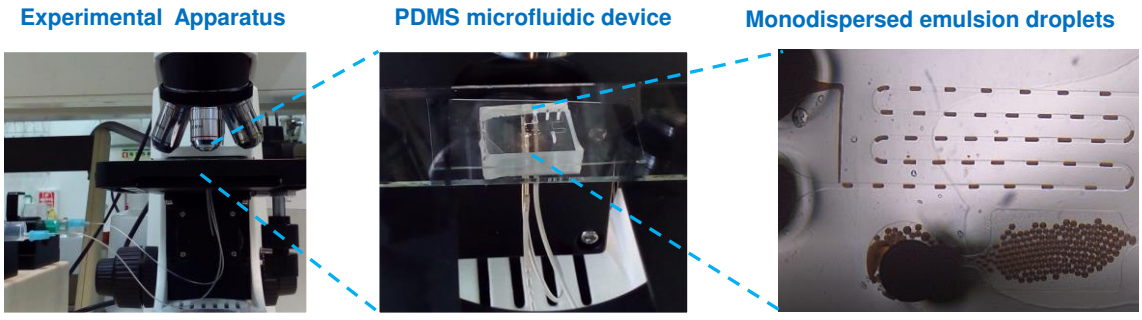

Figure 3.9: Experimental apparatus for the microfluidic droplet generation. PDMS microfluidic circuits in a glass lamella, are placed in the open stage of an inverted optical microscope, with the circuit facing down. Dispersed and continuous phases are injected into the device through polyethylene tubes via syringe pump. Precise controlled flows originate monodispersed emulsion droplets formed at the T-junction and droplet size uniformity can be seen in the collecting chambers.

Besides stabilizing droplet interface, surfactants used in droplet-based microfluidic systems also plays an important role in the derivatization of the microchannels surface.[42] This is why before the emulsification experiments, PDMS microfluidic devices should be conditioned by passing the continuous phase for some time, to allow microchannels surface to be covered by the surfactant molecules forming a monolayer at phase boundaries, thus improving their performance.[50]

Despite the numerous studies investigating the mechanism for droplet formation and break-up in microfluidic devices, the available physical models are not capable of predicting droplet size, uniformity, and production frequency as a function of the relevant parameters, leading to an experimental error and trial approach. After several experiments, where different flow rates, surfactant concentration and droplet collecting modes were tested, experimental procedures and conditions allowing the reproducible generation of monodispersed and stable emulsion droplets, within the intended size range were established.

3.3. Results and discussion

Before resorting to microfluidic droplet formation, other experimental approaches were attempted to produce monodispersed emulsion droplets. Following the work of Yang,[56] the aqueous phase was dispersed by means of syringe injection, either manually or by pressure pumps, into the magnetically or mechanically stirred oil phase. However, the obtained droplets were too large and polydisperse in size, because the magnetic stirring promoted their coalescence, and the mechanical stirring promoted their break-up. In a different strategy following Kim´s work,[57] microwave irradiation was introduced as a fast heating approach without stirring, but was also unable to prevent droplet coalescence, and consequently do not serve our purpose.

In microfluidic T-junction devices, the two immiscible phases flow into separate inlet channels that meet at right angles for droplet formation. The aqueous dispersion of PNP to be dispersed, emerges into the junction, and the cross-flow of the continuous phase, hexadecane with 5 wt% SPAN 80, deforms the emerging interface and leads to break-up of discrete droplet. Relatively small flow

rates i.e., 0.5 µL/min and 5 µL/min of dispersed and continuous phases, respectively, leads to droplet formation under the squeezing regime (Figure 3.10). However, higher flow rates are used for large scale production of emulsion droplets. In such case, the flow rates used are 5 µL/min and 50 µL/min, respectively, for dispersed and continuous phases. Under these conditions, the increase in capillary number upon increasing flows rates, leads to a transition from the squeezing to the dripping regime.

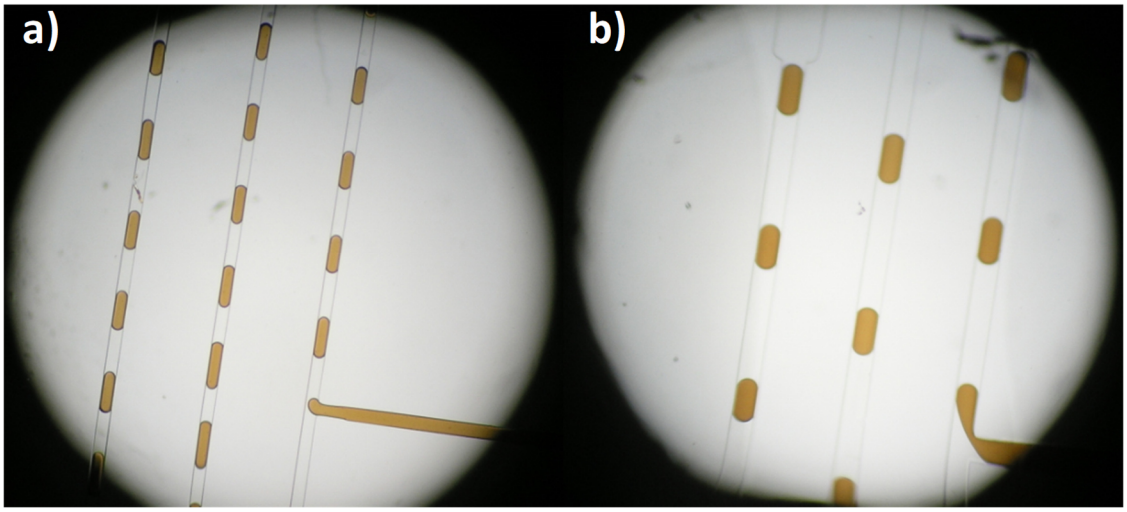

Figure 3.10. Droplet formation at the T-junction of the microfluidic devices, under the squeezing regime at different stages of droplet formation. Microchannels width is 50 µm for continuous and dispersed phases and the flow rate is 0.5 and 5 µL/min for the dispersed and continuous phases, respectively. **a**) Dispersed phase is filling the continuous phase microchannel at the cross-section and a droplet emerges; **b**) Droplet grows large enough and completely obstruct the continuous phase channel apart from the neck, that becomes thinner as the continuous phase is injected, during which time the droplet continues to grow due to the injection of the dispersed phase. Eventually upstream pressure in the continuous phase increases, resulting in an additional force exerted on the interface that promotes droplet break-up.

The production rate of stable and monodispersed emulsion droplets under the dripping regime is quite high, and a large number of droplets is produced in a short period of time. A microscopy image showing stable emulsion droplets with a highly monodispersed size are visible in Figure 3.11.

Emulsion droplets size coefficient of variation, CV, was calculated from the microscopic images obtained immediately after the emulsification process, according to equation 3.2:

$$CV = \left(\frac{\sigma}{D}\right) \times 100 \qquad (3.2)$$

where σ is the standard deviation of droplets size and D is the mean droplet diameter. Values of CV as low as 3% were obtained which indicate precise control of droplet size in our microfluidic experiments.

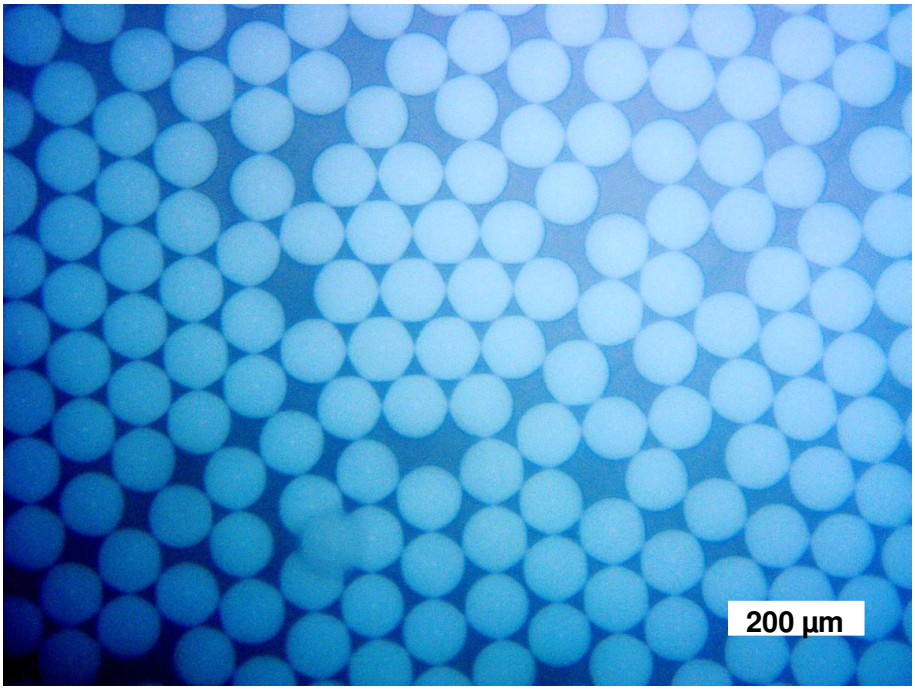

Figure 3.11: Highly monodispersed and stable aqueous droplets containing the PNP were obtained, with a mean diameter of ~100 µm.

3.4. Conclusions

Soft-lithographic techniques made the prototyping for microfluidic devices quite rapid and cheap, with precise microchannels width and height, that meet our purpose. With droplet based microfluidic approaches in T-shaped microchannels geometry, we successfully accomplish our goal: efficient production of monodispersed and stable emulsion droplets composed of an aqueous dispersion of PNP, that can be handled before inducing temperature-driven water evaporation.

Droplets size is determined by different parameters including the characteristic dimensions of the microchannels and the relative flow rates of the two immiscible phases. Larger flow rates and smaller characteristic dimensions results in a decrease in droplet size. The PDMS microfluidic devices are suitable and efficient at producing monodispersed emulsion droplets, with a size coefficient of variation of 3%, at quite high production rates under the dripping regime.

3.5. References

1. Wang, J. & Zhu, J. Recent advances in spherical photonic crystals: Generation and applications in optics. *Eur. Polym. J.* **49**, 3420–3433 (2013).
2. Gorelik, V. S. Optics of Globular Photonic Crystals. *Laser Phys.* **18**, 1479–1500 (2008).
3. Glotzer, S. C. & Solomon, M. J. Anisotropy of building blocks and their assembly into complex structures. *Nat. Mater.* **6**, 557–562 (2007).
4. Wang, J., Wang, J. & Han, J. Fabrication of Advanced Particles and Particle-Based Materials Assisted by Droplet-Based Microfluidics. *Small* **13**, 1728–1754 (2011).
5. Velev, O. D., Lenhoff, A. M. & Kaler, E. W. A Class of Microstructured Particles Through Colloidal Crystallization. *Science* **287**, 2240–2243 (2000).
6. Meldrum, F. C. & O'Shaughnessy, C. Crystallization in Confinement. *Adv. Mater.* **32**, 2001068 (2020).
7. Zhao, Y., Shang, L., Cheng, Y. & Gu, Z. Spherical Colloidal Photonic Crystals. *Acc. Chem. Res.* **47**, 3632–3642 (2014).
8. Zhokhov, A. A., Masalov, V. M., Sukhinina, N. S., Matveev, D. V., Dolganov, P. V., Dolganov, V. K. & Emelchenko, G. A. Photonic crystal microspheres. *Opt. Mater.* **49**, 208–212 (2015).
9. Hou, J., Li, M. & Song, Y. Patterned Colloidal Photonic Crystals. *Angew.Chem.Int. Ed.* **57**, 2544–2553 (2018).
10. Vogel, N., Utech, S., England, G. T., Shirman, T., Phillips, K. R., Koay, N., Burgessd, I. B., Kolle, M., Weitz, D. A. & Aizenberg, J. Color from hierarchy: Diverse optical properties of micron-sized spherical colloidal assemblies. *PNAS* **112**, 10845–10850 (2015).
11. Lima, R. de S., Ré, M.-I. & Arlabosse, P. Drying droplet as a template for solid formation: A review. *Powder Technol.* **359**, 161–171 (2020).
12. Sugiura, S., Nakajima, M., Oda, T., Satake, M. & Seki, M. Effect of interfacial tension on the dynamic behavior of droplet formation during microchannel emulsification. *J. Colloid Interface Sci.* **269**, 178–185 (2004).
13. Sowade, E., Blaudeck, T. & Baumann, R. R. Inkjet Printing of Colloidal Nanospheres: Engineering the Evaporation-Driven Self-Assembly Process to Form Defined Layer Morphologies. *Nanoscale Res. Lett.* **10**, 362 (2015).
14. Sowade, E., Blaudeck, T. & Baumann, R. R. Self-Assembly of Spherical Colloidal Photonic Crystals inside Inkjet-Printed Droplets. *Cryst. Growth Des.* **16**, 1017–1026 (2016).
15. Theberge, A. B., Courtois, F., Schaerli, Y., Fischlechner, M., Abell, C., Hollfelder, F. & Huck, W. T. S. Microdroplets in Microfluidics: An Evolving Platform for Discoveries in Chemistry and Biology. *Angew. Chem. Int. Ed.* **49**, 5846–5868 (2010).

16. Huebner, A., Sharma, S., Srisa-Art, M., Hollfelder, F., Edel, J. B. & deMello, A. J. Microdroplets: A sea of applications? *Lab Chip* **8**, 1244–1254 (2008).

17. Teh, S., Lin, R., Hung, L. & Lee, A. P. Droplet microfluidics. *Lab Chip* **8**, 198–220 (2008).

18. Brugarolas, T., Tu, F. & Lee, D. Directed assembly of particles using microfluidic droplets and bubbles. *Soft Matter* **9**, 9046–9058 (2013).

19. Kumacheva, E., Garstecki, P., Wu, H. & Whitesides, G. M. Two-Dimensional Colloid Crystals Obtained by Coupling of Flow and Confinement. *Phys. Rev. Lett.* **91**, 128301 (2003).

20. Whitesides, G. M. The origins and the future of microfluidics. *Nature* **442**, 368–373 (2006).

21. Hernandez, E. C., Guerrero, J., Fernandez-Nieves, A. & Gordillo, J. M. Drop generation in controlled fluid flows. in *Fluids, Colloids and Soft Materials: An Introduction to Soft Matter Physics,* John Wiley & Sons, Inc., Hoboken (2016).

22. Gunther, A. & Jensenb, K. F. Multiphase microfluidics: from flow characteristics to chemical and materials synthesis. *Lab Chip* **6**, 1487–1503 (2006).

23. Squires, T. M. & Quake, S. R. Microfluidics: Fluid Physics at the Nanoliter Scale. *Rev. Mod. Phys.* **77**, 977–1026 (2005).

24. Whitesides, G. M. & Stroock, A. D. Flexible Methods for Microfluidics. *Phys. Today* **54**, 42–48 (2001).

25. Christopher, G. F. & Anna, S. L. Microfluidic methods for generating continuous droplet streams. *J. Phys. D Appl. Phys.* **40**, R319–R336 (2007).

26. Dittrich, P. S. & Manz, A. Lab-on-a-chip: microfluidics in drug discovery. *Nature* **5**, 210–218 (2006).

27. Gu, H., Duits, M. H. G. & Mugele, F. Droplets Formation and Merging in Two-Phase Flow Microfluidics. *Int. J. Mol. Sci.* **12**, 2572–2597 (2011).

28. Thorsen, T., Roberts, R. W., Arnold, F. H. & Quake, S. R. Dynamic Pattern Formation in a Vesicle-Generating Microfluidic Device. *Phys. Rev. Lett.* **86**, 4163–4166 (2001).

29. Gupta, A. & Kumar, R. Flow regime transition at high capillary numbers in a microfluidic T-junction: Viscosity contrast and geometry effect. *Phys. Fluids* **22**, 122001 (2010).

30. Lee, W., Walker, L. M. & Anna, S. L. Role of geometry and fluid properties in droplet and thread formation processes in planar flow focusing. *Phys. Fluids* **21**, 032103 (2009).

31. Abate, A. R. & Weitz, D. A. High-Order Multiple Emulsions Formed in Poly(dimethylsiloxane) Microfluidics. *Small* **5**, 2030–2032 (2009).

32. Christopher, G. F., Noharuddin, N. N., Taylor, J. A. & Anna, S. L. Experimental observations of the squeezing-to-dripping transition in T-shaped microfluidic junctions. *Phys. Rev. E* **78**, 036317 (2008).

33. H.A. Stone, A.D. Stroock, and A. A. Engineering flows in small devices: Microfluidics Toward a Lab-on-a-Chip. *Annu. Rev. Fluid Mech.* **36**, 381–411 (2004).

34. Seemann, R., Brinkmann, M., Pfohl, T. & Herminghaus, S. Droplet based microfluidics. *Reports Prog. Phys.* **75**, 016601 (2012).

35. Bremond, N. & Bibette, J. Exploring emulsion science with microfluidics. *Soft Matter* **8**, 10549–10559 (2012).

36. Nekouei, M. & Vanapalli, S. A. Volume-of-fluid simulations in microfluidic T-junction devices: Influence of viscosity ratio on droplet size. *Phys. Fluids* **29**, 032007 (2017).

37. Menech, M. De, Garstecki, P., Jousse, F. & Stone, A. Transition from Squeezing to Dripping in a Microfluidic T-Shaped Junction. *J. Fluid Mech.* **595**, 141–161 (2008).

38. Beatus, T., Bar-ziv, R. H. & Tlusty, T. The physics of 2D microfluidic droplet ensembles. *Phys. Rep.* **516**, 103–145 (2012).

39. Zhou, C., Yue, P. & James J. Feng. Formation of simple and compound drops in microfluidic devices. *Phys. Fluids* **18**, 092105 (2006).

40. Nowak, E., Kovalchuk, N. M., Che, Z. & Simmons, M. J. H. Effect of surfactant concentration and viscosity of outer phase during the coalescence of a surfactant-laden drop with a surfactant-free drop. *Colloids Surfaces A Physicochem. Eng. Asp.* **505**, 124–131 (2016).

41. Dai, B. & Leal, L. G. The mechanism of surfactant effects on drop coalescence. *Phys. Fluids* **20**, 040802 (2008).

42. Jean-Christophe Baret. Surfactants in droplet-based microfluidic. *Lab Chip* **12**, 422–433 (2012).

43. Taylor, P. Ostwald ripening in emulsions. *Adv. Colloid Interface Sci.* **75**, 107–163 (1998).

44. Debon, A. P., Wootton, R. C. R. & Elvira, K. S. Droplet confinement and leakage: Causes, underlying effects, and amelioration strategies. *Biomicrofluidics* **9**, 024119 (2015).

45. Zaouk, R., Park, B. Y. & Madou, M. J. Introduction to Microfabrication Techniques. *Methods Mol. Biol.* **321**, 5–15 (2006).

46. Brittain, S., Paul, K., Zhao, X. & Whitesides, G. Soft lithography and microfabrication. *Phys. World* **11**, 30–37 (1998).

47. Tang, S. K. Y. & Whitesides, G. M. Basic Microfluidic and Soft Lithographic Techniques, Chapter 2. in *Optofluidics: Fundamentals, Devices, and Applications,* McGraw-Hil, 7–32 (2010).

48. Mcdonald, J C., Duffy, D. C., Anderson, J. R., Chiu, D. T., Wu, H., Schueller, O. J. A., & Whitesides, G. M. General Fabrication of microfluidic systems in poly(dimethylsiloxane). *Electrophoresis* **21**, 27–40 (2000).

49. Brehmer, M., Conrad, L. & Funk, L. New Developments in Soft Lithography. *J. Dispers. Sci. Technol.* **24**, 291–304 (2003).

50. Mcdonald, J. C. & Whitesides, G. M. Poly(dimethylsiloxane) as a Material for Fabricating Microfluidic Devices. *Acc. Chem. Res.* **35**, 491–499 (2002).

51. Whitesides, G. M., Ostuni, E., Takayama, S., Jiang, X. & Ingber, D. E. Soft Lithography in Biology and Biochemistry. *Annu. Rev. Biomed. Eng.* **3**, 335–373 (2001).

52. Bauer, W.-A. C., Fischlechner, M., Abell, C. & Huck, W. T. S. Hydrophilic PDMS microchannels for high-throughput formation of oil-in-water microdroplets and water-in-oil-in-water double emulsions. *Lab Chip* **10**, 1814–1819 (2010)

53. Yan, J., Bauer, Wolfgang-Andreas C. Fischlechner, M., Hollfelder, F. & Clemens F. Kaminski Huck, W. T. S. Monodisperse Water-in-Oil-in-Water (W/O/W) Double Emulsion Droplets as Uniform Compartments for High-Throughput Analysis via Flow Cytometry. *Micromachines* **4**, 402–413 (2013).

54. www.microchem.com/. Micro.Chem: Innovative Chemical Solutions For MEMS and Microelectronics.

55. Pinto, I. F., Caneira, C. R. F., Soares, R. R. G., Madaboosi, N., Aires-barros, M. R. & Conde, J. P. The application of microbeads to microfluidic systems for enhanced detection and purification of biomolecules. *Methods* **116**, 112–124 (2017).

56. Yi, G-R., Manoharan, V. N., Klein, S., Brzezinska, K. R., Pine, D. J. & Lange, F. F. Monodisperse Micrometer-Scale Spherical Assemblies of Polymer Particles. *Adv. Mater.* **14**, 1137–1140 (2002).

57. Kim, S., Lee, S. Y., Yi, G., Pine, D. J. & Yang, S. Microwave-Assisted Self-Organization of Colloidal Particles in Confining Aqueous Droplets. *J. Am. Chem. Soc.* **128**, 10897–10904 (2006).

4. Polymer nanoparticle assembly inside emulsion droplets

The assembly of PNP in the spherical confinement of emulsion droplets is described in this chapter. The process was monitored in real-time by microscopy imaging from the colors reflected by the ordered arrangement of PNP into crystalline planes as water evaporates. Manipulation of the assembly process by changing the pH of the PNP aqueous dispersion and/or temperature, allowed to control and tailor the desired photonic structures in a reproducible way, ranging from spherical colloidal photonic crystals to photonic glasses.

Hierarchical assembly of polymer nanoparticles (PNP) inside monodispersed emulsion droplets, aided by microfluidic technology, was used as a soft-template method to obtain spherical photonic structures, through temperature-induced water evaporation.[1-6] Both crystalline and amorphous structures can be obtained by colloidal crystallization or agglomeration of PNP confined in aqueous droplet templates suspended in an oil liquid media.[7-9]

Creating such colloidal supraparticles, or photonic microspheres, termed spherical photonic crystals (SPhCs) or spherical photonic glasses (SPhGs) according to the PNP arrangement, is directly related to the balance of forces acting between the particles and the kinetics of the assembly process.[10,11] To control the final structure is necessary to understand and manipulate the forces acting on the PNP, as well as the process conditions.[12-15]

Consequently, the formation of supraparticles requires overcoming repulsive forces between the nanoparticles confined in the aqueous droplets. In a bulk system, the balance of forces to achieve attractive interactions can be introduced, for example, via changes in the electrostatic stabilization (i.e., by changing pH or ion concentration).[12,16] The interplay between attractive and repulsive forces governs the density of the spherical structures.[17,18] The stronger the attractive component, the faster the agglomeration behavior, that can lead to diffusion-limited agglomeration and loose structures.[14,19]

In a disorder–order phase transition driven by entropy in colloidal systems dominated by repulsive inter-particle potential,[16,20,21] the densest packing of spheres in 3D is the fcc lattice, with a volume fraction, $\emptyset \sim 0.74$, whereas the densest disordered packing of spheres occurs at about $\emptyset \sim 0.64$.[22-26] At some volume fraction lower than 0.64, a crystalline solid should have higher vibrational entropy than the fluid: if arranged in an fcc lattice at 0.64 volume fraction, the particles have room to rattle around their lattice sites, whereas in a disordered arrangement, they are jammed.[19,27,28] Counterintuitively, the ordered phase has higher entropy than the disordered phase does at large volume fractions.[19,20,22,27] The reduction in entropy associated with the formation of only long-range order is offset by the increased packing contribution to the entropy associated with the particles greater freedom for local motions in the ordered state.[19,20,29] This explains why random close-packing (rcp) occurs at $\emptyset \sim 0.64$, while a close-packed crystal has $\emptyset \sim 0.74$. Rearranging an amorphous rcp structure into a

crystal increases the configurational space of the particles (free-volume entropy).[19,20,22,27,29]

A disorder–order transition owing to long-range electrostatic repulsions is expected for monodispersed and charged polymer nanoparticles at low ionic strengths. The relation between packing constraints, which are imposed by the spherical confinement of the emulsion droplets and the shape and structure of the nanoparticles, with the structural transitions and the kinetics of the assembly process are the key features to understanding how geometry and entropy govern not only the structure of the supraparticles, but also the dynamics of how it forms.[26,30,31]

4.1. Self-assembly in spherical confinement

Curved geometries add a fundamentally new ingredient to crystallography, not found in the study of order in spatially flat systems.[4,32-34] When colloidal crystallization is constrained by curved surfaces, excess defects known as grain boundary scars, are formed due to the spherical confinement.[4,9,33,35] As the number of particles on the sphere increases, defects are predicted to induce too much strain. This excess strain can be relieved by introducing additional dislocations. The configuration and orientation of these excess defects play an essential role in the crystallography on a spherical template.[34-36]

Evaporating droplets of a colloidal dispersion is a simple and fast approach to self-assembly. In this assembly process, the governing forces result from the interactions between the PNP, however, the PNP arrangement in the final structures is highly dependent on the speed with which the interface is moving inward.[18,31,37-40] The final size of the supraparticles depends not only on the number of PNP inside the droplets, that can be tuned by manipulating either the initial PNP concentration or the droplet diameters, but also on their packing fraction.[18,41-43] Therefore, to obtain reproducible supraparticle structures, and consequently reproducible optical properties, it is necessary to establish precise experimental conditions to control the kinetics of water evaporation.

4.1.1. Experimental procedure

To obtain spherical photonic pigments, aqueous dispersions of monodispersed PNP with diameters ranging from 173 to 331 nm in diameter, were emulsified in

a continuous oil phase by microfluidic PDMS devices. The dispersed aqueous phases, with a volume fraction of ~ 0.2, were injected in the microfluidic T-junction devices at a flow rate of 5 µL/min. The continuous oil phase, composed of hexadecane with 5 wt% of SPAN 80 surfactant, was injected into the device at a flow rate of 50 µL/min. Stable emulsion droplets with narrow size distributions were obtained (Figure 4.1). Droplets are then transferred into vials filled with the oil phase at different temperatures and submitted to controlled orbital stirring conditions. Consequently, temperature-driven water evaporation, results in nanoparticles assembly inside the spherical droplet template and photonic supraparticles are obtained.

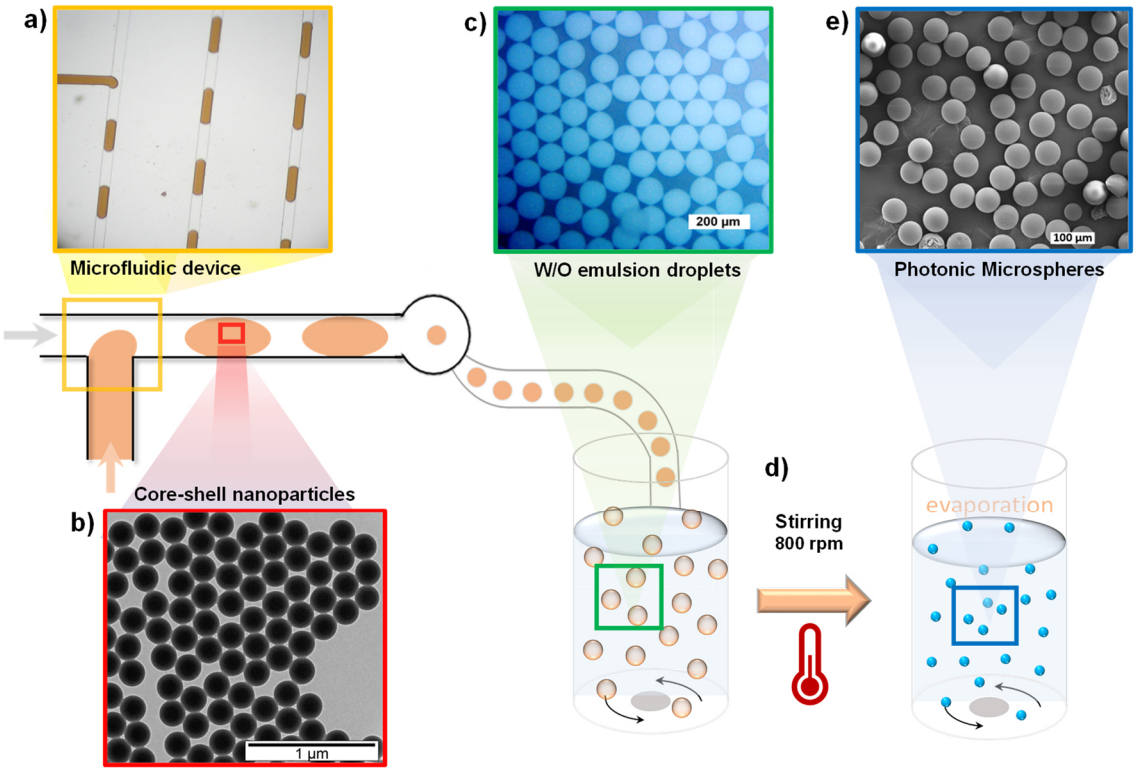

Figure 4.1: Experimental procedure to produce spherical photonic pigments based on W/O emulsification process in PDMS microfluidic devices. **a)** emulsification process by cross-flowing streams in T-shaped junctions for originating monodispersed aqueous droplets containing the PNP. **b)** TEM image of PNP223. **c)** monodispersed and stable W/O emulsion droplets are collected. **d)** droplets are then transferred to vials under controlled temperature and stirring conditions to induce the temperature-driven PNP assembly upon water evaporation. **e)** SEM image of the photonic supraparticles with close-packed structures obtained after PNP assembly.

4.1.2. Direct observation of the assembly process

During self-assembly, the PNP organize themselves in a stable and regular structure, according to the interactions determined by their shape and surface

properties.[44,45] We monitored the assembly process of PNP inside emulsion droplets, at room temperature and without stirring, by optical microscopy in reflectance mode, from the vibrant structural colors reflected by the ordered arrangement of the PNP as water starts to evaporate and droplets shrink.[31,41,43,46] Starting from the aqueous emulsion droplets right after the emulsification procedure, time lapse images summarizing the assembly process are shown in Figure 4.2.

Aqueous PNP emulsion droplets are white because of the strong diffuse scattering due to the lack of ordering. As water starts to evaporate and particle volume fraction increases, droplets display a weak reddish color in the center, that gradually increases suggesting the onset of short-range correlations. The color is blue-shifted and becomes progressively more vivid as the particle volume fraction increases with further droplet shrinkage. The pronounced brilliant colors after 20 minutes in Figure 4.2, indicate the onset of long-range order.

From simulation results[26,47] it is known that the crystallization starts near the spherical interface, initially forming approximately two or three layers. When the packing fraction reaches approximately $\emptyset \sim 0.52$, part of the interior starts to crystallize proceeding inwards and the surface layer becomes less crystalline. Between the volume fractions $\emptyset \sim 0.52$ and $\emptyset \sim 0.53$, the interior completely crystallizes. It is worth noting that this process is very dynamic, as the domains can crystallize and melt several times before the system fully crystallizes into the final structure.[26,47]

Stable emulsion droplets with ~ 90 μm in mean diameter and a size coefficient of variation, CV, under 3% (ratio of the standard deviation of droplets diameter by the mean droplet diameter), lose between 40 to 45% of their initial diameter after water evaporation, resulting in close-packed photonic supraparticles with approximately 50 μm in mean diameter.

Droplets movement caused by Marangoni flows was also observed during the drying process. The motion is due to a spontaneous symmetry breaking at the droplet interface resulting from different surfactant concentrations. Since the surfactant concentration directly influences the surface tension at the droplet interface, a gradient in surface tension emerges. This leads to a jump in shear stress at the interface, which in turn drags adjacent fluid layers in the direction of increased surface tension, which ultimately, leads to droplet propulsion.[48-50]

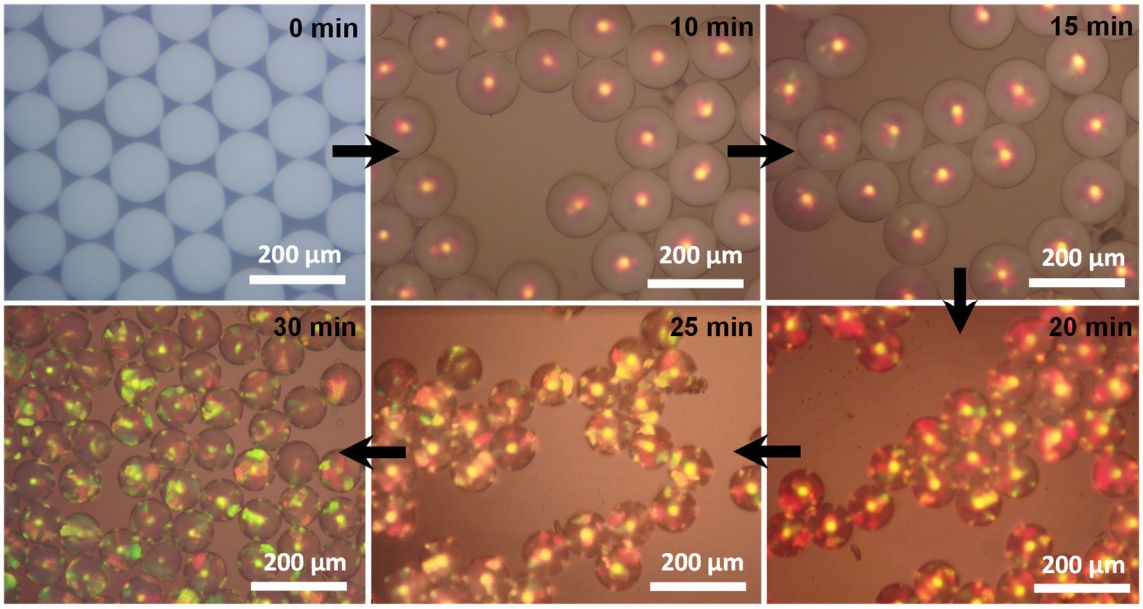

Figure 4.2: Time-lapse optical images of the evaporation-induced crystallization of PNP for the formation of spherical photonic pigments composed of PNP248, at room temperature without stirring. The evolution of structural color was monitored in real time. Even at room temperature, water evaporation from such small droplets is very fast. Starting with emulsion droplets ($t = 0\,min$), white due to diffuse scattering, a reddish spot at droplet center appears at ($t = 10\,min$) indicating the presence of ordered layers. The colored spot at the center spreads through the droplet as water continuous to evaporate ($t = 20\,min$). Upon reaching a critical concentration, the mobility of nanoparticles inside the droplet decreases as it continue to shrink and the color evolution kinetics slows down ($t = 30\,min$) due to slower crystallization rate at volume fractions near the fcc close-packed structure. Dynamic crystallization at the late stage of the assembly process was observed by the color pattern change resulting from the movement of the crystalline planes. See droplet coalescence during the assembly process in Appendix 4.

Intrinsically, evaporation-induced colloidal assembly can be regarded as a concentration process, in which the volume fraction of nanoparticles gradually increases from a low value to a maximum of 0.74. Despite the efforts to characterize the crystallization process during the evaporative drying, the exact kinetic pathways across the liquid-to-solid transition in evaporating aqueous droplets with colloidal nanoparticles remain elusive.[51,52] This is a complex and non-equilibrium system with changing volume fraction, external surface, and nanoparticles arrangement.[18,31] The timescale on which nanoparticles can arrange by diffusion to the hydrodynamic timescale for the nanoparticle transport by convection is given by the inward motion of the liquid droplet interface. If the diffusion time is small compared to the hydrodynamic time, the nanoparticles can arrange into an ordered structure.

In this process, capillary forces provide a compressive force that is spherically symmetrical and ultimately leads to the close-packed arrangement of colloidal nanoparticles into their final spherical configuration, and the van der Waals forces subsequently consolidates the structure. Similar to colloidal crystals in a plane, the surface of the photonic supraparticles also form the (111) plane of the fcc symmetry, consisting of an hexagonal network of nanoparticles with regular pores between them.[15,53-55]

When the structure completely crystallizes (after $t = 30\ min$, Figure 4.2), a final yellow-greenish hue is obtained and the structure achieves the highest packing density of the close-packed fcc structure, with a concentric arrangement of PNP layers towards the supraparticle center (Figure 4.3).

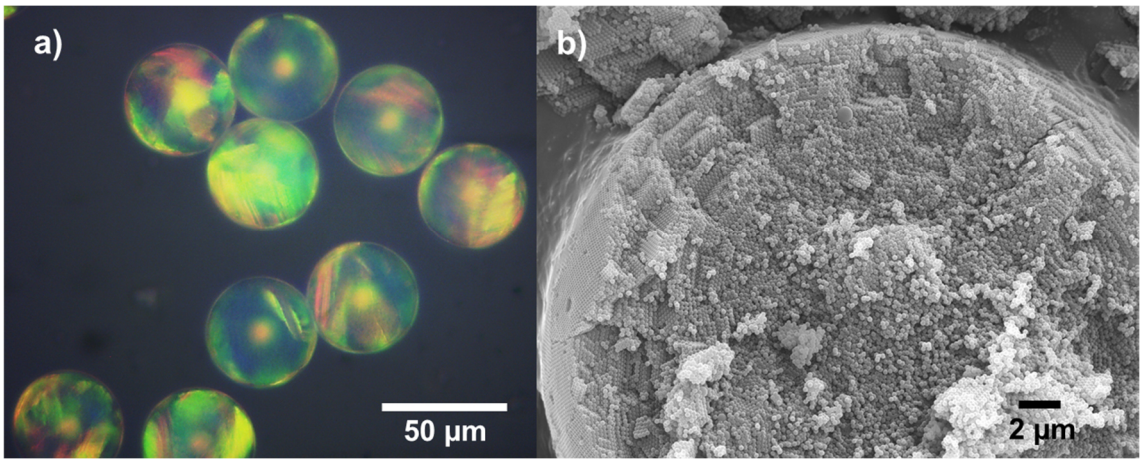

Figure 4.3: a) Optical microscopy image in reflectance mode showing the opal-like hues of yellow-greenish photonic pigments assembled from PNP248. **b)** SEM image of a broken supraparticle showing the hexagonal close-packing of PNP248 at the surface of the photonic structure, and the concentric arrangement of PNP layers packed in a fcc structure towards the center.

4.2. Internal structure tunability

So far, we report the spontaneous assembly of PNP inside emulsion droplets without the influence of external forces. Due to this inherent autonomy, the self-assembly processes are seen as a promising tool in the fabrication of nanostructures with a high degree of precision because the energy minimization that leads to the final state of the assembly, potentially results in fewer defects and more stable structures.[16,56,57] However, as already mentioned, the behavior of colloidal particles is governed by a large number of interactions, and the formation and stability of the photonic supraparticle results from a balance between the different forces. Therefore, changing the assembly conditions would

not only allow to tune the interactions between the PNP, but also the kinetics of the assembly process, thus tuning the internal structure of the supraparticles.
To this end, we evaluated the effect of different experimental conditions in the packing of PNP, resulting either in a more crystalline or an amorphous structure, and how the structure relates to the reflected colors of the spherical pigments. We changed the pH of the PNP dispersions prior to the emulsification and assembly procedure. Different assembly temperatures and different exposure time to a specific temperature during the assembly, were also tested.

4.2.1. Effect of pH

The first strategy we used to tune the structural order of the photonic pigments was to change the pH of the aqueous emulsion droplets during assembly, maintaining constant the temperature, drying time, and stirring rate.
The DLVO theory, named after Derjaguin, Landau, Verwey and Overbeek, describes the interaction potential between two charged surfaces in a liquid medium. The interaction potential for two spherical particles is a combination of the attractive van der Waals interaction potential and the repulsive electrostatic interaction potential due to the electric double layer of the charged surfaces.[58] These interactions lead to a potential energy *vs* distance profile with the primary minimum at close separation, followed by a maximum, called the energy barrier. The height of the barrier corresponds directly to the probability that a particle-particle collision will lead to particle aggregation.[58] However, for PNP with a water soluble shell an extra stabilization effect is obtained by steric repulsion between the surface polymer chains.
The nanoparticles used here, composed of a polystyrene core and a soft poly(methyl methacrylate-co-acrylic acid) (PMMA-*co*-PAA) shell, allow protonation/deprotonation of the carboxylic acid groups by changing the pH (adding either hydrochloric acid or sodium hydroxide solutions, respectively), which is expected to result in different arrangements of the PNP. The relation between the PNP surface charge at different pH, the supraparticle structure and the reflected colors is summarized in Figure 4.4, for supraparticles composed of PNP with 223 nm diameter (PNP223).
Stronger electrostatic repulsion between nanoparticles (at a pH above the pK_a of the PAA segments, $pH = 8$) results from the deprotonation of the PAA carboxylic

acid groups at the PNP surface. On the other hand, at lower pH (pH below the pK_a of the PAA segments, $pH = 4$), protonation of the carboxylic acid groups promotes PNP aggregation.[15,32]

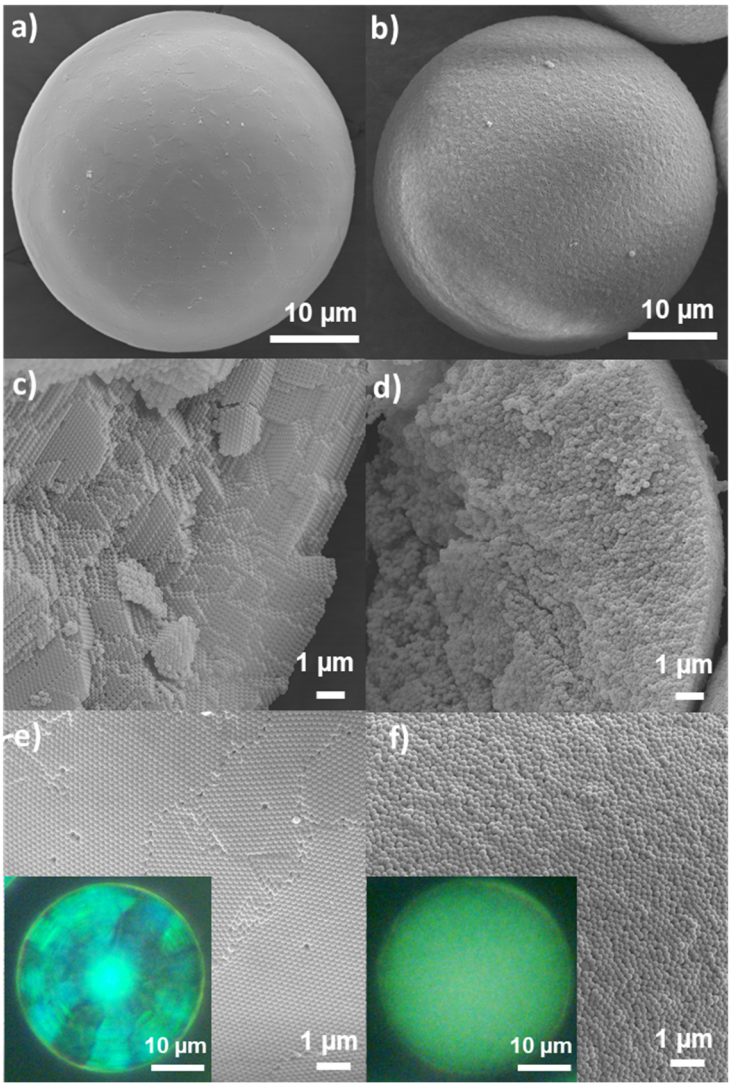

Figure 4.4: Effect of pH on the assembly process of supraparticles composed of PNP232, at 50°C (with orbital stirring at 800 rpm for 30 minutes). Left panel: highly charged PNP due to the deprotonated COO^- groups at $pH > pK_a$ results in a fcc packing of PNP in the spherical confinement and the supraparticle display bright and shiny cyan coloration. **a)** SEM images of a photonic supraparticle; **c)** internal fcc packing of PNP; **e)** magnification of the supraparticle surface showing the (111) planes; the inset shows a reflectance microscopy image of a structural pigment. Right panel: protonated COOH groups at $pH < pK_a$ results in amorphous structures with random close-packing of PNP inside the droplet templates and a pale cyan structural color is reflected from the pigments. **b)** SEM image of a supraparticle; **d)** internal amorphous packing of PNP; **f)** magnification of the amorphous packing of PNP at pigments surface; the inset shows a reflectance microscopy image.

Spherical photonic crystals (SPhCs) are formed when nanoparticles repel each other even at a very high nanoparticle density in the later stage of drying. In

contrast, spherical photonic glasses (SPhGs) with an amorphous packing of PNP are favored when particles attract each other. Attraction at the later stage of the evaporation process, usually forms a more porous structure rather than forming a highly dense packing. However, strong compressive capillary forces during the later drying stage leads to densification of the loose structure.[17,38,59]

4.2.2. Effect of temperature and drying time

An alternative approach to manipulate supraparticles formation, is to change the assembly temperature, maintaining a constant pH, drying time, and stirring rate. The ionization of the functional groups within the polyacrylic acid (PAA) polymer segments at PNP surface is a function of the apparent pK_a values. The intrinsic pK_a of acrylic acid, the monomeric unit of the PAA segments, is approximately 4.3. On the other hand, the apparent pK_a of PAA polymer species is 6.8. The acidity of the polymer is much lower than the monomeric form because ionized carboxylate residues affect the ionization potential of neighboring groups.[60] Therefore, the carboxylic functional groups within the polymer are not identical and the acidity of the polymer is a function of the degree of ionization.

By setting the pH of the PNP dispersion to a value higher than the pK_a of the acrylic acid monomeric units and close to the pK_a of the PAA segments ($pH = 6.2$), there is sufficient electrostatic repulsion between the ionized carboxylate groups to obtain an ordered arrangement of the PNP in the droplets.

With increasing assembly temperature, PNP can attain more kinetic energy to find the proper arrangement sites, thereby decreasing packing defects. However, excessively high temperature accelerates the inward motion of the liquid droplet interface. This reduces the timescale on which particles can arrange by diffusion, hampering the formation of large extensions of ordered PNP packing, because the high rates of water evaporation press the PNP closer together.[18,55,61] The rate at which the interface moves inward increases dramatically with increasing the assembly temperature and with droplet shrinking as water evaporates.

When the assembly temperature is set to 65°C, the increase in interface moving speed determines the packing of the PNP inside the supraparticles, where a more disordered arrangement is observed in the innermost region, in comparison to the more ordered outer layers (Figure 4.5a1, b1, c and e). When assembled at 65°C and dried for 30 minutes, the pigments reflect a bright cyan coloration from

the layers closer to the surface, and a more homogeneous cyan coloration is reflected from the supraparticle center (Figure 4.5b1). Interestingly, we find that the structures assembled at 65°C, when exposed to longer drying times, evolved to completely amorphous structures with high surface roughness, reflecting white coloration (Figure 4.5a2, b2, d and f).

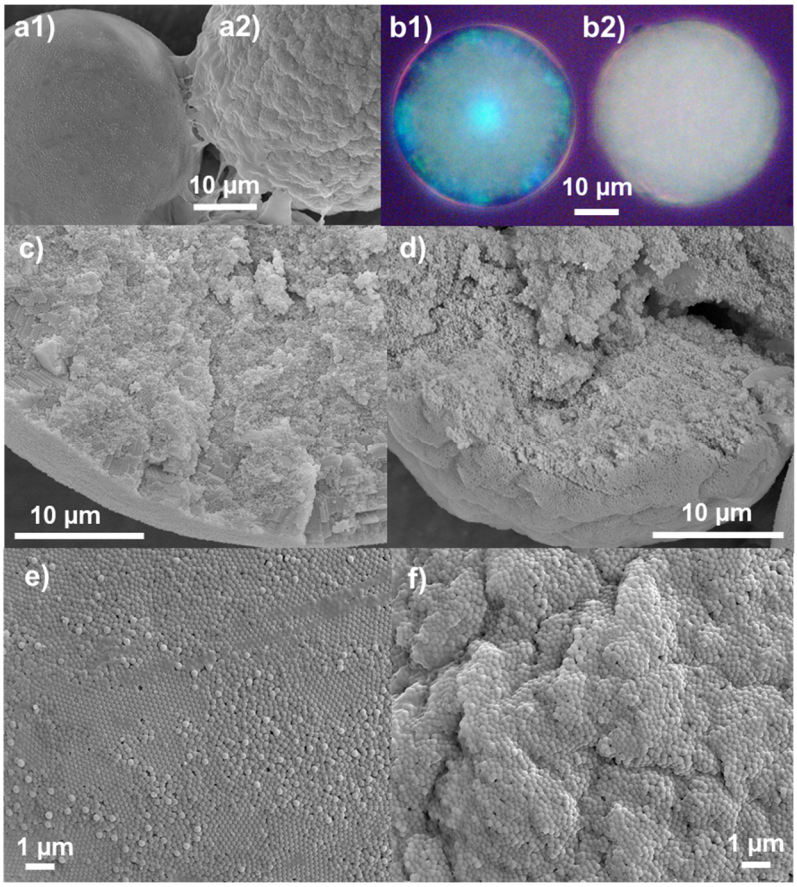

Figure 4.5: Effect of temperature and drying time on the packing of PNP223, at 65°C, pH = 6.2, and an orbital stirring rate of 800 rpm. **a1)** SEM and **b1)** reflectance microscopy image of a supraparticle dried for 30 minutes. **a2)** SEM and **b2)** reflectance microscopy image of a supraparticle dried for 60 minutes. **c)** and **e)** SEM images showing the PNP arrangement at the interior and at the supraparticle surface, when dried for 30 min. **d)** and **f)** SEM images of interior and surface of a completely amorphous supraparticle obtained when dried for 1 hour.

According to Wang *et al*,[62-64] the wettability of colloidal thin films (composed of PNP with similar composition to the ones used here), is controlled by the assembly temperature, not because of higher surface roughness, but instead because of a phase separation of the polymer segments driven toward minimum interfacial energy.[62,63] With the increase in the assembly temperature, the hydrophilic groups at the PNP shell tend to shrink towards the interior of the nanoparticles, while hydrophobic CH_2 groups extend more towards the surface.[64]

This conformation change at the nanoparticles surface may originate an oil phase infiltration, resulting in such wrinkled amorphous supraparticles. These supraparticles do not correspond to the typical buckled structure found in the literature resulting from partially collapse due to a fast water evaporation.[39] Therefore, the final morphology is strongly dependent on the formation process. The importance of the assembly process conditions in the color appearance of the spherical pigments is highlighted by the color patterns reflected from the supraparticles (Figure 4.6).

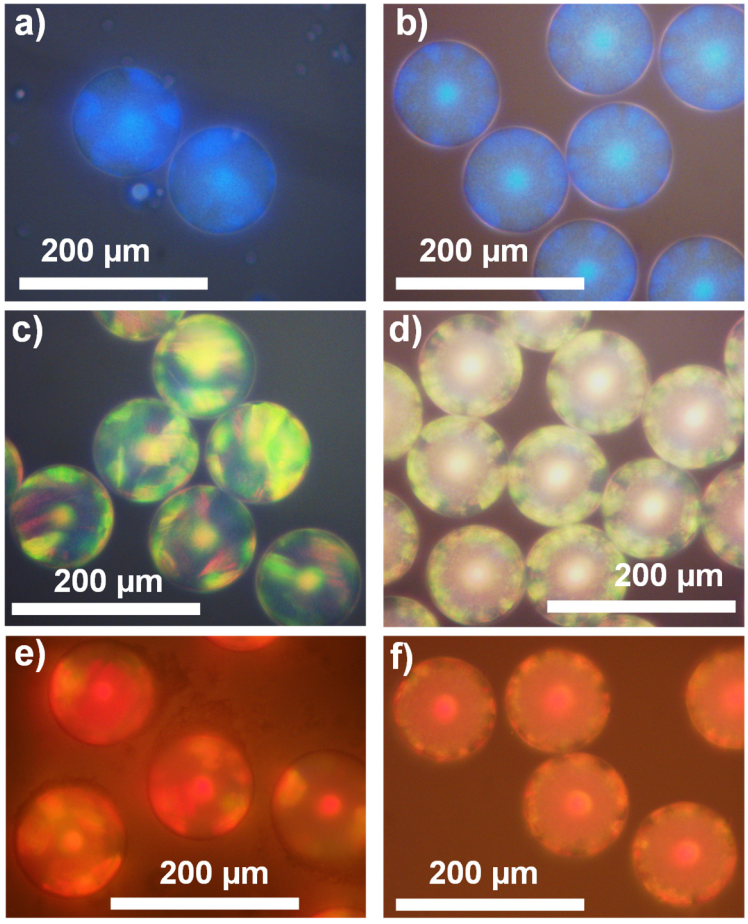

Figure 4.6: Comparison of the colors reflected from supraparticles obtained under different experimental conditions. Left panel: assembled at room temperature without stirring; each pigment exhibits a different color pattern. Right panel: assembled at 50°C with a stirring rate of 800 rpm for 30 minutes; all pigments exhibit the same color pattern. **a)** and **b**) Blue pigments composed of PNP194; **c)** and **d**) Yellow pigments composed of PNP248; **e)** and **f**) Orange pigments composed of PNP260.

Precise control of the experimental conditions is of paramount importance to obtain homogeneous and reproducible structural pigments. Under uncontrolled experimental conditions, although highly bright and shiny structural colors are reflected from the pigments, due to the crystalline packing of PNP across the

entire supraparticles structure, the reflected color patterns change from pigment to pigment (left panel of Figure 4.6). On the contrary, the color patterns exhibited by the supraparticles obtained under controlled temperature and stirring conditions are highly reproducible from pigment to pigment (right panel of Figure 4.6), where the brightly colored patches correspond to regions with a highly ordered packing of PNP and the more homogeneous color closer to the supraparticles center is reflected from the more disordered regions.

By controlling the water evaporation process from the emulsion droplets, we are able to precisely tune and reproduce the optical properties of the photonic pigments, by establishing the experimental conditions that determine the final arrangement of the PNP (from crystalline to amorphous structures). We either obtained structures with a crystalline packing of PNP from the outer surface to the center of the supraparticles, or structures with an amorphous arrangement of PNP from the outer surface to the supraparticles interior (Figure 4.7).

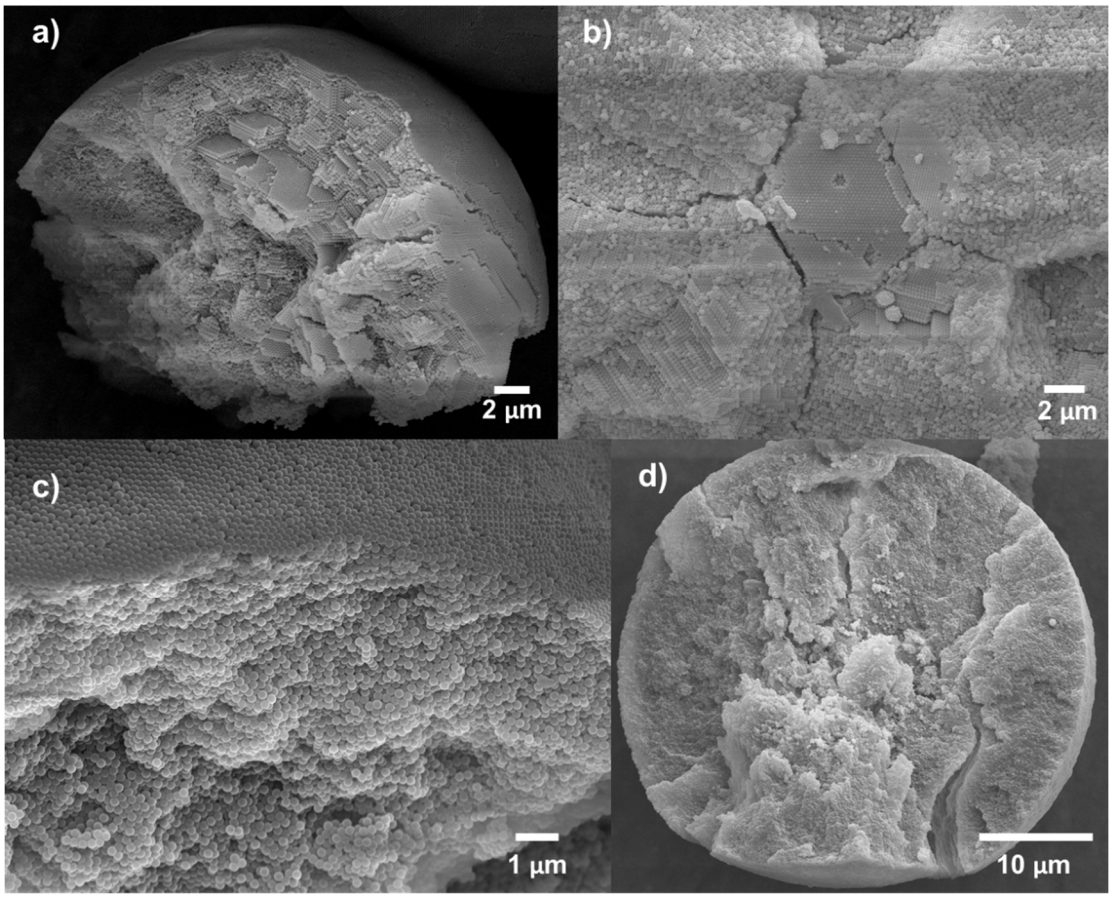

Figure 4.7: SEM images of photonic supraparticles obtained at different assembly conditions. Tuning the nanoparticle packing inside the emulsion droplets can originate structures with a crystalline packing of PNP from the outer surface (**a**) to the center (**b**). A completely isotropic packing of PNP from the outer surface (**c**) to the interior (**d**) of supraparticles, can also be obtained.

The transition from a disordered state to an ordered packing of PNP inside the droplet templates is mainly governed by two processes: the interaction potential between the charged PNP (controlled by the pH of the aqueous PNP dispersions) and the rate of water evaporation (controlled by the assembly temperature).

In order to fine tune the PNP packing, and consequently the colors reflected by the photonic pigments, temperature was chosen as the only parameter to change, maintaining constant other experimental conditions (stirring rate, microfluidic flows, pH, and drying time).

The precise structural tailoring is a major plus in our task to obtain a plethora of structural color hues with different properties. Slower evaporation rates provide time for the individual PNP to minimize their free energy and pack into highly ordered and regular structures. If the assembly process is accelerated by increasing the temperature, the formation process is kinetically controlled and will result in a more disordered packing of PNP both inside and at supraparticle surface. However, the diffusion of particles inside the droplets also affects the final packing (the small diffusion time of PNP with smaller diameters foster the formation of more ordered structures).[18,55,61]

4.3. Conclusions

Precise control of the experimental conditions is mandatory to obtain reproducible photonic pigments structure and color appearance. The packing of PNP inside the spherical template of the emulsion droplets is affected by different parameters, such as the pH of the PNP dispersions prior to the emulsification procedure, the temperature at which water is evaporated, the drying time or the orbital stirring rate during the assembly process. By establishing the appropriated pH, drying time, and stirring rate, temperature was selected as the critical experimental parameter to tailor the supraparticles structure.

Higher water evaporation rates from the emulsion droplets, at higher assembly temperatures, leads to a faster assembly process and consequently a shorter time to reach the most energetically stable structure before complete dying, thus increasing the structural disorder. By tunning the assembly temperature, we can obtain more crystalline or more disordered supraparticle structures exhibiting bright and reproducible structural colors.

4.4. References

1. Brugarolas, T., Tu, F. & Lee, D. Directed assembly of particles using microfluidic droplets and bubbles. *Soft Matter* **9**, 9046–9058 (2013).
2. Wang, J., Wang, J. & Han, J. Fabrication of Advanced Particles and Particle-Based Materials Assisted by Droplet-Based Microfluidics. *Small* **13**, 1728–1754 (2011).
3. Wang, J. & Zhu, J. Recent advances in spherical photonic crystals: Generation and applications in optics. *Eur. Polym. J.* **49**, 3420–3433 (2013).
4. Velev, O. D., Lenhoff, A. M. & Kaler, E. W. A Class of Microstructured Particles Through Colloidal Crystallization. *Science* **287**, 2240–2243 (2000).
5. Yi, G-R., Manoharan, V. N., Klein, S., Brzezinska, K. R., Pine, D. J. & Lange, F. F. Monodisperse Micrometer-Scale Spherical Assemblies of Polymer Particles. *Adv. Mater.* **14**, 1137–1140 (2002).
6. Liu, P., Bai, L., Yang, J., Gu, H., Zhong, Q., Xie, Z. & Gu, Z. Self-assembled colloidal arrays for structural color. *Nanoscale Adv.* **1**, 1672–1685 (2019).
7. Rastogi, V., Melle, S., Calderón, O. G., García, A. A., Marquez, M. & Velev, O. D. Synthesis of Light-Diffracting Assemblies from Microspheres and Nanoparticles in Droplets on a Superhydrophobic Surface. *Adv. Mater.* **20**, 4263–4268 (2008).
8. Zhao, Y., Shang, L., Cheng, Y. & Gu, Z. Spherical Colloidal Photonic Crystals. *Acc. Chem. Res.* **47**, 3632–3642 (2014).
9. Guerra, R. E., Colm, P., Hollingsworth, A. D. & Chaikin, P. M. Freezing on a sphere. *Nature* **554**, 346–350 (2018).
10. Zhokhov, A. A., Masalov, V. M., Sukhinina, N. S., Matveev, D. V., Dolganov, P. V., Dolganov, V. K. & Emelchenko, G. A. Photonic crystal microspheres. *Opt. Mater.* **49**, 208–212 (2015).
11. Vogel, N., Utech, S., England, G. T., Shirman, T., Phillips, K. R., Koay, N., Burgessd, I. B., Kolle, M., Weitz, D. A. & Aizenberg, J. Color from hierarchy: Diverse optical properties of micron-sized spherical colloidal assemblies. *PNAS* **112**, 10845–10850 (2015).
12. Wintzheimer, S., Granath, T., Oppmann, M., Kister, T., Thai, T., Kraus, T., Vogel, N. & Mandel, K. Supraparticles: Functionality from Uniform Structural Motifs. *ACS Nano* **12**, 5093–5120 (2018).
13. Montanarella, F., Altantzis, T., Zanaga, D., Rabouw, F. T., Bals, S., Baesjou, P., Vanmaekelbergh, D. & Blaaderen, A. V. Composite Supraparticles with Tunable Light. *ACS Nano* **11**, 9136–9142 (2017).
14. Li, Q., Jonas, U., Zhao, X. S. & Kappl, M. The forces at work in colloidal self-assembly: a review on fundamental interactions between colloidal particles. *Asia-Pac. J. Chem. Eng.* **3**, 255–268 (2008).

15. Vogel, N., Retsch, M., Fustin, C., Campo, A. & Jonas, U. Advances in Colloidal Assembly: The Design of Structure and Hierarchy in Two and Three Dimensions. *Chem. Rev.* **115**, 6265–6311 (2015).

16. Bishop, K. J. M., Wilmer, C. E., Soh, S. & Grzybowski, B. A. Nanoscale Forces and Their Uses in Self-Assembly. *Small* **5**, 1600–1630 (2009).

17. Sekido, T., Wooh, S., Fuchs, R., Kappl, M., Nakamura, Y., Butt, H.-J. & Fujii, S. Controlling the Structure of Supraballs by pH-Responsive Particle Assembly. *Langmuir* **33**, 1995–2002 (2017).

18. Marín, Á. G., Gelderblom, H., Susarrey-Arce, A., Houselt, A. V., Lefferts, L., Gardeniers, J. G. E., Lohse, D. & Snoeijer, J. H. Building microscopic soccer balls with evaporating colloidal fakir drops. *PNAS* **109**, 16455–16458 (2012).

19. Cheng, Z. Colloidal crystalization. in *Fluids, colloids and soft materials: An introduction to soft matter physics.* 203–248 (2016).

20. Anderson, V. J. & Lekkerkerker, H. N. W. Insights into phase transition kinetics from colloid science. *Nature* **416**, 811–815 (2002).

21. Schu, S., Roller, J., Kick, A., Meijer, J. & Zumbusch, A. Real-space imaging of translational and rotational dynamics of hard spheres from the fluid to the crystal. *Soft Matter* **13**, 8240–8249 (2017).

22. Pusey, P. N., Zaccarelli, E., Valeriani, C., Sanz, E., Poon, W. C. K. & Cates, M. E. Hard spheres: crystallization and glass formation. *Phil. Trans. R. Soc. A* **367**, 4993–5011 (2009).

23. Alsayed, A. M., Islam, M. F., Zhang, J., Collings, P. J. & Yodh, A. G. Premelting at defects within bulk colloidall crystals. *Science* **309**, 1207–1211 (2005).

24. Blaaderen, A. Van & Wiltzius, P. Real-Space Structure of Colloidal Hard-Sphere Glasses. *Science* **270**, 1177–1179 (1995).

25. Lozano, G. S., Dorado, L. A., Depine, R. A. & Míguez, H. Towards a full understanding of the growth dynamics and optical response of self-assembled photonic colloidal crystal films. *J. Mater. Chem. C* **19**, 185–190 (2009).

26. Nijs, B. D., Dussi, S., Smallenburg, F., Meeldijk, J. D., Groenendijk, D. J., Filion, L., Imhof, A., Blaaderen, A. V. & Dijkstra, M. Entropy-driven formation of large icosahedral colloidal clusters by spherical confinement. *Nat. Mater.* **14**, 56–60 (2015).

27. Pusey, P. N. & Megen, W. Van. Phase behaviour of concentrated suspensions of nearly hard colloidal spheres. *Nature* **320**, 340–342 (1986).

28. Monovoukas, Y. & Gast, A. P. Microstructure identification during crystallization of charged colloidal suspensions. *Phase Transitions A Multinatl. J.* **21**, 183–195 (1990).

29. Frenkel, D. Order through entropy. *Nat. Mater.* **14**, 9–12 (2015).

30. Vinothan N. Manoharan. Colloidal matter: Packing, geometry, and entropy. *Science* **349**, 1253751 (2015).

31. Wang, X., Wu, L., Wang, G. & Chen, G. Dynamic Crystallization and Phase Transition in Evaporating Colloidal Droplets. *Nano Lett.* **19**, 8225–8233 (2019).

32. Bhardwaj, R., Fang, X., Somasundaran, P. & Attinger, D. Self-Assembly of Colloidal Particles from Evaporating Droplets: Role of DLVO Interactions and Proposition of a Phase Diagram. *Langmuir* **26**, 7833–7842 (2010).

33. Vitelli, V., Lucks, J. B. & Nelson, D. R. Crystallography on curved surfaces. *PNAS* **103**, 12323–12328 (2006).

34. Einert, T., Lipowsky, P., Schilling, J., Bowick, M. J. & Bausch, A. R. Grain Boundary Scars on Spherical Crystals. *Langmuir* **21**, 12076–12079 (2005).

35. Meng, G., Paulose, J., Nelson, D. R. & Manoharan, V. N. Elastic Instability of a Crystal Growing on a Curved Surface. *Science* **343**, 634–637 (2014).

36. Bausch, A. R., Bowick, M. J., Cacciuto, A., Dinsmore, A. D., Hsu, M. F., Nelson, D. R., Nikolaides, M. G., Travesset, A. & Weitz, D. A. Grain Boundary Scars and Spherical Crystallography. *Science* **299**, 1716–1718 (2003).

37. Maki, K. L. & Kumar, S. Fast Evaporation of Spreading Droplets of Colloidal Suspensions. *Langmuir* **27**, 11347–11363 (2011).

38. Fijneman, A. J., Högblom, J., Palmlöf, M., With, G. D., Persson, M. & Friedrich, H. Multiscale Colloidal Assembly of Silica Nanoparticles into Microspheres with Tunable Mesopores. *Adv. Funct. Mater.* **30**, 2002725 (2020).

39. Wang, J., Mbah, C. F., Przybilla, T., Zubiri, B. A., Spiecker, E., Engel, M. & Vogel, N. Magic number colloidal clusters as minimum free energy structures. *Nat. Commun.* **9**, 5259 (2018).

40. Palberg, T. Crystallization kinetics of colloidal model suspensions: recent achievements and new perspectives. *J. Phys. Condens. Matter* **26**, 333101 (2014).

41. Wang, J., Sultan, U., Goerlitzer, E. S. A., Mbah, C. F., Engel, M. & Vogel, N. Structural Color of Colloidal Clusters as a Tool to Investigate Structure and Dynamics. *Adv. Funct. Mater.* **30**, 1907730 (2020).

42. Ohnuki, R., Sakai, M., Takeoka, Y. & Yoshioka, S. Optical Characterization of the Photonic Ball as a Structurally Colored Pigment. *Langmuir* **36**, 5579−5587 (2020).

43. Choi, T. M., Lee, G. H., Kim, Y.-S., Park, J-G., Hwang, H. & Kim, S-H. Photonic Microcapsules Containing Single-Crystal Colloidal Arrays with Optical Anisotropy. *Adv. Mater.* **31**, 1900693 (2019).

44. Whitesides, G. M. & Grzybowski, B. Self-Assembly at All Scales. *Science* **295**, 2418–2421 (2002).

45. Koh, Y. K., Yip, C. H., Chiang, Y. & Wong, C. C. Kinetic Stages of Single-Component Colloidal Crystallization. *Langmuir* **24**, 5245–5248 (2008).

46. Kim, S., Park, J., Choi, T. M., Manoharan, V. N. & Weitz, D. A. Osmotic-pressure-controlled concentration of colloidal particles in thin-shelled capsules. *Nat. Commun.* **5**, 1–8 (2014).

47. Montanarella, F., Geuchies, J. J., Dasgupta, T., Prins, P. T., Overbeek, C. V., Dattani, R., Baesjou, P., Dijkstra, M., Petukhov, A. V., Blaaderen, A. V. & Vanmaekelbergh, D. Crystallization of Nanocrystals in Spherical Confinement Probed by in Situ X-ray Scattering. *Nano Lett* **18**, 3675–3681 (2018).

48. Schmitt, M. & Stark, H. Marangoni flow at droplet interfaces: Three-dimensional solution and applications. *Phys. Fluids* **28**, 012106 (2016).

49. Nowak, E., Kovalchuk, N. M., Che, Z. & Simmons, M. J. H. Effect of surfactant concentration and viscosity of outer phase during the coalescence of a surfactant-laden drop with a surfactant-free drop. *Colloids Surfaces A Physicochem. Eng. Asp.* **505**, 124–131 (2016).

50. Schmitt, M. & Stark, H. Active Brownian motion of emulsion droplets: Coarsening dynamics at the interface and rotational diffusion. *Eur. Phys. J. E* **39**, 80 (2016).

51. Tan, P., Xu, N. & Xu, L. Visualizing kinetic pathways of homogeneous nucleation in colloidal crystallization. *Nat. Phys.* **10**, 73–79 (2014).

52. Arai, S. & Tanaka, H. Surface-assisted single-crystal formation of charged colloids. *Nat. Phys.* **13**, 503–509 (2017).

53. Vlasov, Y. A., Astratov, V. N., Baryshev, A. V., Kaplyanskii, A. A., Karimov, O. Z. & Limonov, M. F. Manifestation of intrinsic defects in optical properties of self-organized opal photonic crystals. *Phys. Rev. E* **61**, 5784–5793 (2000).

54. Míguez, H., Meseguer, F., López, C., Mifsud, A., Moya, J. S. & Vázques, L. Evidence of FCC Crystallization of SiO_2 Nanospheres. *Langmuir* **7463**, 6009–6011 (1997).

55. Liu, F., Xiu, J., Tang, B., Zhao, D. & Zhang, S. Dynamic monitoring of thermally assisted assembly of colloidal crystals. *J. Mater. Sci.* **52**, 7883–7892 (2017).

56. Dommelen, R. Van, Fanzio, P. & Sasso, L. Surface self-assembly of colloidal crystals for micro- and nano-patterning. *Adv. Colloid Interface Sci.* **251**, 97–114 (2018).

57. Cho, Y., Kim, S., Yi, G. & Yang, S. Self-organization of colloidal nanospheres inside emulsion droplets: Higher-order clusters, supraparticles, and supraballs. *Colloids Surfaces A Physicochem. Eng. Asp.* **345**, 237–245 (2009).

58. Israelachvili, J. N. *Intermolecular and Surface Forces. Third Edition, Elsevier*. (2011).

59. Liu, W., Kappl, M. & Butt, H. Tuning the Porosity of Supraparticles. *ACS Nano* **13**, 13949−13956 (2019).

60. Charman, W. N., Christy, D. P., Geunin, E. P. & Monkhouse, D. C. Interaction between calcium, a model divalent cation, and a range of poly(acrylic acid) resins as a function of solution pH. *Drug Dev. Ind. Pharm.* **17**, 271–280 (1991).

61. Ye, Y.-H., LeBlanc, F., Haché, A. & Truong, V.-V. Self-assembling three-dimensional colloidal photonic crystal structure with high crystalline quality. *Appl. Phys. Lett.* **78**, 52–54 (2001).

62. Wang, J., Hu, J., Wen, Y., Song, Y. & Jiang, L. Hydrogen-Bonding-Driven Wettability Change of Colloidal Crystal Films: From Superhydrophobicity to Superhydrophilicity. *Chem. Mater.* **18**, 4984–4986 (2006).

63. Wang, J., Zhang, Y., Wang, S., Song, Y. & Jiang, L. E. I. Bioinspired Colloidal Photonic Crystals with Controllable Wettability. *Acc. Chem. Res.* **44**, 405–415 (2011).

64. Wang, J., Wen, Y., Feng, X., Song, Y. & Jiang, L. Control over the Wettability of Colloidal Crystal Films by Assembly Temperature. *Macromol. Rapid Commun.* **27**, 188–192 (2006).

4.5. Appendix 4

Although monodispersed emulsion droplets, are less prone to destabilization mechanisms (Ostwald ripening, etc.), coalescence was also observed. When the droplets dried without stirring, at room temperature, coalescence during water evaporation could be observed, leading to supraparticles with different size and color appearance. (Figure A4.1).

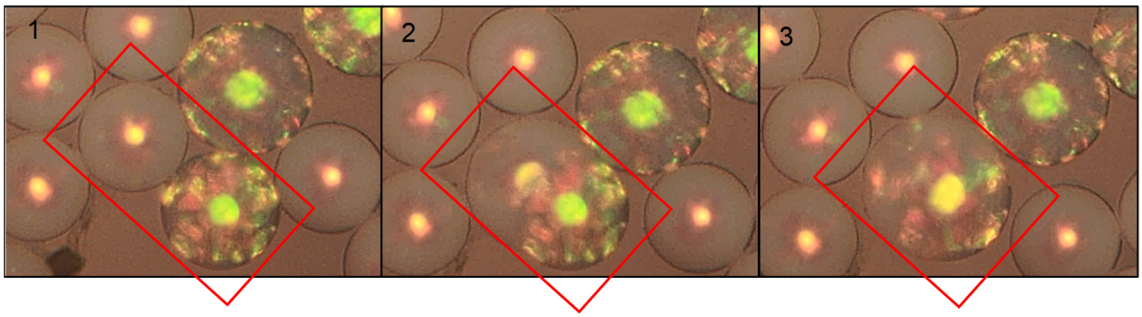

Figure A4.1: Droplet coalesce during the assembly process at room temperature without stirring, leading to emulsion droplet coarsening despite the use of surfactants to provide an energy barrier.

Under controlled assembly process, apart from the temperature and stirring rate, two other experimental conditions must be assured to avoid droplet coalescence: small oil volumes and a low amount of emulsion droplets should be used in the collecting vials, to guarantee efficient stirring and prevent droplets contact. Under such condition's droplet coalescence is negligible, and highly monodispersed supraparticles are obtained. Either way, coalescence can occur, but because the drying process is so fast, the two droplets may be attached by necks, before complete drying (Figure A4.2).

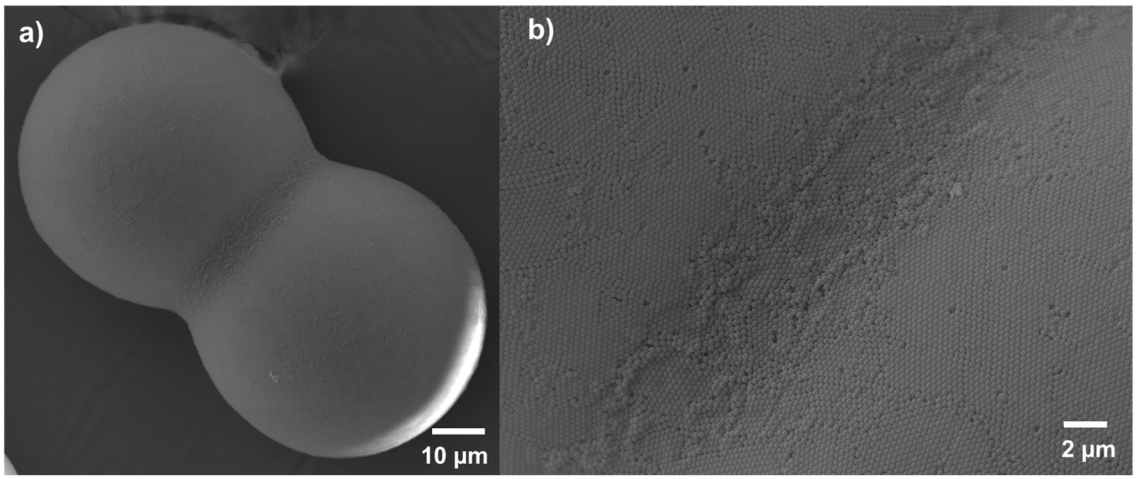

Figure A4.2: SEM image of two connected supraparticles due to the neck formation between coalescing droplets, before complete drying.

5. PNP arrangement in spherical photonic pigments probed by reflectance confocal microscopy

Here we describe the use of reflectance confocal microscopy (RCM) as a simple, fast, and non-destructive imaging technique to gain insight of the PNP packing inside the entire spherical photonic pigment structure. The sequence of images obtained at different depths within the photonic structure, under illumination with different laser light wavelengths, provides direct visualization of the crystalline regions and defect propagation. This valuable and readily available technique helps to correlate the structural morphology and the corresponding optical properties of the spherical photonic pigments.

The self-assembly of monodisperse colloidal nanoparticles is a valuable method for fast and cheap production of photonic materials that hold promise for applications in the development of novel optical devices or pigmentary technologies.[1-4]

Photonic crystals composed of orderly packed colloidal nanoparticles (colloidal crystals) diffract light in the visible range because of the size of the constituent nanoparticles and their periodic arrangement, making them shine with bright iridescent colors.[5,6]

Imaging of colloidal crystals by optical microscopy can provide direct insight into the crystal growth mechanisms and the propagation of defects.[7-13] The structural colors predominantly observed in reflection mode result whenever a (111) plane is oriented perpendicular to the incident light so that light reflected from the colloidal structure is recollected by the objective lens.[14-16] Only lightwaves that match the Bragg condition interfere constructively, thus producing structural colors with wavelength determined by the size and refractive index of the colloidal particles.

Some degree of disorder is inherent to self-assembly processes due to the limited efficiency of error correction mechanisms. For example, this can lead to the formation of domains of unknown size and orientation corresponding to the displacement of crystal planes in the lateral directions.[17] This stacking disorder, results in diffuse scattering along lines, along the defects. Other defects include dislocations and vacancies (or point defects).[8,10,18] The optical properties of colloidal photonic crystals depend not only on the average crystal structure, but also on the presence of these various defects and their spatial distribution.[19]

The crystallization of colloidal nanoparticles in spherical confinement suffers from packing constrains due to the curvature of the surface, in addition to the inherent disorder introduced by the self-assembly process. When crystals form on curved surfaces, new defect structures may arise. Dislocations consisting of pairs of tightly bound 5- and 7-fold coordinated defects form in sufficiently large and rigid curved crystals because they lower the total elastic energy.[20] They are present above a critical particle number,[15,21] in the form of novel freely terminating high-angle grain boundaries or scars.[22] Crystals growing on curved surfaces have been probed by in situ X-ray scattering,[23] confocal microscopy[24] and electron tomography measurements.[25]

5.1. Techniques to probe the internal structure of colloidal photonic materials

Detailed knowledge about the packing of colloidal nanoparticles into large photonic structures and the interplay between order and disorder in colloidal photonic materials it is of paramount importance. The development of appropriate structural characterization methods to fully understand the relation of both the crystal and defect structures with their optical properties must be obtained. However, despite the efforts, a simple, reliable, and widely applicable method to probe the internal structure of colloidal photonic materials have not yet been accomplished. For instance, most of what is known about the colloidal crystal structure is obtained through either surface methods, such as scanning electron microscopy (SEM) or diffraction methods such as X-rays (Table 5.1).[26]

The most widely used technique is SEM, that although acquiring direct images with high special resolution, is inherently surface specific. The only possibility for studying the internal structure of crystals by SEM is through physical cutting.[27] Besides being destructive, the cutting procedure can damage the crystal structure. SEM tomography assisted by focused ion beam (FIB) can reduce the damage risk and allows high resolution SEM images on the exposed section of the crystal by in situ precision milling by FIB.[28] However, the FIB procedure is time-consuming, expensive and the reduction in structural damage risk is quite limited for soft materials such as colloidal photonic structures composed of polymer nanoparticles (PNP). Especial care should be taken when performing FIB of such structures not to provoke structure melting at temperatures above the Tg of the polymers.

Electron tomography is nowadays a standard technique yielding a 3D description of the morphology and inner structure of nano-assemblies. In comparison to diffraction techniques such as small-angle X-ray scattering,[29] electron tomography enables a detailed description of non-periodic features such as defects and surface morphology. Despite the valuable information obtained by electron tomography, 3D reconstructions based on classical algorithms, suffer from a number of restrictions.[30,31]

Recent developments in X-ray methods have also yielded a spectrum of techniques with the potential to access the internal structure of colloidal photonic crystals, such as high-resolution X-ray microscopy and X-ray tomography.[26] The

relatively high penetration power of X-rays enables studies of almost any material and thickness, but interpretation of resulting data remains challenging.[32,33] In addition, X-ray image acquisition requires synchrotron facilities, and irradiation damage of soft materials can occur.

Confocal laser scanning microscopy (CLSM) is a powerful and simple technique for a less invasive study of the 3D internal structure,[5,34] widely used for imaging biological systems,[35,36] but also in a range of soft matter physics problems and material science, such as colloidal crystallization.[10,11,34,37] 3D images are obtained by moving the sample through the focal plane of the objective and acquiring a sequence of high-contrast 2D images of the focal plane.[12,13,38,39]

Depending on the source of image contrast, CLSM can be performed in either fluorescence or reflectance mode. Fluorescence confocal microscopy (FCM) requires the labelling of the structures with fluorescent probes to generate contrast (that can alter the properties of the materials studied).[40-43] On the other hand, reflectance confocal microscopy (RCM) relies only on refractive index differences between the constituents of the material studied, which provide the image contrast.[9,44,45] Thus, reflected light imaging can be used to observe the scattering properties of colloidal photonic structures.[46]

Table 5.1. Microscopic techniques used for the characterization of photonic crystals: scanning electron microscopy (SEM), confocal laser scanning microscopy (CLSM), and diffraction pattern analysis using X-ray microscopy (XM). Adapted from Nho *et al.*[26]

	Optical microscopy	**Electron microscopy**	**Soft X-ray microscopy**	
Important features	Confocal laser scanning microscopy (CLSM)	Field emission scanning electron microscopy (FE-SEM)	Scanning transmission X-ray microscopy (STXM)	Full-field transmission X-ray microscopy (TXM)
Field of view (μm)	Up to 50 x 50	6000 at 25X	5 x 5	10 x 10
Sample thickness (μm)	10 - 100	0.010 – 0.1	~ 0.6 – 6.5	~ 2
Acquisition speed (sec/frame)	0.25 - 10	A few tens of seconds	360 (500 x 500 pix/image)	~10 (500 x 500 pix/image)
Spatial resolution (nm)	200 - 1000	2 - 10	30	46
Sample preparation	Fluorescent labelling	Au or Pt coating	Not required	Not required

5.2. Reflectance confocal microscopy

Reflectance confocal microscopy (RCM) is based on the backscattered fraction of the incident light delivered to the sample.[46,47] RCM is a noninvasive imaging method requiring no external contrast agents and provides images with high resolution and contrast. By acquiring images in a horizontal plane, at different depths across the samples it is possible to obtain information on the internal features of the samples. This non-destructive technique, although extensively used in the fields of biology and medical science,[48-50] has found few applications in the study of polymeric materials.[51-53]

Any commercial CLSM can be operated in reflectance mode by setting the microscope's detector or collection filter for the excitation laser wavelength. In this mode, the images are based on the scattering properties of the samples. The reflected light is collected through a pinhole, which is conjugated with the focus of the lens located within the sample. Only light scattered back from the focal plane will reach the detector.[54] The rejection of out-of-focus light in CLSM, results in images with better contrast and resolution when compared to conventional microscopy.[14] The collection of reflectance from the focus is a function of the scattering properties of the sample where the optical reflectance properties $R(z)$ are obtained as a function of the depth of focus, z. Scanning versus depth along the z-axis is accomplished by moving the focus to different depths within the sample. By repeating the acquisition for a series of z positions, a full 3D dataset can be generated, $R(x, y, z)$.

Optical sectioning of microscopic colloidal photonic samples with confocal microscopy allows to examine, reconstruct and measure structural features providing insight into the localization of defects, and the interplay between the ordered and disordered packing of nanoparticles.[55]

Light penetration into a sample from below in an inverted confocal microscope in reflectance mode involves three steps: 1) laser light is delivered to the focal point within the sample; 2) the interaction of light within the confocal volume at the focal point; and 3) the collection of the reflected light through a pinhole, for detection. Steps 1 and 3 involve the attenuation of light by the sample. Step 2 involves the process of scattering within the confocal volume.

The incident light distribution in photonic samples is influenced by the morphology of the scattering features and their spatial distribution within the probed volume. Depending on the structure of the sample they can scatter photons either isotropically or in a backward-directed manner (Figure 5.1). If scattering is isotropic, it will optimally prevent photons from reaching the focus. If scattering is backward directed, then photons can propagate to the focus despite multiple scattering.[54]

Although spectroscopic measurements of angle resolved reflectance or transmittance properties of colloidal photonic samples are the most widely used technique to obtain bulk optical information about their internal structure,[56,57] the use of complementary techniques to obtain structural and optical information and indirect correlation between the two is usually necessary.[14] Here we show that 3D-RCM using different laser light wavelengths can be applied to evaluate the wavelength dependent scattering properties of photonic supraparticles in connection with the internal structure of the spherical colloidal crystals and glasses.

Crystalline domains backscatter light due to the periodic refractive index modulation at different crystalline planes of orderly packed polymer nanoparticles. On the other hand, glassy samples scatter incident light photons isotopically in all directions due to the lack of periodic inhomogeneities in refractive index associated with the isotropic packing of PNP (Figure 5.1).

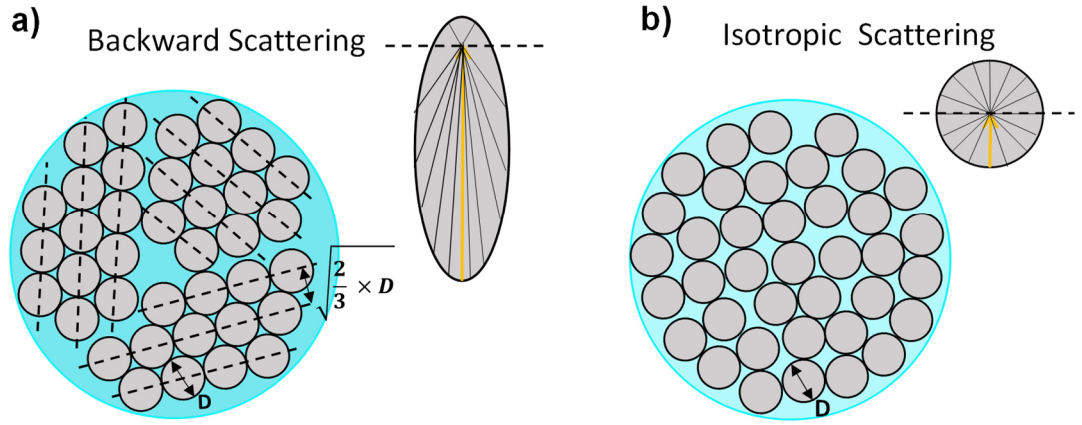

Figure 5.1: Schematic depiction how spherical photonic structures can scatter photons either isotropically or in a backward-directed manner (the black dotted line indicates the focal plane inside the photonic samples). Adapted from Jacques.[54] **a)** Crystalline planes of PNP scatter incident photons in a highly backward-directed manner. The distance between (111) diffracting planes is given by $\sqrt{2/3} \times D$, where D correspond to the PNP diameter. **b)** Amorphous arrangement of PNP scatter incident photons in all directions.

Determination of the structural crystalline domains/grain boundary defects visualized in 3D after reconstruction of the 2D images obtained at different depths within the photonic supraparticles was successfully accomplished. This allowed a full characterization of the microscopic structure of spherical photonic pigments. In addition, by varying the incident laser wavelength a $R(x, y, z, \lambda)$ image can be obtained, and a direct correlation of the structural and optical properties of the samples can be achieved. To the best of our knowledge, no previous studies on spherical colloidal crystal in reflectance mode using CM were conducted to evaluate their wavelength dependent scattering properties.

5.3. Experimental part

5.3.1. Instruments

RCM images were recorded with a Leica TCS SP5 inverted confocal microscope (DMI6000, Leica Microsystems CMS GmbH) equipped with a CW Argon ion laser (available excitation lines at 458, 465, 488, 496 and 514 nm) and Ne:He with 633 nm laser line. Confocal Z-series stacks were acquired using a 63x1.2NA (HCX PL APO CS 63.0×WATER UV) by recording the backscaterred light with an HyD hybrid detector. Typically, 55 x 55 µm images where collected with 1064 x 1064 pixels and a scan rate of 100-200 Hz per frame. Individual images recorded at different wavelenghts were pseudo-colored with RGB values corresponding to the photonic supraparticle refraction spectral profiles. The reflectance intensity profiles of RCM images were obtained with imageJ software.

Reflectance optical microscopy images of the structurally colored spherical photonic pigments in hexadecane were performed on a KERN OKM 173 microscope equipped with an ODC 832 camera at a magnification of 40x.

Transmittance optical microscopy images of spherical photonic pigments in hexadecane were performed on an Olympus Bx 51 optical microscope equipped with an Olympus C5060 wide zoom camera at a magnification of 20x.

Reflectance spectra of the crystalline and amorphous supraparticles were obtained under incident white light illumination at 45° relative to surface normal and collected at the backscattering angle (0° relative to incidence).

The surface packing and the internal arrangement of PNP were characterized by SEM.

5.3.2. Sample preparation

Highly crystalline spherical photonic crystals, SPhCs, and amorphous spherical photonic glasses, SPhGs, composed of polymer nanoparticles with a diameter of 223 nm (PNP223) were used for RCM imaging. These supraparticles were obtained by microfluidic droplet templating under controlled assembly conditions described in Chapter 4. The different PNP packing inside the supraparticles was obtained from PNP dispersions at different pH before the emulsification procedure: crystalline structures (SPhC-PNP223) were assembled at pH $= 8$, and a completely amorphous packing of PNP (SPhG-PNP223) was obtained at pH $= 4$.

The crystalline and amorphous photonic supraparticles were placed on a glass cover slip and positioned on the optical stage of an inverted laser scanning confocal microscope, using water as an immersion medium. The sample was kept moist with hexadecane (but not immersed), to avoid refractive-index mismatch between the dry photonic structures and the air, which restricts imaging to the first or second PNP layers, preventing the study of the innermost structure.

5.4. Results

Conventional optical microscopy provides images of the structural colors reflected or transmitted by the photonic structures, and allows direct observation of colloidal crystals and glasses, and gives an overview of the structure morphology. In the reflectance images of SPhC shown in Figure 5.2a, crystalline planes oriented according to the Bragg diffraction ((111) planes perpendicular to the surface normal) reflect light in the direction of the objective, and appear brightly cyan colored, whereas crystalline planes with different orientation scatter less light in the direction of the objective and appear darker.[58,15] At certain crystal orientations, striations occurs as shown in Figure 5.2a, which indicate alternating crystal lattice orientations within the crystalline domain (rhcp structures).[59] In transmission optical microscopy images, dark “cracks” that run radially along the supraparticle are visible for SPhCs (Figure 5.2b), that probably correspond to the disordered regions identifying the grain boundary scars between different crystalline domains.

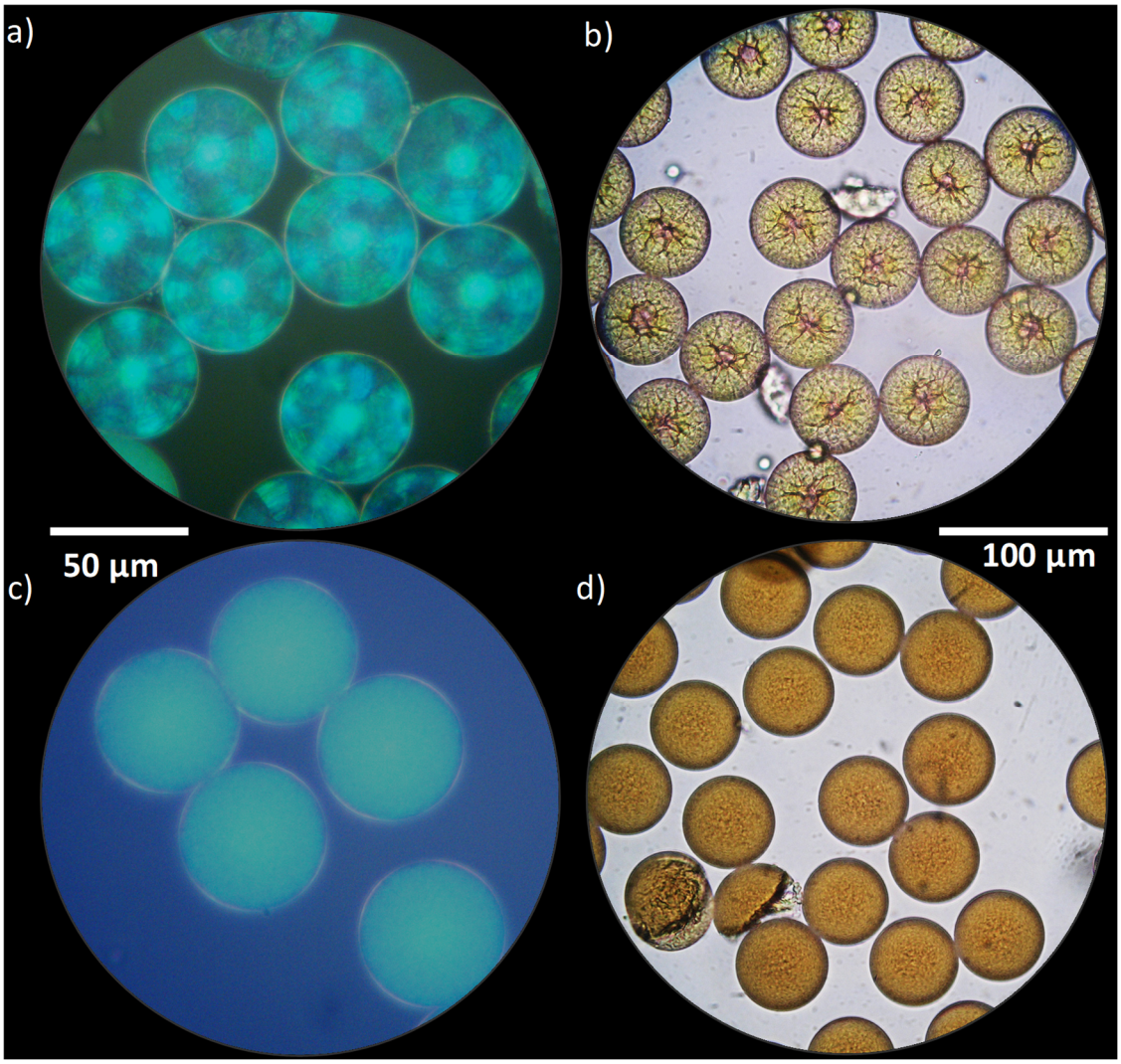

Figure 5.2: Conventional optical microscopy images of SPhCs (**a**, **b**) and SPhGs (**c**, **d**) composed of PNP223 in reflectance (**a**, **c**) and transmission modes (**b**, **d**). Photonic supraparticles transmit incident light unless Bragg reflections occur. In this particular sample, blue-cyan-green light is reflected (left panel) and the yellow-red part of the optical spectrum is transmitted (right panel). Close-packed crystal planes according to Bragg orientation ((111) planes of fcc structure) reflect cyan light and appear brightly colored. Striations within crystallites indicate twinning of the fcc lattice. SPhGs reflects homogeneous cyan coloration from coherent multiple scattering.

In the case of the reflectance images of SPhGs in Figure 5.2c, an isotropic cyan color is visible throughout the structure resulting from the amorphous packing of PNP. On the other hand, when observed in transmission mode the images of the spherical photonic glasses in Figure 5.2d, lack the big “cracks” observed in SPhCs and a more homogeneous topology is observed.[60]

High spatial resolution images of the surface and internal structure of the SPhCs and SPhGs, composed of highly monodispersed PNP223 were obtained by SEM (Figure 5.3). A highly ordered hexagonal packing of PNP is visible at the SPhCs

surface (Figure 5.3d). Boundary regions delimiting the different crystalline domains can be observed in Figure 5.3c (highlighted by the red lines), and some point defects (denoted by the yellow circles). A line defect is also visible in Figure 5.3d (indicated by the black arrow). The internal fcc packing of PNP is visible when imaging a broken supraparticle (Figure 5.3e and f).

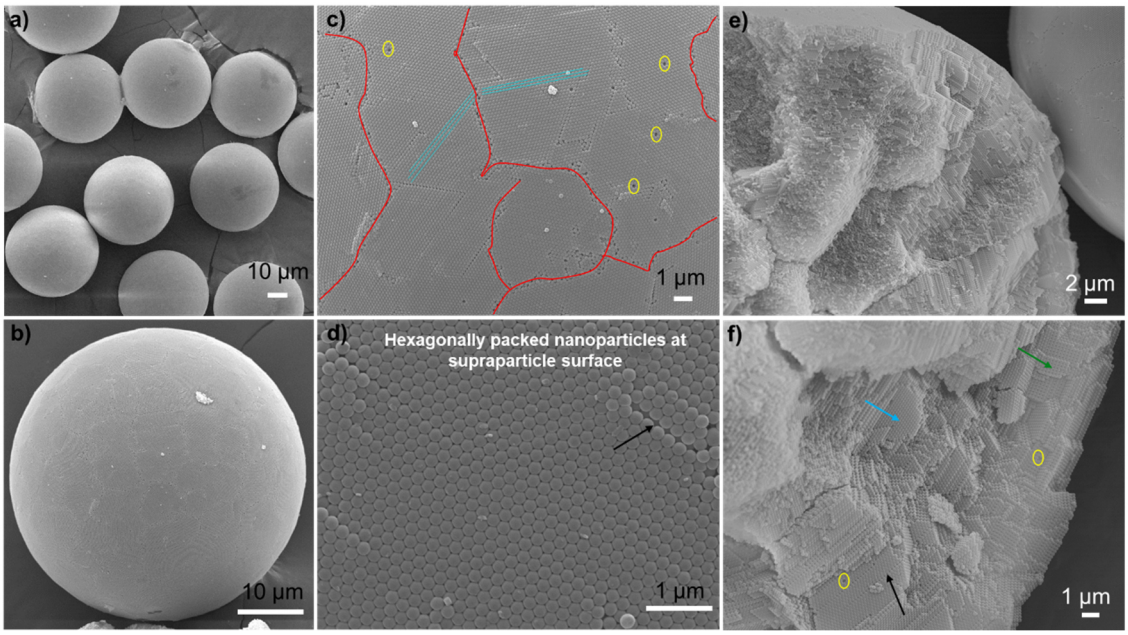

Figure 5.3: SEM images of SPhCs showing the surface and internal packing of PNP223. Images **a)** and **b)** shows perfectly spherical and monodispersed photonic pigments composed of PNP223. **c)** Supraparticle surface showing different crystalline domains (highlighted by the cyan lines) circumscribed by large grain boundary scars (red lines). Vacancies or point defects are denoted by yellow circles. **d)** Amplification of c) where hexagonally packed nanoparticles are visible. A line defect or dislocation denoted by the black arrow is also visible at sample surface. **e)** Crystalline internal packing of PNP inside a broken supraparticle showing the ordered and concentric arrangement of PNP extending from the surface to the supraparticle center. **f)** Zoom in of e) showing different facets of the fcc packing of PNP: (111) directed crystalline planes of the fcc packing is denoted by the cyan arrow; the green arrow indicates the (100) directed facets. Internal point defects (highlighted by yellow circles) and dislocations (denoted by the black arrow) are also visible.

For SPhGs, the SEM images in Figure 5.4 reveal a perfectly isotropic packing of PNP223, both at the supraparticle surface (Figure 5.4b) and in the inner structure (Figure 5.4c). Despite the apparently disordered packing of PNP223, these structures have short range-order correlations, resulting in the matte and homogeneous cyan structural coloration observed in Figure 5.2.

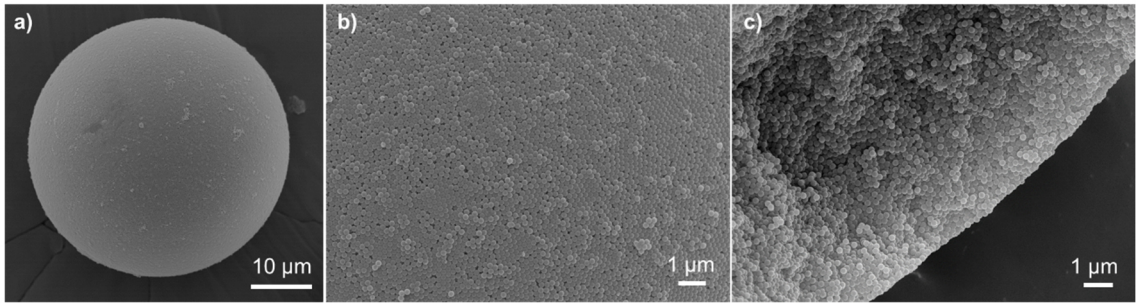

Figure 5.4: SEM images of SPhGs showing the outer and internal amorphous packing of PNP223. **a)** Perfectly spherical supraparticle composed of a disordered arrangement of PNP. **b)** Randomly packed PNP at supraparticle surface, where only small regions with hexagonally packed nanoparticles is visible. **c)** Internal structure of a broken supraparticle showing the disordered and random packing of the nanoparticles that spreads to supraparticle center, resulting in a dense isotropic structure.

The wavelength of the structural color reflected from these spherical photonic structures is determined by the size and refractive index of the PNP. However, the crystalline or amorphous packing of PNP arrangement inside the structures results in different optical properties. The narrow and sharp reflectance band from SPhCs contrast with a much broader reflectance band from the SPhGs (Figure 5.5).

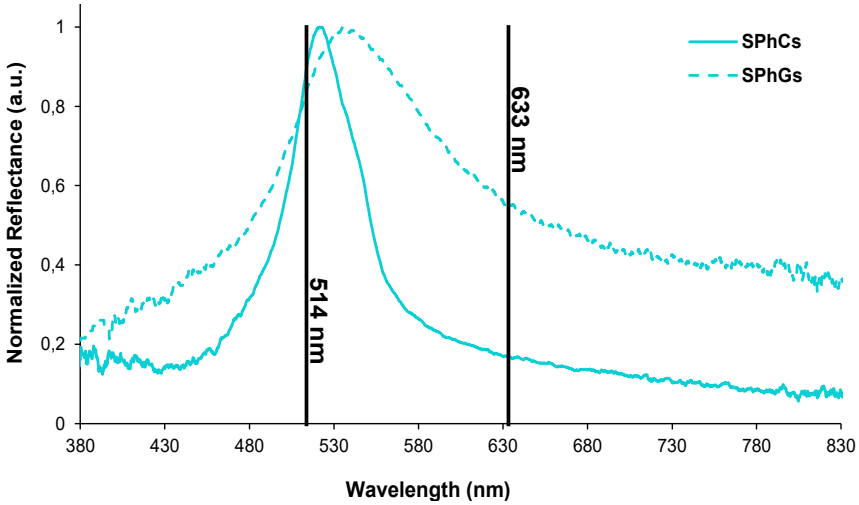

Figure 5.5: Normalized reflectance spectra of spherical photonic crystals (SPhCs – cyan full line) and glasses (SPhGs – cyan dotted line) composed of PNP223, under white light illumination. The black lines at 514 nm and 633 nm, denote the laser lines used to image these photonic structures under RCM.

Figure 5.5 also shows the differences in the diffuse scattering background between these two structures: diffuse scattering contribution to the reflectance properties of SPhGs is tremendous across the entire visible range. However, despite being crystalline, the disorder of the colloidal assembly process inside the

spherical templates also contributes with diffuse scattering to the reflectance properties of SPhCs samples, although in a much lower extent.

In the case of SPhC-PNP223 a pseudo-photonic bandgap (p-PBG or stop-band) opens at a frequency corresponding to a wavelength of maximum reflectance of 521 nm. The intensity of light reflected by the crystalline supraparticles results from a combination of the highly backward-directed reflection from the stop-band (light waves that match the Bragg condition interfere constructively) and from the isotropic scattering of incident light, the later due to the disorder always present in such assembled structures.[61] In the case of SPhGs, the amorphous packing of PNP223 inside the supraparticles originates a much broader reflectance band ($\lambda_{max} = 535$ nm) and largely increases the diffuse scattering of incident light due to its isotropic nature.

The wavelength position highlighted by the black lines in Figure 5.5, 514 nm and 633 nm, indicates the laser lines used to image these photonic structures under RCM. The 514 nm laser light wavelength falls on the structures stop-band. At 633 nm diffuse scattering from the disordered regions is the main source of the reflectance observed. Thus, under illumination at 514 nm, ordered crystalline domains are observed by Bragg reflection in RCM images of Figure 5.6. Under illumination with 633 nm laser light, the incoherent diffuse scattering from the disordered boundaries between crystalline domains and the overall structural imperfections accounting for point and line defects are observed in Figure 5.7. The wavelength dependent images give a full overview of the crystalline structure and the defects spreading, elucidating the nanoparticle arrangement under spherical confinement. In the case of SPhGs, the absence of crystalline planes due to the amorphous packing of PNP, results in isotropic scattering of incident photons regardless the wavelength of illumination. For that reason, the same patterns are observed under illumination at 514 nm and 633 nm light wavelengths (Figures A5.1 to A5.3, Appendix 5).

When SPhCs are illuminated with laser light of wavelengths falling on the stop-band, the crystalline planes oriented in the [111] direction of the fcc structure appear brightly colored due to the strong backscattering of light. Therefore, the planes responsible for the reflected structural color can be easily distinguished from other crystalline orientations or disordered regions, which shows weaker interactions (scatters less light) with this wavelength and appears darker.

Consequently, 3D-RCM at wavelengths within the stop-band allows to image the size, morphology, and orientation of the different crystalline domains at different depths along the supraparticle structure (Figure 5.6).

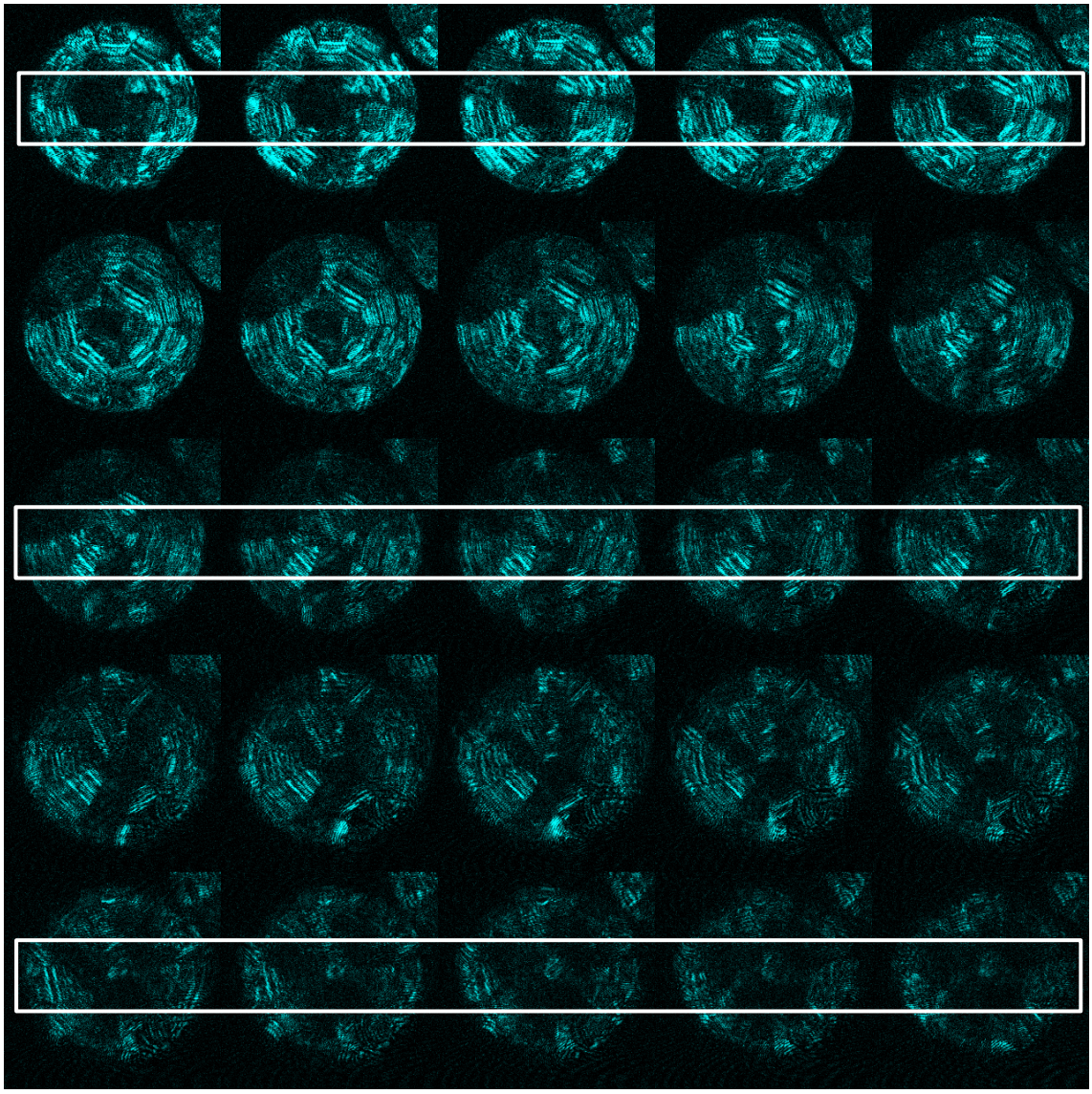

Figure 5.6: RCM images of SPhC-PNP223 illuminated with 514 nm laser light, reveals the concentric arrangement of crystalline planes towards the center of the supraparticle, their size and different orientations. The Z-depth increases from the left to the right and from top to bottom; the distance between slices corresponds to 1µm. The white rectangles denote the area used to trace the intensity profile of Figure 5.8, for cuts closer to the glass slide (top, depth from 16 to 20 µm), close to supraparticle center (middle, depth from 26 to 30 µm) and further away from the supraparticle center (bottom, depth from 36 to 40 µm).

The presence of large defect areas, such as grain boundary scars that corresponds to the interfaces between neighboring crystal domains (similar in structure but differing in orientation), are critical to the optical properties of polycrystalline materials such as SPhCs. Thus, it is important to identify and study

the properties of the disordered regions, offering insight about the topology and spreading of the boundary dislocations inside the supraparticles.[61,62] Defects distribution inside SPhC-PNP223 were imaged by 3D-RCM under illumination at 633 nm (Figure 5.7).

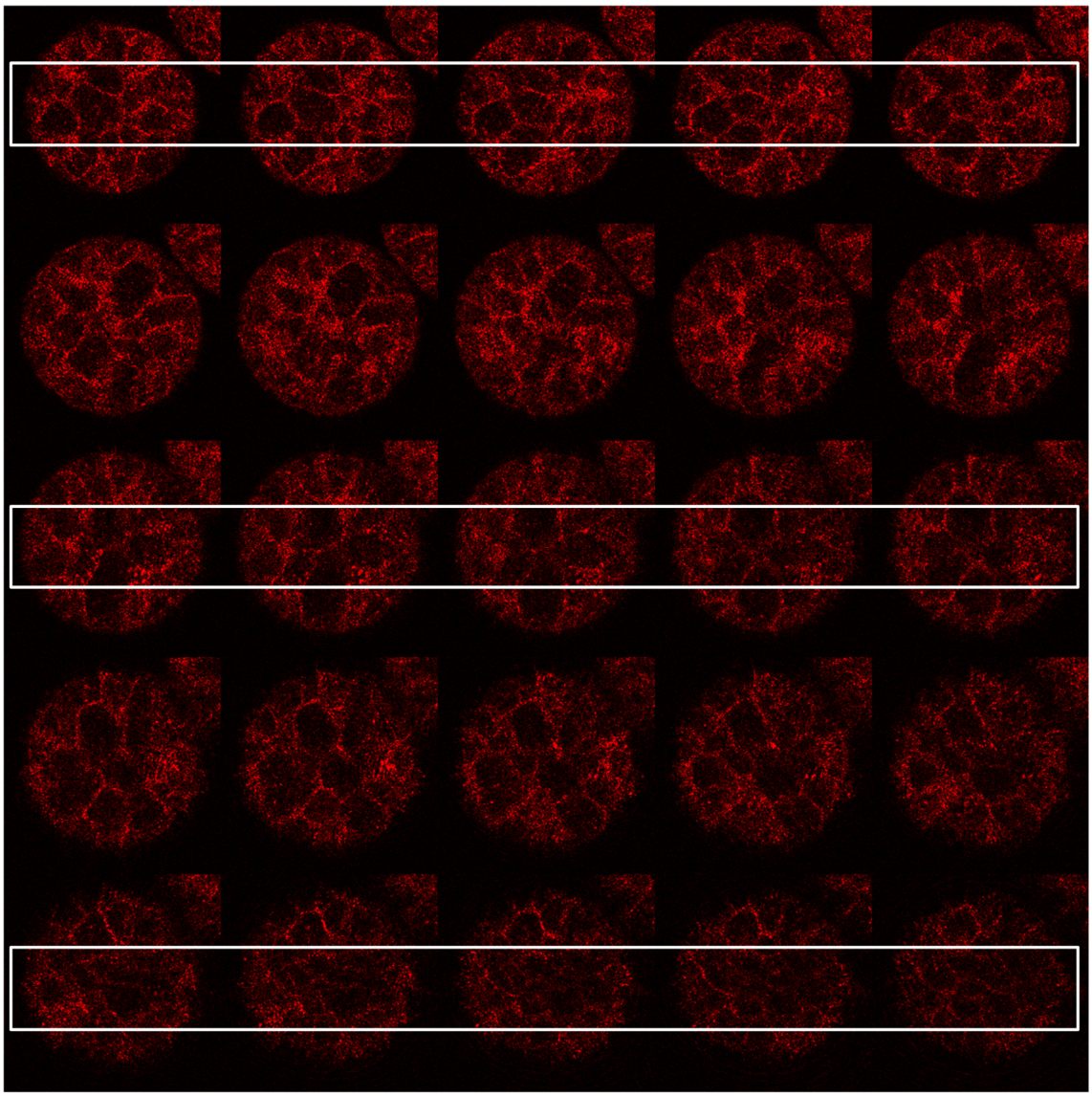

Figure 5.7: RCM images of SPhC-PNP223 illuminated with 633 nm laser light, reveals the diffuse light scattering from the disordered regions. Grain boundary scars, corresponding to misorientations between neighboring crystal grains are accommodated by arrays of edge dislocations delimiting crystalline domains with different sizes, are observed. The Z-depth increases from the left to the right and from top to bottom; the distance between each slice corresponds to 1μm. The white rectangles denote the area used to trace the intensity profile of Figure 5.8, for cuts closer to the glass slide (top, depth from 16 to 20 μm), close to supraparticle center (middle, depth from 26 to 30 μm) and further away from the supraparticle center (bottom, depth from 36 to 40 μm).

The confined darker regions in Figure 5.7 that correspond to the crystalline domains are delimited by bright regions which identify the disordered packing of PNP223 at the grain boundary scars. Regions with a powder-like background

scattering are also visible, corresponding to the overall disorder caused by dislocations and point-like defects inside the crystalline domains (have in mind that some polydispersity degree in PNP diameter is always present).

By integrating the areas denoted by the white rectangles in Figures 5.6 and 5.7, the reflectance intensity profiles with depth increase, were obtained (Figure 5.8).

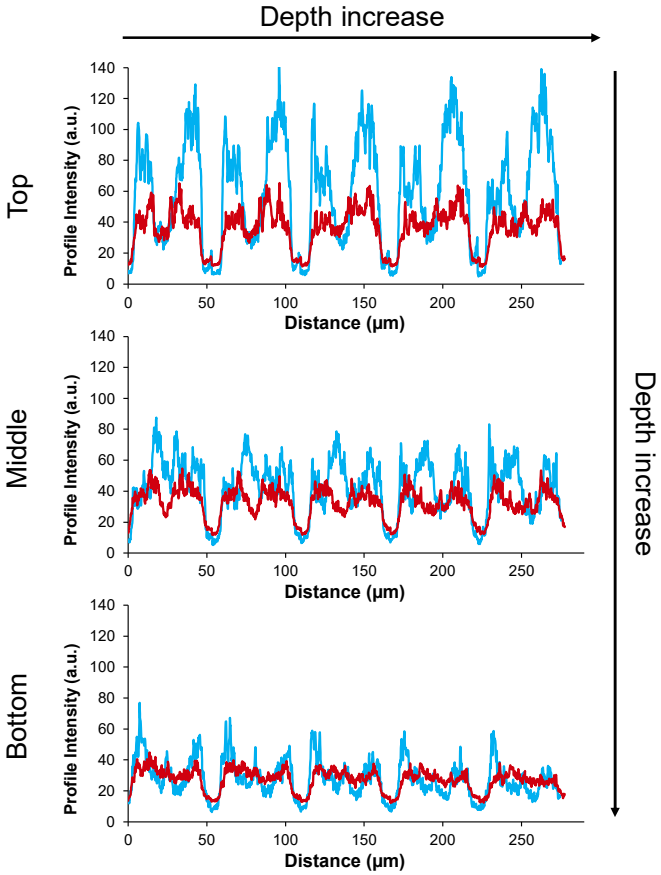

Figure 5.8: Reflectance intensity profile with increasing depth (highlighted by the white rectangles in Figures 5.6 and 5.7) for SPhC-PNP223 illuminated with light of 514 nm (cyan profiles) and 633 nm (red profiles). The (111) planes of the fcc structure shows strong interaction with 514 nm light. The attenuation effect in the intensity of the reflectance profile with depth increase lowers from a maximum value of ~100 a.u. in the top panel (depth from 16 to 20 μm), to 60 in the middle (depth from 26 to 30 μm) and 40 in the lower panel (depth from 36 to 40 μm). Under illumination with 633 nm laser light, the effect of light attenuation is negligible with depth increase (values ranging between 60-40 a.u). Light reflected from the disordered regions is scattered more isotropically and lower fluctuations in light distribution are observed in the intensity profiles across the entire supraparticle structure, because some degree of disorder is always present.

Under illumination with 514 nm, reflectance is highly backward directed, and the main source of the collected photons are reflected from the structure stop-band. When imaged under illumination with 633 nm laser light the main reflectance

contribution comes from the structural disorder, which scatter photons isotropically.

The overlay image in Figure 5.9 highlights the colocalization of the crystalline domains oriented according to the Bragg condition with many of the observed confined dark regions. The patterns are not mutually exclusive because disorder is always present.

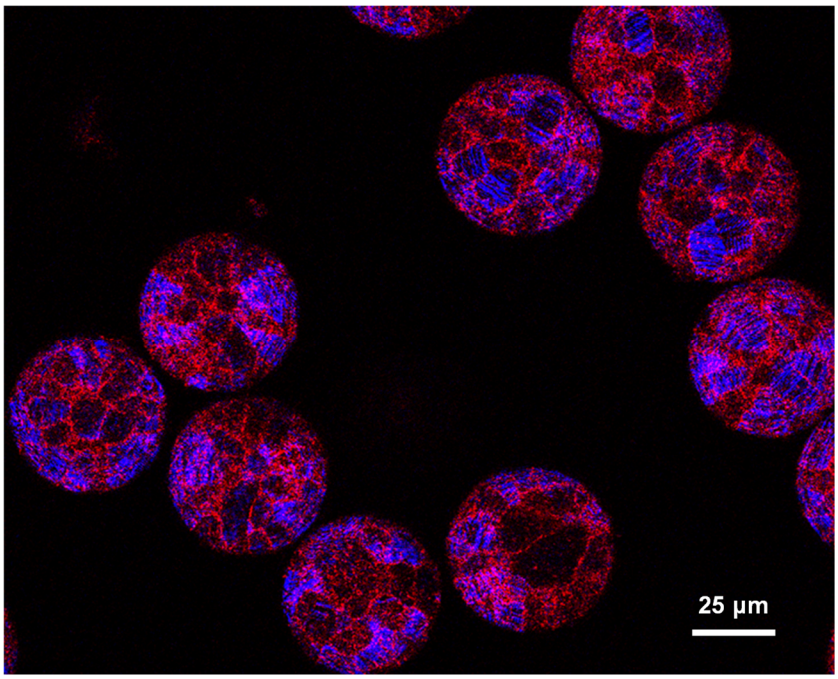

Figure 5.9: Superposition of RCM images under illumination with 514 nm light (blue) and 633 nm (red) laser light, showing the light reflected at a depth corresponding to the supraparticles center (26 µm). The (111) oriented fcc crystalline planes observed at 514 nm (blue) corresponds to some of the dark regions visualized at 633 nm (red).

RCM can resolve the diffracting planes of the packed PNP in SPhCs, but it cannot resolve the packing structure of individual nanoparticles due to the diffraction limit of visible light. Although lacking the resolution of other imaging techniques, 3D-RCM offers reliable data on the crystalline/amorphous extent of the entire spherical photonic structure. The 3D images of SPhCs obtained by RCM are shown in Figure 5.10, after stacking the 2D images obtained at different depths, for 514 nm and 633 nm laser wavelengths.

The large probed volume inside such photonic pigment supraparticles is a feature not easily assessed by other imaging techniques. The images obtained by 3D-RCM agree with the results obtained by combining scanning electron microscopy and conventional optical microscopy experiments. This is a simple, fast, non-

destructive, and readily available optical microscopy technique that finds practical applications in the fields of colloidal photonics.

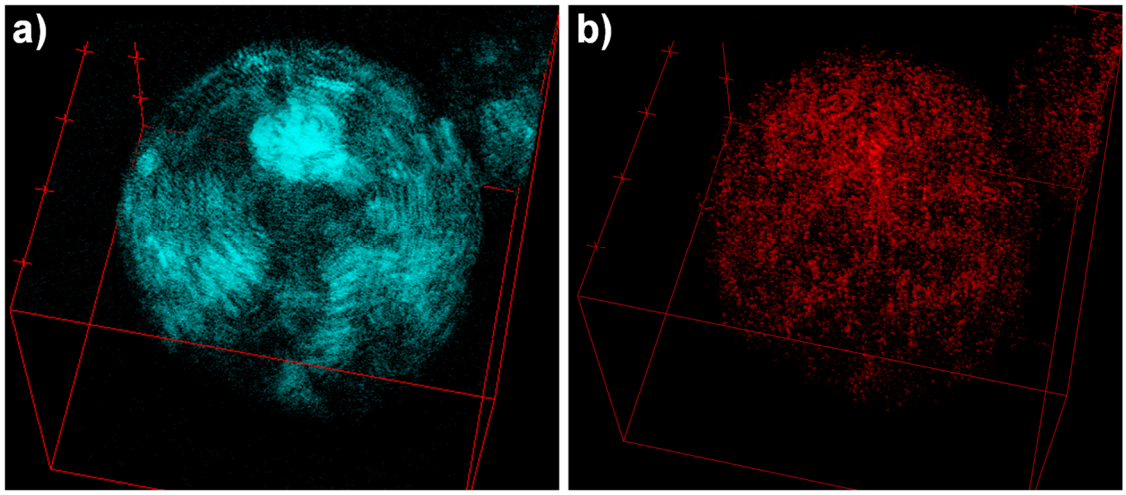

Figure 5.10: Full 3D reconstruction of SPhC-PNP223. **a)** Under illumination with 514 nm, crystalline domains with different orientations are visible from the supraparticle surface to interior. The brighter regions correspond to the (111) crystalline planes (similarly to the brightly colored patches observed in conventional reflectance microscopy images). **b)** Diffuse scattering from the boundary scars in between crystalline plains and overall disorder is visible across the entire supraparticle when illuminated with 633 nm light.

5.5. Conclusions

Here we demonstrated that 3D-RCM is a simple, non-destructive and valuable tool to obtain direct correlation between ordered/disordered structural morphology in colloidal crystals and glasses, and their corresponding optical properties. Wavelength selective 3D-RCM provides information on the number and size of crystalline domains and different crystal orientations with excellent contrast. Visible light wavelengths falling on the stop-band of the structure allows imaging of crystalline planes, while diffuse scattering from the disordered regions is imaged at wavelengths outside the stop-band. In contrast with fluorescence confocal microscopy, RCM requires no labelling (contrast is given by refractive index differences inside the structure) and gives direct spatially resolved information on the optical properties.

The resolution of RCM is diffraction limited and therefore cannot image individual colloidal nanoparticles with diameters below 300 nm. However, it does provide a full three-dimensional picture of the real internal crystalline/amorphous region distribution inside spherical photonic pigments, avoiding uncertainties due to complicated 3D-reconstruction methods and limited number of cross-sections

inherent to SEM imaging, as well ambiguities due to damage of soft materials induced by sample preparation or irradiation with high energy photons (X-rays). These results clearly demonstrate that the full picture given by 3D-RCM is able to accurately characterize the microstructure of spherical colloidal crystals.

5.6. References

1. Kim, S., Lee, S. Y., Yang, S. & Yi, G. Self-assembled colloidal structures for photonics. *NPG Asia Mater* **3**, 25–33 (2011).
2. Goerlitzer, E. S. A., Taylor, R. N. K. & Vogel, N. Bioinspired Photonic Pigments from Colloidal Self-Assembly. *Adv. Mater.* **30**, 1706654 (2018).
3. Hou, J., Li, M. & Song, Y. Patterned Colloidal Photonic Crystals. *Angew.Chem.Int. Ed.* **57**, 2544–2553 (2018).
4. Hou, J., Li, M. & Song, Y. Recent advances in colloidal photonic crystal sensors: Materials, structures and analysis methods. *Nano Today* **22**, 132–144 (2018).
5. Schall, P. Laser diffraction microscopy. *Rep. Prog. Phys.* **72**, 076601 (2009).
6. Dumanli, G. A. & Savin, T. Recent advances in the biomimicry of structural colours. *Chem. Soc. Rev.* **45**, 6698–6724 (2016).
7. Palberg, T. Crystallization kinetics of colloidal model suspensions: recent achievements and new perspectives. *J. Phys. Condens. Matter* **26**, 333101 (2014).
8. Hilhorst, J., Abramova, V. V., Sinitskii, A., Sapoletova, N. A., Napolskii, K. S., Eliseev, A. A., Byelov, D. V., Grigoryeva, N. A., Vasilieva, A. V., Bouwman, W. G., Kvashnina, K., Snigirev, A., Grigoriev, S. V. & Petukhov, A. V. Double Stacking Faults in Convectively Assembled Crystals of Colloidal Spheres. *Langmuir* **25**, 10408–10412 (2009).
9. Wei, H., Meng, L., Y. Jun & Norris, D. J. Quantifying stacking faults and vacancies in thin convectively assembled colloidal crystals. *Appl. Phys. Lett.* **89**, 241913 (2006).
10. Weeks, E. R., Cracker, J. C., Levitt, A. C., Schofield, A. & Weitz, D. A. Three-Dimensional Direct Imaging of Structural Relaxation Near the Colloidal Glass Transition. *Science* **287**, 2–6 (2000).
11. Besseling, R., Isa, L., Weeks, E. R. & Poon, W. C. K. Quantitative imaging of colloidal flows. *Adv. Colloid Interface Sci.* **146**, 1–17 (2009).
12. Hell, S. W. Far-Field Optical Nanoscopy. *Science* **316**, 1153–1158 (2007).
13. Harke, B., Ullal, C. K., Keller, J. & Hell, S. W. Three-Dimensional Nanoscopy of Colloidal Crystals. *Nano Lett.* **8**, 1309–1313 (2008).
14. Choi, T. M., Lee, G. H., Kim, Y.-S., Park, J-G., Hwang, H. & Kim, S-H. Photonic Microcapsules Containing Single-Crystal Colloidal Arrays with Optical Anisotropy. *Adv. Mater. 2019,* **31**, 1900693 (2019).

15. Wang, J., Sultan, U., Goerlitzer, E. S. A., Mbah, C. F., Engel, M. & Vogel, N. Structural Color of Colloidal Clusters as a Tool to Investigate Structure and Dynamics. *Adv. Funct. Mater.* **30**, 1907730 (2020).

16. Shirk, K., Steiner, C., Kim, J. W., Marquez, M. & Martinez, C. J. Assembly of Colloidal Silica Crystals Inside Double Emulsion Drops. *Langmuir* **29**, 11849−11857 (2013).

17. Alsayed, A. M., Islam, M. F., Zhang, J., Collings, P. J. & Yodh, A. G. Premelting at defects within bulk colloidall crystals. *Science* **309**, 1207–1211 (2005).

18. Mau, S. & Huse, D. A. Stacking entropy of hard-sphere crystals. *Phys. Rev. E* **59**, 4396–4401 (1999).

19. Astratov, V. N. Interplay of order and disorder in the optical properties of opal photonic crystals. *Phys. Rev. B* **66**, 165215 (2002).

20. Einert, T., Lipowsky, P., Schilling, J., Bowick, M. J. & Bausch, A. R. Grain Boundary Scars on Spherical Crystals. *Langmuir* **21**, 12076–12079 (2005).

21. Wang, J., Mbah, C. F., Przybilla, T., Zubiri, B. A., Spiecker, E., Engel, M. & Vogel, N. Magic number colloidal clusters as minimum free energy structures. *Nat. Commun.* **9**, 5259 (2018).

22. Lipowsky, P., Bowick, M. J., Meinke, J. A. N. H., Nelson, D. R. & Bausch, A. R. Direct visualization of dislocation dynamics in grain-boundary scars. *Nat. Mater.* **4**, 407–411 (2005).

23. Montanarella, F., Geuchies, J. J., Dasgupta, T., Prins, P. T., Overbeek, C. V., Dattani, R., Baesjou, P., Dijkstra, M., Petukhov, A. V., Blaaderen, A. V. & Vanmaekelbergh, D. Crystallization of Nanocrystals in Spherical Confinement Probed by in Situ X-ray Scattering. *Nano Lett* **18**, 3675–3681 (2018).

24. Meng, G., Paulose, J., Nelson, D. R. & Manoharan, V. N. Elastic Instability of a Crystal Growing on a Curved Surface. *Science* **343**, 634–637 (2014).

25. Nijs, B. D., Dussi, S., Smallenburg, F., Meeldijk, J. D., Groenendijk, D. J., Filion, L., Imhof, A., Blaaderen, A. V. & Dijkstra, M. Entropy-driven formation of large icosahedral colloidal clusters by spherical confinement. *Nat. Mater.* **14**, 56–60 (2015).

26. Nho, H. W., Kalegowda, Y., Shin, H. & Yoon, T. H. Nanoscale characterization of local structures and defects in photonic crystals using synchrotron-based transmission soft X-ray microscopy. *Sci Rep* **6**, 24488 (2016).

27. Jiang, P., Bertone, J. F., Hwang, K. S. & Colvin, V. L. Single-Crystal Colloidal Multilayers of Controlled Thickness. *Chem. Mater.* **11**, 2132–2140 (1999).

28. Hoeven, van der J. E. S., Wee, van der E. B., Matthijs de Winter, D. A., Hermes, M., Liu, Y., Fokkema, J., Bransen, M., Huis, van M. A., Gerritsen, H. C., Jongh, de P. E. & Blaaderen, van A. Bridging the gap: 3D real-space characterization of colloidal assemblies via FIB-SEM tomography. *Nanoscale* **11**, 5304–5316 (2019).

29. Zanaga, D., Bleichrodt, F., Altantzis, T., Winckelmans, N., Palenstijn, W. J., Sijbers, J. Nijs, B. D., Huis, M. A. V., Sánchez-Iglesias, A., Liz-Marzán, L. M., Blaaderen, A. V., Batenburg, K. J., Bals, S. & Tendeloo, G. V. Quantitative 3D analysis of huge nanoparticle assemblies. *Nanoscale* **8**, 292–299 (2016).

30. Mayence, A., Wang, D., Salazar-Alvarez, G., Oleynikov, P. & Bergström, L. Probing planar defects in nanoparticle superlattices by 3D small-angle electron diffraction tomography and real space imaging. *Nanoscale* **6**, 13803–13808 (2014).

31. Faber, D. J., Meer, F. J. Van Der & Aalders, M. C. G. Quantitative measurement of attenuation coefficients of weakly scattering media using optical coherence tomography. *Opt. Express* **12**, 590–592 (2004).

32. Hilhorst, J., Schooneveld, M. M. V., Wang, J., Smit, E. D., Tyliszczak, T., Raabe, J., Hitchcock, A. P., Obst, M., Groot, F. M. F. D. & Petukhov, A. V. Three-Dimensional Structure and Defects in Colloidal Photonic Crystals Revealed by Tomographic Scanning Transmission X-ray Microscopy. *Langmuir* **28**, 3614–3620 (2012).

33. Schooneveld, M. M. V., Hilhorst, J., Petukhov, A. V., Tyliszczak, T., Wang, J., Weckhuysen, B. M., Groot, F. M. F. D. & Smit, E. D. Scanning Transmission X-Ray Microscopy as a Novel Tool to Probe Colloidal and Photonic Crystals. *Small* **6**, 804–811 (2011).

34. Prasad, V., Semwogerere, D. & Weeks, E. R. Confocal microscopy of colloids. *J. Phys. Condens. Matter* **19**, 1–25 (2007).

35. Batta, M. M., Kessler, S. E., White, P. F., Zhu, W. & Fox, C. A. Reflectance Confocal Microscopy: An Overview of Technology and Advances in Telepathology. *Cutis* **95**, 39–46 (2015).

36. Ilie, M. A., Caruntu, C., Lupu, M., Lixandru, D., Tampa, M., Georgescu, S.-R., Bastian, A., Constantin, C., Neagu, M., Zurac, S. A. & Boda, D. Current and future applications of confocal laser scanning microscopy imaging in skin oncology. *Oncol. Lett.* **17**, 4102–4111 (2019).

37. Blaaderen, A. Van & Wiltzius, P. Real-Space Structure of Colloidal Hard-Shere Glasses. *Science* **270**, 1177–1179 (1995).

38. Wilson, T. Resolution and optical sectioning in the confocal microscope. *J. Microsc.* **244**, 113–121 (2011).

39. Dinsmore, A. D., Weeks, E. R., Prasad, V., Levitt, A. C. & Weitz, D. A. Three-dimensional confocal microscopy of colloids. *Appl. Opt.* **40**, 4152–4159 (2001).

40. Schu, S., Roller, J., Kick, A., Meijer, J. & Zumbusch, A. Real-space imaging of translational and rotational dynamics of hard spheres from the fluid to the crystal. *Soft Matter* **13**, 8240–8249 (2017).

41. Montanarella, F., Altantzis, T., Zanaga, D., Rabouw, F. T., Bals, S., Baesjou, P., Vanmaekelbergh, D. & Blaaderen, A. V. Composite Supraparticles with Tunable Light. *ACS Nano* **11**, 9136–9142 (2017).

42. Lin, K.-H., Crocker, J. C., Prasad, V., Schofield, A., Weitz, D. A., Lubensky, T. C. & Yodh, A. G. Entropically Driven Colloidal Crystallization on Patterned Surfaces. *Phys. Rev. Lett.* **85**, 1770–1773 (2000).

43. Kim, S., Lee, S. Y., Yi, G., Pine, D. J. & Yang, S. Microwave-Assisted Self-Organization of Colloidal Particles in Confining Aqueous Droplets. *J. Am. Chem. Soc.* **128**, 10897–10904 (2006).

44. Paddock, S. W. Principles and Practices of Laser Scanning Confocal Microscopy. *Mol. Biotechnol.* **16**, 127–149 (2000).

45. Rajadhyaksha, M., Grossman, M., Esterowitz, D., Webb, R. H. & Anderson, R. R. In Vivo Confocal Scanning Laser Microscopy of Human Skin: Melanin Provides Strong Contrast. *J. Invest. Dermatol.* **104**, 946–952 (1995).

46. Jacques, S. L. Confocal Laser Scanning Microscopy Using Scattering as the Contrast Mechanism. in *Handbook of Coherent-Domain Optical Methods* 1157–1171 (2013).

47. Jacques, S., Samatham, R., Choudhury, N. & Gareau, D. Specifying tissue optical properties using axial dependence of confocal reflectance images: confocal scanning laser microscopy and optical coherence tomography. *Proc. SPIE* **6446**, 1–5 (2007).

48. Samatham, R., Phillips, K. G. & Jacques, S. L. Assessment of optical clearing agents using reflectance-mode confocal scanning laser microscopy. *J. Innov. Opt. Health Sci.* **3**, 183–188 (2010).

49. Samatham, R., Jacques, S. L. & Campagnola, P. Optical properties of mutant versus wild-type mouse skin measured by reflectance-mode confocal scanning laser microscopy (rCSLM). *J. Biomed. Opt.* **13**, 1–7 (2008).

50. Tom Collier, Follen, M., Anais Malpica & Richards-Kortum. Sources of scattering in cervical tissue determination of the scattering coefficient by confocal microscopy. *Appl. Opt.* **44**, 2072–2081 (2005).

51. Jacques, S. L., Wang, B. & Samatham, R. Reflectance confocal microscopy of optical phantoms. *Biomed. Opt. Express* **3**, 1162–1172 (2012).

52. Verhoogt, H., Dam, J. van, Boer, A. P. de, Draaijer, A. & Houpt, P. M. Confocal laser scanning microscopy: a new method for determination of the morphology of polymer blends. *Polymer* **34**, 1325–1329 (1993).

53. Jinnai, H., Nishikawa, Y., Koga, T. & Hashirnot, T. Direct Observation of Three-Dimensional Bicontinuous Structure Developed via Spinodal Decomposition. *Macromolecules* **28**, 4782–4784 (1995).

54. Jacques, S. L., Levitz, D., Samatham, R., Gareau, D. S., Choudhury, N. & Truffer, F. Light Scattering in Confocal Reflectance Microscopy, Chapter 7. in *Biomedical Applications of Light Scattering*, 171–191 (2010).

55. Jenkins, M. C. & Egelhaaf, S. U. Confocal microscopy of colloidal particles: Towards reliable, optimum coordinates. *Adv. Colloid Interface Sci.* **136**, 65–92 (2008).

56. Vlasov, Y. A., Astratov, V. N., Baryshev, A. V., Kaplyanskii, A. A., Karimov, O. Z. & Limonov, M. F. Manifestation of intrinsic defects in optical properties of self-organized opal photonic crystals. *Phys. Rev. E* **61**, 5784–5793 (2000).

57. Mccomb, D. W., Treble, B. M., Smith, C. J., Rue, M. D. La & Johnson, N. P. Synthesis and characterisation of photonic crystals. *J. Mater. Chem.* **11**, 142–148 (2001).

58. He, Y., Olivier, B. & Ackerson, B. J. Morphology of Crystals Made of Hard Spheres. *Langmuir* **13**, 1408–1412 (1997).

59. Monovoukas, Y. & Gast, A. P. Study of Colloidal Crystal Morphology and Orientation via Polarizing Microscopy. *Langmuir* **7**, 460–468 (1991).

60. Schope, H. J., Fontecha, A. B., Konig, H., Hueso, J. M. & Biehl, R. Fast Microscopic Method for Large Scale Determination of Structure, Morphology, and Quality of Thin Colloidal Crystals. *Langmuir* **22**, 1828–1838 (2006).

61. Koenderink, A. F., Megens, M., Soest, G. Van, Vos, W. L. & Lagendijk, A. Enhanced backscattering from photonic crystals. *Phys. Lett. A* **268**, 104–111 (2000).

62. Lauterbach, M. A., Ullal, C. K., Westphal, V. & Hell, S. W. Dynamic Imaging of Colloidal-Crystal Nanostructures at 200 Frames per Second. *Langmuir* **26**, 14400–14404 (2010).

5.7. Appendix 5

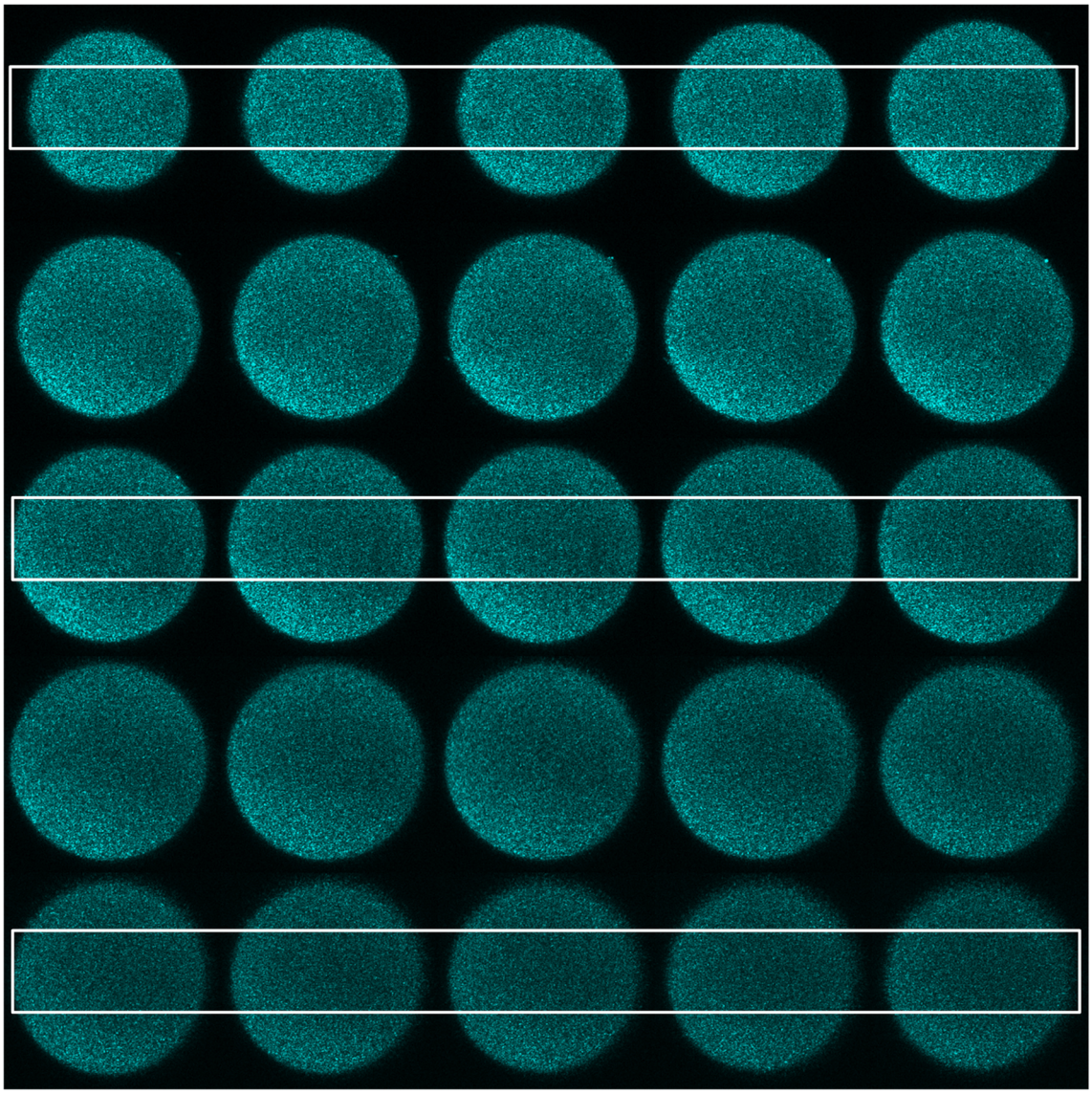

Figure A5.1: RCM images of SPhG-PNP223 illuminated with 514 nm laser light, revealing the amorphous packing of PNP223 from the supraparticle surface to interior. The Z-depth increases from the left to the right and from top to bottom; the distance between slices corresponds to 1μm. The white rectangles denote the area used to trace the intensity profile of Figure A5.3, for cuts closer to the glass slide (top, depth from 16 to 20 μm), close to supraparticle center (middle, depth from 26 to 30 μm) and further away from supraparticle center (bottom, depth from 36 to 40 μm).

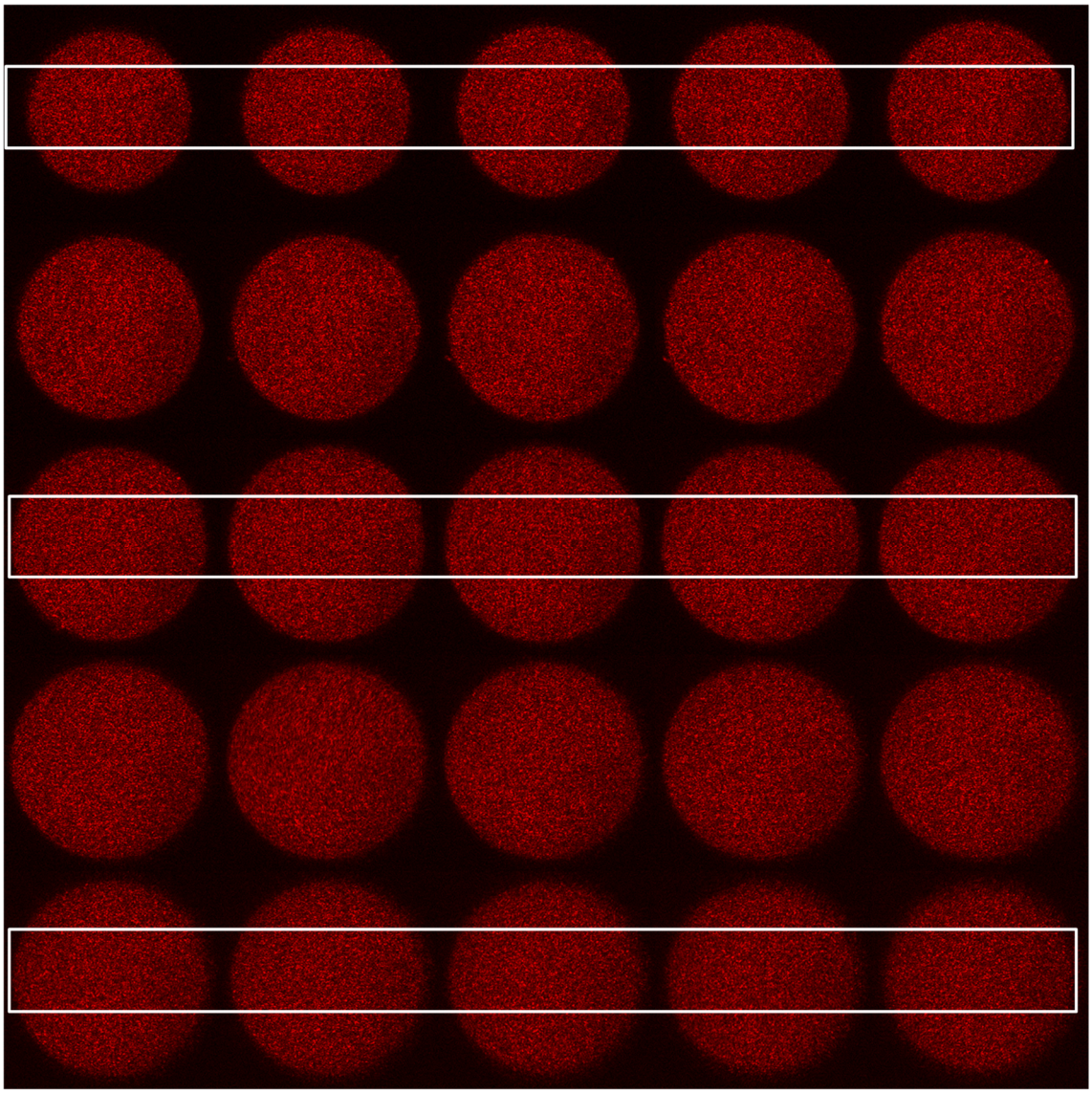

Figure A5.2: RCM images of SPhG-PNP223 illuminated with 633 nm laser light. The pattern observed for this isotropic structure does not change with the wavelength of incident light. *Z*-depth increases from the left to the right and from top to bottom; the distance between slices corresponds to 1μm. The white rectangles denote the area used to trace the intensity profile of Figure A5.3, for cuts closer to the glass slide (top, depth from 16 to 20 μm), close to supraparticle center (middle, depth from 26 to 30 μm) and further away from supraparticle center (bottom, depth from 36 to 40 μm).

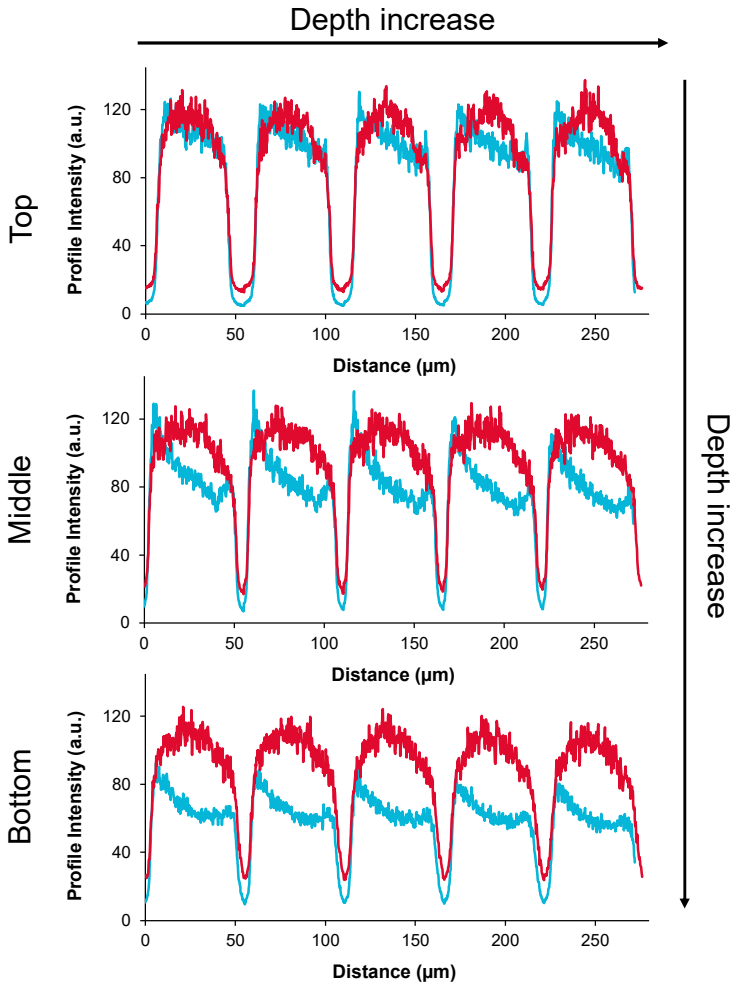

Figure A5.3: Reflectance intensity profile with increasing depth (highlighted by white rectangles in Figures A5.1 and A5.2) for SPhG-PNP223 illuminated with light wavelength of 514 nm (cyan) and 633 nm (red). The isotropic arrangement of PNP in the entire supraparticle structure, shows similar interactions with both wavelengths, because light reflected from the amorphous structure is scattered evenly in all directions. A lower attenuation effect in the intensity of the reflectance profile with depth increase is obtained under illumination with 514 nm, in comparison to the crystalline supraparticle (in the main text). Under illumination with 633 nm laser light, the effect of attenuation is negligible with depth increase and a higher background signal is obtained.

6. Variation of structural and optical properties with the assembly temperature

Pigments reflecting colors ranging from blue to red wavelengths were produced by assembling PNP with increasingly larger diameters. Changing the rate of water evaporation (directly related to the temperature at which PNP are assembled), allowed tuning the structural arrangement of PNP inside the photonic supraparticles. Therefore, depending on the assembly temperature, pigments exhibiting different color saturation were obtained for each hue. Here, a thorough characterization of the structural and optical properties of the prepared spherical photonic pigments is presented.

Due to the ability of monodisperse polymer nanoparticles (PNP) to self-assemble into close-packed 3D structures, they were selected as the building blocks to obtain structurally colored photonic materials.[1,2,3,4]

The self-assembly of monodisperse colloidal nanoparticles into crystalline or amorphous materials, called colloidal photonic crystals (PhCs) or glasses (PhGs) respectively, is a phenomenon commonly observed in nature, such as in opals. Gem opals usually have irregular macroscopic appearance, exhibiting a play of brilliant structural colors based on a pseudo-PBG by Bragg reflection of visible light.[5-7] In most manmade colloidal PhCs materials, the commonest structure corresponds to a three-layer repeat sequence, representative of the face-centered cubic structure (fcc), obtained from the staking of close-packed hexagonal layers of spherical nanoparticles. Nanoparticles packed in this way correspond to crystallographic (111) planes and the direction normal to the three-layer repeat sequence is the [111] direction. Under illumination, these structures strongly reflect colors of different wavelengths, λ. The pseudo-PBG or stop-band position of flat colloidal PhCs, that corresponds to the wavelength reflected by the (111) planes, can be estimated from equation 6.1 according to the Bragg and Snel's law:[8]

$$\lambda_{111} = 2d_{(111)}\left(n_{eff}^2 - sin^2\theta\right)^{1/2} \qquad (6.1)$$

where λ_{111} is the wavelength of the reflected light, n_{eff} is the effective refractive index of the photonic colloidal crystals, $d_{(111)}$ is the interplanar spacing between (111) diffracting planes and θ is the angle of incidence of white light. From equation 6.1, is apparent that the structural colors arising from colloidal photonic crystal structures changes with the angle of illumination. As the angle of incidence increases, so the wavelength diffracted will decrease. This feature imparts PhC materials with brilliant iridescent colors that can be useful for many applications, such as anticounterfeiting devices.[9,10] However, this angle dependence is disadvantageous for the construction of optical materials in which wide viewing angles are desired.[11,12] Contrarily to the flat structures of colloidal crystal films, in spherical colloidal photonic structures because of the spherical symmetry, the wavelengths reflected by pseudo-PBG are independent of the rotation under illumination of the surface at a fixed incident angle of light. This feature broadens their applications,[13-15] ranging from test agents in sensing materials, paints

industry, or in wide angle reflecting displays where low iridescent properties are desired.

Based on the droplet templates containing PNP (described in Chapter 4) emulsified by microfluidics technology (described in Chapter 3), we obtained monodispersed microscopic photonic supraparticles by a simple temperature-induced and fast evaporation procedure, resulting in the crystallization/aggregation of the PNP.[16-18]

By changing the temperature of the assembly process, from 50°C to 60°C and 65°C, supraparticles with different PNP arrangement were obtained, ranging from the more crystalline structures obtained at 50°C, to the more amorphous structures obtained at 65°C. In this chapter we describe the optical characterization of these photonic supraparticles based on their surface and internal degree of ordered/disordered PNP arrangement and how the structure relates with their optical properties and structural colors.

6.1. Experimental section

Scanning electron microscopy (SEM) images of photonic pigments were obtained on a JEOL scanning electron microscope (Model JSM7001F, JEOL, Tokyo, Japan), with an accelerating voltage of 15 kV. Dried photonic supraparticles were glued onto double sided carbon tape and coated with gold using a turbo-pumped sputter coater from Quorum Technology (model Q150T ES, Quorum Technology, Ashford, UK) for 1 min. SEM images were processed with ImageJ software (http://rsbweb.nih.gov/ij/).

The Autocorrelation function (ACF or radial distribution function, RDF) of the surface SEM images was obtained by applying the RDF macro of ImageJ software, which gives information about the typical feature size in an image (nanoparticles and interstices). This plugin produces a profile plot of normalized integrated intensities around concentric circles as a function of distance from a point in the image. The profile x-axis can be plotted as pixel values or according to the spatial calibration of the input image. The first maximum of the autocorrelation gives the distance between two nanoparticles or interstices.

Focused Ion Beam (FIB) was performed using a gallium source within an evacuated SEM chamber. Pt was deposited locally by means of electron beam and assisted by ion beam as protection layer. FIB-SEM images were obtained

from a SEM: HELIOS 450S, lens mode: immersion lens, detector: TLD, Electron beam energy/current: 5kV/100pA; FIB: gallium ion beam, operated at energy/current 30keV/9.3nA or 21 nA for cross-sectioning and at 30 keV/0.79 nA for cross-section cleaning; angle between E-beam and Ion-beam is 52°.

Angle-dependent reflectivity measurements were performed using a multi-angle probe holder, where light can either hit or be collected from the sample at different incident/collecting angles. The sample holder does not move or rotate from its original position. White light from a tungsten light source is conducted through a bifurcated optical fiber cable to the sample. The reflected signal is collected with an optical fiber cable into a portable SPEC RES+ spectrometer (SPEC RES+UV/Vis, SARSPEC) connected by an USB cable to a computer where reflectance is obtained and analyzed with Lightscan spectroscopy software (SARSPEC). Calibration of the apparatus was accomplished with white (100% reflection intensity) and black (0% reflection intensity) Teflon discs. Supraparticles in hexadecane are placed on top of a black Teflon disc with a depression of about 0.5 mm. Specular reflectance of the different photonic pigments was measured as a function of wavelength under illumination at 45° for collecting angles varying from 0° to 75°.

Commission Internationale de l'Éclairage (CIE) color maps were obtained from reflectance spectra using ColorCalculator software from OSRAM Sylvania, Inc. (https://www.osram.us/). Reflectance ($R(\lambda)$) to color (x,y) conversion accounts for the illumination dependence of the perceived colors by multiplying $R(\lambda)$ with a standard white illumination spectrum (CIE Standard Illuminant D_{65}). This spectrum is then converted via the three CIE 1931 2° Standard Observers color matching functions to get the tristimulus in CIE $XY\,Z$ colorspace. The tristimulus is converted to the normalized CIE xyY color space where $x = X/(X + Y + Z)$ and $y = Y/(X + Y + Z)$ are the chromaticity coordinates defining the colors hue and Y is the color luminance. By normalizing to a certain luminance $Y = 1$, the whole range of colors called *visible gamut* can be located in a $2D$ plane spanned by x and y coordinates. The CIE color map boundary is determined by the values for single wavelength colors in the visible range, where the endpoints at $\lambda = 360\ nm$ and $\lambda = 830\ nm$ are connected by the *line of purples*. Color saturation is defined as the distance to the white point (D_{65} white point).

Optical reflectance microscopy images were performed on a KERN OKM 173 microscope equipped with an ODC 832 camera at a magnification of 40x.

RCM images were recorded with a Leica TCS SP5 inverted confocal microscope (DMI6000, Leica Microsystems CMS GmbH) equipped with a CW Argon ion laser (available excitation lines at 458, 465, 488, 496 and 514 nm) and Ne:He with 633 nm laser line. Confocal Z-series stacks were acquired using a 63x1.2NA (HCX PL APO CS 63.0×WATER UV) by recording the backscaterred light with an HyD hybrid detector. Typically, 55 x 55 µm images where collected with 1064 x 1064 pixels and a scan rate of 100-200 Hz per frame. Individual images recorded at different wavelenghts were pseudo-colored with RGB values corresponding to the photonic supraparticle refraction spectral profiles.

6.2. Temperature dependent size and structural color

PNP dispersions were emulsified into monodispersed and stable aqueous emulsion droplets with ~90 µm in mean diameter. Droplets shrinkage upon temperature-driven water evaporation, resulted in photonic supraparticles composed of highly packed nanoparticles with approximately 50 µm in mean diameter (droplets lose between 40 to 45% of their initial diameter).

Interestingly, differences in the mean diameter of supraparticles assembled at different temperatures were noticed. When assembled at 50°C smaller mean diameters were obtained (approximately 2 µm), in comparison with the mean diameters obtained at 65°C (Figure 6.1). This difference, although small, is indicative of the different PNP packing inside the spherical assemblies.

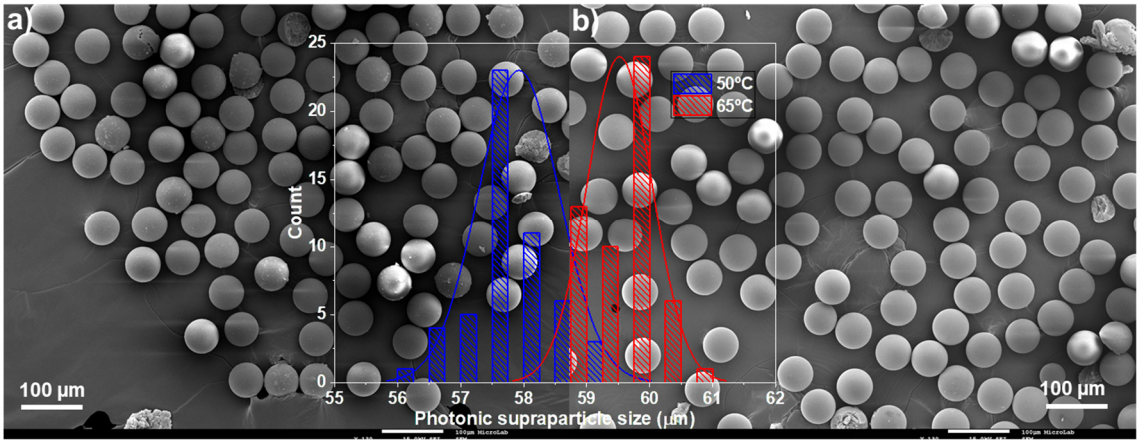

Figure 6.1: SEM images of spherical photonic pigments composed of PNP287, PhP-PNP287, obtained at **a)** 50°C and **b)** 65°C. The blue and red histogram corresponds to the supraparticles size distribution when assembled at 50°C and 65°C, respectively.

Starting from equally sized emulsion droplets, photonic supraparticles with smaller mean diameters were obtained at 50°C (Table A6.1 of Appendix 6, resumes the results obtained for all the samples). This highlights the interplay between the water evaporation rates and the packing density of PNP inside the supraparticle structure and is indicative of a lower volume fraction of PNP inside the supraparticles assembled at 65°C.

The number of constituent nanoparticles, N, in the initial aqueous droplet can be calculated according to equation 6.2,[19] assuming a rhcp or fcc arrangement of PNP with a packing density of about 0.74 (the densest ordered packing of spheres in 3D):[20-22]

$$N = 0.74 \times \left(\frac{D_S}{D_{PNP}}\right)^3 \tag{6.2}$$

where D_S is the diameter of the photonic supraparticle and D_{PNP} is the PNP diameter. Since the number of PNP remains the same and the supraparticles diameter increases with temperature, at 65°C the volume fraction of nanoparticles would be lower than at 50°C, and closer to the volume fraction of random close packing (the densest disordered packing of spheres occurs at about 0.64 volume fraction). Indeed, the volume fraction values estimated at 65°C for the different supraparticles ranges from 0.62−0.69.

The formation of close-packed fcc or rhcp structures can also be predicted from the diameter difference between the droplet template and the supraparticle after water evaporation, according to equation 6.3:[23]

$$\emptyset = c\left(\frac{D_d}{D_S}\right)^3 \tag{6.3}$$

where $\emptyset$ is the volume fraction of PNP inside the photonic supraparticle, c is the volume fraction of PNP inside the emulsion droplets, D_d is the diameter of aqueous droplet template, and D_S is the diameter of the photonic supraparticle. Using the average values of D_S and c for the different photonic samples at each assembly temperature, the corresponding average volume fraction of PNP inside the supraparticles assembled at 65°C is 0.87, a lower value than the one obtained at 50°C, that corresponds to 0.98. Although these values are unrealistically high (due to the uncertainties in determining c and D_d), they clearly show that photonic structures assembled in spherical confinement change significantly when changing the shrinking rate of the droplet templates.[24,25]

Reflectance microscopy images of the photonic pigments (PhP) highlight the differences in structure and color between pigments obtained at different assembly temperatures. Figure 6.2 shows the color differences reflected from blue, green, and red PhP, composed respectively of PNP194, PNP232 and PNP287, when assembled at 50°C and 65°C.

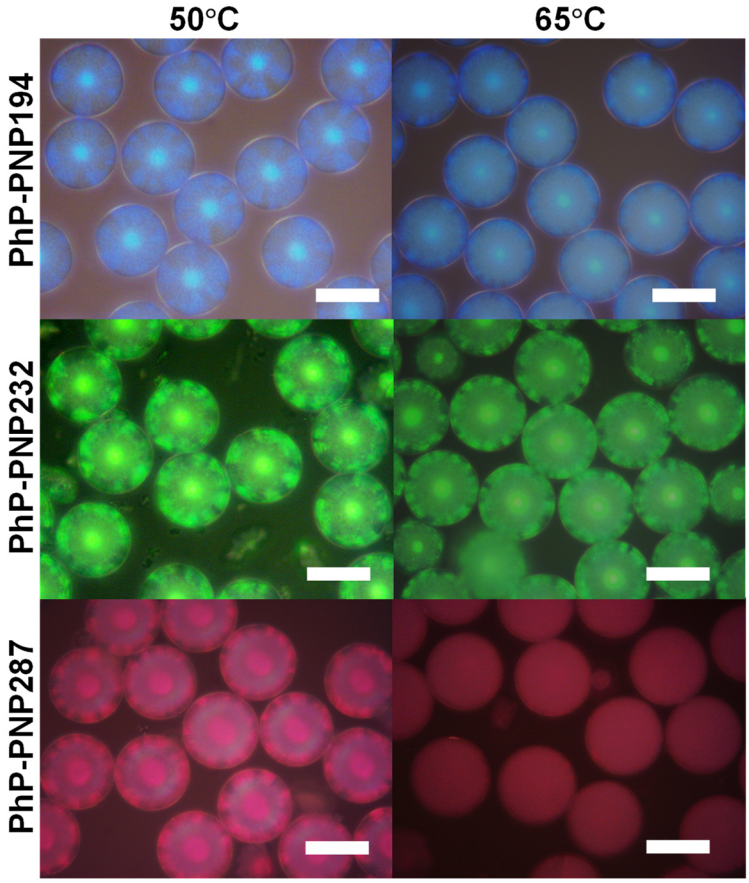

Figure 6.2: Reflectance microscopy images of blue (PhP-PNP194), green (PhP-PNP232) and red (PhP-PNP287) photonic pigments showing the color patterns obtained at 50°C (left panel) and at 65°C (right panel). Scale bar: 50 µm.

Pigments assembled at 50°C, exhibit large color patches spreading across the entire supraparticle, on the other hand, when assembled at 65°C, the bright patches are only visible near the supraparticles surface, and a more homogeneous color is observed in the interior. These brightly colored patches result from large crystalline domains whose diffraction is attributed to the (111) planes spreading from the spherical surface towards the supraparticles interior. The darker regions are attributed to diffraction from other planes of the fcc lattice that do not contribute to the stop-band.[26-28] The degree of crystallization, as determined by the size of the colored patches, is reduced with increasing the assembly temperature. When assembled at 65°C, PNP only pack into a fcc lattice

close to the supraparticles surface and a more disordered arrangement is obtained towards the center. This is particularly evident for red pigments assembled at 65°C where only a weakly bright color ring appears at the surface of PhP-PNP287-65°C (Figure 6.2).

6.3. Structural characterization of the PNP arrangement

Self-assembly of PNP usually leads to structures possessing both short and long-range order.[3] The spherical confinement prevent the packing into fcc structures with the highest packing fraction of a close-packed structure (0.74), because large areas with a random close-packing (rcp) of PNP are obtained in between the crystalline domains.[29,30] How does the rate at which water evaporates relates with the packing of the different PNP inside the supraparticles?

6.3.1. SEM imaging

A direct observation of the topological and internal packing of PNP and the evaluation of the ordered/disordered regions were obtained from the SEM images of photonic pigments assembled at different temperatures. Figures 6.3, 6.4 and 6.5 show a comparison between the supraparticles structure when assembled at the different temperatures, for blue (PhP-PNP194), green (PhP-PNP232) and red (PhP-PNP287) photonic pigments, respectively. The Figures also show the two-dimensional fast Fourier transform (2D-FFT) and the autocorrelation function (ACF) profile of the SEM images. The images corresponding to pigments obtained with other PNP diameters are compiled in appendix 6 (Figures A6.1 to A6.7, Appendix 6).

The ACF describes the correlation of the contrast function and gives a measure of the translational symmetry in the system. If the nanoparticles have the same shape and size and are arranged with a certain local order, that is, with a regular distance between first neighbors, the function presents a maximum at the corresponding distance. On the contrary, the autocorrelation function of an amorphous isotropic arrangement of monodispersed nanoparticles without positional correlations is a monotonic decay function.[31,32]

In turn, the fast Fourier transform (FFT) of the SEM images, gives spatial information about the structure frequency domain.[33] In the case of ordered structures, the resulting frequency plot contain pixels that are concentrated along

a specific axis, where the presence of hexagonal sharp peaks confirms the presence of crystalline order or structural periodicity. On the contrary, frequency plots of disordered structures contains clusters of white pixels that are concentrated in symmetrical, circular patterns around the origin, which indicate that the spatial variation of the refractive index is equivalent in all directions in those planes within the structure.

When assembled at 50°C, the SEM images of supraparticles surface (Figures 6.3, 6.4 and 6.5), shows ordered PNP in a polycrystalline, hexagonally close-packed lattice, assigned as the (111) lattice plane of the fcc structures formed in spherical confinement, whose curvature prevents the formation of a perfectly ordered crystal.[34]

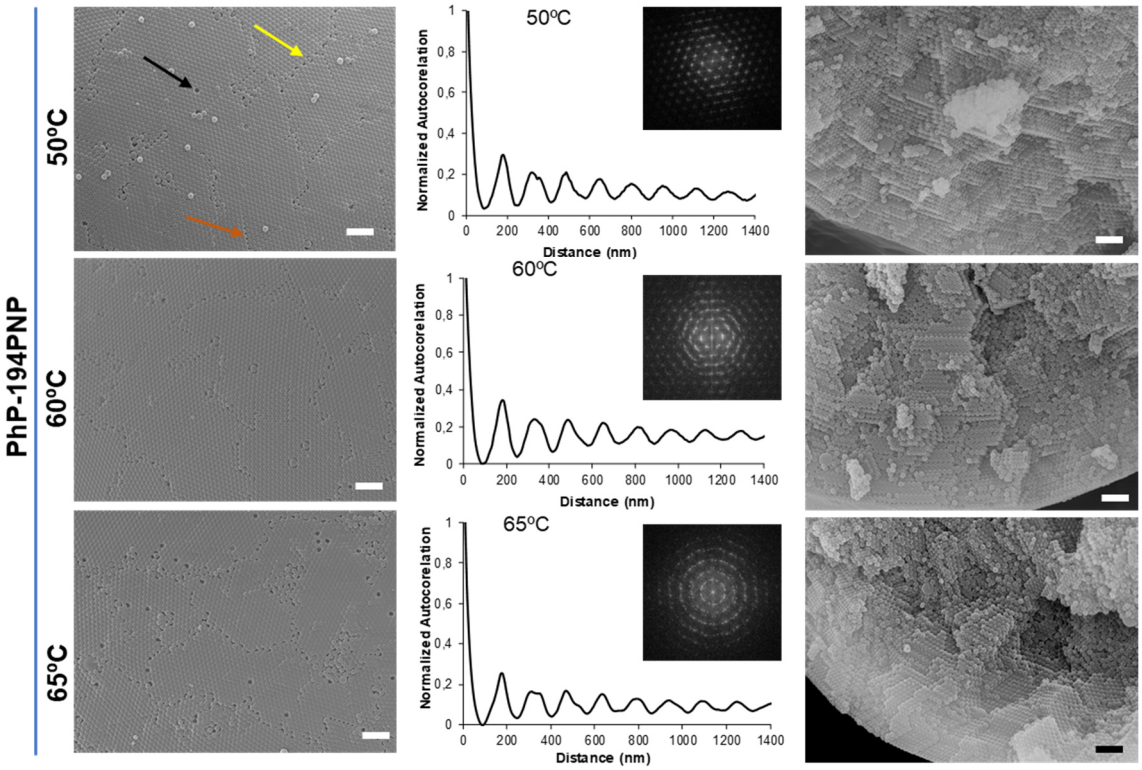

Figure 6.3: SEM images of blue photonic pigments, PhP-PNP194, assembled at 50°C (upper row), 60°C (middle row) and 65°C (lower raw). The left panel shows SEM images of supraparticles surface. The number of intrinsic defects increases with increasing the assembly temperature: black arrow indicates point defects; yellow arrow indicates a grain boundary scar; orange arrow indicates a dislocation (or staking fault). The middle panel represents the ACF and the 2D-FFT patterns obtained from the SEM images in the right panel; distance between first neighbors corresponds to 180 nm. Right panel shows SEM images of a broken supraparticle inner structure. Scale bar: 1 μm.

With increasing the assembly temperature from 50° to 65°C, the number of lattice defects at the supraparticles surface increases for all the pigments. This happens

for boundary scars, staking faults and point defects, which is particularly evident in the case of red pigments assembled at 65°C (PhP-PNP287-65°C, Figure 6.5) where large regions of amorphously packed PNP are visible. This is expected, because of the increased water evaporation rate. In addition, the inner disorder also increases with increasing the assembly temperature. The number of concentric layers with fcc packing towards supraparticles center decreases with increasing the assembly temperature.

The number of defects at supraparticles surface and the internal disorder also increases with increasing the PNP diameter from 173 nm to 331 nm (Figures A6.1-A6.6, Appendix 6 for other samples).

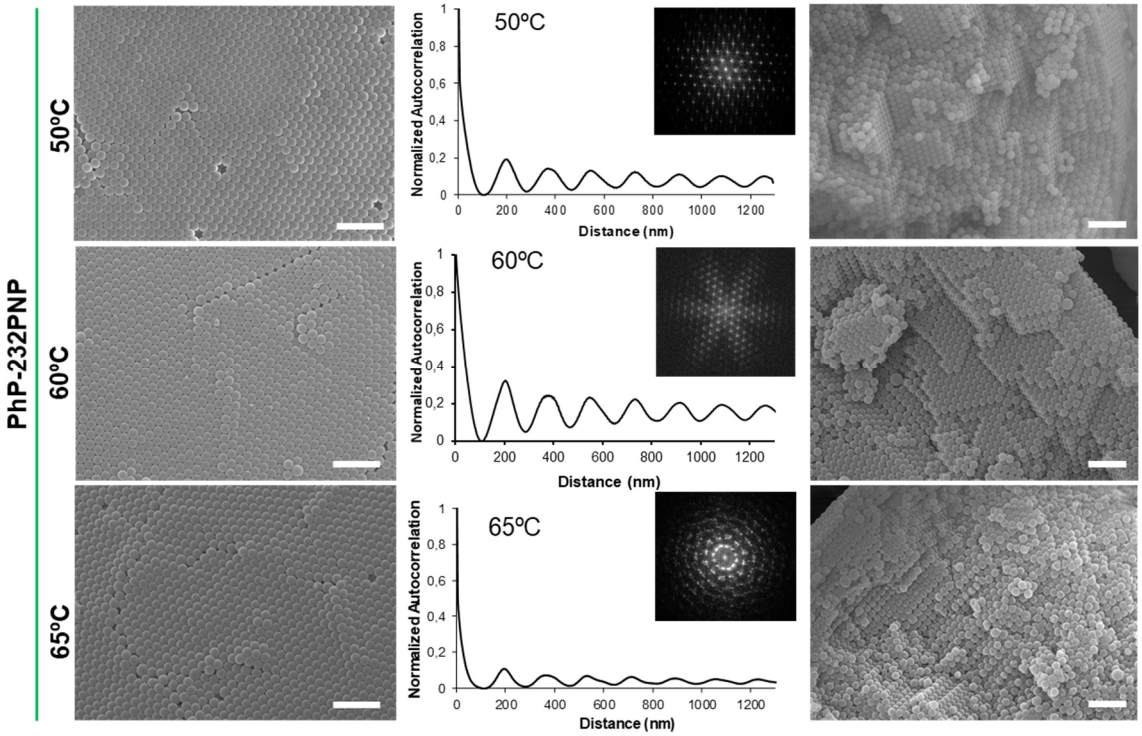

Figure 6.4: SEM images of green photonic pigments (PhP-PNP232) assembled at 50°C, 60°C and 65°C. Left panel: SEM images of supraparticles surface. Middle panel: ACF and 2D-FFT patterns obtained from the SEM images in the right panel; distance between first neighbors corresponds to 203 nm. Right panel: SEM images of a broken supraparticles inner structure. Scale bar: 1 µm.

The six-fold symmetry in the 2D-FFT patterns from the surface SEM images of blue, green and red supraparticles assembled at 50°C, results from the crystalline packing of PNP with long-range order and periodicity, despite the intrinsic defects (Figures 6.3, 6.4 and 6.5). However, with increasing the assembly temperature, concentric circles displaying bright spots with a high number of rings indicates the presence of partly ordered structures (between the crystalline and amorphous

packing of PNP).[35] In the case of PhP-PNP287-65°C, the amorphous packing of PNP at supraparticle surface originates a circular ring pattern indicating the spatially isotropic structural correlations from the random arrangement of PNP.

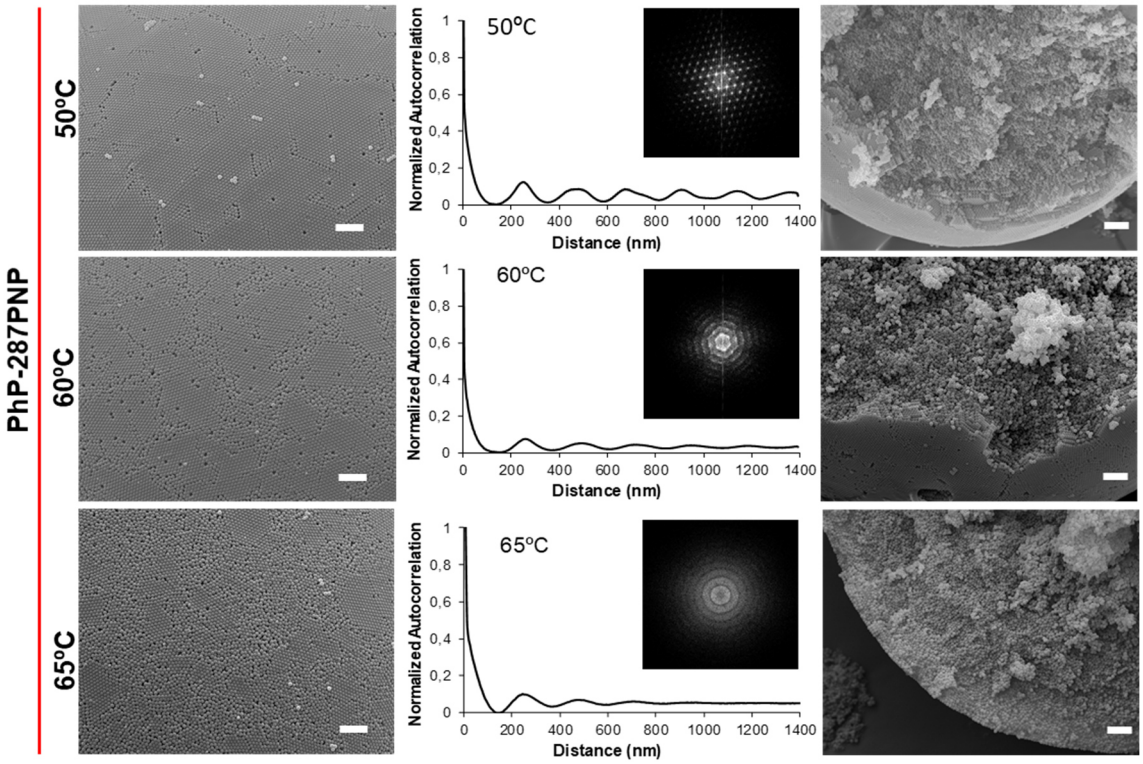

Figure 6.5: SEM images of red (PhP-PNP287) photonic pigments, assembled at 50°C, 60°C and 65°C. Left panel: SEM images of supraparticles surface. Middle panel: ACF and 2D-FFT patterns obtained from the SEM images in the right panel; distance between first neighbors corresponds to 258 nm. Right panel: SEM images of a broken supraparticles inner structure. Scale bar: 1 μm.

Figures 6.3 to 6.5 also show the ACF of the surface SEM images at different assembly temperatures. The first maximum of the radial profile plots of the autocorrelation function gives the typical distance between two PNP (or voids). As expected, the distance between first neighbors increases with increasing PNP diameter, and corresponds to 180 nm, 203 nm and 258 nm, for blue, green and red pigments, respectively (for other photonic samples see Figure A6.7, Appendix 6). The difference between PNP diameter (194 nm, 232 nm and 287 nm, respectively for blue, green, and red pigments) and the first neighbor distance is probably due to the packing and deformation of the PNP in the supraparticles structure. The radial profile plots of the ACF of the surface SEM images obtained at 50°C contains a periodic distribution of maxima along an extended distance for blue, green, and red pigments. Lower intensity peaks are observed as the

assembly temperature increases, and the periodic distribution of maxima for larger distances is no longer visible, especially in the case of PhP-PNP287-65°C supraparticles, due to the lack of crystalline periodicity. This is indicative of more disordered structures with increasing the assembly temperature.[32,36]

These results show that we successfully tune the ordered/disordered degrees of the spherical photonic pigments by changing the assembly temperature, obtaining either a more crystalline or amorphous packing of PNP.

The assembly of PNP towards the center of the supraparticles appears increasingly disordered with increasing the PNP diameter from 173 nm to 331 nm, presumably as a consequence of increasing crystallization frustration.[28,37,38]

The higher the level of confinement is (i.e., the smaller the ratio of the photonic supraparticle to the PNP diameters, D_S/D_{PNP}), the fewer ordered layers are observed in the SEM images. Broadened and less intense peaks are observed in the radial profile plots of the ACF with increasing PNP diameters. This is also indicative of different degrees of order for the different photonic pigments: order decreases with increasing PNP diameter.

6.3.2. FIB-SEM analysis and thermal treatment

A more detailed information about irregularities in PNP packing and/or concentration of intrinsic structural defects was obtained by cutting the supraparticles with focused ion beam (FIB) coupled to SEM imaging. FIB-SEM images of PhP-PNP232 assembled at 60°C (PhP-PNP232-60°C) in Figure 6.6, show a more disorder packing of PNP232 for cross-sections closer to the supraparticles center due to higher confinement (Figure 6.6a and c). The surface texture at the cut plane and the inner structure is blurry due to charging effects. Nevertheless, FIB cuts at different depth position inside the supraparticles shows increasingly disordered cross-sections with depth increase: the size of the crystalline domains diminishes, and larger boundary disordered regions are visible (Figure 6.6b and d).

The concentric arrangement of PNP inside the photonic pigments shows crystalline domains with different size and orientation. However, as the assembly temperature increases from 50°C to 65°C, the average size of the crystalline domains diminishes and their number increases, resulting in structures with a higher degree of defects (Figures A6.8 and A6.9, Appendix 6).

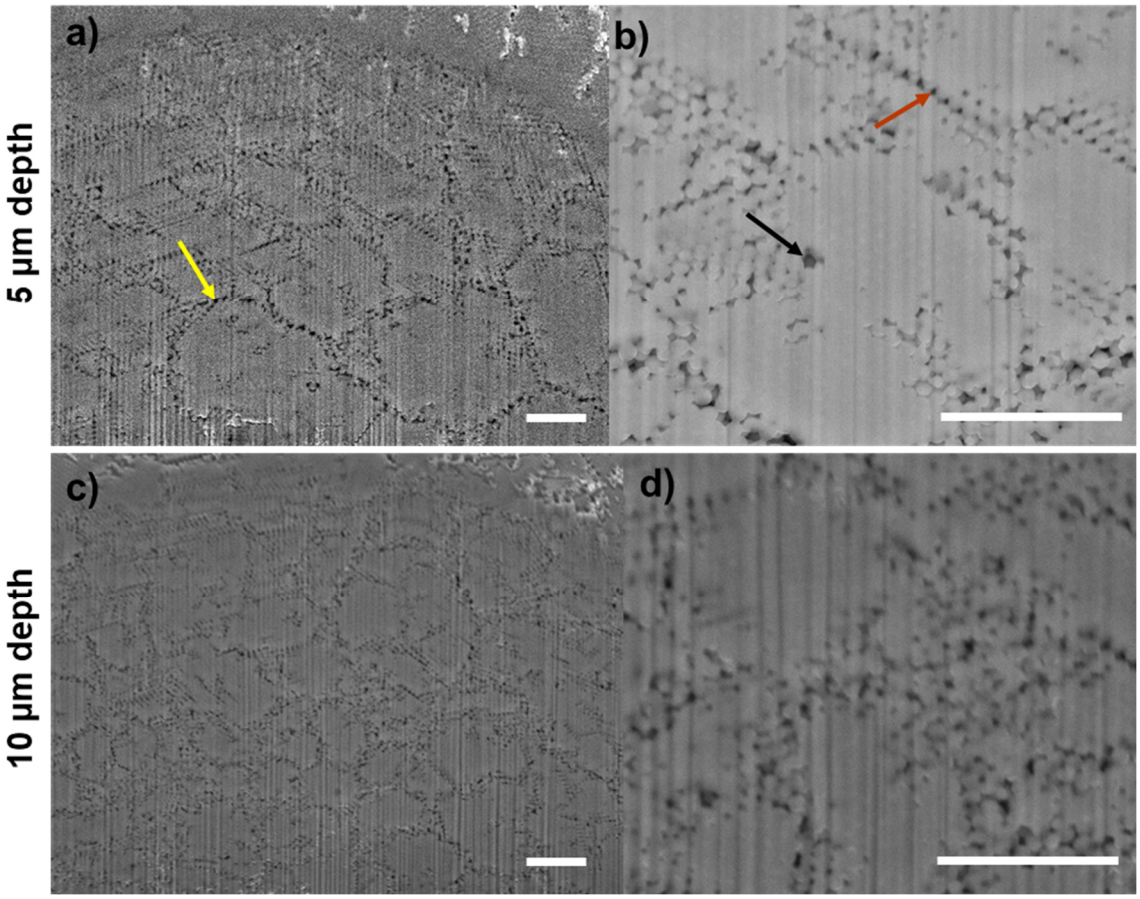

Figure 6.6: FIB-SEM images of PhP-PNP232-60°C (supraparticle diameter ~ 50 µm) at different depths. **a)** and **b)** 5 micrometers depth cross-sections; **c)** and **d)** 10 micrometers depth cross-sections. Right panel shows a zoom-in of the inner structure in a) and c): disorder increases towards supraparticle center, resulting in smaller crystalline domains and higher number of defects (yellow arow indicates a boundary scar; black arrow denotes a vacancies or point defect, and the orange arrow highlights a stacking faults). Scale bar: 2 µm.

Although it is difficult to derive the packing sequence of the ordered layers from the cross-sectional images due to the nature of the FIB method, in combination with the cracked structures imaged by SEM, we know that the supraparticles are completely filled with obvious domain formation, most probably arranged in a mixture of close-packed fcc and rhcp layers, in between boundary disordered regions. The regions with a disordered packing of PNP increases with increasing depth towards the supraparticle center and with increasing the assembly temperature.

The robustness and structure stability of PhP-PNP332-60°C was also assessed by FIB-SEM imaging of pigments annealed at 150°C for 5 minutes. The results show that high temperatures did not cause drastic viscoelastic deformation of the PNP under these conditions (heating/cooling rate 5°C/min).[29,39] After increasing

the temperature to 150°C (above the Tg of the PNP), PNP coalescence was not observed in FIB-SEM images of the supraparticles surface and interior (Figure A6.10, Appendix 6). This indicates the high structural stability of the photonic pigments. Absence of coalescence to uniform density due to maximum deformation of PNP was also confirmed in reflectance microscopy images where pigments still exhibit structural coloration (Figure A6.11, Appendix 6).

FIB-SEM imaging confirmed the increased disorder with increasing depth and assembly temperature, although observation of the whole internal structure of the supraparticles was not possible due to the impractical large sizes.

6.3.3. RCM imaging

Due to the difficulties in performing FIB cuts at higher depths (structure melting and resolution issues) we imaged the photonic structures by reflectance confocal microscopy (RCM), trying to gain insight of the entire supraparticle structure.[40-42] RCM allows imaging crystalline planes based on the backscattered fraction of the incident light delivered to the samples under illumination with wavelengths falling on the structures pseudo-PBGs (Chapter 5). Brighter regions correspond to more backward directed light reflected from the (111) planes of the fcc structure. Darker regions correspond to planes in directions other than the [111], that do not contribute to the stop-band.

Here, RCM was used to image the different structural order degrees of PhP-PNP194 (blue), PhP-PNP232 (green), and PhP-PNP287 (red) photonic pigments assembled at 50°C and 65°C. Each of the pigments was imaged with laser light of wavelength matching to the wavelength of the pseudo-PBG: 458 nm, 514 nm and 633 nm for PhP-PNP194, PhP-PNP232, and PhP-PNP287, respectively (Figure 6.7).

In Figure 6.7, the Z-depth increases from the left ($15\ \mu m$) to the right ($35\ \mu m$), and the distance between each slice corresponds to 5 µm. Panels a), b) and c), show cross-section images of blue, green, and red photonic pigments, respectively. The white rectangles denote the area used to trace the intensity profile of light distribution within the supraparticles structure at different depths: $15\ \mu m$ (a1, a4, b1, b4, c1, c4); $25\ \mu m$ (a2, a5, b2, b5, c2, c5); $35\ \mu m$ (a3, a6, b3, b6, c3, c6).

A larger concentric arrangement of brightly colored crystalline planes towards the photonic pigments center are visible when structures are assembled at 50°C

(Figure 6.7 a1-a3; b1-b3; c1-c3). At 65°C the number and the extension of the highly reflecting regions diminishes, especially in the case of PhP-PNP287 (Figure 6.7 a4-a6; b4-b6; c4-c6). Confocal images corroborate the disorder increase towards supraparticles center for higher assembly temperatures, especially for pigments composed of larger PNP.

Different scattering properties originate the differences observed when light interacts with the structures. The effect of light attenuation with depth increase is stronger in the intensity profile of more ordered samples. A comparison of the intensity profile plots obtained at 50°C and 65°C for the cross-sections at $25\ \mu m$ depth (a2 and a5; b2 and b5; c2 and c5), was performed by calculating the difference between their maximum and minimum intensity values. The black dotted lines in the intensity profiles at $25\ \mu m$ depth in Figure 6.7 (a2, a5, b2, b5, c2, and c5) correspond to average values used to obtain the maximum intensity value of light interacting with the structure. The full black lines in the same profiles correspond to the average value at the minimum of the intensity profile.

The differences in the intensity between these two regions is higher for supraparticles assembled at 50°C. Blue and green photonic pigments have a maximum to minimum intensity difference of 53 a.u. and 29 a.u., respectively, when assembled at 50°C. On the other hand, the intensity difference lowers to 24 a.u. and 10 a.u., respectively for PhP-PNP194-65°C and PhP-PNP232-65°C. This is indicative of the smaller extension of the crystalline packing of PNP inside the supraparticles assembled at higher temperatures, where a more disordered structure is obtained.

In the case of red photonic pigments, we were only able to obtain the maximum to minimum intensity difference for supraparticles assembled at 50°C. This is due to the absence of brighter regions identifying crystalline planes inside PhP-PNP287-65°C, which originates a more homogeneous and flattened intensity profile. The isotropic nature of the amorphous packing of PNP at PhP-PNP287-65°C is also evident by the higher intensity of the profile plot (Figure 6.7 c4-c6) relatively to the ones obtained at 50°C (Figure 6.7 c1-c3), highlighting the contribution of diffuse scattering. For PhP-PNP194 and PhP-PNP232 the opposite behavior is observed: the higher profile plot intensity values are obtained for pigments assembled at 50°C (Figure 6.7 a1-a3 and b1-b3), due to the larger extent of the crystalline regions.

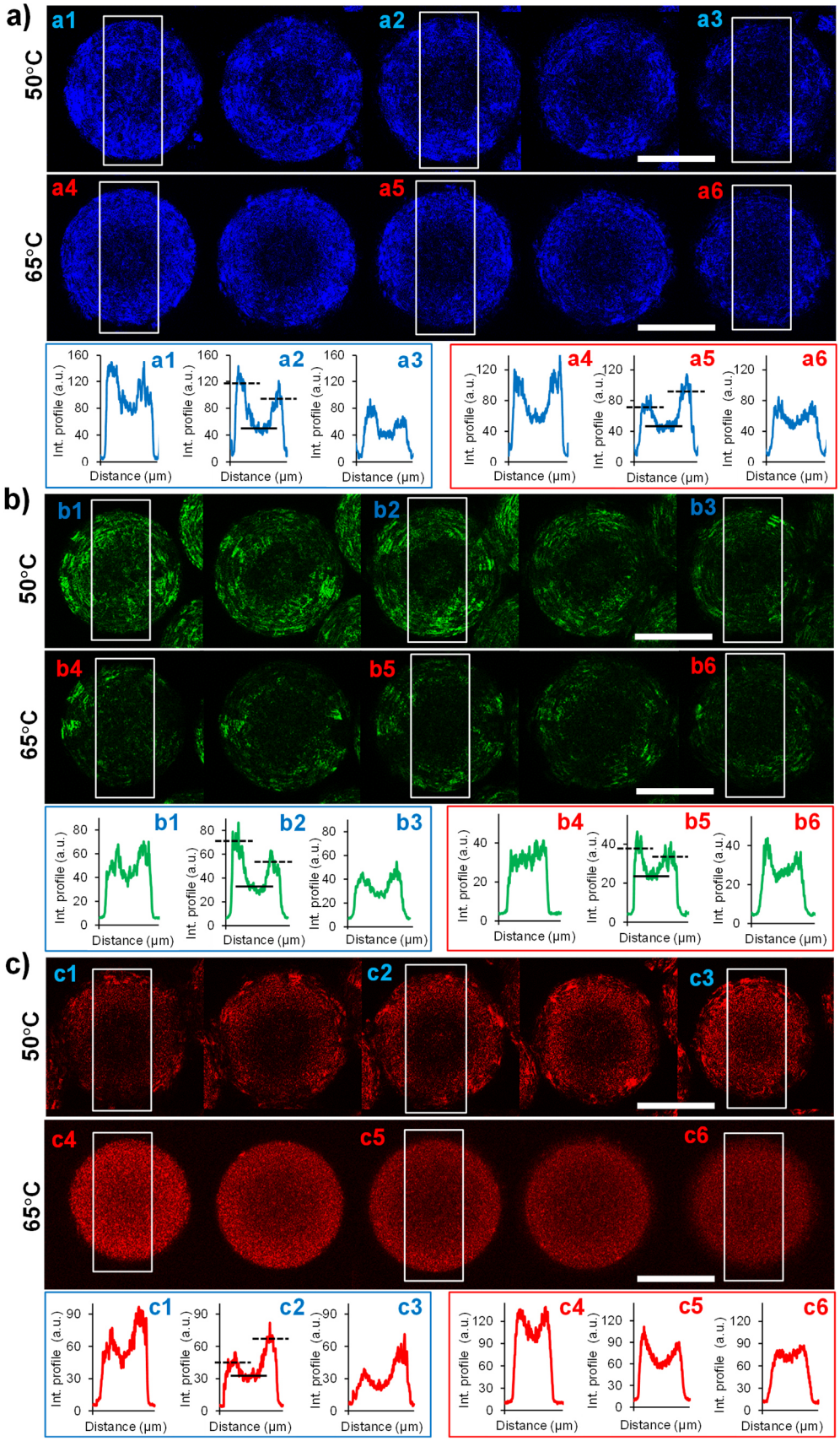

Figure 6.7: RCM images of **a)** PhP-PNP194; **b)** PhP-PNP232; **c)** PhP-PNP287 illuminated with 458 nm, 514 nm, and 633 nm light respectively, assembled at 50°C and 65°C. Z-depth increases from left to right; distance between slices: 5 μm. Intensity profile plots corresponds to the area denoted by the white rectangles. Scale bar: 25 μm.

Because light is either reflected by the stop-band of the fcc structure or diffusely scattered by the isotropic nature of the amorphous regions, PhP-PNP194 and PhP-PNP232 assembled at 50°C and 65°C, were also imaged by RCM under illumination with 633 nm laser light, to observe the overall disorder inside the structures (Figure A6.12, Appendix 6). The shape and the intensity of the profiles obtained when illuminated with 633 nm light, significantly differs from the ones obtained when imaged with wavelengths falling on the pseudo-PBG, and light attenuation is negligible with depth increase. The higher intensity values are obtained for pigments assembled at 65°C, because of their increased structural disorder.

The brighter patterns observed in the RCM images under illumination with 633 nm light in Figure A6.12 of Appendix 6, show the strong diffuse scattering from the disordered regions. The images show a darker region at supraparticles surface because the ordered layers of PNP do not interact with this wavelength. The brighter regions are located at supraparticles center, identifying a more disordered PNP arrangement, whose diffuse scattering strongly interacts with 633 nm light.

Therefore, combining results from SEM, FIB-SEM and RCM an accurate structural characterization of the PNP packing is obtained, at the length scale corresponding to the entire spherical structure, allowing thus, to probe and correlate the ordered/disordered degrees for the different assembly temperatures with the optical properties of the spherical pigments.

6.4. Optical characterization of spherical photonic pigments

Photonic pseudo-bandgaps (or stop-bands) in ordered structures are fundamentally different from the ones in amorphous counterparts.[43] In amorphous photonic structures, they originate from the short-range order while in crystalline structures they arise from long-range order correlations. As a result, the photonic pseudo-bandgaps that give rise to structural colors by constructive interference of light reflected at the individual crystalline planes of the fcc lattice are direction dependent, leading to iridescent coloration. On the contrary, photonic pseudo-bandgaps in amorphous photonic structures originate non-iridescent structural colors, because light is evenly scattered in all directions (there is no direction discrimination in rcp photonic structures).[44,45] At the same

time, due to the incompatibility of large crystalline order with the spherical symmetry, it is known that the structural color reflected by spherical photonic crystals remains unchanged when the structure is rotated under light illuminating the surface at a fixed incident angle.[13,46] This characteristic arises because the entire surface of the photonic supraparticles has the (111) lattice symmetry of the fcc structure.[24]

Knowing that the structural disorder increases with increasing the assembly temperature, we must evaluate how this affects the optical properties of the spherical photonic pigments. To understand how the crystallinity degree influences the color appearance arising from the photonic pigments and the mechanisms associated with it, we conducted angle resolved reflectance measurements of the pigments assembled at different temperatures. First, we evaluate how the angle of detection (or collecting angle) relative to the angle of incident light affect the reflectance properties of the supraparticles.

Bragg reflections from the (111) planes of the fcc structure at the surface of the photonic pigments were measured at different incident angles relative to surface normal (0°, 45° and 65°) and by both changing incident and collecting angles (Figure 6.8). When white light illuminates the surface at a fixed incident angle (Figure 6.8c), the intensity of the reflectance bands did not change drastically with increasing the collecting angle, whereas the band position slightly shifted towards shorter wavelengths. The shift in the wavelength of maximum reflectance, λ_{max}, with increasing collecting angle for geometry 1 correspond to 50 nm (0° incident angle relative to surface normal; collecting angle varying from 0° to 80°). For geometry 2 the shift correspond to 52 nm (45° incident angle relative to surface normal; collecting angle varying from 0° to 75°) and in the case of geometry 3, the shift correspond to 57 nm (65° incident angle relative to surface normal; reflectance was collected at every ~20° for angles varying from 0° to 85°).

The small shift in λ_{max} with increasing collecting angle (Figure 6.8c), shows the low color dependence on the observation angle.[47,48] This blue shift in λ_{max} is indeed much smaller than the one observed when simultaneously changing incident and collecting angles, which correspond to 92 nm (Figure 6.8b). In this geometry, for incident/collecting angles above 55°, reflectance bands are no longer visible. This data is consistent with the low iridescent properties of the spherical photonic pigments when illuminated under a fixed incident angle.[49]

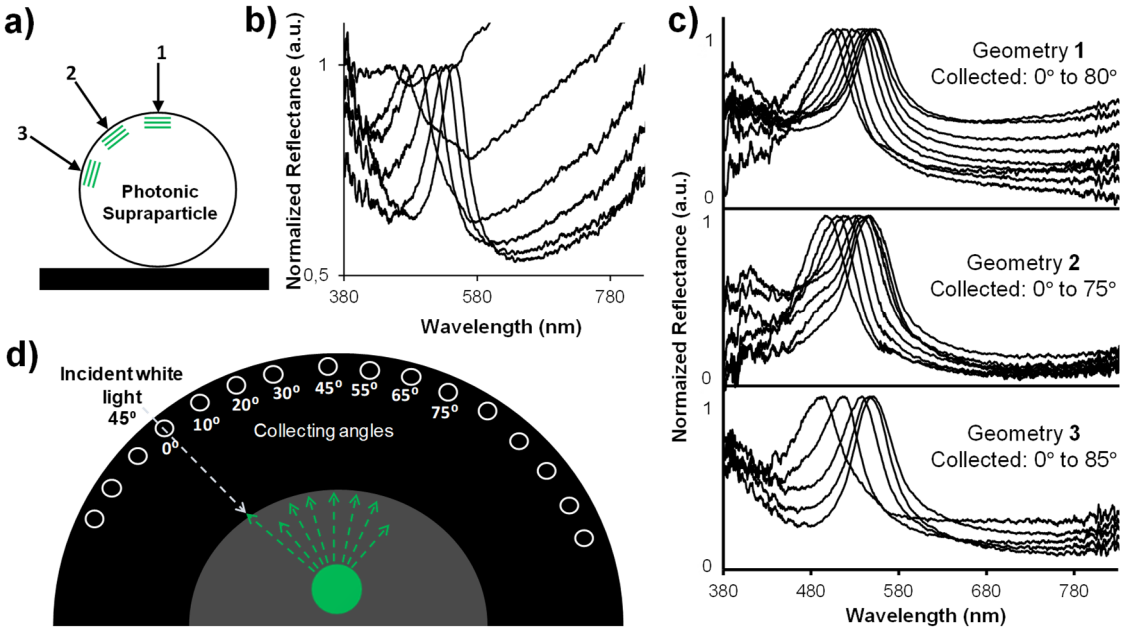

Figure 6.8: Normalized angle resolved reflectance spectra of PhP-PNP232-50°C, for different incident angles of white light. **a)** Schematic representation of the measurement geometries: 1 - 0° incident angle relative to surface normal; 2 - 45° incident angle relative to surface normal; 3 - 65° incident angle relative to surface normal (green lines highlight the (111) planes); **b)** Reflectance spectra under simultaneous change of incident and collecting angle. **c)** Upper panel show reflectance spectra corresponding to geometry 1 in a); middle panel show the reflectance spectra corresponding to geometry 2 in a); lower panel show the reflectance spectra corresponding to geometry 3 in a); **d)** Schematic representation of the multi-angle probe holder depicting incident white light illuminating the sample at 45° (geometry 2). Green arrows illustrate the light reflected from the photonic samples for collecting angles varying from 0° to 75°.

Due to the lower background signal of the reflectance spectra collected under geometry 2 in Figure 6.8c, we performed the optical characterization of the photonic pigments under illumination at 45°. The reflectance spectra of the different photonic pigments at the backscattering angle (0° collecting angle relative to incident light at 45°), for the different assembly temperatures are shown in Figure 6.9 (color coding relates to the colors reflected by the photonic pigments).

Reflectance bands responsible for the colors observed for the different photonic pigments at the backscattering position, cover the entire visible range increasing from 400 nm to 800 nm, with increasing PNP diameter from 173 nm to 331 nm (Figure 6.9). Photonic pigments assembled at 50°C exhibits narrower and sharper reflectance bands due to the more perfectly packed PNP at pigments surfaces and also due to the increased number of ordered PNP layers towards

supraparticles interior.[50] Results for the other collecting angles are summarized in Figures A6.13-A6.15 in Appendix 6.

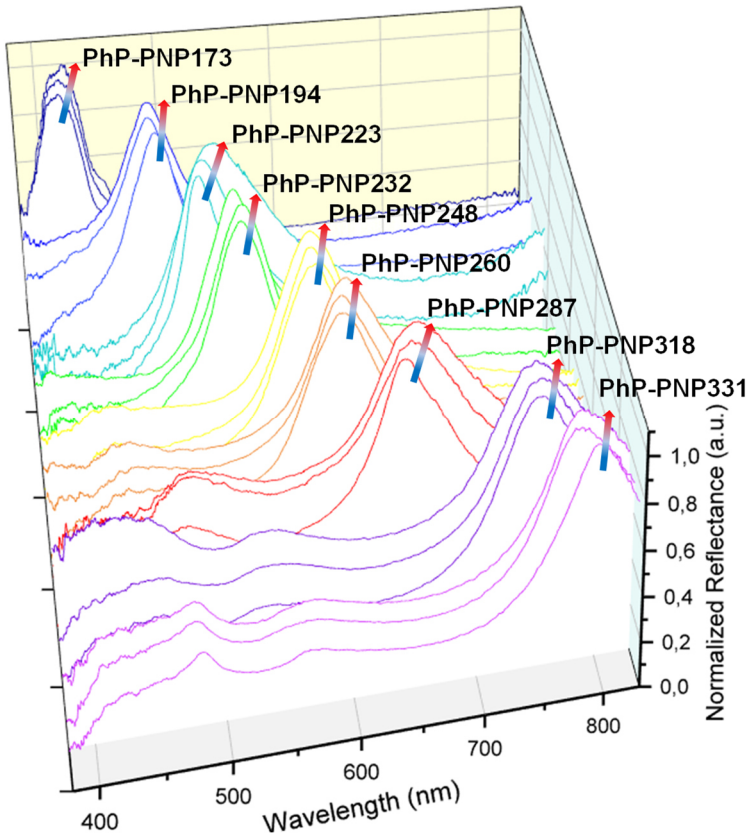

Figure 6.9: Compilation of normalized reflectance spectra of all photonic pigments at the backscattering angle (0° relative to incidence), for the different assembly temperatures. Photonic pigments assembled from PNP with diameters ranging from 173 nm to 331 nm, reflect colors that cover the entire visible light range, exhibiting different reflectance properties within the same photonic samples. The colored arrow indicates the spectra towards the direction of temperature increase: blue, gray, and red corresponds to 50°C, 60°C and 65°C, respectively. As the assembly temperature increases reflectance bands broadens and slightly shift towards longer wavelengths.

The fact that the sharper and more intense reflectance bands occur at the backscattering angle indicates that the incident light is less scattered in the specular direction, while being more backscattered. Because coloration in the specular direction can become unsaturated for larger incident angles,[51] backscattering is a desirable characteristic for photonic pigments.

The iridescence degree of the reflected colors expressed as the shift in the wavelength of maximum reflectance for collecting angles varying from 0° to 75°, can be observed in Figure 6.10.

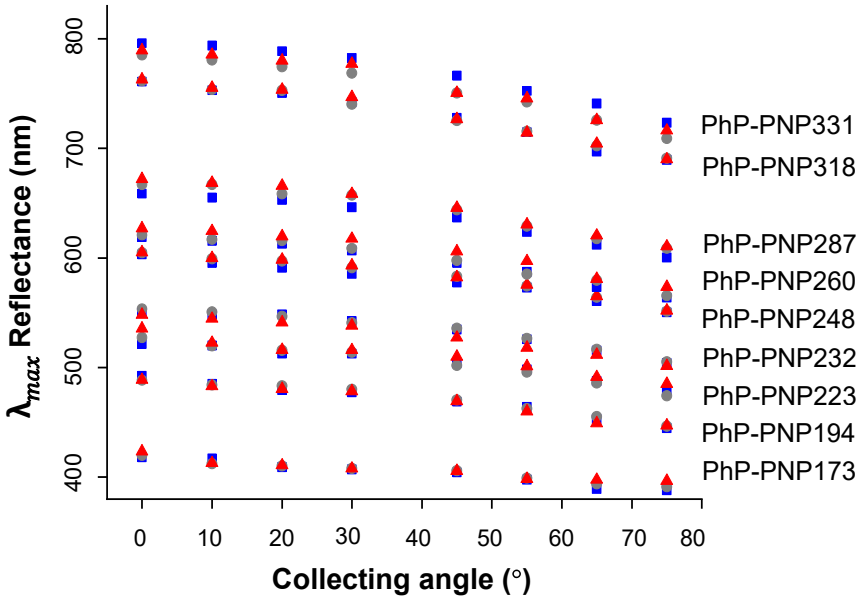

Figure 6.10: Shift in the wavelength of maximum reflectance with increasing collecting angle from 0° to 75°, for pigments assembled at different temperatures (blue squares: 50°C; grey dots: 60°C; red triangles: 65°C). The iridescence degree shows no dependence on the assembly temperature.

Although slightly larger shifts are observed for pigments reflecting colors with longer wavelengths (composed of larger PNP) in comparison to blue or green pigments, the iridescence degree does not show significant differences with increasing the assembly temperature. Irrespective of the PNP arrangement inside the supraparticles (Figure 6.10), the pigments display orientation-independent structural colors for the different assembly temperatures.

In addition to the reflectance bands from the (111) planes of the fcc lattice in Figure 6.9, the reflectance spectra of all photonic pigments have a background component across the entire visible region that gradually increases with increasing PNP diameter and assembly temperature. This background component is due to diffusely scattered light from the structural disorder and largely affects the color perception because all three cone cells in the retina of the human eye respond to light.[52] The presence of a higher amount of defects increases the diffuse scattering, that contributes to a less saturated color.[53,54]

For photonic pigments composed of PNP with diameter ≥ 248 nm, a small reflectance band is visible in the blue part of the spectrum (Figure 6.9 and Figures A6.14-A6.15, Appendix 6). Intriguingly, this low intensity band responsible for the high reflectivity at small wavelengths only appear for angles near backscattering (from 0° to 30° collecting angles) and not over all angles. Figure 6.11 exemplifies

this behavior for PhP-PNP331. This band is attributed to single-particle scattering resonances (constructive interference of light inside the PNP), which imprint a faint whitening into the reflected colors above or equal to 600 nm, and could therefore compromise red hues by color mixing.[55,56] With increasing the collecting angle from 0° to 30° the intensity of this reflectance band decreases and shifts towards red wavelengths (Figure 6.11). For blue, cyan and green photonic pigments, these single-particle scattering resonances do not affect our perception of the reflected colors because they occur in the UV region.[44]

For PhP-PNP318 and PhP-PNP331, another (low in intensity) sharp reflectance band, appears in the blue wavelength range, around 460-490 nm (Figure 6.11). This band exhibits the typical fingerprint of opalescent samples: the wavelength of maximum reflectance shifts towards the blue as the angle between incidence and observation increases. This band correspond to the second order reflectance planes from the fcc structure and appears at approximately half the wavelength of the first order reflectance band (originated from the (111) planes).[50,57,58]

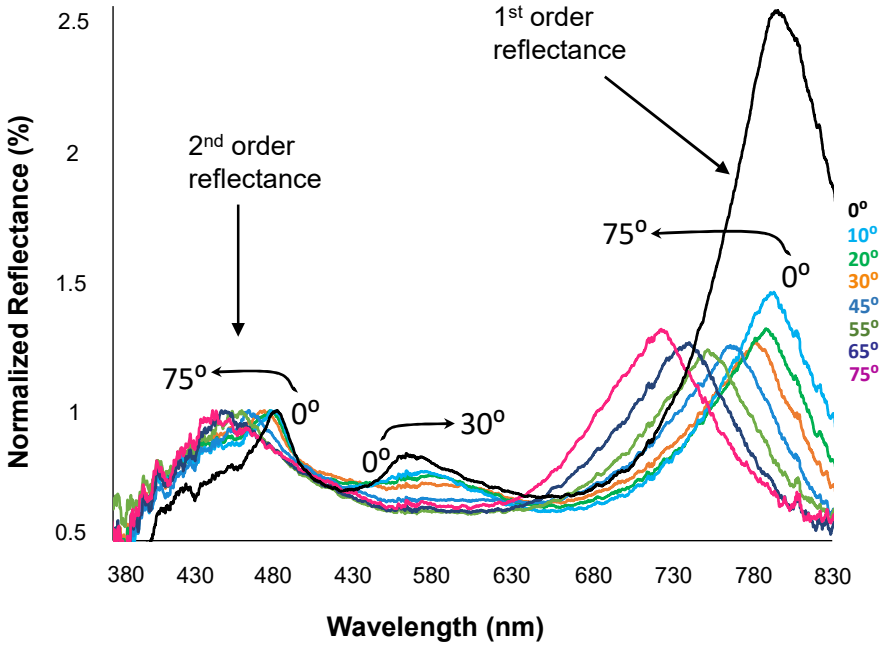

Figure 6.11: Angle resolved reflectance of PhP-PNP331-50°C, normalized to the second order reflectance band. This low intensity but sharp band appears at approximately 483 nm for the backscattering angle, and shift towards shorter wavelengths (443 nm) with increasing the collecting angle from 0° to 75°. Between the 2nd and the 1st order reflectance bands, another low intensity band associated with single-particle scattering resonances appears at 564 nm for the backscattering angle. This band slightly red shift to 579 nm with increasing the collecting angle to 30° and cease to exist for higher collecting angles.

The observation of multiple diffraction bands gives an indication of the quality of the structures prepared.[59] If the scattering background becomes too pronounced with increasing the assembly temperature, it obscure the presence of multiple diffraction bands due to the high structural disorder.

6.4.1. Scattering ratio

The color saturation of the pigments obtained at the different assembly temperatures can be quantified by the scattering ratio. This is obtained by dividing the intensity reflected at the wavelength of maximum reflectance (I_{max}) by the intensity of the scattering background ($I_{background}$). The latter is obtained by averaging the scattering background intensities at short wavelengths (420–435 nm) and at long wavelengths (between 550-800 nm, depending on λ_{max} for each pigment). The lower the ratio value, the more whitish the color appears.[46,60] With increasing PNP diameter and assembly temperature, colors with lower saturation are reflected from the photonic pigments(Figure 6.12).

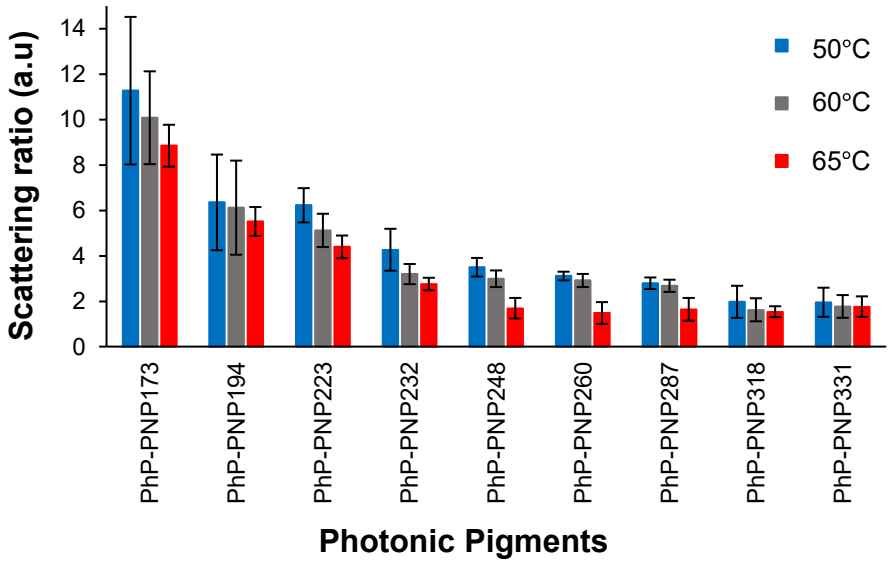

Figure 6.12: Average scattering ratio ($I_{max}/I_{background}$) for photonic pigments assembled at different temperatures (blue: 50°C; gray: 60°C; red: 65°C). The colored columns represent the average value obtained from the reflectance spectra at the different collecting angles for each assembly temperature. The error bars correspond to the average standard deviation of the scattering ratio for collecting angles varying from 0° to 75°.

The scattering ratio decreases gradually as the reflected colors approaches the red part of the visible spectrum, due to the color mixing of the reflectance bands. Furthermore, lower scattering ratios are also obtained for pigments assembled at

higher temperatures, indicating a lower color saturation. This decrease in color saturation with increasing the assembly temperature is due to the increased diffuse scattering across the entire visible region from the more disordered structures.[46,60]

Despite the lower color saturation of photonic pigments assembled at 65°C, the small error bars in Figure 6.12, that correspond to the average standard deviation of the scattering ratio from 0° to 75° collecting angles, are indicative of isotropic structures whose reflectance properties are more uniform and less angle-dependent.

6.4.2. Gap to midgap ratio

The broader reflectance bands also indicate a strong color desaturation. The spectral bandwidth of the reflectance band from the (111) planes of the fcc structure broadens for pigments composed of larger PNP, and for higher assembly temperatures (Figure 6.9). The bandwidth of the reflectance bands was used to estimate the gap to midgap ratios, that gives a measure of the relative width of the pseudo-PBG (or stop-band) for the photonic pigments.[61-63] The width of the pseudo-PBG at the backscattering angle for the photonic pigments assembled at different temperatures was obtained by the ratio of $\Delta\lambda/\lambda_{max}$, where $\Delta\lambda$ corresponds to the full width at half maximum (FWHM) of the reflectance band, and λ_{max} represents the wavelength of maximum reflectance (Figure 6.13).

The gap to midgap ratio of the photonic pigments increases with increasing the assembly temperature and is bigger than 10% for all samples, which is much larger than the value of 4.9%[64] theoretically predicted for the (111) planes of a flat fcc crystal (represented by the dashed line in Figure 6.13). This difference results from the imperfect arrangement of PNP in the spherical confinement and increases for higher assembly temperatures due to the limited number of crystalline layers and overall structural disorder increase.

The broader widths of the reflectance bands from supraparticles assembled at 65°C results in higher gap to midgap ratios, an optical property characteristic of colloidal amorphous structures. These results highlight the trade-off in optical performance between more crystalline or more isotropic spherical structures.

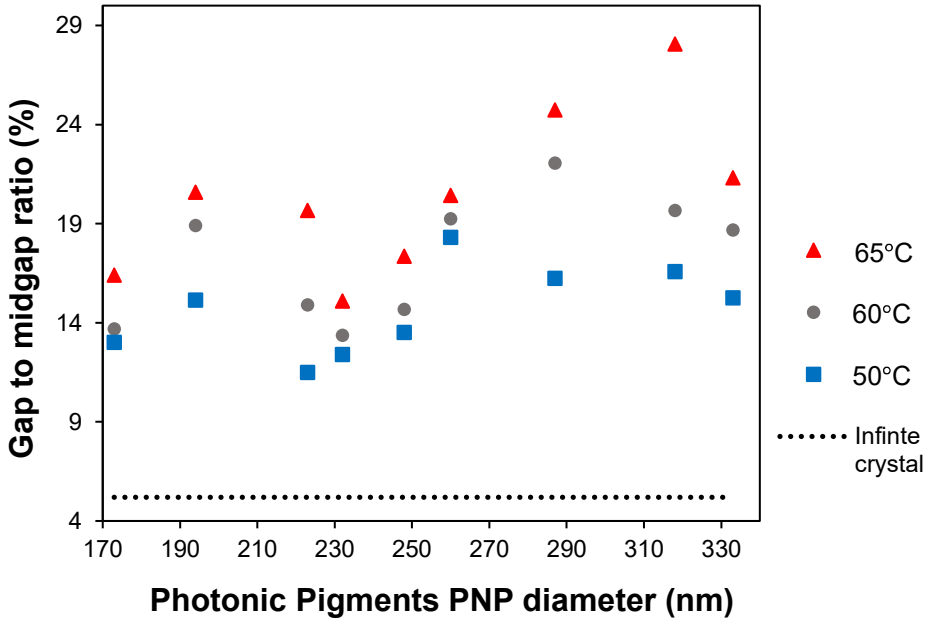

Figure 6.13: Gap to midgap ratio of the photonic pigments illustrating the width of the pseudo-PBG for the different assembly temperatures, at the backscattering angle. The dashed line represents the expected result for a perfectly ordered and flat colloidal crystal.

6.4.3. Experimental determination of PNP volume fraction in the spherical pigments

A theoretical approximation for the predicted wavelengths reflected from the spherical pigments at a fixed angle of incident light was obtained using the Bragg−Snel's law (equation 6.1), considering a fcc structure of packed PNP (0.74 volume fraction). The relation between the PNP diameter (D) and the spacing between the (111) planes is given by equation 6.4:[65,66]

$$d_{111} = \sqrt{\frac{2}{3}} \times D \tag{6.4}$$

The effective refractive index, n_{eff}, can be calculated from the volume fractions of PNP and interstices (filled with air or any solvent), and is given by equation 6.5:

$$n_{eff}^2 = \emptyset_{PNP} n_{PNP}^2 + (1 - \emptyset_{PNP}) n_{int}^2 \tag{6.5}$$

where $\emptyset_{PNP}$ and n_{PNP} corresponds to the volume fraction and refractive index of the PNP inside the photonic structures, respectively, and n_{int} correspond to the refractive index of the material filling the interstices.

The refractive index of the PNP was calculated by averaging the volume occupied by their components, considering the refractive indices of polystyrene ($n_{PS} = 1.592$), poly(methyl methacrylate) ($n_{PMMA} = 1.473$) and poly(acrylic acid) ($n_{PAA} = 1.527$), according to equation 6.6:

$$n_{PNP} \approx 0.87 \times n_{PS} + 0.05 \times n_{PMMA} + 0.08 \times n_{PAA} \approx 1.581 \qquad (6.6)$$

When comparing the experimentally measured wavelengths of maximum reflectance for each photonic pigment at the different collecting angles, with those predicted for a perfect fcc structure according to equation 6.1, we corroborate the low angular dependence of the spherical photonic pigments when compared to highly ordered flat colloidal photonic crystals (Figure 6.14).

The shift in the wavelength of maximum reflectance of the spherical photonic pigments, represented by the red dots in Figure 6.14, is 2.5 times smaller than what would be expected for a flat crystalline sample (black lines) according to equations 6.1, 6.4 and 6.5.

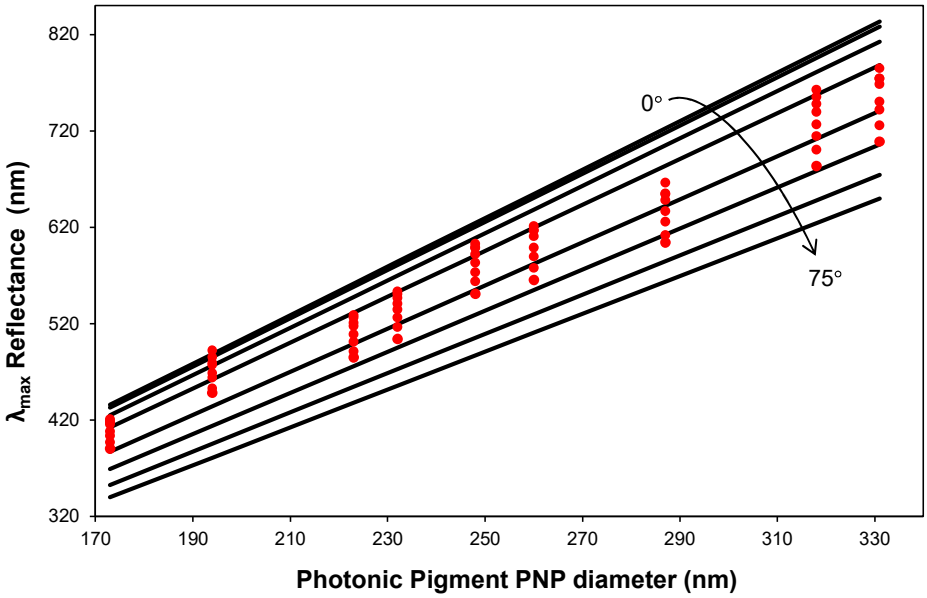

Figure 6.14: Experimental (red dots) *vs* predicted (black lines) wavelengths of maximum reflectance with increasing the collecting angle from 0° to 75° (denoted by the black arrow) for photonic pigments assembled at 50°C. It is evident that the spherical templating originates structures reflecting wavelengths with lower angular dependence.

An approximate value of the volume fraction of PNP inside the supraparticles can be obtained from the effective refractive index of the photonic structures, according to equation 6.5. The effective refractive index, n_{eff}, was experimentally predicted for the green supraparticles (PhP-PNP232-50°C) by plotting the square

of the wavelength diffracted from the (111) planes versus $sin^2\theta$ according to equations 6.7 and 6.8 (using the data collected at the different incident angles in Figure 6.8b):[45,65,66]

$$\lambda_{111} \approx 1.633D \left(n_{eff}^2 - sin^2\theta\right)^{\frac{1}{2}} \quad (6.7)$$

$$\lambda_{111}^2 \approx (1.633D)^2 \left(n_{eff}^2 - sin^2\theta\right) \quad (6.8)$$

From the linear interpretation in Figure 6.15a, one can obtain the PNP diameter, $D = 226\ nm$, and the effective refractive index of the supraparticle, $n_{eff} = 1.496$. To estimate an average value for the PNP volume fraction inside the supraparticles for each assembly temperature, we plot the wavelength of maximum reflectance from the (111) planes at the backscattering angle ($\theta = 0°$) versus the PNP diameter according to equation 6.9:

$$\lambda_{111} \approx 1.633D\ n_{eff} \quad (6.9)$$

The average value of n_{eff} is given by the slope of the linear graph in Figure 6.15b, n_{eff} (50°C) = 1.410; n_{eff} (60°C) = 1.394; and n_{eff} (65°C) = 1.387.

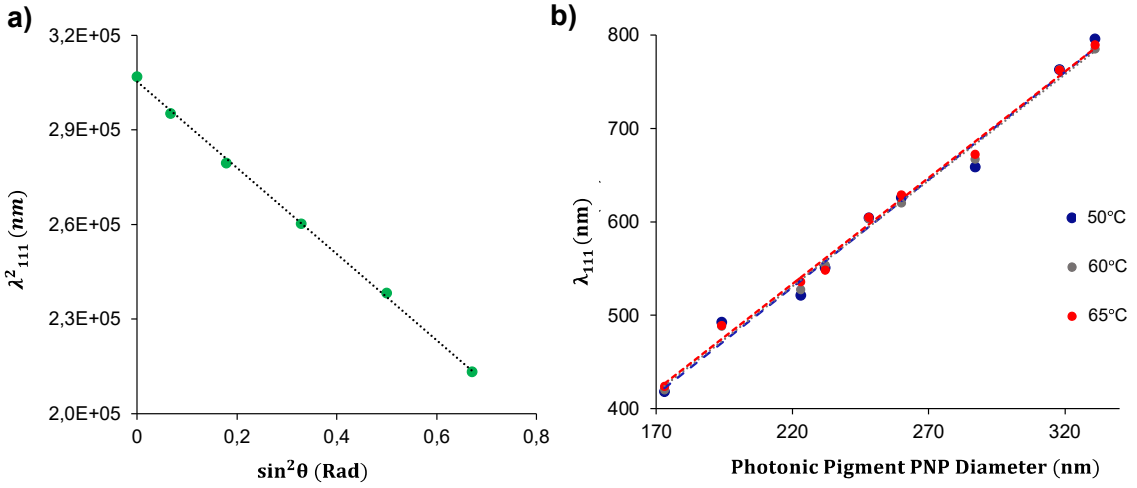

Figure 6.15: a) Plot of λ_{111}^2 versus $sin^2\theta$; λ_{111} is the wavelength diffracted by the (111) planes of green supraparticles assembled at 50°C; θ is the angle between the normal to the sample surface and the incident beam of white light. **b)** Plot of λ_{111} versus PNP diameter; λ_{111} is the wavelength of maximum reflectance at the backscattering angle for the photonic pigments assembled at different temperatures.

From the n_{eff} values, the estimated volume fraction of PNP inside the supraparticles assembled at 50°C and 65°C correspond respectively to 0.70 and 0.67, considering air filling the interstices. As expected, the estimated volume fractions of PNP decreases with increasing the assembly temperature due to the

more disordered arrangement of PNP. Although these values are approximate, they are consistent with the slightly larger diameter of supraparticles assembled at 65°C and are commensurate with a more random close-packing of PNP for higher assembly temperatures. For a more accurate determination of the effective refractive index from the reflectance data for each photonic pigment assembled at the different temperatures, the structures should be illuminated at different incident angles.[66]

6.5. Reflectance microscopy images

Reflectance microscopy images for photonic pigments assembled at 50°C, 60°C and 65°C are shown in Figure 6.16. When assembled at 65°C, crystallization is suppressed by the fast concentration of PNP, thus resulting in disordered structures with an amorphous PNP arrangement, especially towards the supraparticles center, where a more uniform and isotropic color is observed in comparison with the thin sparkling color ring closer to supraparticles surface.

On the other hand, pigments assembled at 50°C, exhibit colored patches that spreads from the surface to the center of the supraparticles, indicating the large dimensions of the different crystalline domains that satisfies the Bragg condition under the experimental conditions (Figure 6.16). The size of the color patches visible in reflection microscopy images, is reduced as the assembly temperature increases, which is consistent with a lower degree of crystallization.[67,68]

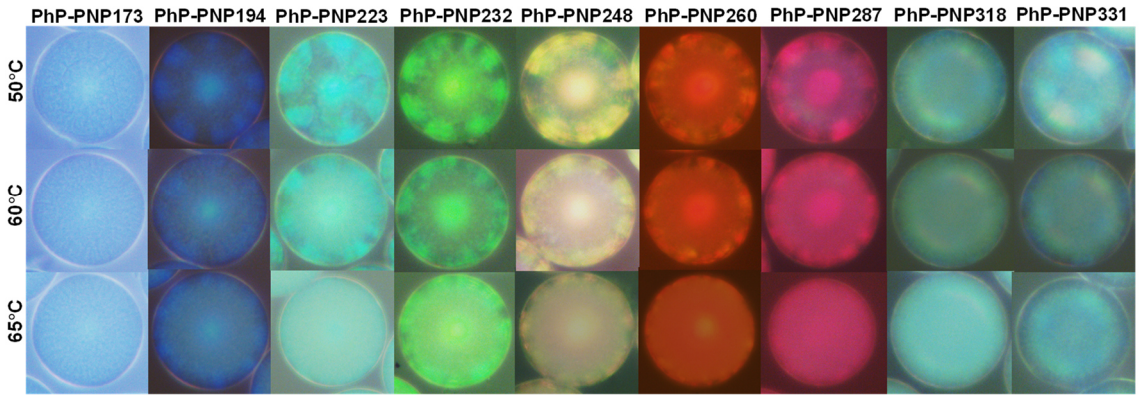

Figure 6.16: Reflectance microscopy images of photonic pigments assembled at different temperatures, showing their structural colors. Upper panel: 50°C; middle panel: 60°C; lower panel: 65°C. The more amorphous pigments assembled at higher temperature show colors that are more uniform across the entire pigment, whereas the more crystalline pigments, obtained at lower temperatures, show brighter colored patches across the entire supraparticle.

Interestingly, the color patterns of PhP-PNP318 and PhP-PNP331 in Figure 6.16 differ substantially from the ones exhibited by their analogs composed of PNP with smaller diameters. They display rainbow-like colored patterns that are assigned to grating diffraction at the supraparticles surface.[14,68-70] The highly ordered, close-packed arrangement of PNP318 and PNP331 at the pigments surface is responsible for this bright, multichromatic colored optical effect, that becomes less evident with increasing the assembly temperature, due to the higher degree of defects at the supraparticles surface (see SEM images in Figure A6.6 of Appendix 6).

6.6. CIE color maps

To quantify the differences in the perceived color by the human eye, color coordinates were calculated for photonic pigments assembled at different temperatures. Reflectance spectra at the backscattering angle, was converted to x, y color coordinates according to the Commission Internationale de l'Éclairage (CIE).

The CIE color space of Figure 6.17 show brightly colored pigments exhibiting saturated colors, when assembled at 50°C. With increasing the assembly temperature, color coordinates shift towards less saturated colors (closer to the white point at $(x, y) = (0.33; 0.33)$), due to the increase in diffuse scattering background across the entire visible region. This component, that increases with increasing the assembly temperature and PNP diameter, largely affects the perceived colors.[52] To obtain more saturated colors for higher assembly temperatures, diffuse scattering should be reduced.

To visualize the differences in the perceived colors reflected for the different collecting angles, we compare the iridescence properties of PhP-PNP223 assembled at 50°C (highly ordered) and 65°C (more disordered). The color map in Figure A6.16 of Appendix 6 show the low iridescence properties of the spherical photonic structures regardless of assembly temperature, because the perceived colors do not change drastically with increasing the viewing angle. However, despite the lower color saturation, the shift in the perceived hues is smaller for the more disordered pigments, as expected. A local and spatially isotropic structural correlation reflect structural colors with lower variation with the collecting angle.

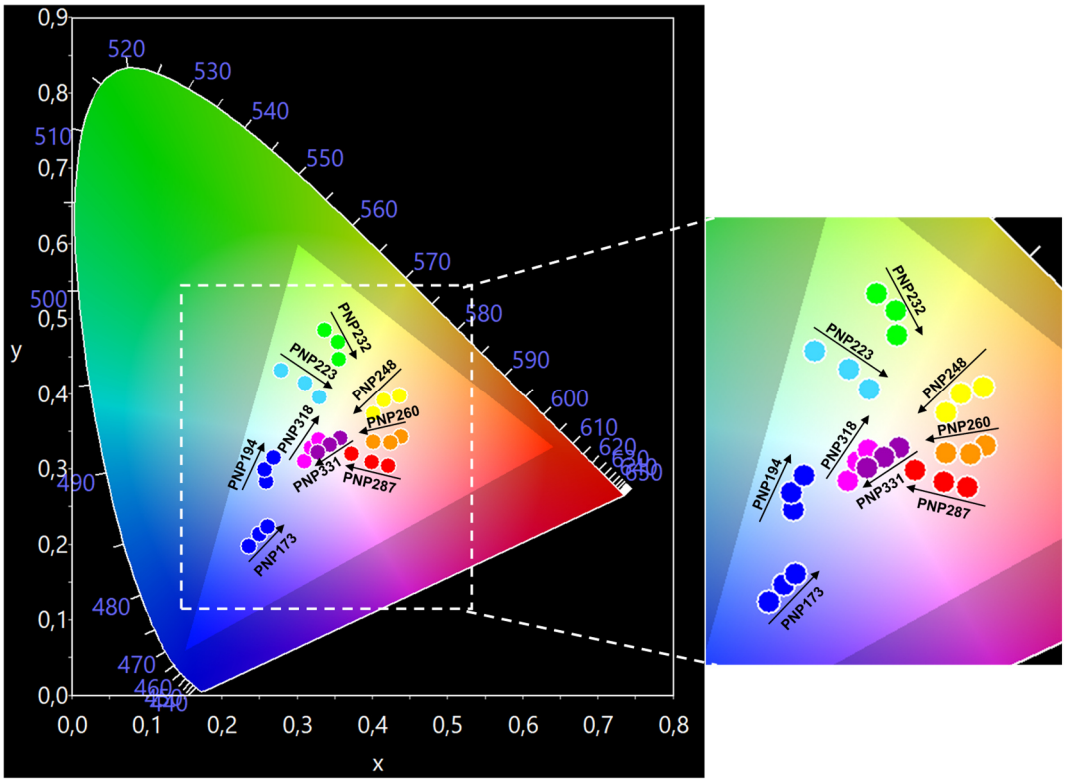

Figure 6.17: CIE x, y chromaticity diagram labeled with the limits of the RGB color gamut. Colored dots represent the color coordinates for the different photonic pigments (at 0° collecting angle). Black arrows direction indicates temperature increase from 50°C, to 60°C and 65°C. With increasing the assembly temperature, the reflected colors move towards the white point ($x = 0.33$; $y = 0.33$), especially for photonic pigments composed of larger PNP. Different color saturation is obtained for the different hues.

Non-iridescent structurally colored pigments exhibiting wide viewing angles with different hues and saturation, were manipulated just by altering the rate of water evaporation. Therefore, by using this strategy, we successfully and simultaneously controlled the optical and structural features of the prepared spherical photonic pigments, providing new opportunities for obtaining structurally colored pigments for different applications, with precise control over reflectance properties.

6.7. Conclusions

The structural colors exhibited by the spherical photonic pigments can be controlled kinetically by changing the rate of water evaporation, determined by the temperature at which PNP are assembled. These results show that by tuning the PNP diameter and the assembly temperature, dispersible structural pigments with low-iridescent colors covering the entire visible light range are obtained, with different hues and saturation.

The decrease in color saturation observed for pigments composed of larger PNP at higher assembly temperatures, is not only due to the lower scattering ratios, but is also affected by the broadening of the reflectance bands, which combined compromise the perceived hues. Although less saturated, the pigments assembled at higher temperatures display more isotropic colors, due to the higher degree of internal disorder.

The results obtained from the reflectance data analysis are corroborated by SEM and RCM characterization of the PNP arrangement at the surface and inner structure of the photonic supraparticles. All tools combined, this proved to be a powerful strategy to probe the internal packing of PNP and correlate the structural order with the optical properties at a length scale corresponding to the entire spherical structure of the photonic pigments.

We demonstrated that with increasing the assembly temperature, a simple, yet efficient strategy to obtain different color saturations from photonic pigments reflecting all visible colors, it is possible to obtain a palette of structural colors that holds a promise for a wide range of bright and colorful applications.

6.8. References

1. Joannopoulos, J. D., Villeneuve, P. R. & Fan, S. Photonic crystals: putting a new twist on light. *Nature* **386**, 143–149 (1997).
2. Galisteo-Lopez, J. F., Palacios-Lidon, E., Castillo-Martınez, E. & Lopez, C. Optical study of the pseudogap in thickness and orientation controlled artificial opals. *Phys. Rev. B* **68**, 115109 (2003).
3. Joannopoulos, J. D., Johnson, S. G., Winn, J. N. & Meade, R. D. *Photonic Crystals: Molding the Flow of Light. Second Edition, Princeton University Press.* (2008).
4. Xia, B. Y., Gates, B. & Li, Z. Self-Assembly Approaches to Three-Dimensional Photonic Crystals. *Adv. Mater.* **13**, 409–413 (2001).
5. Darragh, P. J., Gaskin, A. J., Terrell, B. C. & Sanders, J. V. Origin of precious opals. *Nature* **209**, 13–16 (1966).
6. Lai, C. & Li, J. Self-assembly of colloidal Poly (St-MMA-AA) core/shell photonic crystals with tunable structural colors of the full visible spectrum. *Opt. Mater.* **88**, 128–133 (2019).
7. Goerlitzer, E. S. A., Taylor, R. N. K. & Vogel, N. Bioinspired Photonic Pigments from Colloidal Self-Assembly. *Adv. Mater.* **30**, 1706654 (2018).
8. Dumanli, G. A. & Savin, T. Recent advances in the biomimicry of structural colours. *Chem. Soc. Rev.* **45**, 6698–6724 (2016).

9. Meng, Z., Wu, S., Tang, B., Ma, W. & Zhang, S. Structurally colored polymer films with narrow stop band, high angle-dependence and good mechanical robustness for trademark anticounterfeiting. *Nanoscale* **10**, 14755–14762 (2018).

10. Pan, M., Wang, L., Dou, S., Zhao, J., Xu, H., Wang, B., Zhang, L., Li, X., Pan, L. & Li, Y. Recent Advances in Colloidal Photonic Crystal-Based Anti-counterfeiting materials. *Crystals* **9**, 417 (2019).

11. Hou, J., Li, M. & Song, Y. Patterned Colloidal Photonic Crystals. *Angew. Chem. Int. Ed.* **57**, 2544–2553 (2018).

12. Topçu, G., Tugrul, G. & Demir, M. M. Non-iridescent structural colors from uniform-sized SiO_2 colloids. *Photonics Nanostructures – Fundam. Appl.* **29**, 22–29 (2018).

13. Zhao, Y., Shang, L., Cheng, Y. & Gu, Z. Spherical Colloidal Photonic Crystals. *Acc. Chem. Res.* **47**, 3632–3642 (2014).

14. Vogel, N., Utech, S., England, G. T., Shirman, T., Phillips, K. R., Koay, N., Burgessd, I. B., Kolle, M., Weitz, D. A. & Aizenberg, J. Color from hierarchy: Diverse optical properties of micron-sized spherical colloidal assemblies. *PNAS* **112**, 10845-10850 (2015).

15. Wiersma, D. S. Disordered photonics. *Nat. Photonics* **7**, 188–196 (2013).

16. Wang, J. & Zhu, J. Recent advances in spherical photonic crystals: Generation and applications in optics. *Eur. Polym. J.* **49**, 3420–3433 (2013).

17. Choi, T. M., Je, K., Park, J.-G., Lee, G. H. & Kim, S.-H. Photonic Capsule Sensors with Built-In Colloidal Crystallites. *Adv. Mater.* **30**, 1803387 (2018).

18. Henderson, S. I., Mortensen, T. C., Underwood, S. M. & Megen, W. van. Effect of particle size distribution on crystallisation and the glass transition of hard sphere colloids. *Physica A* **233**, 102–116 (1996).

19. Sowade, E., Blaudeck, T. & Baumann, R. R. Self-Assembly of Spherical Colloidal Photonic Crystals inside Inkjet-Printed Droplets. *Cryst. Growth Des.* **16**, 1017–1026 (2016).

20. Pusey, P. N., Zaccarelli, E., Valeriani, C., Sanz, E., Poon, W. C. K. & Cates, M. E. Hard spheres: crystallization and glass formation. *Phil. Trans. R. Soc. A* **367**, 4993–5011 (2009).

21. Taylor, P., Monovoukas, Y. & Gast, A. P. Microstructure identification during crystallization of charged colloidal suspensions. *Phase Transitions A Multinatl. J.* **21**, 183–195 (1990).

22. Fijneman, A. J., Högblom, J., Palmlöf, M., With, G. D., Persson, M. & Friedrich, H. Multiscale Colloidal Assembly of Silica Nanoparticles into Microspheres with Tunable Mesopores. *Adv. Funct. Mater.* **30**, 2002725 (2020).

23. Sun, C., Zhao, X., Zhao, Y., Zhu, R. & Gu, Z. Fabrication of Colloidal Crystal Beads by a Drop-Breaking Technique and Their Application as Bioassays. *Small* **4**, 592–596 (2008).

24. Nijs, B. D., Dussi, S., Smallenburg, F., Meeldijk, J. D., Groenendijk, D. J., Filion, L., Imhof, A., Blaaderen, A. V. & Dijkstra, M. Entropy-driven formation of large icosahedral colloidal clusters by spherical confinement. *Nat. Mater.* **14**, 56–60 (2015).

25. Wang, J., Mbah, C. F., Przybilla, T., Zubiri, B. A., Spiecker, E., Engel, M. & Vogel, N. Magic number colloidal clusters as minimum free energy structures. *Nat. Commun.* **9**, 5259 (2018).

26. Choi, T. M., Park, J., Kim, Y., Manoharan, V. N. & Kim, S. Osmotic-Pressure-Mediated Control of Structural Colors of Photonic Capsules. *Chem. Mater.* **27**, 1014–1020 (2015).

27. Kim, S., Jeon, S. & Yang, S. Optofluidic Encapsulation of Crystalline Colloidal Arrays into Spherical Membrane. *J. Am. Chem. Soc.* **130**, 6040–6046 (2008).

28. Kim, S., Park, J., Choi, T. M., Manoharan, V. N. & Weitz, D. A. Osmotic-pressure-controlled concentration of colloidal particles in thin-shelled capsules. *Nat. Commun.* **5**, 3068 (2014).

29. Hunter, G. L. & Weeks, E. R. The Physics of the Colloidal Glass Transition. *Reports Prog. Phys.* **75**, 066501 (2012).

30. Míguez, H., Yang, S. M. & Ozin, G. A. Optical Properties of Colloidal Photonic Crystals Confined in Rectangular Microchannels. *Langmuir* **19**, 3479–3485 (2003).

31. Shi, L., Zhang, Y., Dong, B., Zhan, T., Liu, X. & Zi, J. Amorphous Photonic Crystals with Only Short-Range Order. *Adv. Mater.* **25**, 5314–5320 (2013).

32. García, P. D., Sapienza, R., Blanco, Á. & López, C. Photonic Glass: A Novel Random Material for Light. *Adv. Mater.* **19**, 2597–2602 (2007).

33. Harun-Ur-Rashid, M., Imran, B., Seki, T., Ishii, M., Nakamura, H. & Yukikazu T. Angle-Independent Structural Color in Colloidal Amorphous Arrays. *Chem.Phys.Chem.* **11**, 579–583 (2010).

34. Bausch, A. R., Bowick, M. J., Cacciuto, A., Dinsmore, A. D., Hsu, M. F., Nelson, D. R., Nikolaides, M. G., Travesset, A. & Weitz, D. A. Grain Boundary Scars and Spherical Crystallography. *Science* **299**, 1716–1718 (2003).

35. Bai, L., Mai, V. C., Lim, Y., Hou, S., Möhwald, H. & Duan, H. Large-Scale Noniridescent Structural Color Printing Enabled by Infiltration-Driven Nonequilibrium Colloidal Assembly. *Adv. Mater.* **30**, 1705667 (2018).

36. Garcia, P. D., Sapienza, R. & López, C. Photonic Glasses: A Step Beyond White Paint. *Adv. Mater.* **22**, 12–19 (2010).

37. Marín, Á. G., Gelderblom, H., Susarrey-Arce, A., Houselt, A. V., Lefferts, L., Gardeniers, J. G. E., Lohse, D. & Snoeijer, J. H. Building microscopic soccer balls with evaporating colloidal fakir drops. *PNAS* **109**, 16455–16458 (2012).

38. Meng, G., Paulose, J., Nelson, D. R. & Manoharan, V. N. Elastic Instability of a Crystal Growing on a Curved Surface. *Science* **343**, 634–637 (2014).

39. Mazur, S., Beckerbauer, R. & Buckholz, J. Particle Size Limits for Sintering Polymer Colloids without Viscous Flow. *Langmuir* **13**, 4287–4294 (1997).

40. Magkiriadou, S., Park, J., Kim, Y. & Manoharan, V. N. Disordered packings of core-shell particles with angle-independent structural colors. *Opt. Mater. Express* **2**, 1343–1352 (2012).

41. Jacques, S. L. Confocal Laser Scanning Microscopy Using Scattering as the Contrast Mechanism. in *Handbook of Coherent-Domain Optical Methods*, 1157–1171 (2013).

42. Samatham, R., Jacques, S. L. & Campagnola, P. Optical properties of mutant versus wild-type mouse skin measured by reflectance-mode confocal scanning laser microscopy (rCSLM). *J. Biomed. Opt.* **13**, 1–7 (2008).

43. Freymann, G. von, Kitaev, V., Lotsch, B. V. & Ozin, G. A. Bottom-up assembly of photonic crystals. *Chem Soc Rev.* **42**, 2528–2554 (2013).

44. Dong, B. Q., Liu, X. H., Zhan, T. R., Jiang, L. P., Yin, H. W., Liu, F. & Zi, J. Structural coloration and photonic pseudogap in natural random close-packing photonic structures. *Opt. Express* **18**, 14430–14438 (2010).

45. Saranathan, V., Forster, J. D., Noh, H., Liew, S.-F., Mochrie, S. G. J., Cao, H., Dufresne, E. R. & Prum, R. O. Structure and optical function of amorphous photonic nanostructures from avian feather barbs: a comparative small angle X-ray scattering (SAXS) analysis of 230 bird species. *J. R. Soc. Interface* **9**, 2563–2580 (2012).

46. Park, J.-G., Kim, S.-H., Magkiriadou, S., Choi, T. M., Kim, Y.-S. & Manoharan, V. N. Full-Spectrum Photonic Pigments with Non-iridescent Structural Colors through Colloidal Assembly. *Angew. Chem. Int. Ed.* **53**, 2899–2903 (2014).

47. Teshima, M., Seki, T., Ryuji K., Takeuchi, S., Yoshioka, S. & Takeoka, Y. Preparation of structurally colored, monodisperse spherical assemblies composed of black and white colloidal particles using a micro-flow-focusing device. *J. Mater. Chem. C* **3**, 769–777 (2014).

48. Noh, H., Liew, S.-F., Saranathan, V., Mochrie, S. G. J., Prum, R. O., Dufresne, E. R. & Cao, H. How Noniridescent Colors Are Generated by Quasi-ordered Structures of Bird Feathers. *Adv. Mater.* **22**, 2871–2880 (2010).

49. Zhokhov, A. A., Masalov, V. M., Sukhinina, N. S., Matveev, D. V., Dolganov, P. V., Dolganov, V. K. & Emelchenko, G. A. Photonic crystal microspheres. *Opt. Mater.* **49**, 208–212 (2015).

50. Vinteler, E., Farcău, C. & Astilean, S. Disorder effects in reflectance spectra of colloidal photonic crystals. *Nucl. Instruments Methods Phys. Res. B* **267**, 393–396 (2009).

51. Takeoka, Y., Yoshioka, S., Takano, A., Arai, S., Nueangnoraj, K., Nishihara, H., Teshima, M., Ohtsuka, Y. & Seki, T. Production of Colored Pigments with Amorphous Arrays of Black and White Colloidal Particles. *Angew. Chem.* **125**, 7402–7406 (2013).

52. Roorda, A. & Williams, D. R. The arrangement of the three cone classes in the living human eye. *Nature* **397**, 520–522 (1999).

53. Forster, J. D., Noh, H., Liew, S.-F. Saranathan, V., Schreck, C. F., Yang, L., Park, J.-G., Prum, R. O., Mochrie, S. G. J., Hern, C. S. O., Cao, H. & Dufresne, E. R. Biomimetic Isotropic Nanostructures for Structural Coloration. *Adv. Mater.* **22**, 2939–2944 (2010).

54. Liu, F., Xiu, J., Tang, B., Zhao, D. & Zhang, S. Dynamic monitoring of thermally assisted assembly of colloidal crystals. *J. Mater. Sci.* **52**, 7883–7892 (2017).

55. Magkiriadou, S., Park, J., Kim, Y. & Manoharan, V. N. Absence of red structural color in photonic glasses, bird feathers, and certain beetles. *Phys. Rev. E* **90**, 062302 (2014).

56. Scholz, S. M., Vacassy, R., Dutta, J., Hofmann, H. & Akinc, M. Mie scattering effects from monodispersed ZnS nanospheres. *J. Appl. Phys.* **83**, 7860–7866 (1998).

57. Aguirre, C., Reguera, E. & Stein, A. Colloidal Photonic Crystal Pigments with Low Angle Dependence. *ACS Appl. Mater. Interfaces* **2**, 3257–3262 (2010).

58. Astratov, V. N. Interplay of order and disorder in the optical properties of opal photonic crystals. *Phys. Rev. B* **66**, 165215 (2002).

59. Wostyn, K., Zhao, Y., Yee, B., Clays, K., Persoons, A., Schaetzen, G. D. & Hellemans, L. Optical properties and orientation of arrays of polystyrene spheres deposited using convective self-assembly. *J. Chem. Phys.* **118**, 10752–10757 (2003).

60. Yuan, W., Zhou, N., Shi, L. & Zhang, K. Structural Coloration of Colloidal Fiber by Photonic Band Gap and Resonant Mie Scattering. *ACS Appl. Mater. Interfaces* **7**, 14064–14071 (2015).

61. Colomer, J.-F., Simonis, P., Bay, A., Cloetens, P., Suhonen, H., Rassart, M., Vandenbem, C. & Vigneron, J. P. Photonic polycrystal in the greenish-white scales of the African longhorn beetle Prosopocera lactator (Cerambycidae). *Phys. Rev. E* **85**, 011907 (2012).

62. Cefe López. A little disorder is just right. *Nat. Phys.* **4**, 755–756 (2008).

63. Bertone, J. F., Jiang, P., Hwang, K. S., Mittleman, D. M. & Colvin, V. L. Thickness Dependence of the Optical Properties of Ordered Silica-Air and Air-Polymer Photonic Crystals. *Phys. Rev. Lett.* **83**, 300–303 (1999).

64. Takeoka, Y., Yoshioka, S., Teshima, M., Takano, A., Harun-Ur-Rashid, M. & Seki, T. Structurally Coloured Secondary Particles Composed of Black and White Colloidal Particles. *Sci. Rep.* **3**, 02371 (2013).

65. Mccomb, D. W., Treble, B. M., Smith, C. J., Rue, M. D. La & Johnson, N. P. Synthesis and characterisation of photonic crystals. *J. Mater. Chem.* **11**, 142–148 (2001).

66. Tilley, R. J. D. Colour Due to Diffraction, Chapter 6 in *Colour and the Optical Properties of Materials. Wiley, Second edition* 211–234 (2011).

67. Ohnuki, R., Sakai, M., Takeoka, Y. & Yoshioka, S. Optical Characterization of the Photonic Ball as a Structurally Colored Pigment. *Langmuir* **36**, 5579−5587 (2020).

68. Ohnuki, R., Isoda, S., Sakai, M., Takeoka, Y. & Yoshioka, S. Grating Diffraction or Bragg Diffraction? Coloration Mechanisms of the Photonic Ball. *Adv. Opt. Mater.* **7**, 1900227 (2019).

69. Kim, J. Bin, Lee, S. Y., Lee, J. M. & Kim, S. Designing Structural-Color Patterns Composed of Colloidal Arrays. *ACS Appl. Mater. Interfaces* **11**, 14485–14509 (2019).

70. Rastogi, V., Melle, S., Calderón, O. G., García, A. A., Marquez, M. & Velev, O. D. Synthesis of Light-Diffracting Assemblies from Microspheres and Nanoparticles in Droplets on a Superhydrophobic Surface. *Adv. Mater.* **20**, 4263–4268 (2008).

6.9. Appendix 6

6.9.1. SEM imaging 153
6.9.2. FIB-SEM analysis and thermal treatment 157
6.9.3. RCM imaging 159
6.9.4. Angle-dependent reflectivity measurements 160
6.9.5. CIE color maps 163

6.9.1. SEM imaging

Table A6.1: Comparison of photonic pigments (PhP) size, when assembled at 50°C and 65°C. Larger supraparticles size for higher assembly temperature is consistent and observed for all samples.*

PNP code	**Photonic pigments** (PhP)	**Size at 50°C** (μm)	**Size at 65°C** (μm)
PNP173	PhP-PNP173	47.2 ± 1.1	49.6 ± 1.0
PNP194	PhP-PNP194	53.9 ± 1.0	55.2 ± 1.2
PNP223	PhP-PNP223	47.1 ± 0.9	49.9 ± 1.0
PNP232	PhP-PNP232	55.2 ± 1.1	56.8 ± 1.1
PNP248	PhP-PNP248	52.1 ± 1.4	53.8 ± 1.3
PNP260	PhP-PNP260	53.2 ± 1.2	55.3 ± 1.4
PNP287	PhP-PNP287	57.1 ± 0.8	58.7 ± 1.1
PNP318	PhP-PNP318	51.8 ± 0.9	53.6 ± 1.2
PNP331	PhP-PNP331	50.9 ± 0.9	52.6 ± 1.2

*Several factors can affect the size results, e.g. the formation of small satellite droplets in case of any flow fluctuations or obstruction in the microchannels.

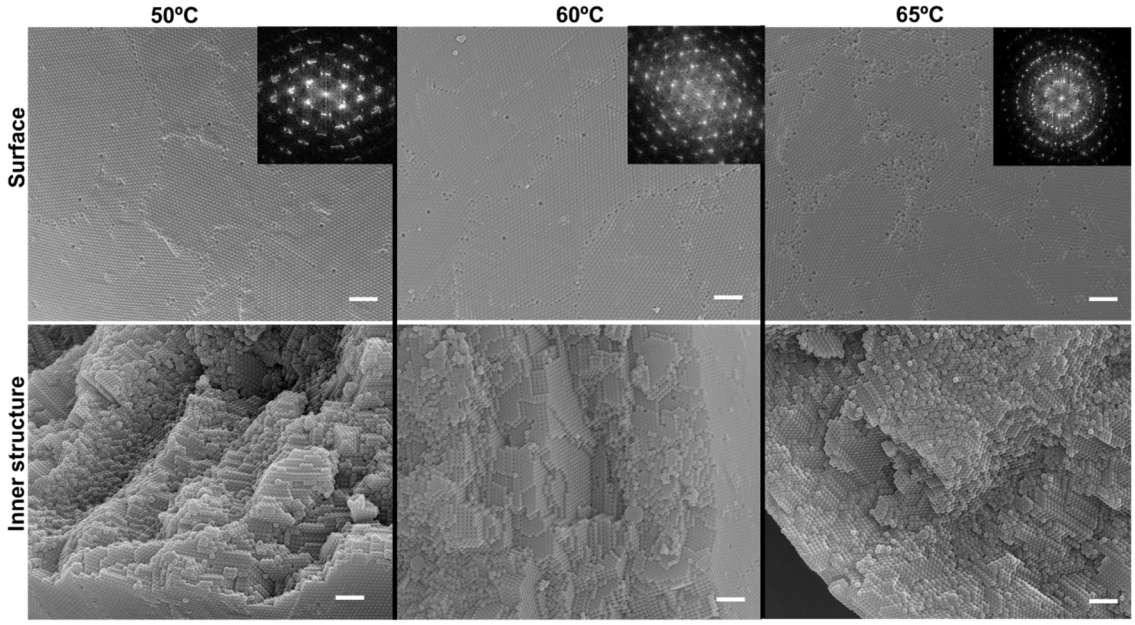

Figure A6.1: SEM images of the surface and inner structure of PhP-PNP173, assembled at 50°C, 60°C and 65°C. Inset shows the FFT pattern from the SEM images of the pigments surface. Scale bar: 1 μm. As the assembly temperature increases disorder on the pigments surface increases, but the ordered layers of PNP towards supraparticles center remains considerably high.

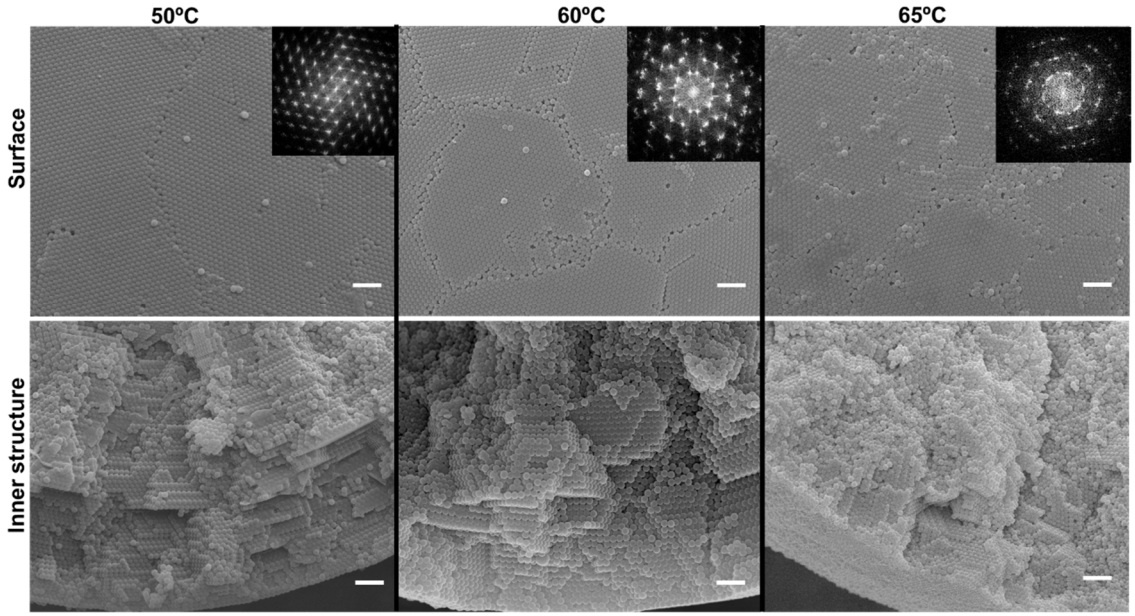

Figure A6.2: SEM images of the surface and inner structure of PhP-PNP223, assembled at 50°C, 60°C and 65°C. Inset shows the FFT pattern from the SEM images of the pigments surface. Scale bar: 1 µm. With increasing the assembly temperature disorder on pigments surface increases and the extention of PNP223 ordered layers towards supraparticles center diminishes.

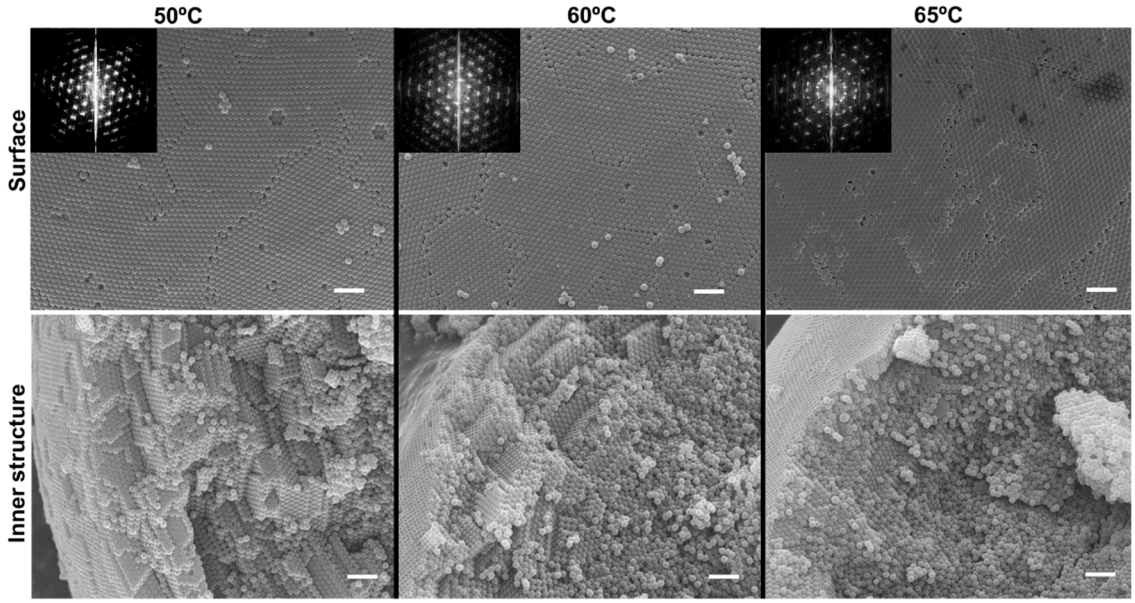

Figure A6.3: SEM images of the surface and inner packing of PNP248 into photonic pigments (PhP-PNP248), assembled at 50°C, 60°C and 65°C. Inset shows the FFT pattern from the SEM images of the pigments surface. Scale bar: 1 µm. Disorder increase at higher assembly temperatures is perfectly seen towards supraparticles center, increasing the extension of the amorphous packing of PNP248.

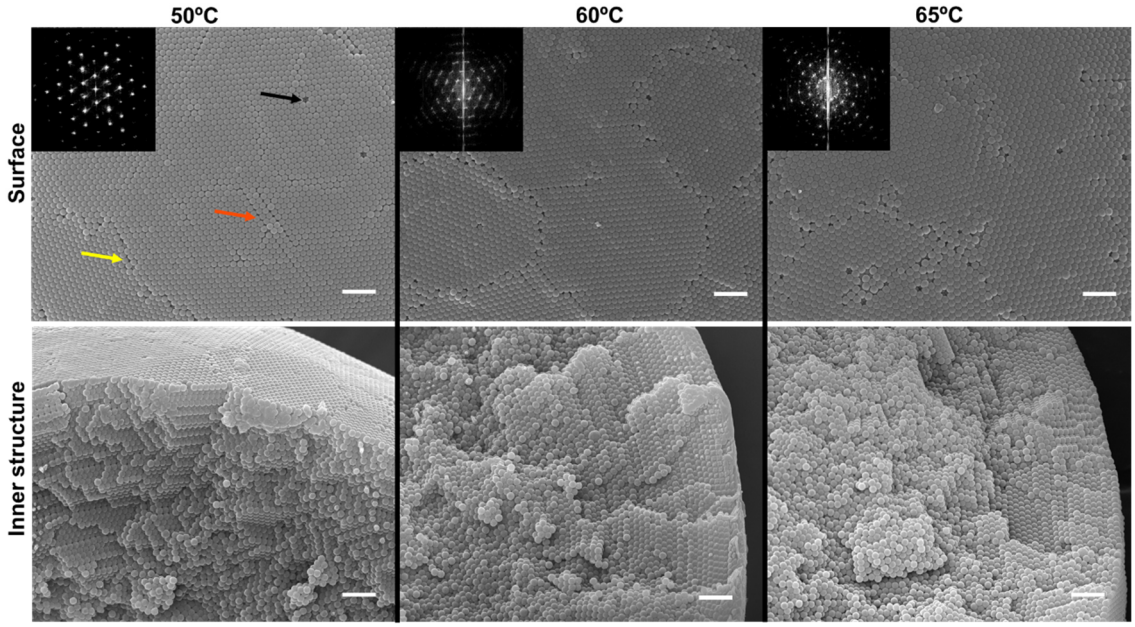

Figure A6.4: SEM images of the surface and inner structure of PhP-PNP260, assembled at 50°C, 60°C and 65°C. Inset shows the FFT pattern from the SEM images of the pigments surface. Scale bar: 1 μm. Yellow arrow indicates a domain boundary defect; orange arrow indicates a stacking fault defect and the black arrow indicates a point defect. With increasing the assembly temperature, the number of PNP260 ordered layers towards supraparticle center clearly diminishes.

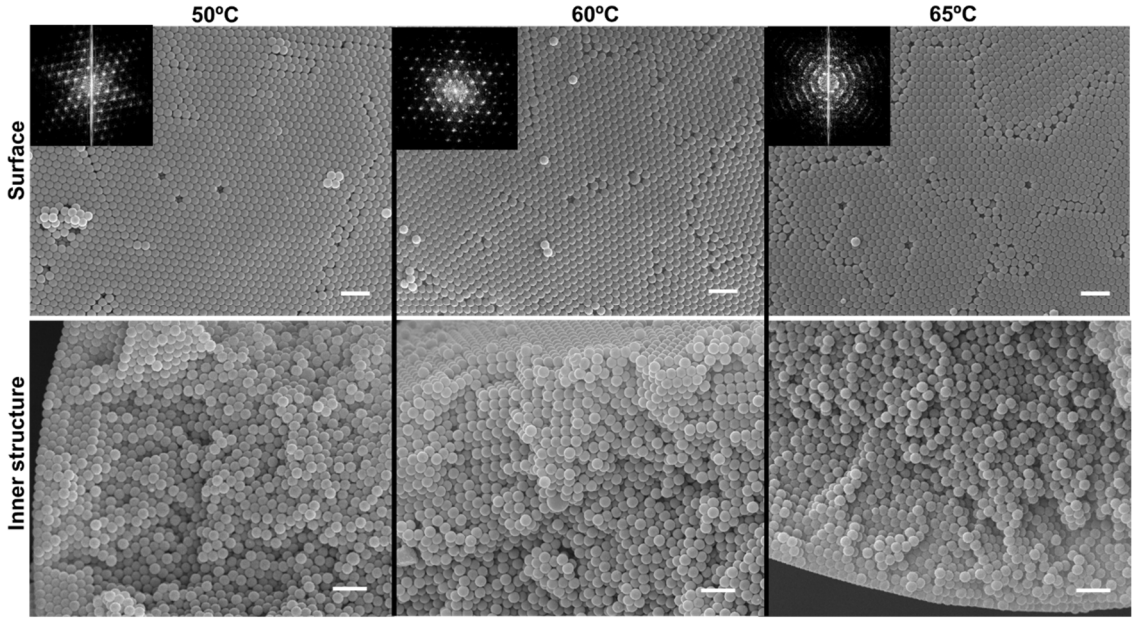

Figure A6.5: SEM images of the surface and inner structure of PhP-PNP318, assembled at 50°C, 60°C and 65°C. Inset shows the FFT pattern from the SEM images of the pigments surface. Scale bar: 1 μm. At higher assembly temperature disorder on the pigments surface increases, although no significant difference is observed regarding the small extension of ordered PNP318 layers towards supraparticle center.

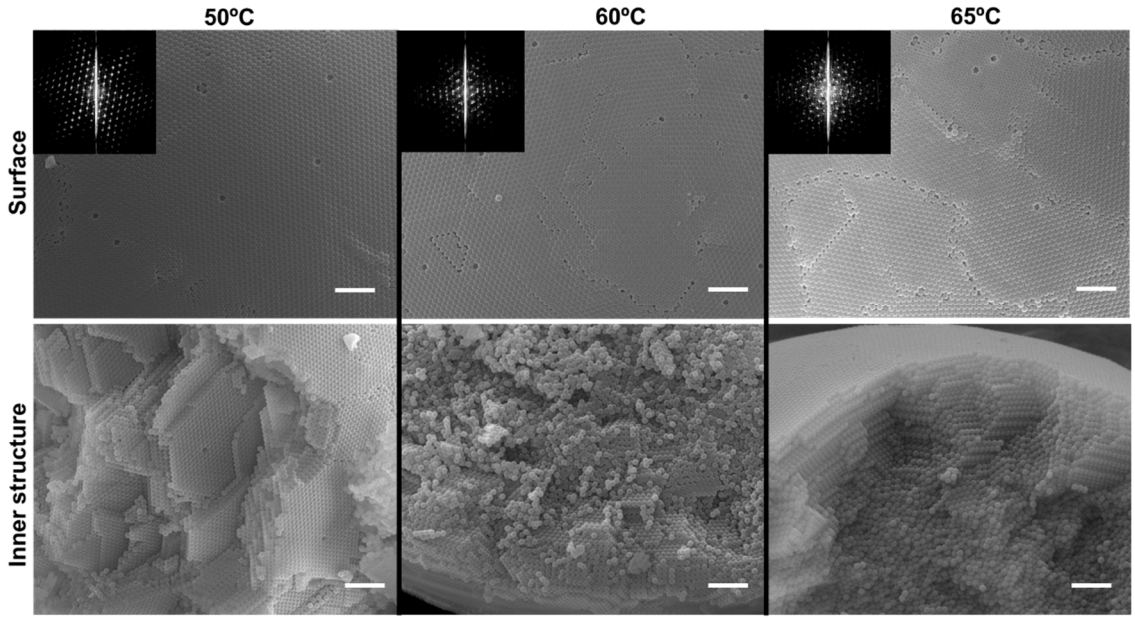

Figure A6.6: SEM images of surface and inner structure of PhP-PNP331, assembled at 50°C, 60°C and 65°C. Inset shows the FFT pattern from the SEM images of the pigments surface. Scale bar: 2 µm. Increasing the assembly temperature from 50°C to 65°C increases disorder at supraparticle surface and inner packing of PNP331.

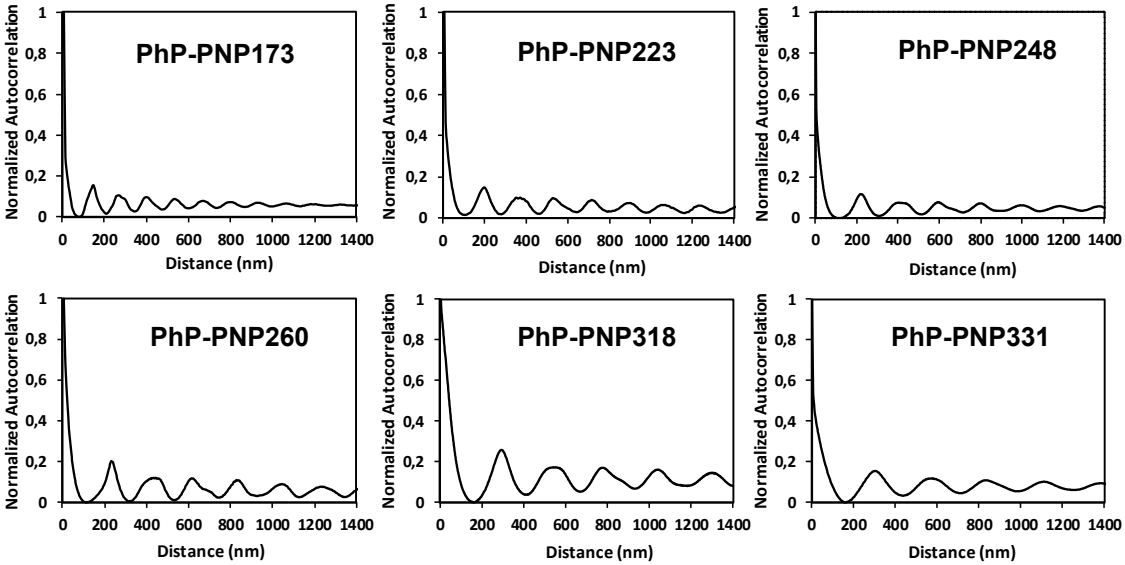

Figure A6.7: Radial profile plots of the ACF of the surface SEM images of the photonic pigments assembled at 60°C, showing a periodic distribution of maxima. First neighbor distance increases accordingly to PNP size, and corresponds to 148 nm in the case of PhP-PNP173; 198 nm in the case of PhP-PNP223; 223 nm in the case of PhP-PNP248; 231 nm in the case of PhP-PNP260; 291 nm in the case of PhP-PNP318; and 308 nm in the case of PhP-PNP331. Interestingly, PNP diameters, as determine by the first neighbor distance, although smaller than the ones obtained by SEM (before PNP assembly) are in good agreement. This may be explained by the PNP compression due to the high degree of packing inside the photonic supraparticles.

6.9.2. FIB-SEM analysis and thermal treatment

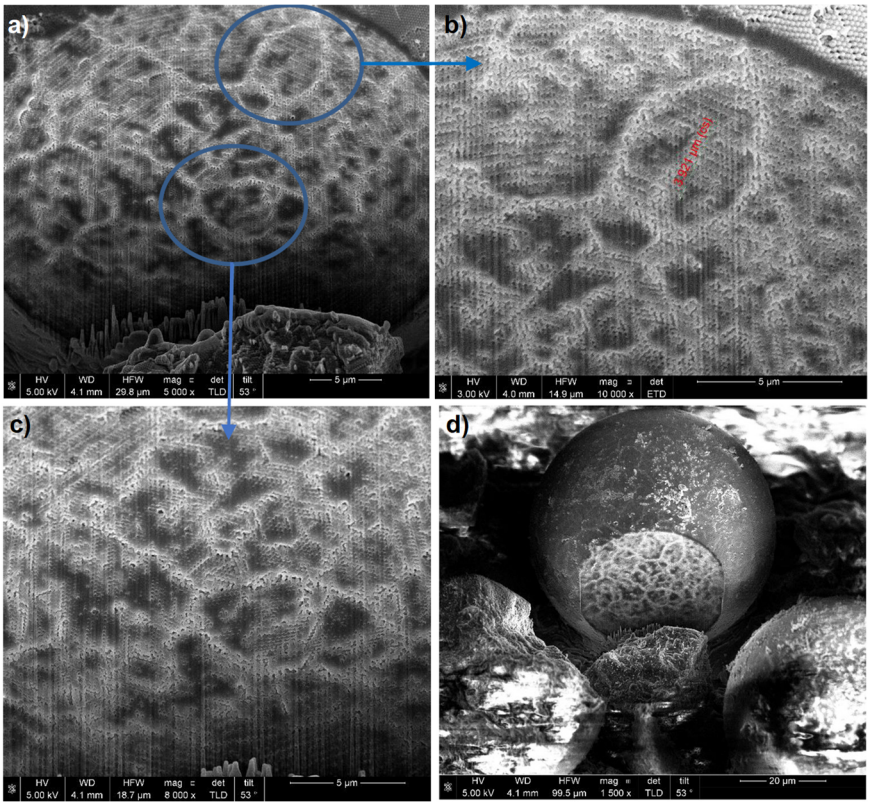

Figure A6.8: FIB-SEM images of PhP-PNP232 assembled at 50°C. Regions with different degrees of order can be identified: **a)** magnification of the 5 µm depth cut shown in **d)**; **b)** concentric ordered layers of PNP near the supraparticle surface; **c)** more disordered packing of PNP closer to the center of the supraparticle. The spreading of boundary scars is visible from the interior to the outermost layers, resulting in polycrystalline supraparticles.

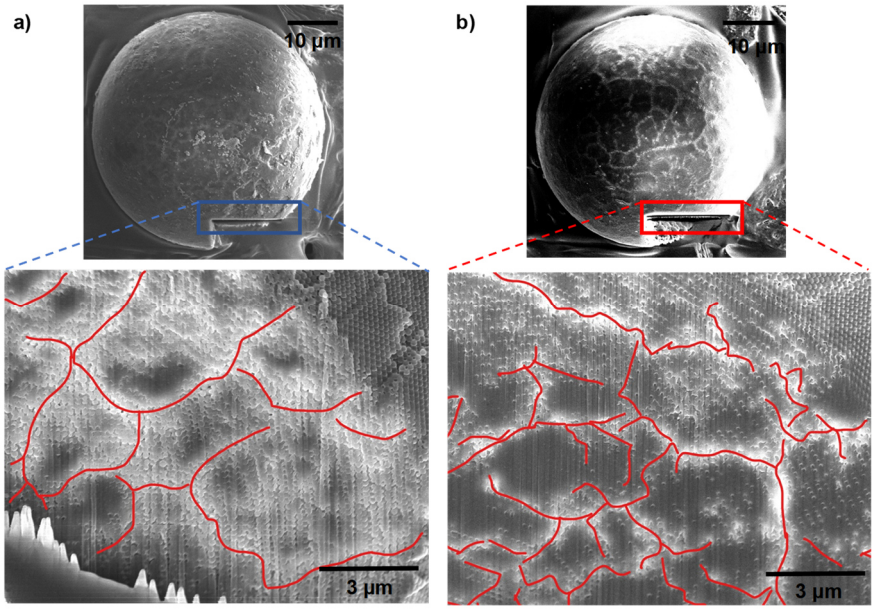

Figure A6.9: 5 µm depth FIB-SEM images of PhP-PNP232 assembled at different temperatures. **a)** 50°C and **b)** 65°C. The crystalline domains size, denoted by the red lines, diminishes with increasing the assembly temperature.

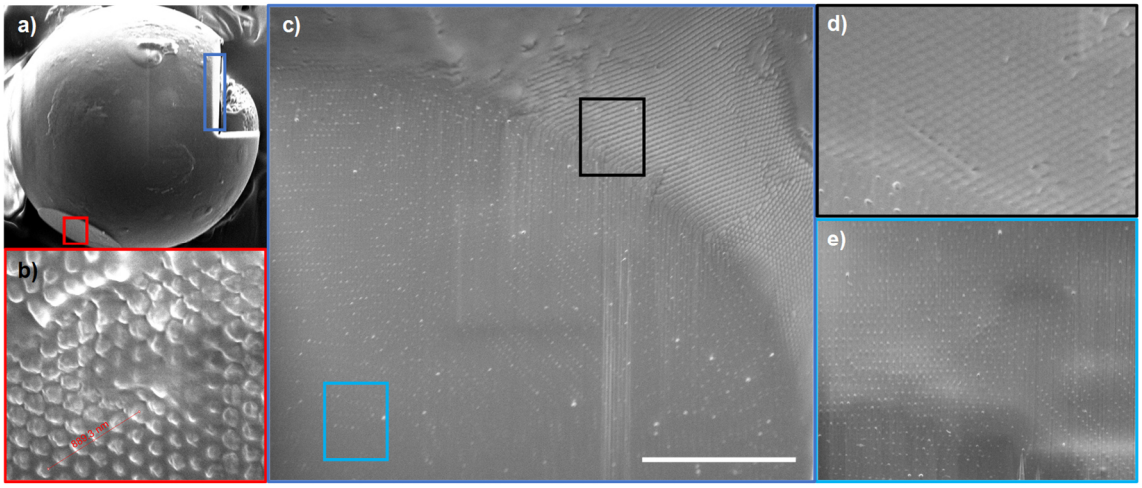

Figure A6.10: FIB-SEM images of annealed PhP-PNP232 assembled at 60°C; scale bar: 5µm. Supraparticles were submitted to thermal treatment at 150°C and a heating rate of 5°C/min. The interstitial space is reduced due to deformation (under which defects and nanoparticles position can rearrange) but no complete melting is observed. **a)** supraparticle shape after the thermal treatment. with a 5µm deep cut; **b)** deformed supraparticle bottom denoted by the red square in a), where ordered PNP layers are visible, confirming PNP integrity; **c)** magnification of supraparticle interior and surface highlighted by the blue rectangle in a) showing the interstitial voids; **d)** zoom in of supraparticle surface in c); **e)** zoom in of supraparticle interior in c).

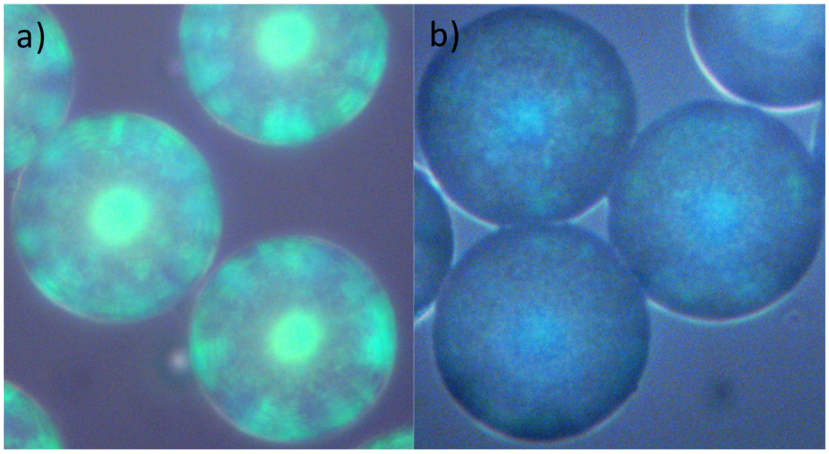

Figure A6.11: Reflectance microscopy images of PhP-PNP232 before (**a**) and after (**b**) being submitted to thermal treatment above the glass transition temperature of PNP. **a)** brightly green colored pigments before thermal treatment; **b)** faint green-blue structural color after pigments submission to thermal treatment at 150°C. Annealing at a temperature higher than the glass transition temperature of PNP reduces the interstitial space due to PNP deformation.

6.9.3. RCM imaging

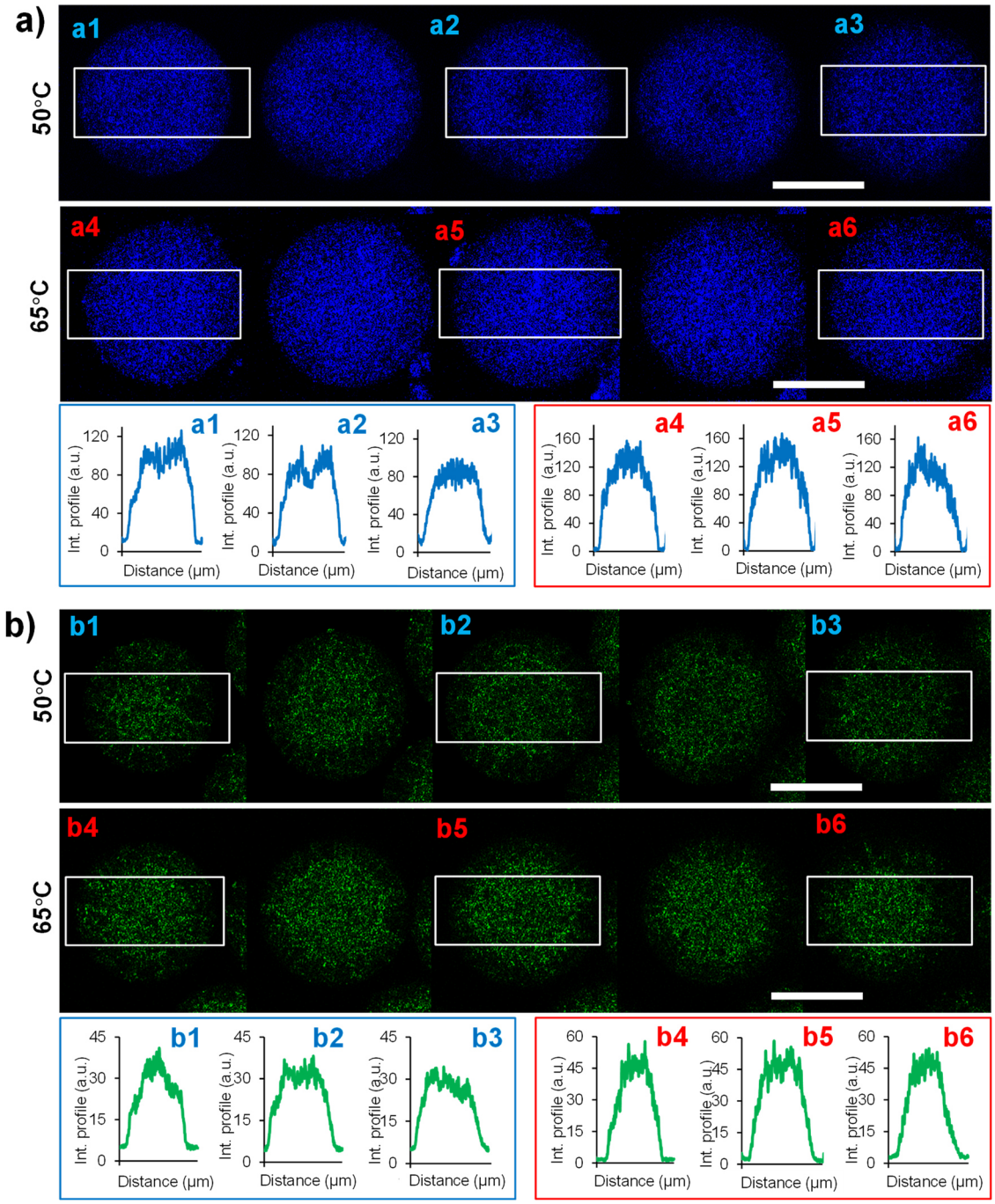

Figure A6.12: RCM images of supraparticles inner structure for PhP-PNP194 (**a**) and PhP-PNP323 (**b**) assembled at 50°C (a1-a3; b1-b3) and 65°C (a4-a6; b4-b6), under illumination with 633 nm laser light. The Z-depth increases from the left to right; the distance between each slice corresponds to 5 µm. The white rectangle denotes the area used to trace the intensity profile of light interacting with structure for three different depths (a1, a4, b1 and b4: $\sim 15\ \mu m$ depth); (a2, a5, b2 and b5: $\sim 25\ \mu m$ depth) (a3, a6, b3 and b6: $\sim 35\ \mu m$ depth). Scale bar: 25 µm. The pattern becomes increasingly brighter towards supraparticle center particularly for pigments assembled at 65°C, indicating higher diffuse scattering from disordered regions, whereas a darker region is observed at supraparticles surface. Light attenuation with increasing depth is negligible.

6.9.4. Angle-dependent reflectivity measurements

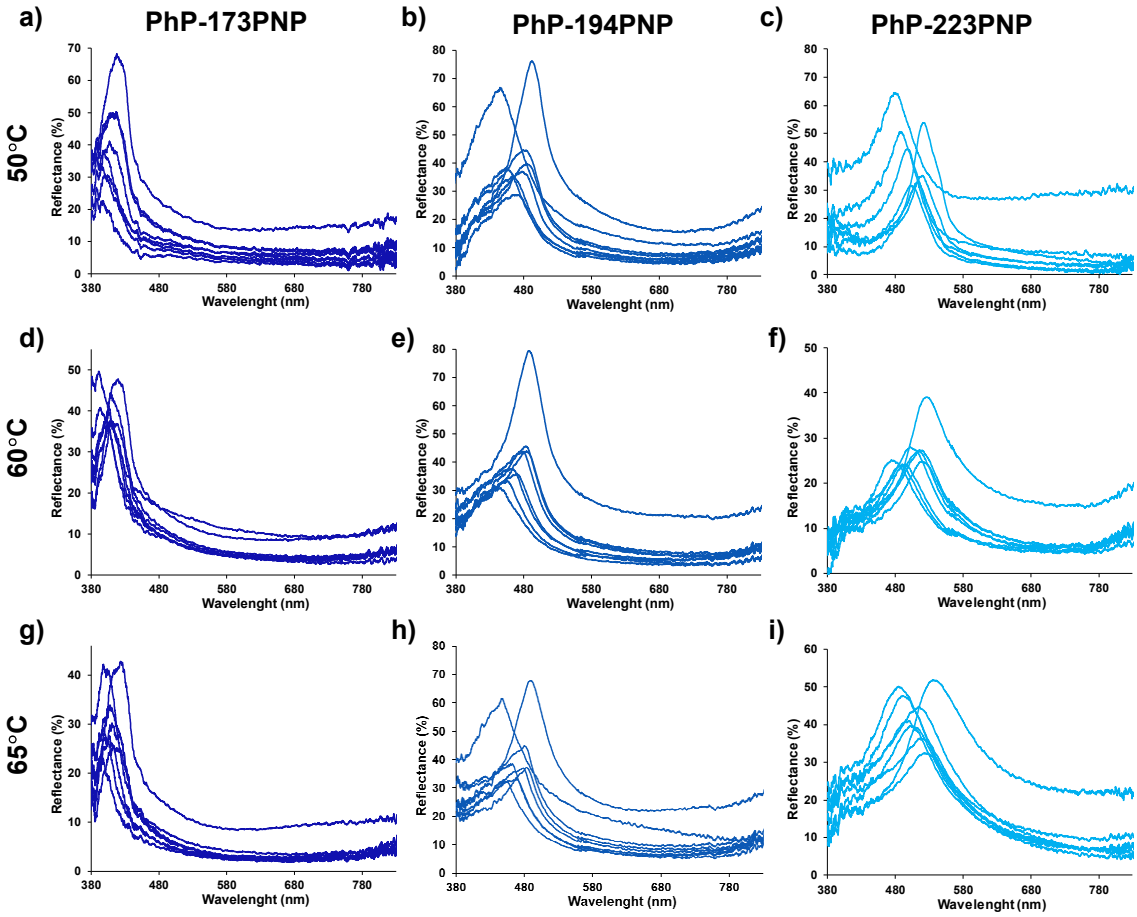

Figure A6.13: Angle resolved reflectance measurements for photonic pigments assembled at different temperatures (**a-c**: 50°C; **d-f**: 60°C; **g-i**: 65°C), for viewing angles varying from 0° to 75°. PhP-PNP173 (a, d, g) reflect wavelengths around 420 nm; PhP-PNP194 (b, e, h) reflect wavelengths around 485 nm; PhP-PNP223 (c, f, i) reflect wavelengths around 530 nm. Absolute intensity values cannot be compared because it depends on the amount of sample measured.

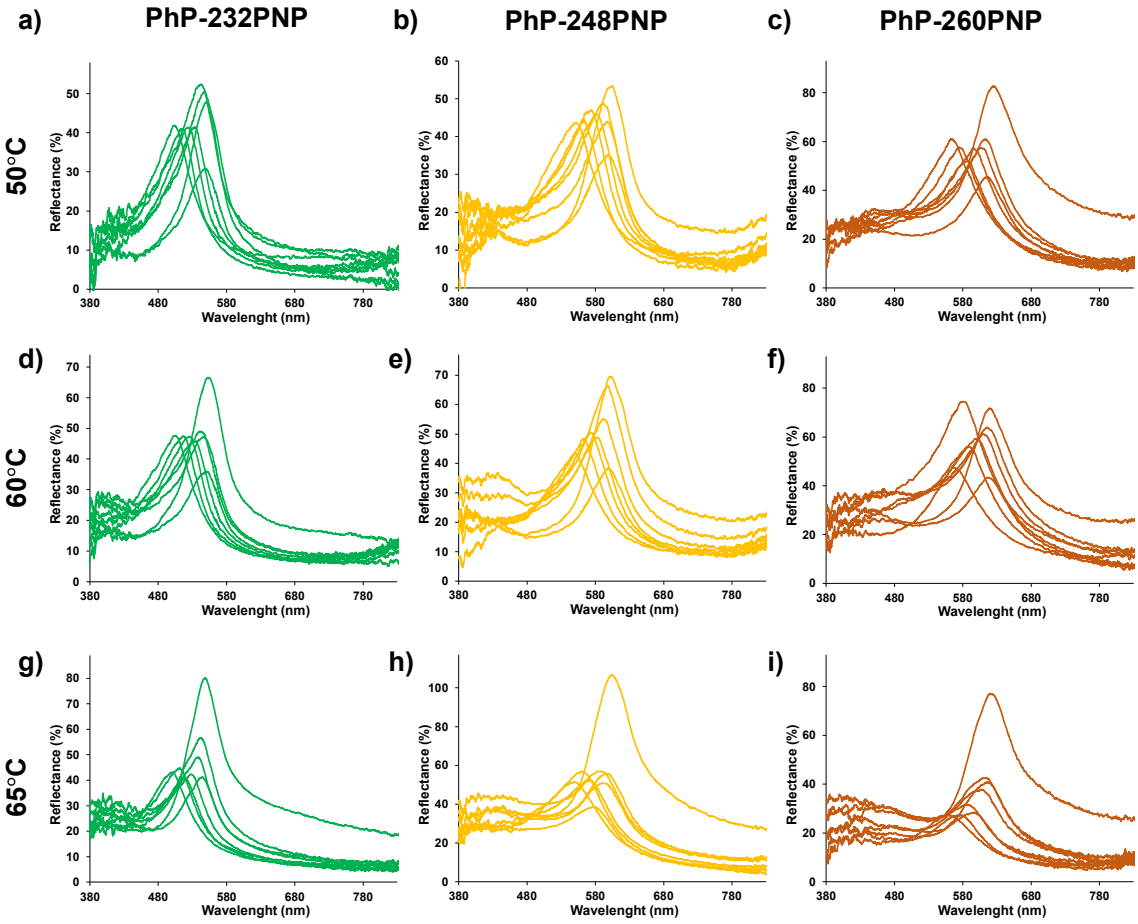

Figure A6.14: Angle resolved reflectance measurements for photonic pigments assembled at different temperatures (**a-c**: 50°C; **d-f**: 60°C; **g-i**: 65°C), for viewing angles varying from 0° to 75°. PhP-PNP232 (a, d, g) reflect wavelengths around 550 nm; PhP-PNP248 (b, e, h) reflect wavelengths around 600 nm; PhP-PNP260 (c, f, i) reflect wavelengths around 630 nm. Absolute intensity values cannot be compared because it depends on the amount of sample measured.

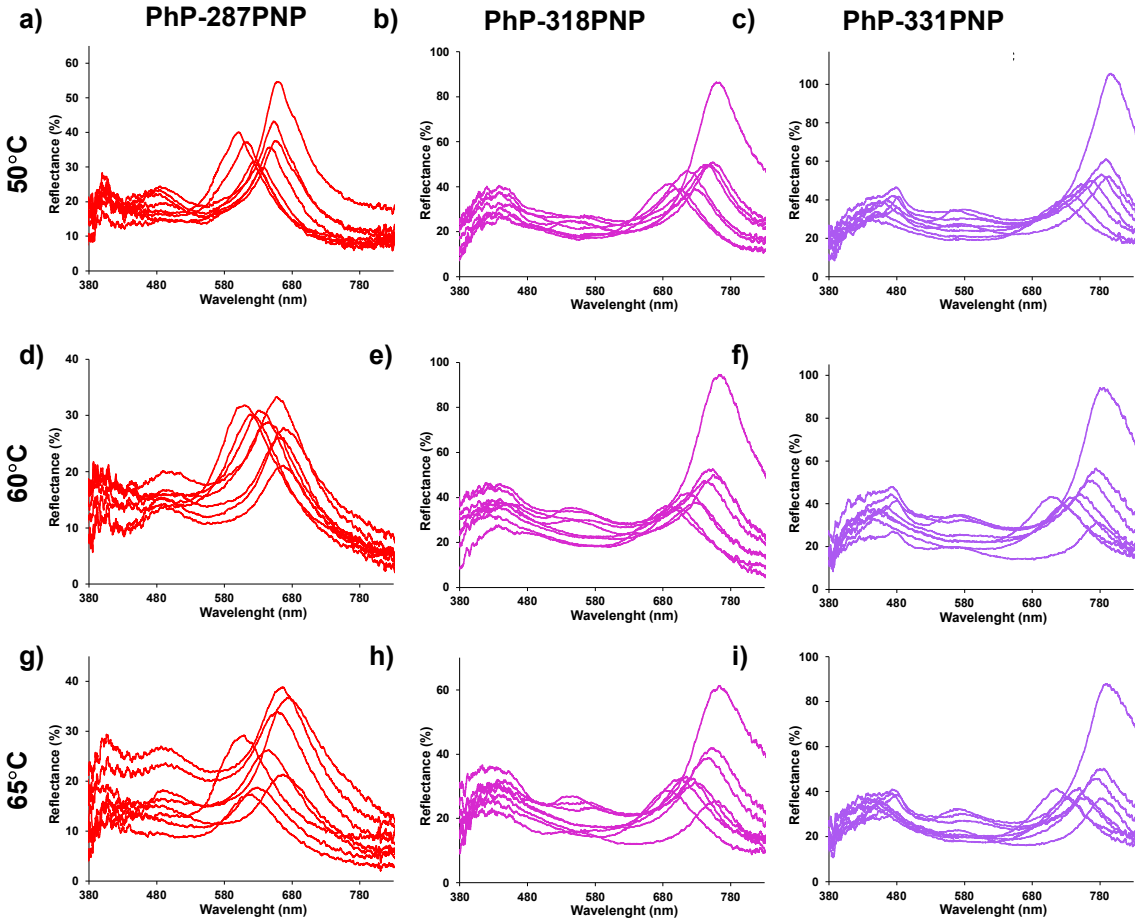

Figure A6.15: Angle resolved reflectance measurements for photonic pigments assembled at different temperatures (**a-c**: 50°C; **d-f**: 60°C; **g-i**: 65°C), for viewing angles varying from 0° to 75°. PhP-PNP287 (a, d, g) reflect wavelengths around 670 nm; PhP-PNP318 (b, e, h) reflect wavelengths around 760 nm; PhP-PNP331 (c, f, i) reflect wavelengths around 800 nm. Absolute intensity values cannot be compared because it depends on the amount of sample measured.

6.9.5. CIE color maps

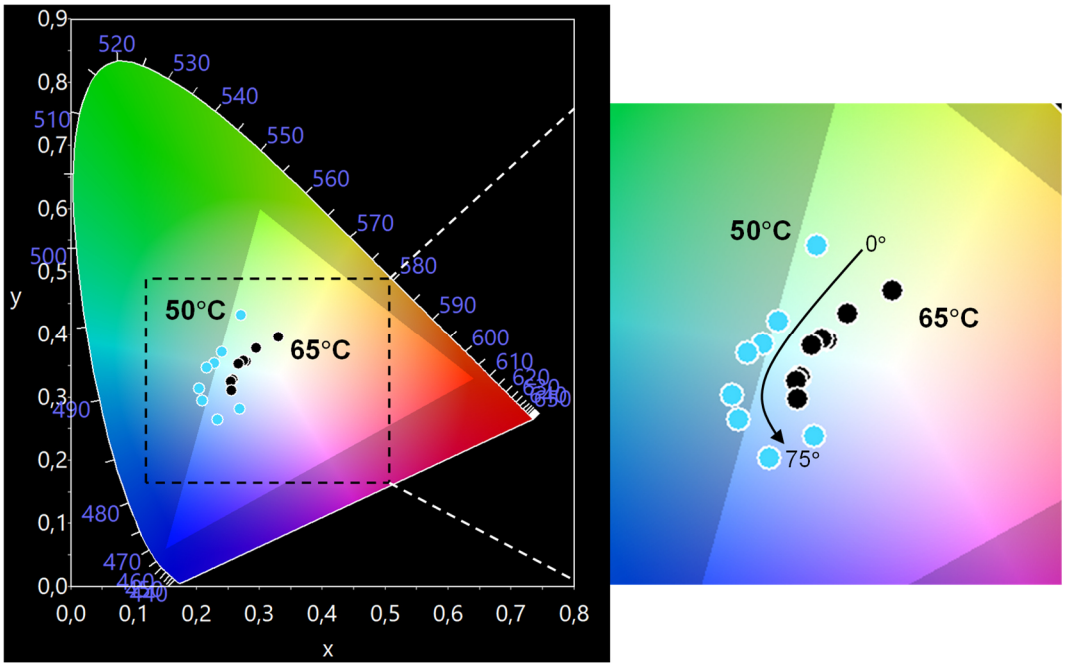

Figure A6.16: CIE x, y color space with the limits of the RGB subspace (denoted by the triangle) comparing the iridescence properties of PhP-PNP223 assembled at 50°C (colored dots) and 65°C (black dots) with increasing viewing angle. Pigments assembled at 65°C are closer to the white point and exhibits less saturated hues in comparison with the ones obtained at 50°C. However, the perceived color variation with increasing viewing angle from 0° to 75° (denoted by the black arrow direction) is lower for pigments assembled at 65°C, consistent with more isotropic structures.

7. Increasing color saturation through disorder

This chapter describes a strategy to enhance the color saturation of the spherical pigments that is also able to contribute to a more isotropic structural coloration. This was accomplished by incorporating a small amount of polydopamine nanoparticles (PDNPs), a broad-spectrum absorber, into the supraparticles structure. The structural and optical properties of the pigments doped with PDNPs, as well as the appearance of the colors reflected by them, were characterized, and compared against their undoped counterparts.

When assembled at lower temperatures, the spherical photonic pigments described in Chapter 6, exhibit saturated and non-iridescent structural colors from their multi-crystalline domains. Because of their non-fading and low-iridescent properties they are suitable as dispersible structurally colored pigments for several applications.[1-4]

However, as the assembly temperature increases, pigments with short-range ordered structures were obtained due to the increased disorder of the polymer nanoparticles (PNP) arrangement.[5-7] Although these pigments have lower color saturation due to the higher diffuse scattering of light from the disordered nature of the structure, they reflect more isotropic colors for wider viewing angles.[8-10]

An efficient and biomimetic approach to overcome the limited color saturation was inspired in bird's feathers, and consists in adding black components to the structure, able to absorb the diffusely scattered light, that otherwise contribute to color whitening.[11-14]

Doping structures with broad-spectrum absorbers, such as carbon black, or selective wavelength absorbers, such as gold nanoparticles, successfully improved the saturation of the colors reflected from photonic glasses.[15-20] In order to mimic the role of the melanin granules in the natural structural coloration of many bird's feathers[21,22] we added black polydopamine nanoparticles (PDNPs) to the supraparticles structure. This broad-spectrum absorbing material can suppress diffuse light scattering, and therefore is crucial to improve the color saturation.

In this chapter, the spherical photonic pigments assembled at 60°C were doped with polydopamine nanoparticles. Besides acting as diffuse light scattering absorber was also intended to increase structural disorder by packing in between the PNP, hampering long range-order.

7.1. Experimental section

7.1.1. Synthesis of polydopamine nanoparticles

Polydopamine nanoparticles, PDNPs, were synthesized by the oxidation and self-polymerization of dopamine hydrochloride in basic aqueous media (pH $>$ 7.5) at room temperature.[23] Although the polymerization mechanism is still not fully

understood, it involves the oxidation of the catechol unit in dopamine to quinone by alkaline pH-induced oxidation.[24,25]

A typical reaction was prepared as follows: ammonia aqueous solution (2.5 mL, 28-30%) was mixed with ethanol (40 mL) and deionized water (90 mL) under mild magnetic stirring at 30°C for 30 min. Dopamine hydrochloride (0.5 g) was dissolved in deionized water (10 mL) and then added to the above mixture solution. The color of the solution immediately turned to pale yellow and gradually changed to dark brown. The reaction proceeded for 24 hours. Polydopamine nanoparticles with an average diameter of 92 nm by TEM and 113 nm by DLS, were obtained after centrifugation and washing with water. These nanoparticles are quasi-spherical in shape but polydisperse in size (Figure 7.1). After reconstitution to 1% (w/v) aqueous colloidal dispersion, PDNPs were stored in the fridge.

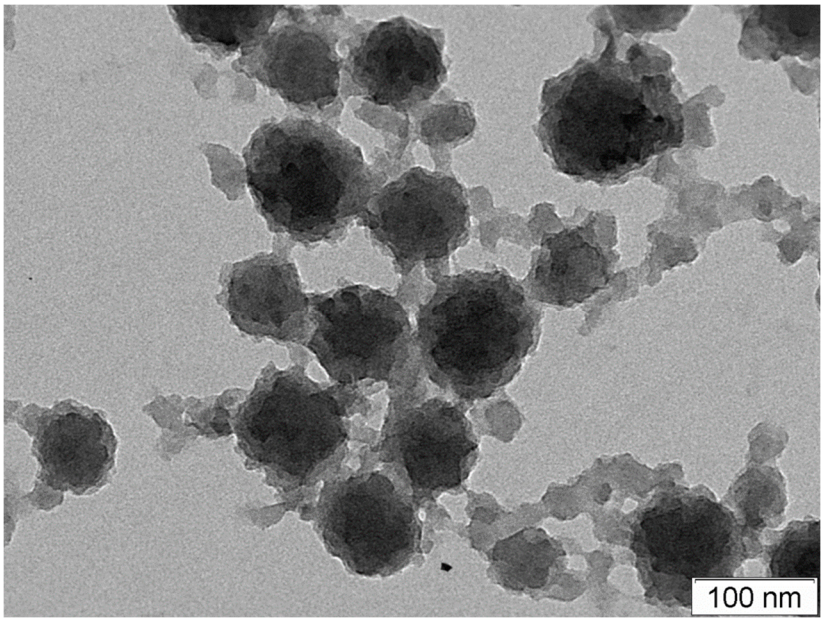

Figure 7.1: TEM image of polydopamine nanoparticles, PDNPs, with 92 nm mean diameter, synthesized in alkaline aqueous/ethanol medium.

7.1.2. Co-assembly of PDNPs and PNP into photonic structures

The synthesized PDNPs were used to dope the supraparticles structure by adding a small amount to the PNP dispersion prior to the emulsification procedure (3 wt% of PDNPs relative to PNP). The co-assembly process was conducted in the same experimental conditions described in Chapter 4, and the temperature-driven water evaporation was performed at 60°C.

Red pigments, PhP-PNP287, were further doped by the concomitant addition of PDNPs and carbon dots (both at 3 wt% relative to PNP dispersion) and assembled at 50°C.

7.1.3. Characterization techniques

SEM, FIB-SEM and RCM imaging were performed in the same conditions described in Chapter 6. The ACF profile of the SEM images and the 2D-FFT of photonic pigments were also obtained by the procedure described in Chapter 6. Angle-dependent reflectivity measurements were performed using the multi-angle probe holder under illumination at 45°, in the same conditions described in Chapter 6. The CIE x, y color maps were obtained by converting the reflectance spectra to color coordinates according to the procedure described in Chapter 6. Optical reflectance microscopy images were performed on a KERN OKM 173 microscope equipped with an ODC 832 camera at a magnification of 40x.

7.2. Topological and internal order/disorder probed by SEM

The packing of PNP at the surface and inside photonic pigments doped with 3 wt% of PDNPs was analyzed and compared to the PNP arrangement in undoped supraparticles. Because the PDNPs average diameter is approximately equal or lower than half the diameter of the PNP, they would be located interstitially in the voids between packed polymer nanoparticles.[9]

Here we want to know how this co-assembly strategy affects the packing of PNP inside droplet templates and how they are distributed within the supraparticles structure. SEM images of the surface and internal packing of PNP in doped (with PDNPs) and undoped (without PDNPs) blue, green and red photonic pigments, are summarized in Figures 7.2, 7.3 and 7.4. The structures were analyzed with the two-dimensional fast Fourier transform (2D-FFT) and the autocorrelation function (ACF) profile.[26-28] Comparison of the SEM images for the other doped and undoped supraparticles are shown in Figures A7.1−A7.6, Appendix 7.

The main difference visible between the SEM images of doped (PhP-PNP194-PD) and undoped (PhP-PNP194) blue supraparticles structures is the slightly increased disorder at the surface of doped pigments (Figure 7.2a1 and b1). This is evident when comparing the 2D-FFT pattern obtained from the surface SEM images (Figure 7.2a3 and b3): the hexagonal sharp peaks distribution for

undoped pigments, transform into a concentric distribution of bright peaks when the structure is doped with PDNPs. This pattern difference confirms the presence of a less crystalline arrangement of PNP at doped pigments surface. The autocorrelation function from the surface SEM images of undoped and doped supraparticles (Figure 7.2a2 and b2) are very similar. The presence of intense and narrow peaks with a periodic distribution of maxima along an extended distance, is visible both for PhP-PNP194 and PhP-PNP194-PD, indicating that PNP are arranged with a periodic order. For these pigments, the addition of PD nanoparticles shows no evident effect on the packing of PNP inside the supraparticles, because both undoped and doped structures have a large number of concentric ordered layers towards the supraparticles center (Figure 7.2a4 and b4).

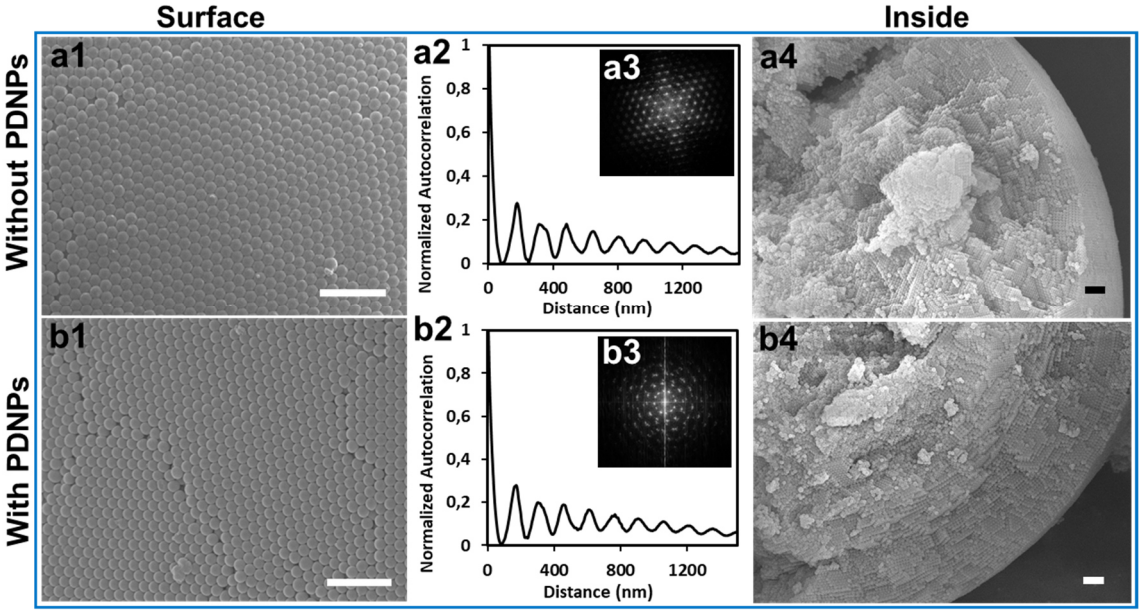

Figure 7.2: SEM images of supraparticles composed of PNP194, without (a) and with (b) PDNPs. **a1)** and **a4)** Undoped pigment surface and internal structure, respectively (PhP-PNP194); **a2)** and **a3)** ACF profile and 2D-FFT patterns from the surface SEM images of undoped supraparticles. **b1)** and **b4)** Doped pigment surface and internal structure, respectively (PhP-PNP194-PD); **b2)** and **b3)** ACF profile and 2D-FFT patterns from the surface SEM images of supraparticles doped with PDNPs. Scale bar: 1µm.

With increasing the PNP diameter, surface and internal structural disorder increases and clear differences are noticed between doped and undoped pigment supraparticles. Upon addition of PDNPs, short-range defects such as vacancies (or voids) increase at doped supraparticles surfaces (Figures A7.1−A7.6, Appendix 7). In the structure of doped pigments, the number of

orderly packed PNP layers towards the supraparticles center decreases to only a few, near the surface, contrarily to undoped ones (where a larger extent of well packed PNP layers is visible). PDNPs are randomly distributed in the supraparticles structure but are mainly found in the inner layers, where a more disordered packing of PNP is visible (Figures A7.3 and A7.4, Appendix 7).
SEM images comparing doped (PhP-PNP232-PD) and undoped (PhP-PNP232) green pigments structure are summarized in Figure 7.3.

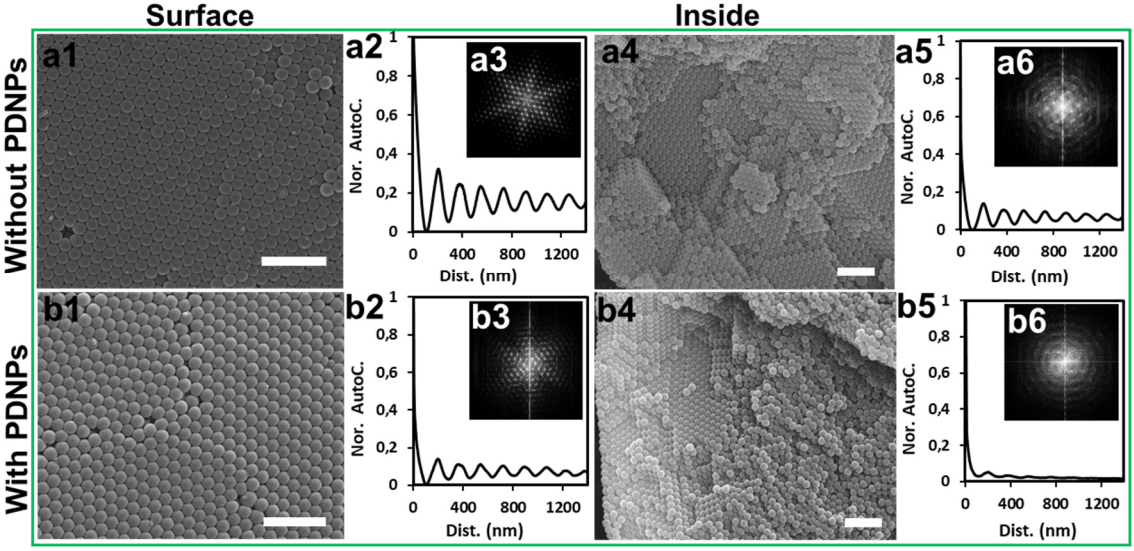

Figure 7.3: SEM images of supraparticles composed of PNP232, without (a) and with (b) PDNPs. **a1)** and **a4)** surface and internal structure of undoped supraparticles, PhP-PNP232. **b1)** and **b4)** surface and internal packing of PNP in supraparticles doped with 3 wt% of PDNPs, PhP-PNP232-PD. **a2)**, **a3)** and **b2)**, **b3)** correspond to the ACF profile and the 2D-FFT patterns obtained from the surface SEM images of undoped and doped pigments, respectively. Because an almost horizontal cross-section was obtained from broken supraparticles interior, images **a5)**, **a6)** and **b5)**, **b6)** correspond to the ACF profile and the 2D-FFT patterns obtained from the SEM images of the internal structure for undoped and doped pigments, respectively. Scale bar: 1µm.

A slightly more disordered packing of PNP at doped supraparticles surface is visible in comparison to undoped ones (Figure 7.3a1 and b1). This is confirmed by the 2D-FFT patterns (Figure 7.3a3 and b3) where a mixture of bright spots and a faint circular pattern, consistent with a more disordered structure, is obtained for doped supraparticles.[29,30] Disorder increase at doped pigments surface is also confirmed by the radial profile plots of the ACF (Figure 7.3a2 and b2), that show distinct features from the ones obtained for undoped pigments. Although a periodic distribution of maxima along extended distances is also

visible for doped pigments, their intensity is much lower, in comparison to the profile of undoped pigments

However, the main differences between doped and undoped green pigments are visible in the SEM images of the broken supraparticles interior (Figure 7.3a4 and b4). A drastic decrease in the number of orderly packed PNP layers produces clearly different features in the 2D-FFT pattern and the ACF profiles of doped and undoped supraparticles. The circular 2D-FFT pattern without sharp peaks (characteristic of amorphous structures) obtained from the SEM image of the doped supraparticle interior confirms the more disordered PNP packing (Figure 7.3a6 and b6). This is corroborated by the ACF profile of doped supraparticles, where at the position corresponding to the nearest neighbor distance, only a small hint of a peak appears, and the periodic distribution of maxima is no longer visible for extended distances (Figure 7.3a5 and b5).

Larger differences are obtained in the SEM images between doped (PhP-PNP287-PD) and undoped (PhP-PNP287) red pigments (Figure 7.4). The surface and internal packing of PNP287 show a significantly more disordered packing of PNP in the case of supraparticles doped with PDNPs.

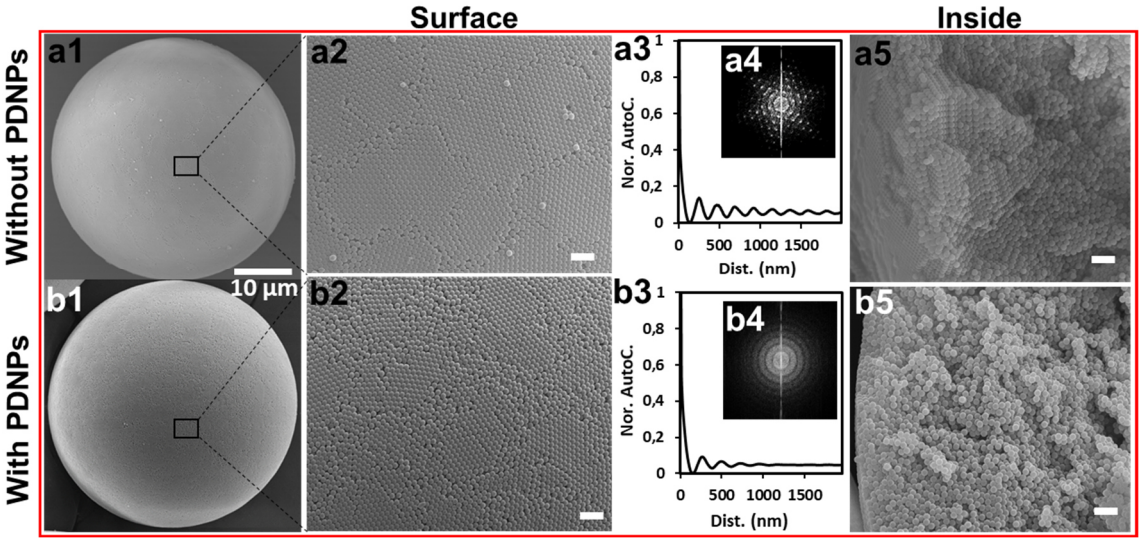

Figure 7.4: SEM images of supraparticles composed of PNP287, without (a) and with (b) PDNPs. **a1)** and **a2)** Undoped supraparticle surface (PhP-PNP287); **a3)** and **a4)** ACF profile and 2D-FFT patterns from the surface SEM images of undoped supraparticles; **a5)** Undoped supraparticle interior. **b1)** and **b2)** Doped supraparticle surface (PhP-PNP287-PD); **b2)** and **b3)** ACF profile and 2D-FFT patterns from the surface SEM images of supraparticles doped with PDNPs; **b5)** Doped supraparticle interior. Scale bar: 1µm.

In the surface SEM images of PhP-PNP287-PD, larger regions with an amorphous packing of PNP are visible in comparison to undoped ones (Figure 7.4a1, b1, a2 and b2). Small areas with hexagonally close-packed PNP separated by large amorphous regions at the surface of doped pigments gives rise to a 2D-FFT pattern with clusters of white pixels concentrated in symmetrical, circular patterns. This is characteristic of an amorphous structure with local and spatial isotropic structural correlation (Figure 7.4a4 and b4).

The radial profile from the ACF of the supraparticles surface (Figure 7.4a3 and b3) also corroborates the differences in structural order between doped and undoped red pigments. The lower intensity of the first maximum and the significantly smaller extent of the periodic distribution of maxima on the ACF profile of doped pigments in comparison to undoped ones, confirms the higher structural disorder in the presence of PDNPs. In addition, a completely amorphous arrangement of PNP is visible in the internal structure of doped supraparticles. This contrasts with the few ordered layers observed in undoped supraparticles (Figure 7.4a5 and b5).

7.3. FIB-SEM imaging of doped and undoped structures

To obtain a more detailed information on the structural arrangement of PNP upon the addition of 3 wt% of PDNPs, cross-sections of doped and undoped supraparticles composed of PNP232, were obtained with focused ion beam (FIB) and imaged by SEM (Figure 7.5).

Although a small amount of PDNPs was co-assembled with PNP, the cross-sections at 5 μm depth from sample surface (Figure 7.5), shows smaller sized crystalline domains and larger disordered regions inside the doped supraparticle structure in comparison to undoped ones.

By converting the images to binary we find that the average area of the crystalline domains is smaller in the case of doped pigments, $7.97 \pm 2.90\ \mu m^2$ in comparison to $14.72 \pm 4.63\ \mu m^2$ of undoped structures. On the other hand, the mean length of the disordered regions in between crystalline domains is larger in the case of doped pigments, $0.83 \pm 0.20\ \mu m$, relative to the $0.65 \pm 0.13\ \mu m$ for undoped pigments structure. FIB-SEM images at different depths inside the doped supraparticle reveal the expected disorder increase with increasing depth (Figure A7.7, Appendix 7).

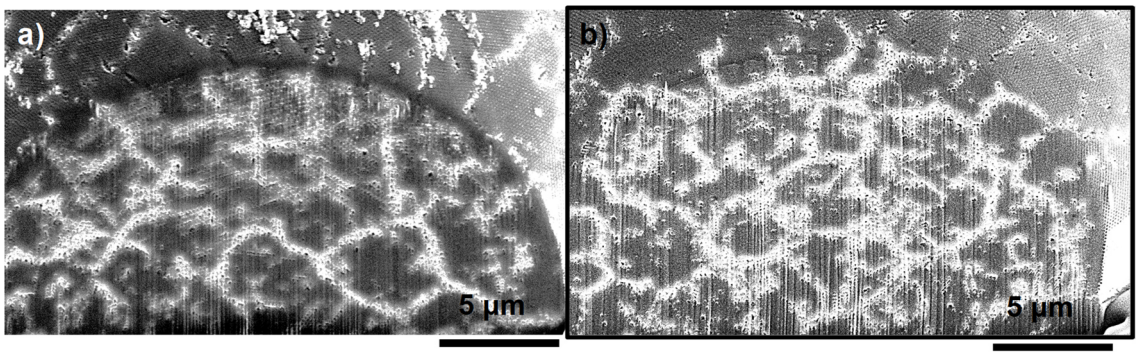

Figure 7.5: FIB-SEM images of supraparticles composed of PNP232, at 5 µm depth. **a)** Undoped supraparticle cross-section. **b)** Cross-section of a supraparticle doped with 3 wt% of PDNPs. Despite disordered regions are visible in both structures, a higher disorder degree is obtained upon doping the pigments with PDNPs, resulting thus, in smaller crystalline domains separated by larger disordered boundary regions.

7.4. Effect of PDNPs addition by RCM

RCM imaging[31,32] was also used to probe the internal packing of PNP when co-assembled with PDNPs. Cross-sectional images at different depths close to the center of doped and undoped blue, green, and red pigments are summarized in Figure 7.6. Blue (PhP-PNP194, Figure 7.6a), green (PhP-PNP232, Figure 7.6b) and red photonic pigments (PhP-PNP287, Figure 7.6c) were imaged under illumination with laser light (matching the wavelengths of their pseudo-bandgaps) at 458 nm, 514 nm and 633 nm, respectively.

The Z-depth increase from the left (15 μm) to the right (35 μm), and the distance between each slice corresponds to 5 µm. The white rectangles denotes the area used to trace the intensity profile of light distribution within the supraparticles structure at different depths: 15 μm (a1, a4, b1, b4, c1, c4); 25 μm (a2, a5, b2, b5, c2, c5); and 35 μm (a3, a6, b3, b6, c3, c6).

The intensity profile plots of doped *vs* undoped blue, green, and red supraparticles were compared for the cross-sections at 25 µm depth by calculating the difference between their maximum and minimum intensity values. The black dotted lines in the intensity profiles at 25 µm depth in Figure 7.6 (a2, a5, b2, b5, c2, and c5) correspond to average values used to obtain the maximum intensity value of light interacting with the structure. The full black line in the same profiles correspond to the average value at the minimum of the intensity profile.

For undoped blue pigments, bright and big (111) crystalline planes from the fcc structure are visible, extending from the supraparticle surface towards the center (Figure 7.6 a1-a3). In the case of doped blue pigments, such large bright regions

are not visible, and a more isotropic pattern is observed throughout the supraparticle structure (Figure 7.6 a4-a6). No significant differences exist between the intensity profile values with depth increase for doped and undoped blue pigments. The same holds true for the difference between the maximum and minimum average intensity values at the supraparticles center (Figure 7.6 a2 and a5). However, the shape of their intensity profiles shows a large difference: doped structures present a large plateau at the supraparticle center (corresponding to the average minimum intensity value), indicating the presence of a more disordered and isotropic inner structure. This plateau is absent in the case of undoped blue supraparticles because the crystalline domains extend close to the supraparticle center.

When doped and undoped blue pigments are imaged with 633 nm laser light – a wavelength outside the stopband – one observes the diffusely reflected light from the more disordered regions (Figure A7.8, Appendix 7). The pattern reflected by the doped blue pigments is brighter across the entire supraparticle and the reflected intensities are more uniformly distributed. This confirms the more isotropic nature of the doped blue pigments structure in comparison to undoped ones.

For green pigments, imaged under 514 nm light (Figure 7.6b), despite a larger extent of crystalline domains is visible for undoped pigments in comparison to doped ones, the differences between the higher and lower values of the intensity profile closer to the supraparticles center is similar for both samples(Figure 7.6b2 and b5). No visible plateau is identified in the intensity profile at the central depth for undoped supraparticles (Figure 7.6b2), indicating the absence of a highly disordered inner structure. For green pigments doped with PDNPs, there is a larger plateau at the minimum average intensity (Figure 7.6b5), consistent with a more disordered and isotropic packing of PNP at the innermost structure of doped supraparticles.

When illuminated with 633 nm laser light (Figure A7.8, Appendix 7), a homogeneous distribution of diffuse scattering is visible from the doped supraparticle structure (with exception of a thin darker region closer to the surface), whereas in the case of undoped pigments the brighter regions are mostly observed at the disordered boundaries in between darker crystalline domains.

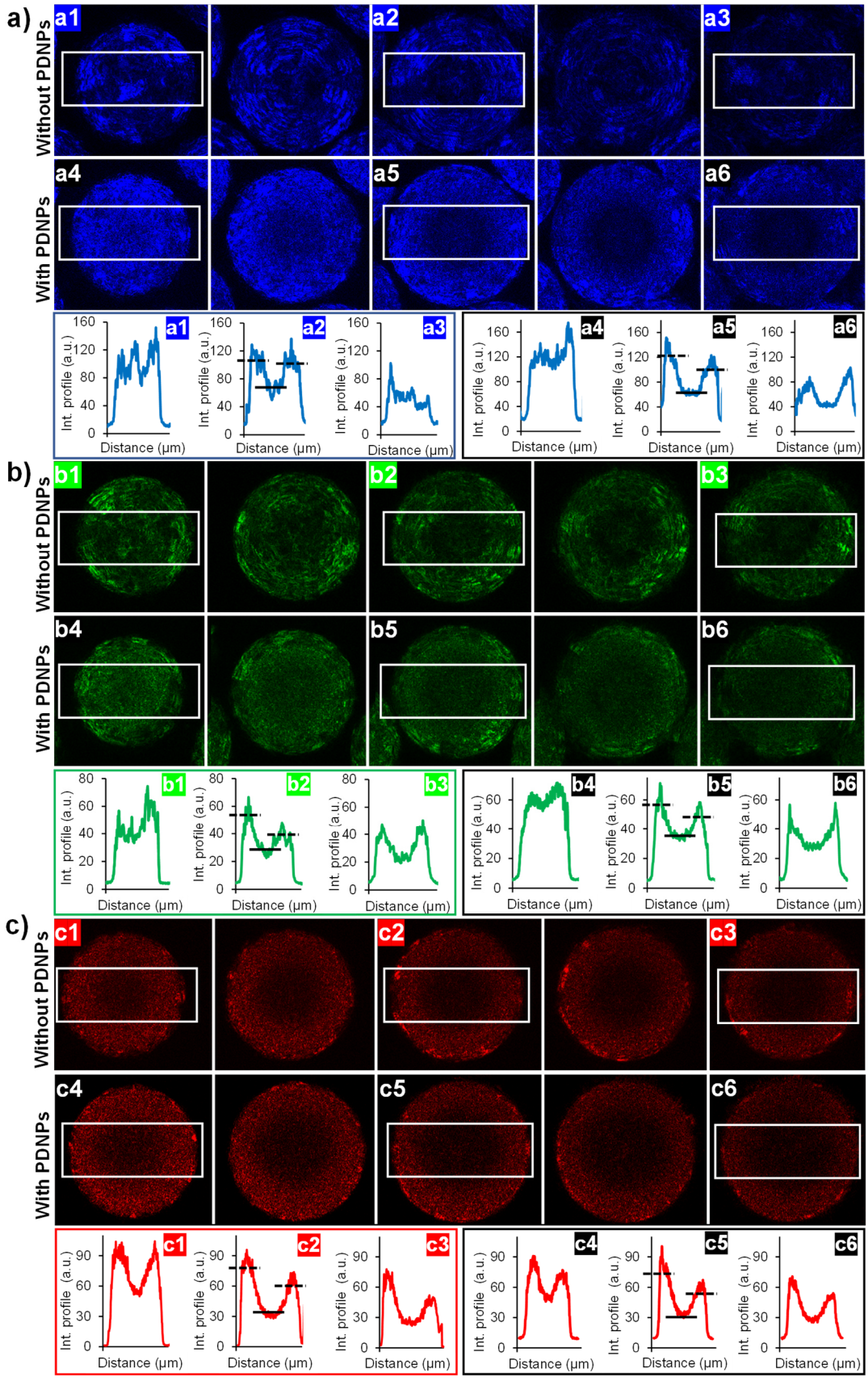

Figure 7.6: RCM images of blue (**a**), green (**b**) and red (**c**) photonic pigments with and without PDNPs, illuminated with 458 nm, 514 nm, and 633 nm light, respectively. Z-depth increases from the left (15 μm) to the right (35 μm). Distance between slices: 5 μm. White rectangle denote the area used to trace the intensity profile at different depths.

In the case of red photonic pigments, imaged under 633 nm light (Figure 7.6c), large crystalline regions of perfectly packed PNP287 are not observed for either doped or undoped pigments, and the intensity profiles are very similar both in shape and intensity. This is indicative of a disordered arrangement of PNP287 inside doped and undoped red pigments structure.

Thus, the RCM results corroborate those from SEM and FIB-SEM: upon doping the structures with PDNPs, the size of the crystalline domains decreases, and larger disordered regions are obtained, contributing to a more isotropic arrangement of PNP.

7.5. Reflectance properties of doped *vs* undoped pigments

The reflectance properties of doped and undoped pigments were evaluated from the specular reflectance measurements for collecting angles varying from 0° to 75°. Results for blue (PhP-PNP194), green (PhP-PNP232) and red (PhP-PNP287) photonic pigments, with and without the addition of 3 wt% of PDNPs, are shown in Figure 7.7 (results for the other pigments are shown in Figure A7.9, Appendix 7).

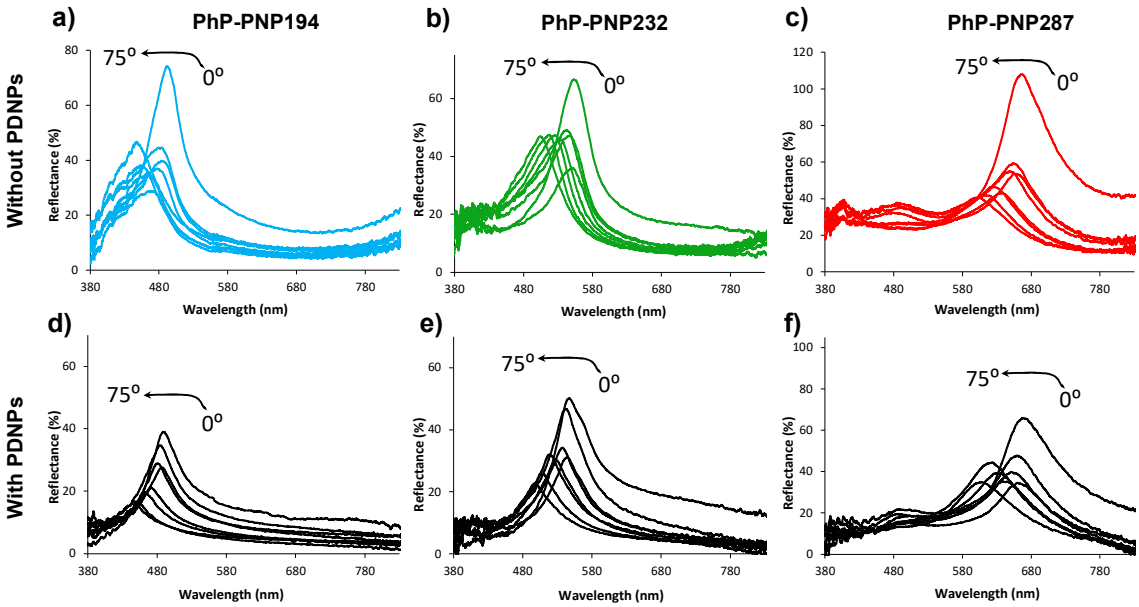

Figure 7.7: Angle-resolved reflectance measurements of blue (**a**, **d**), green (**b**, **e**) and red (**c**, **f**) photonic pigments for collecting angles varying from 0° to 75°. The upper panel correspond to the undoped structures of PhP-PNP194, PhP-PNP232 and PhP-PNP287, respectively. The lower panel correspond to the structures doped with 3 wt% of PDNPs, PhP-PNP194-PD, PhP-PNP232-PD, PhP-PNP287-PD, respectively.

The most striking difference between the reflectance spectra from undoped and doped pigments is the significant decrease in the scattering background signal across the entire visible light range. This is due to the lower contribution of diffuse scattering to the reflectance properties of doped pigments because it is absorbed by the randomly distributed PDNPs inside the supraparticles structure. A more uniform and gradual decrease in the reflected intensity with increasing viewing angle is also observed for doped pigments.

The addition of PDNPs to the pigments structure proved to be a very efficient strategy to reduce the contribution of diffuse scattering to the reflectance spectra of doped pigments. In the case of doped green pigments, PhP-PNP232-PD, PDNPs absorbed almost 70% of the scattering background signal with respect to undoped structures, PhP-PNP232 (Figure 7.7b and e). The averaged background reflectance intensity, calculated from the mean lower values on each side of the reflectance band from 0° to 75° collecting angle, lowered from 14% to 4% in the case of green pigments. With increasing PNP diameter, although diffuse scattering increases, the ability of PDNPs reduce its contribution to the overall reflectance properties is very efficient. In the case of red pigments, PhP-PNP287, the addition of PDNPs absorbed approximately 60% of the diffuse scattering contribution to the reflectance spectra. The averaged background reflectance intensity of 26%, for undoped red pigments, was reduced for 10% upon doping the structures with PDNPs (Figure 7.7c and f).

For pigments composed of larger PNP (diameters ≥ 248 nm), the reflectance band shifts to red wavelengths and another band appears at the blue part of the spectrum for small collecting angles (from 0° to 30°). The addition of PDNPs shows no significant effect on those reflectance bands (Figures 7.7 and Figure A7.9 of Appendix 7), attributed to single-particle scattering resonances, that compromise red hues by color mixing.[33-36]

On the contrary, the addition of PDNPs indeed lowered the intensity of the second order reflectance bands (around 460−490 nm) from the fcc structure of PhP-PNP318-PD and PhP-PNP331-PD, in comparison to their undoped analogs (Figure A7.9, Appendix 7). This fact is consistent with a decrease in the crystalline packing of PNP inside the photonic supraparticles structure when co-assembled with PDNPs, thus resulting in more isotropic structures.

Because the low iridescence properties (small shift in the wavelength of maximum reflectance with increasing viewing angle), are due to the spherical symmetry of the supraparticles and do not depend on the structural order degree, doping the pigment structures with 3 wt% of PDNPs shows a negligible effect on their angular dependence (Figure 7.8).

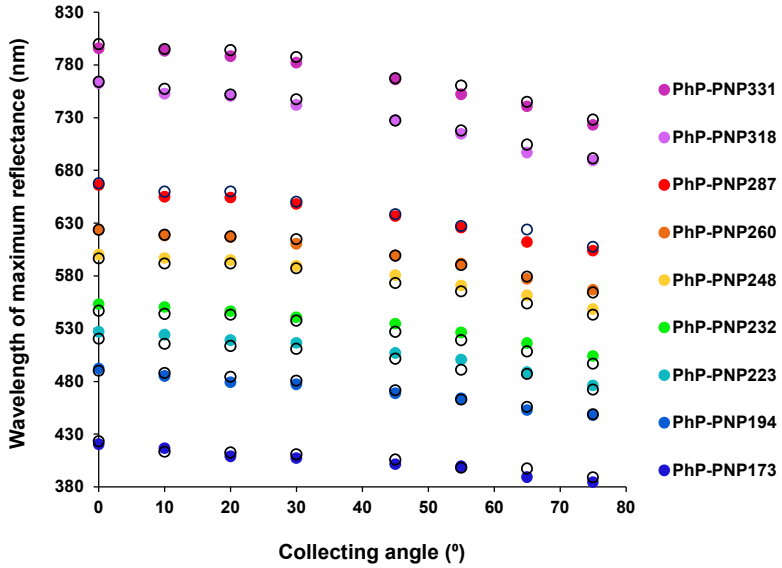

Figure 7.8: Angular dependence of the wavelength of maximum reflectance for doped (open black circles) and undoped (colored circles) photonic pigments, from 0° to 75° viewing angles. The addition of PDNPs, despite increasing the structural disorder inside the photonic pigments, shows no significant effect on their iridescence properties.

Only a small blue shift in the wavelength of maximum reflectance of the colors reflected from doped and undoped pigments, λ_{max}, is visible with increasing viewing angle, mostly for angles higher than 45° (Figure 7.8). The λ_{max} from 0° to 75° viewing angle shifts only about 40 nm for pigments composed of smaller PNP, and this shift gradually increases with increasing PNP diameter, up to a maximum of 70 nm. The larger shift in the wavelength of maximum reflectance and the increase in background diffuse scattering with the increase of PNP diameter are summarized in Figure 7.9, for doped and undoped photonic supraparticles.

When compared to other photonic pigments with low iridescent properties the shift exhibited by our pigments at 75° is on the order of magnitude of the shift they exhibited at 45° viewing angle.[37,38] Although the addition of PDNPs has no significant effects on the iridescence properties of the photonic pigments (compare the filled blue and black columns in the left y-axis, Figure 7.9), it efficiently decreased the background diffuse scattering inside the doped pigment

structures (compare the white striped blue and black bars – right y-axis, Figure 7.9).

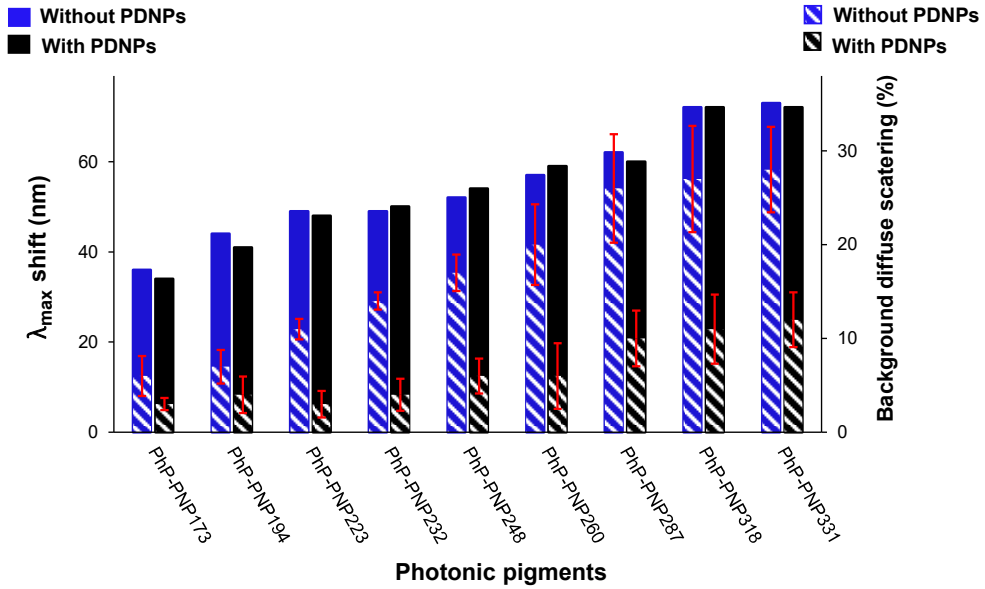

Figure 7.9: Comparison between the shift in the wavelength of maximum reflectance (left y-axis) and the background diffuse scattering (right y-axis) for doped (black patterns) and undoped (blue patterns) pigments. The λ_{max} shift correspond to the difference in the wavelength of maximum reflectance between 0° and 75° viewing angles. The background diffuse scattering (stripped patterns) represents the mean scattering background intensity values on both sides of the reflectance bands (except for PhP-PNP173 and PhP-PNP331) for all collecting angles. The error bars correspond to the average standard deviation of the background diffuse scattering of all collecting angles.

Besides working as a diffuse scattering absorber intended to increase color saturation,[39,40] the addition of PDNPs also introduces point defects, and consequently the packing of PNP inside the photonic supraparticles became more isotropic. This is clearly visible in Figure 7.10, when comparing the full width at half maximum (FWHM) of the reflectance bands at each collecting angle between undoped (Figure 7.10a) and doped supraparticles (Figure 7.10b).

The FWHM of the reflectance bands increases with increasing the PNP diameter. For undoped pigments at 0° collecting angle, the FWHM of PhP-PNP173, PhP-PNP232 and PhP-PNP287 correspond to 60 nm, 74 nm and 121 nm, respectively (Figure 7.10a). FWHM determination at all collecting angles for undoped pigments composed of larger PNP (with diameters ≥ 260 nm) was not possible due to the asymmetry of the reflectance bands and the high background diffuse scattering.

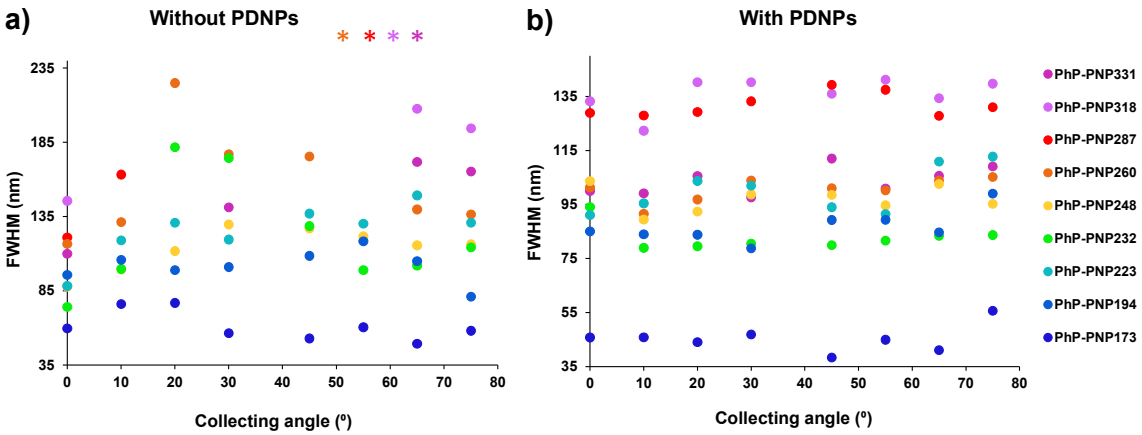

Figure 7.10: Full width at half maximum of the reflectance bands for the photonic pigments, from 0° to 75° viewing angles. **a)** Undoped photonic pigments; FWHM determination was not possible for all angles (*55° for PhP-PNP260; *20°-75° for PhP-PNP287, *10°-55° for PhP-PNP318 and *10°, 20°, 45°, 55° for PhP-PNP331). **b)** Pigments doped with 3 wt% of PDNPs. Pigments without PDNPs show very inconsistent bandwidths with collecting angle. Upon addition of PDNPs, a more constant FWHM for all collecting angles is obtained, due to more symmetric reflectance bands and lower background diffuse scattering.

The addition of PDNPs to the pigments structure, besides absorbing up to 60% of diffusely scattered light from pigments composed of larger PNP, resulted in more symmetric reflectance bands. This allowed to determine the FWHM of the reflectance bands at all collecting angles for the different photonic pigments. Doped supraparticles exhibit a more uniform and slightly broader reflectance bands, which resulted in more constant FWHM with increasing viewing angle, as shown in Figure 7.10b. This is indicative of more isotropic structures.

We used the bandwidth of the reflectance bands to estimate the gap to midgap ratio for doped and undoped photonic pigments. This gives a measure of the relative width of the pseudo-bandgap and corresponds to the ratio between the FWHM and the wavelength of maximum reflectance ($\Delta\lambda/\lambda_{max}$).[41] The gap to midgap ratio for doped (black dots) and undoped (blue dots) photonic pigments are represented in Figure 7.11a. The black and blue dots in Figure 7.11a, represents the gap to midgap ratio at the backscattering angle (0° collecting angle relative to incidence) and the error bars correspond to the average standard deviations of the gap to midgap ratio for collecting angles varying from 0° to 75°. The most striking feature of Figure 7.11a is the much smaller error bars on the gap to midgap ratio for photonic pigments doped with 3 wt% of PDNPs. This

clearly demonstrates the lower angular dependence of the optical properties reflected by the doped pigments.

Because the addition of PDNPs to the photonic structures not only lowers the contribution of diffuse scattering to the reflectance spectra, but also lowers the overall reflectance intensity, in Figure 7.11b is shown a comparison of the color saturation obtained for doped and undoped pigments, based on the differences in the maximum to minimum reflected intensity values for all collecting angles.

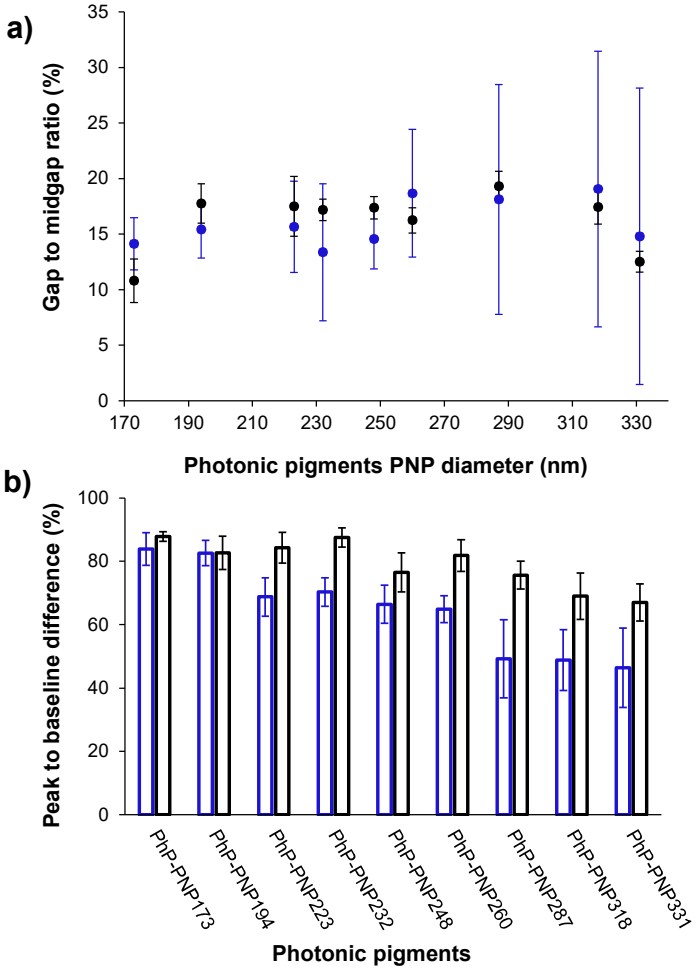

Figure 7.11: Angular dependence of the optical properties of doped and undoped photonic pigments. **a)** Gap to midgap ratios expressing the bandwidth of the stop-bands for undoped (blue dots) and doped (black dots) photonic pigments, at the backscattering angle. The error bars correspond to the standard deviation of the values obtained for all collecting angles; **b)** Average peak to baseline difference comparing the color saturation of doped (black columns) and undoped (blue columns) photonic pigments for all collecting angles. Error bars correspond to the standard deviation of the values obtained for the different collecting angle.

The lower the peak to baseline difference, the whiter the color appears. For undoped pigments, represented by the blue columns in Figure 7.11b, the peak to baseline difference largely decrease with increasing PNP diameter, which

indicates a strong color desaturation for red wavelengths. In contrast, the smaller decrease in the peak to baseline difference with increasing PNP diameter for pigments doped with PDNPs (represented by the black columns in Figure 7.11b), indicates a higher color saturation in comparison to undoped structures.

The optical properties of the pigment structures doped with 3 wt% PDNPs, are consistent with a more isotropic packing of PNP, because they show a lower dependence on the collecting angle. Despite the addition of a higher amount of PDNPs to the photonic structure may not be desirable because it also decreases the intensity of the reflectance band, the addition of 3 wt% of such a broad-spectrum absorber efficiently increased the peak to baseline difference, increasing thus, the color saturation. We indeed create saturated colors through isotropic structures.

7.6. Color appearance

Besides displaying optical and structural features akin to isotropic structures with short-range order, such as photonic glasses, the most striking characteristic of doped pigments is the lower contribution of diffuse scattering to the reflected colors. From the reflectance spectra at the backscattering angle, the x, y color coordinates of doped and undoped photonic pigments were calculated and represented in the CIE chromaticity diagram (Figure 7.12), where the color saturation is given by the distance to the white point ($x = 0.33$; $y = 0.33$).[42]

In the case of undoped photonic pigments (colored dots, Figure7.12a), only the ones composed PNP318 and PNP 333 are close to the white point, not only due to the higher diffuse scattering, but also due to the contribution of multiple diffraction bands as well as to single-particle scattering resonances (Section 7.5 and Figure A7.9 of Appendix 7). Upon doping the pigment structures with PDNPs (black dots, Figure7.12a) the color appearance in the CIE chromaticity diagram changes for more vivid and saturated hues, further away from the white point.

The variation of the perceived color with increasing the viewing angle was also compared for doped and undoped blue, green, and red photonic pigments (Figure 7.12b). Undoped pigments, represented by the colored symbols, exhibit low color variation with increasing viewing angle: the hue of undoped blue, green, and red pigments shifts to deep blue, cyan, and light pink, respectively, with increasing the viewing angle from 0° to 75°.

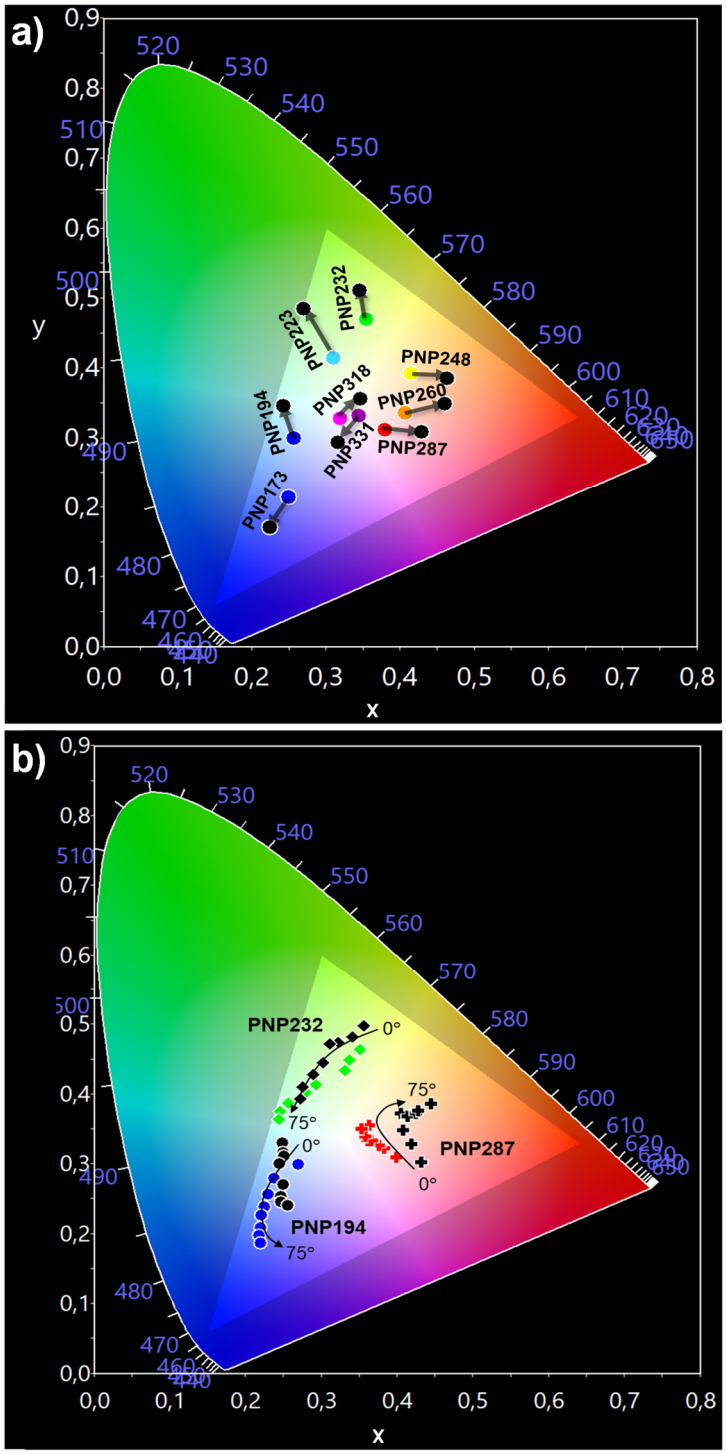

Figure 7.12: CIE chromaticity diagrams. **a)** x, y color coordinates at the backscattering angle for undoped (colored dots) and doped (black dots) photonic pigments. The addition of PDNPs shifts the color coordinates further away from the white point. **b)** Hue variation with increasing the viewing angle from 0° to 75° for undoped (colored symbols) and doped (black symbols) blue, green and red photonic pigments. Doped pigments exhibit more saturated hues with lower dependence on the viewing angles.

For pigments doped with PDNPs, represented by the black symbols (Figure 7.12b), the perceived colors exhibit even lower variation with increasing the

viewing angle, due to the more isotropic packing of PNP inside the pigment structures. In addition, for doped red pigments, the reflected hues no further go in the direction of the white point with increasing the viewing angle. Instead, their color shifts into a dark orange hue, because PDNPs lowers the contribution of diffuse scattering and increases the peak to baseline difference.

Reflectance optical microscopy images of doped and undoped pigments (Figure 7.13), show bright and vivid colored patches, whose size give an indication of the structural order degree inside the pigments structure. The disorder increase resulting from the co-assembly of PNP with 3 wt% of PDNPs, is noticed mostly for photonic pigments composed of PNP with diameters ≥ 223 nm (Figure 7.13). The color patches observed for doped pigments are restricted to the outermost layers close to supraparticle surface, whereas for undoped pigments large colored patches extending towards supraparticles center are visible. This is indicative of a more ordered packing of PNP inside undoped pigments structure. The random distribution of PDNPs mostly in the inner structure of doped pigments contributes to the reflectance of a more isotropic coloration, exhibiting more homogeneous and saturated hues.

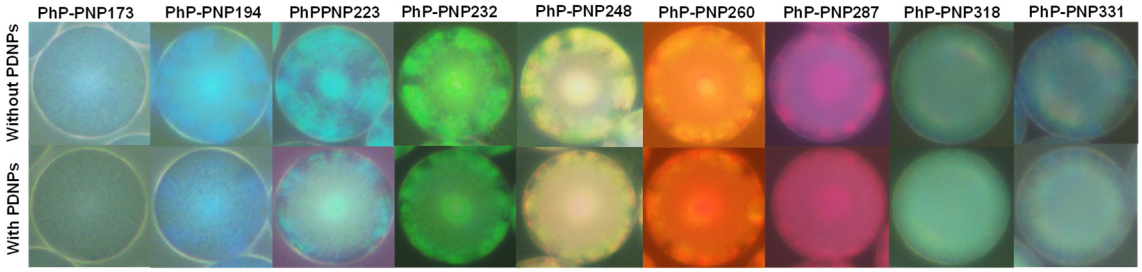

Figure 7.13: Reflectance optical microscopy of structural photonic pigments without (upper panel) and with PDNPs (lower panel). The patterns visible at the outer layers of undoped pigments that extends to the center of the supraparticle, is reflected by large (111) crystalline planes of the fcc structure. In the case of doped pigments, the size of the crystalline domains decreases and do not extend to the supraparticles center, reflecting thus, a more isotropic coloration.

The bright and multichromatic colored optical effect at PhP-PNP318 and PhP-PNP 331, assigned to grating diffraction[2,14,43-45] arising from the periodic arrangement of large PNP at supraparticle surface, are no longer visible for doped pigments (Figure 7.13). This clearly indicates a more disordered packing of PNP318 and PNP331 at supraparticles surface when co-assembled with PDNPs.

7.7. Further improving the saturation of red hues

To further increase the red color saturation, photonic pigments composed PNP287 were doped with PDNPs and carbon dots (3 wt% of each relative to the amount of PNP dispersion) and assembled at 50°C. The addition of carbon dots with a wavelength of maximum absorbance at $\lambda_{max} = 350$ nm, with a tail until 580 nm (Figure 7.14a), reduces the diffuse scattering at short wavelengths due to the selective absorption of blue light, but do not contribute to increase the structural disorder due to their small size (diameter lower than 10 nanometers).

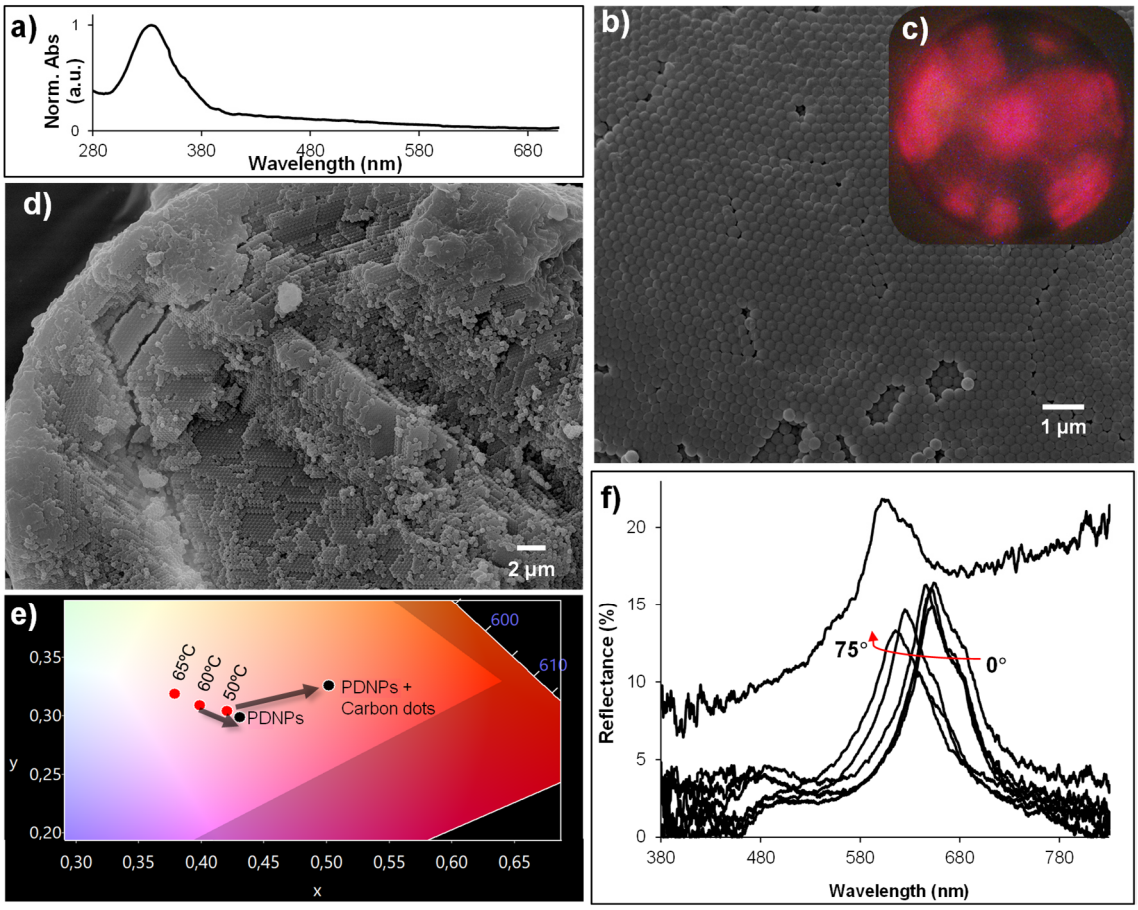

Figure 7.14: a) Absorption spectra of the carbon dots. **b)** SEM image of the supraparticle surface showing hexagonally packed PNP. **c)** Microscopy image in reflectance mode showing large colored patches with a dark red hue. **d)** SEM image of the supraparticle interior. **e)** CIE color map comparing the color saturation of red pigments: pigments doped with PDNPs assembled at 60°C reflect more saturated hues, but the pigments assembled at 50°C when doped with PDNPs and carbon dots shifts to much more saturated hues. **f)** Angle resolved reflectance of PhP-PNP287 doped with PDNPs and carbon dots.

The ordered packing of PNP at supraparticle surface (Figure 7.14b) and inside the pigment structure (Figure 7.14d) is visible in SEM images. This may be

related to the slower water evaporation inside the emulsion droplets composed of PNP, PDNPs and carbon dots, because the infiltration of such small particles in between PNP hinders water evaporation and could provide enough time for the PNP pack in the most energetically favored structures.[9] This is visible by the large size of the dark red colored patches in the reflectance microscopy image (Figure 7.14c).

Visibly narrow and sharp reflectance bands were obtained for collecting angles varying from 0° to 75° (Figure 7.14f), and only a small blue shift in the wavelength of maximum reflectance was observed with increasing the collecting angle. The contribution of diffuse scattering to the overall reflectance is negligible (Figure 7.14f). Despite the low intensity of the reflectance bands, the color saturation was greatly increased, as shown by the chromaticity diagram (Figure 7.14e).

These results reinforce the role of controlling the kinetics of water evaporation. Color saturation decreased with increasing the assembly temperature from 50°C to 65°C, due to a more disordered packing of PNP inside the pigments structure. In turn, the color saturation of pigments assembled at 60°C, doped with PDNPs, increased despite increasing the structural disorder. However, one can obtain ordered structures with highly saturated colors when co-assembled with PDNPs and carbon dots, if the PNP packing is not kinetically arrested by the rate of water evaporation, imposed by the assembly temperature.

7.8. Conclusions

The co-assembly of PDNPs and PNP proved to be an efficient strategy to increase the saturation of the colors reflected from spherical photonic pigments. The randomly distributed PDNPs not only decrease the contribution of diffuse scattering through absorption, but also contributed to a more disorder packing of PNP inside the pigment structures, resulting in short-range order correlations.

Due to the higher peak to baseline difference, highly saturated colors are reflected from the isotropic structure of doped pigments in comparison to undoped ones. Furthermore, they also exhibit more homogeneous optical properties with increasing the collecting angle. The lower angular dependence of the optical properties of doped pigments, given by the smaller standard deviation of the gap to midgap ratios, results in isotropic colors with a more homogeneous hue and saturation even for wide viewing angles.

Despite the low intensity of the reflectance bands, the addition of carbon dots indeed contributed to further increase the color saturation of pigments reflecting colors above 600 nm, due to negligible contribution of diffuse scattering to the reflectance properties.

The doped pigments described here, hold great potential for use in color reflective displays, not only because they reflect colors with low iridescence properties but also due to the low decrease in color saturation for wide viewing angles. Doped pigments reflect constant optical properties with highly saturated structural colors. In addition, both doped and undoped supraparticles can be used as dispersive pigments for paints and coatings, due to their non-fading properties, and have the potential to replace the traditional coloring solutions using light absorbing pigments and dyes.

7.9. References

1. Zhao, Y., Shang, L., Cheng, Y. & Gu, Z. Spherical Colloidal Photonic Crystals. *Acc. Chem. Res.* **47**, 3632–3642 (2014).
2. Vogel, N., Utech, S., England, G. T., Shirman, T., Phillips, K. R., Koay, N., Burgessd, I. B., Kolle, M., Weitz, D. A. & Aizenberg, J. Color from hierarchy: Diverse optical properties of micron-sized spherical colloidal assemblies. *PNAS* **112**, 10845–10850 (2015).
3. Teshima, M., Seki, T., Ryuji K., Takeuchi, S., Yoshioka, S. & Takeoka, Y. Preparation of structurally colored, monodisperse spherical assemblies composed of black and white colloidal particles using a micro-flow-focusing device. *J. Mater. Chem. C* **3**, 769–777 (2014).
4. Sun, C., Zhao, X., Zhao, Y., Zhu, R. & Gu, Z. Fabrication of Colloidal Crystal Beads by a Drop-Breaking Technique and Their Application as Bioassays. *Small* **4**, 592–596 (2008).
5. Schertel, L., Siedentop, L., Meijer, J.-M., Keim, P., Aegerter, C. M., Aubry, G. J. & Maret, G. The Structural Colors of Photonic Glasses. *Adv. Opt. Mater.* **7**, 1900442 (2019).
6. Noh, H., Liew, S.-F., Saranathan, V., Mochrie, S. G. J., Prum, R. O., Dufresne, E. R. & Cao, H. How Noniridescent Colors Are Generated by Quasi-ordered Structures of Bird Feathers. *Adv. Mater.* **22**, 2871–2880 (2010).
7. Gottardo, S., Sapienza, R., García, P. D., Blanco, A., Wiersma, D. S. & López, C. Resonance-driven random lasing. *Nat. Photonics* **2**, 429–432 (2008).

8. Forster, J. D., Noh, H., Liew, S.-F. Saranathan, V., Schreck, C. F., Yang, L., Park, J.-G., Prum, R. O., Mochrie, S. G. J., Hern, C. S. O., Cao, H. & Dufresne, E. R. Biomimetic Isotropic Nanostructures for Structural Coloration. *Adv. Mater.* **22**, 2939–2944 (2010).

9. Wang, J., Yang, L., Lin, D., Luo, Y., Li, D. & Meng, Q. Optical studies of random disorder of colloidal photonic crystals and its evolution in evaporation induced self-assembly. *J. Chem. Phys.* **137**, 234111 (2012).

10. Garcia, P. D., Sapienza, R. & López, C. Photonic Glasses: A Step Beyond White Paint. *Adv. Mater.* **22**, 12–19 (2010).

11. Xiao, M., Hu, Z., Wang, Z., Li, Y., Tormo, A. D., Thomas, N. L., Wang, B., Gianneschi, N., C., Shawkey, M. D. & Dhinojwala, A. Bioinspired bright noniridescent photonic melanin supraballs. *Sci. Adv.* **3**, 1701151 (2017).

12. Goerlitzer, E. S. A., Taylor, R. N. K. & Vogel, N. Bioinspired Photonic Pigments from Colloidal Self-Assembly. *Adv. Mater.* **30**, 1706654 (2018).

13. Sakai, M., Seki, T. & Takeoka, Y. Bioinspired Color Materials Combining Structural, Dye, and Background Colors. *Small* **14**, 1800817 (2018).

14. Sakai, M., Takeoka, Y., Kim, H., Arai, Y., Teratani, T., Kawai, Y., Kuwahara, Y., Abe, K., Kuwana, Y., Ikeda, K. & Yamada, K. Monodisperse Silica Nanoparticle-Carbon Black Composite Microspheres as Photonic Pigments. *ACS Appl. Nano Mater.* **3**, 7047–7056 (2020).

15. Yukikazu Takeoka, Iwata, M., Seki, T., Khanin Nueangnoraj, H. N. & Yoshioka, S. Structural Coloration of a Colloidal Amorphous Array is Intensified by Carbon Nanolayers. *Langmuir* **34**, 4282–4288 (2018).

16. Iwata, M., Teshima, M., Seki, T. & Yoshioka, S. Bio-Inspired Bright Structurally Colored Colloidal Amorphous Array Enhanced by Controlling Thickness and Black Background. *Adv. Mater.* **29**, 1605050 (2017).

17. Huang, D., Zeng, M., Wang, L., Zhang, L. & Cheng, Z. Biomimetic colloidal photonic crystals by co-assembly of polystyrene nanoparticles and graphene quantum dots. *RSC Adv.* **8**, 34839–34847 (2018).

18. Nijs, B. D., Dussi, S., Smallenburg, F., Meeldijk, J. D., Groenendijk, D. J., Filion, L., Imhof, A., Blaaderen, A. V. & Dijkstra, M. Entropy-driven formation of large icosahedral colloidal clusters by spherical confinement. *Nat. Mater.* **14**, 56–60 (2015).

19. Kim, B. S., Jeon, S., Yi, G., Heo, C. & Choi, J. H. Optofluidic Assembly of Colloidal Photonic Crystals with Controlled Sizes, Shapes, and Structures. *Adv. Mater.* **20**, 1649–1655 (2008).

20. Takeoka, Y., Yoshioka, S., Takano, A., Arai, S., Nueangnoraj, K., Nishihara, H., Teshima, M., Ohtsuka, Y. & Seki, T. Production of Colored Pigments with Amorphous Arrays of Black and White Colloidal Particles. *Angew. Chem.* **125**, 7402–7406 (2013).

21. Dumanli, G. A. & Savin, T. Recent advances in the biomimicry of structural colours. *Chem. Soc. Rev.* **45**, 6698–6724 (2016).

22. Saranathan, V., Forster, J. D., Noh, H., Liew, S.-F., Mochrie, S. G. J., Cao, H., Dufresne, E. R. & Prum, R. O. Structure and optical function of amorphous photonic nanostructures from avian feather barbs: a comparative small angle X-ray scattering (SAXS) analysis of 230 bird species. *J. R. Soc. Interface* **9**, 2563–2580 (2012).

23. Xiao, M., Li, Y., Allen, M. C., Deheyn, D. D., Yue, X., Zhao, J., Gianneschi, N. C., Shawkey, M. D. & Dhinojwala, A. Bio-Inspired Structural Colors Produced via Self-Assembly of Synthetic Melanin Nanoparticles. *ACS Nano* **9**, 5454–5460 (2015).

24. Wei, Q., Zhang, F., Li, J., Li, B. & Zhao, C. Oxidant-induced dopamine polymerization for multifunctional coatings. *Polym. Chem* **1**, 1430–1433 (2010).

25. Ding, Y. H., Floren, M. & Tan, W. Mussel-inspired polydopamine for bio-surface functionalization. *Biosurface and Biotribology* **2**, 121–136 (2016).

26. Harun-ur-rashid, M., Imran, B., Seki, T., Ishii, M. & Nakamura, H. Angle-Independent Structural Color in Colloidal Amorphous Arrays. *Chem.Phys.Chem.* **11**, 579–583 (2010).

27. Shi, L., Zhang, Y., Dong, B., Zhan, T., Liu, X. & Zi, J. Amorphous Photonic Crystals with Only Short-Range Order. *Adv. Mater.* **25**, 5314–5320 (2013).

28. García, P. D., Sapienza, R., Blanco, Á. & López, C. Photonic Glass: A Novel Random Material for Light. *Adv. Mater.* **19**, 2597–2602 (2007).

29. Shklover, V., Braginsky, L. & Hofmann, H. Domain structure and optical properties of colloidal photonic crystal. *Mater. Sci. Eng. C* **26**, 142–148 (2006).

30. Wiersma, D. S. Photonic crystals with controlled disorder. *Phys. Rev. A* **84**, 023813 (2011).

31. Samatham, R., Jacques, S. L. & Campagnola, P. Optical properties of mutant versus wild-type mouse skin measured by reflectance-mode confocal scanning laser microscopy (rCSLM). *J. Biomed. Opt.* **13**, 1–7 (2008).

32. Choi, T. M., Lee, G. H., Kim, Y.-S., Park, J-G., Hwang, H. & Kim, S-H. Photonic Microcapsules Containing Single-Crystal Colloidal Arrays with Optical Anisotropy. *Adv. Mater. 2019,* **31**, 1900693 (2019).

33. Magkiriadou, S., Park, J., Kim, Y. & Manoharan, V. N. Absence of red structural color in photonic glasses, bird feathers, and certain beetles. *Phys. Rev. E* **90**, 062302 (2014).

34. Dong, B. Q., Liu, X. H., Zhan, T. R., Jiang, L. P., Yin, H. W., Liu, F. & Zi, J. Structural coloration and photonic pseudogap in natural random close-packing photonic structures. *Opt. Express* **18**, 14430–14438 (2010).

35. Aguirre, C., Reguera, E. & Stein, A. Colloidal Photonic Crystal Pigments with Low Angle Dependence. *ACS Appl. Mater. Interfaces* **2**, 3257–3262 (2010).

36. Astratov, V. N. Interplay of order and disorder in the optical properties of opal photonic crystals. *Phys. Rev. B* **66**, 165215 (2002).

37. Bai, L., Mai, V. C., Lim, Y., Hou, S., Möhwald, H. & Duan, H. Large-Scale Noniridescent Structural Color Printing Enabled by Infiltration-Driven Nonequilibrium Colloidal Assembly. *Adv. Mater.* **30**, 1705667 (2018).

38. Song, D.-P., Zhao, T. H., Guidetti, G., Vignolini, S. & Parker, R. M. Hierarchical Photonic Pigments via the Confined Self-Assembly of Bottlebrush Block Copolymers. *ACS Nano* **13**, 1764–1771 (2019).

39. Kohri, M., Nannichi, Y., Taniguchi, T. & Kishikawa, K. Biomimetic non-iridescent structural color materials from polydopamine black particles that mimic melanin granules. *J. Mater. Chem. C* **3**, 720–724 (2015).

40. Kohri, M., Yanagimoto, K., Kawamura, A., Hamada, K., Imai, Y., Watanabe, T., Ono, T., Taniguchi, T. & Kishikawa, K. Polydopamine-Based 3D Colloidal Photonic Materials: Structural Color Balls and Fibers from Melanin-Like Particles with Polydopamine Shell Layers. *ACS Appl. Mater. Interfaces* **10**, 7640–7648 (2018).

41. Takeoka, Y., Yoshioka, S., Teshima, M., Takano, A., Harun-Ur-Rashid, M. & Seki, T. Structurally Coloured Secondary Particles Composed of Black and White Colloidal Particles. *Sci. Rep.* **3**, 02371 (2013).

42. Hunt, R. W. G. & Pointer, M. R. *Measuring Colour, John Wiley & Sons, Ltd* (2011).

43. Kim, J. Bin, Lee, S. Y., Lee, J. M. & Kim, S. Designing Structural-Color Patterns Composed of Colloidal Arrays. *ACS Appl. Mater. Interfaces* **11**, 14485–14509 (2019).

44. Rastogi, V., Melle, S., Calderón, O. G., García, A. A., Marquez, M. & Velev, O. D. Synthesis of Light-Diffracting Assemblies from Microspheres and Nanoparticles in Droplets on a Superhydrophobic Surface. *Adv. Mater.* **20**, 4263–4268 (2008).

45. Ohnuki, R., Sakai, M., Takeoka, Y. & Yoshioka, S. Optical Characterization of the Photonic Ball as a Structurally Colored Pigment. *Langmuir* **36**, 5579−5587 (2020).

7.10. Appendix 7

7.10.1. SEM imaging 191
7.10.2. FIB-SEM imaging..... 194
7.10.3. RCM images..... 195
7.10.4. Angle resolved reflectance spectra..... 196

7.10.1. SEM imaging

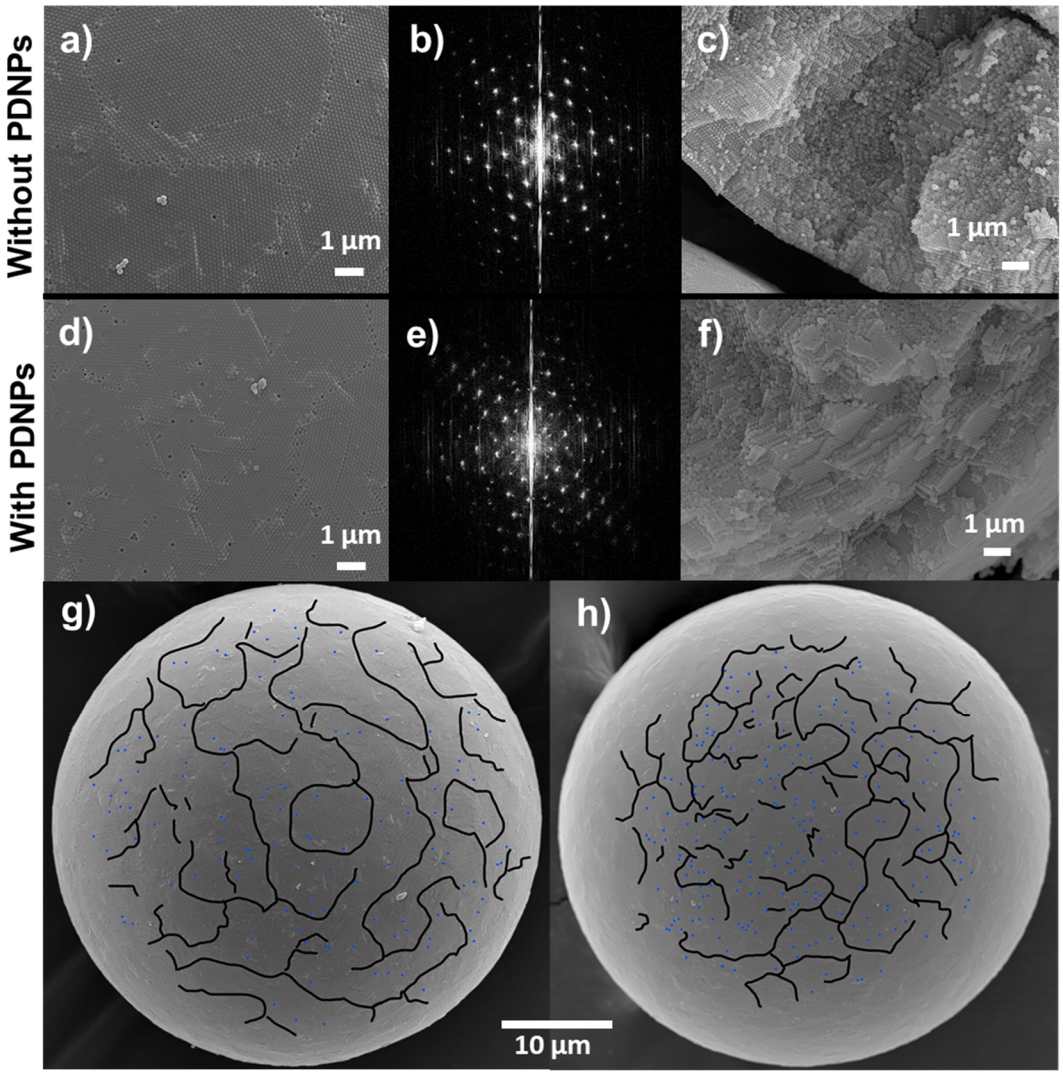

Figure A7.1: SEM images of undoped and doped photonic pigments composed of PNP173. **a)** surface of PhP-PNP173; **b)** 2D-FFT pattern of SEM image in a) indicating long-range ordered packing of PNP; **c)** large number of concentric ordered layers of PNP inside undoped supraparticles. **d)** surface of PhP-PNP173-PD showing a high number of voids (short-range defects); **e)** 2D-FFT pattern of SEM image in d); **f)** internal packing of PNP inside doped pigments. **g)** PhP-PNP173 supraparticle and **h**) PhP-PNP173-PD supraparticle. The main difference between the two structures is the increased number of point defects (highlighted by blue dots), although the size of the crystalline domains separated by boundary scars (highlighted by black lines) diminishes for doped structures.

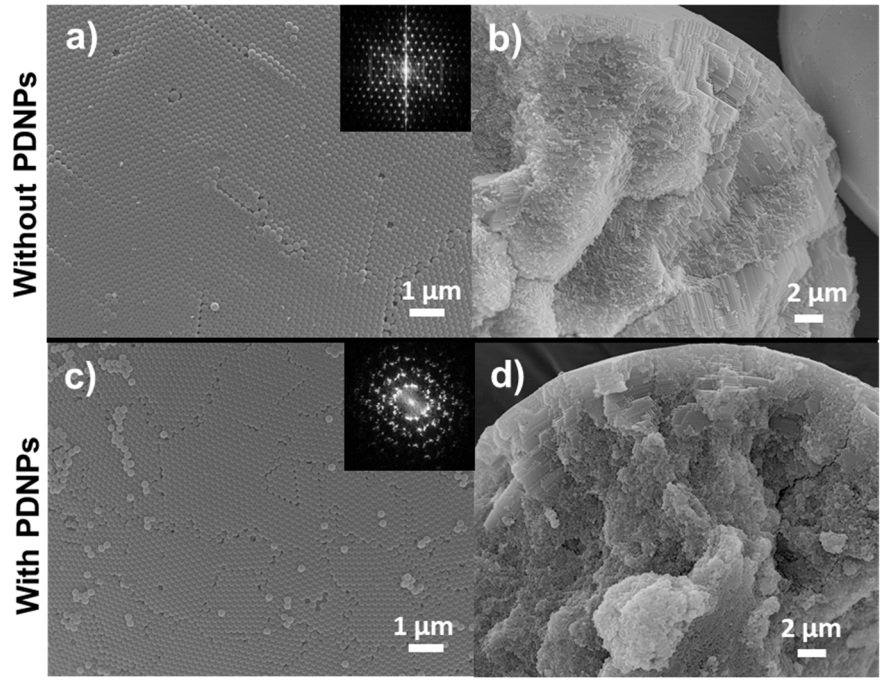

Figure A7.2: SEM images of surface (left panel) and inner structure (right panel) of undoped *vs* doped photonic pigments composed of PNP223. **a)** and **b)** PhP-PNP223. **c)** and **d)** PhP-PNP223-PD. Inset shows the FFT pattern from the SEM images of the pigments surface. Besides the smaller crystalline domains size on supraparticles surface the number of concentric ordered layer of PNP is clearly smaller for doped pigments.

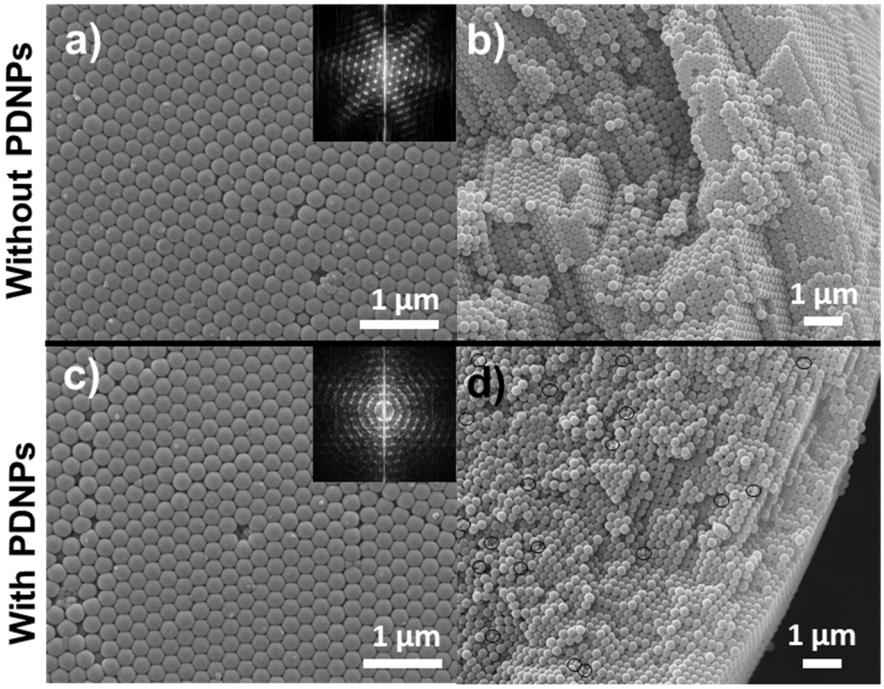

Figure A7.3: SEM images of surface (left panel) and inner structure (right panel) of undoped *vs* doped photonic pigments composed of PNP248. **a)** and **b)** PhP-PNP248. **c)** and **d)** PhP-PNP248-PD. Inset shows the FFT pattern from the SEM images of the pigments surface. The random distribution of PDNPs, highlighted by the black circles in **d)** is mainly visible towards supraparticle center. Undoped pigments shows highly ordered PNP, both at pigments surface and interior in comparison to doped ones, where only the outermost layers are highly packed.

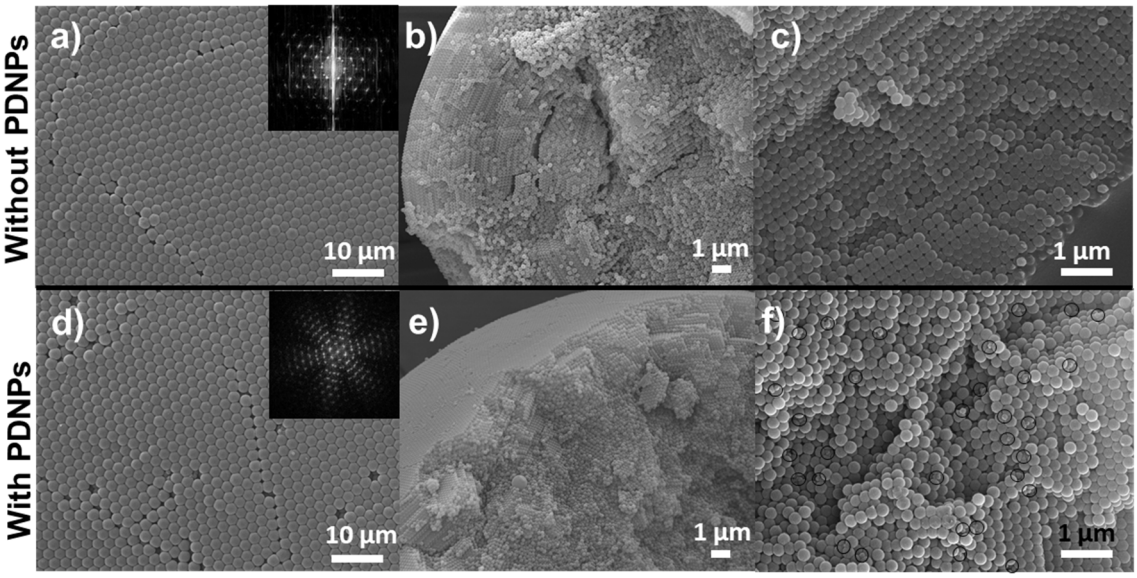

Figure A7.4: SEM images of photonic pigments composed of PNP260 without (upper panel) and with PDNPs (lower panel). **a)** and **b)** shows PhP-PNP260 surface and interior; **c)** zoom in of the inner packing of PNP in **b)**. **d)** and **e)** shows PhP-PNP260-PD surface and interior; **f)** zoom in of the inner structure in **e)** showing the random distribution of PDNPs, highlighted by the black circles. Inset corresponds to the FFT pattern from the SEM images of the pigments surface.

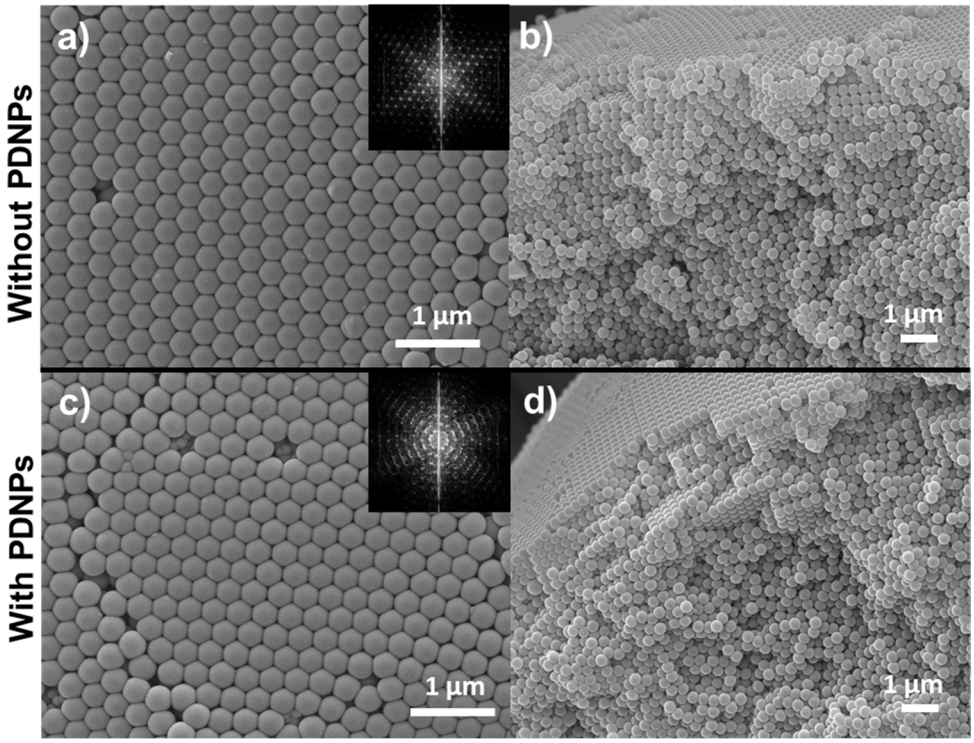

Figure A7.5: SEM images of surface (left panel) and inner structure (right panel) of undoped *vs* doped photonic pigments composed of PNP318. **a)** and **b)** PhP-PNP318. **c)** and **d)** PhP-PNP318-PD. Inset shows the FFT pattern from the SEM images of the pigments surface. PDNPs are visible in the point defects at supraparticles surface.

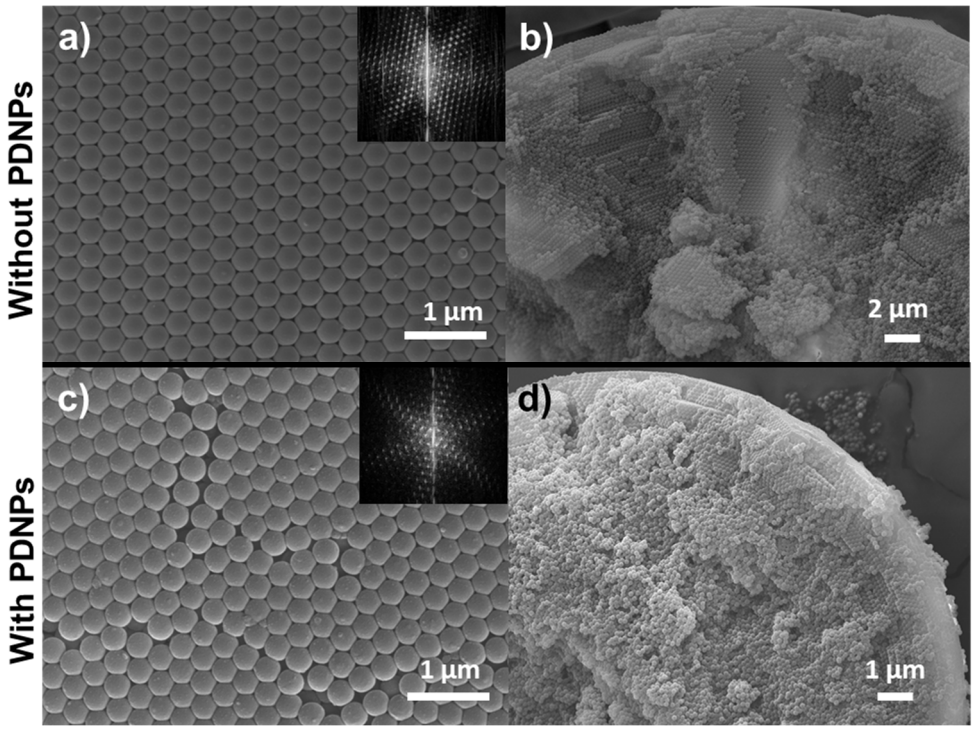

Figure A7.6: SEM images of surface (left panel) and inner structure (right panel) of undoped *vs* doped photonic pigments composed of PNP331. **a)** and **b)** PhP-PNP331. **c)** and **d)** PhP-PNP331-PD. Inset shows the FFT pattern from the SEM images of the pigments surface. Undoped pigments shows highly ordered PNP, both at pigments surface and interior. In contrast, when doped with PDNPs, a more disordered packing of PNP is visible at supraparticle surface and the number of ordered layers towards the center diminishes.

7.10.2. FIB-SEM imaging

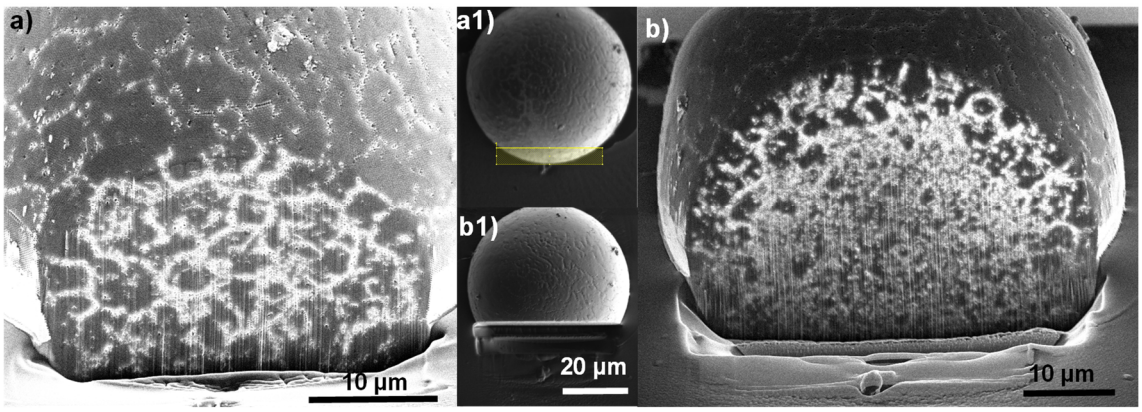

Figure A7.7: FIB-SEM images of green pigments doped with 3 wt% of PDNPs, PhP-PNP232-PD, at different depths. **a)** and **a1)** Cross-section at 5 µm depth. **b)** and **b1)** Cross-section at 10 µm depth. Disorder increase towards supraparticle center. The larger crystalline domains closer to supraparticle surface diminishes in size with depth increase towards supraparticle center, and a more isotropic arrangement of PNP is obtained.

7.10.3. RCM images

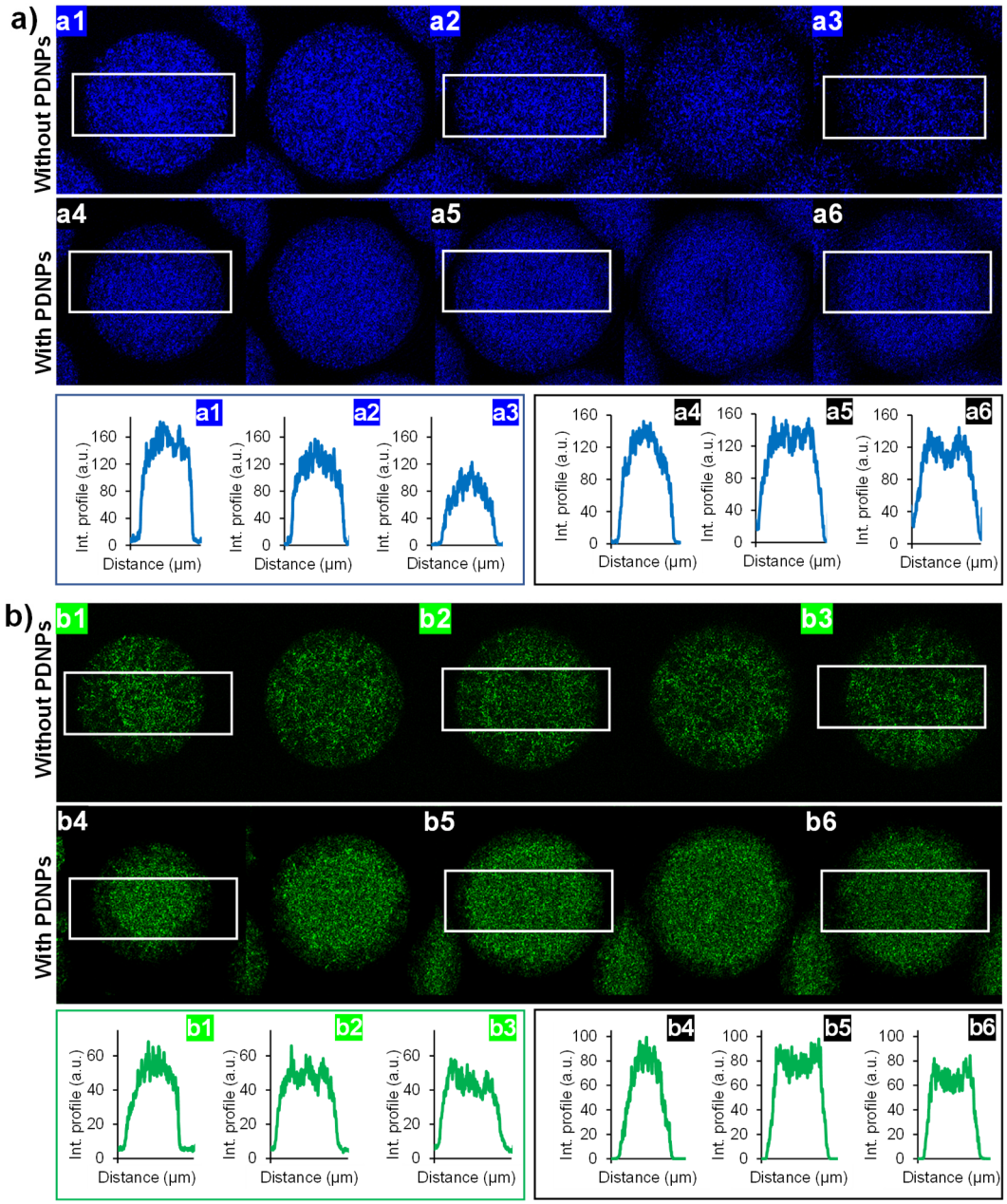

Figure A7.8: Undoped *vs* doped with 3 wt% PDNPs RCM images of supraparticles inner structure illuminated with 633 nm laser light for blue, PhP-PNP194 (**a**) and green photonic pigments, PhP-PNP323 (**b**). The Z-depth increases from the left to the right; the distance between each slice corresponds to 5 μm. The white rectangle denote the area used to trace the intensity profile of light interacting with the structure for three different depths (a1, a4, b1 and b4: $\sim 15\ \mu m$ depth); (a2, a5, b2 and b5: $\sim 25\ \mu m$ depth) (a3, a6, b3 and b6: $\sim 35\ \mu m$ depth). The pattern becomes increasingly brighter towards supraparticle center particularly for pigments doped with PDNPs, indicating higher diffuse scattering from disordered regions. Only a thin darker region is observed at the supraparticle surface of doped pigments contrarily to undoped ones, where bright disordered regions in between darker regions, that corresponds to bigger crystalline domains, are uniformly spread across the entire supraparticle. Light attenuation with increasing depth is negligible.

7.10.4. Angle resolved reflectance spectra

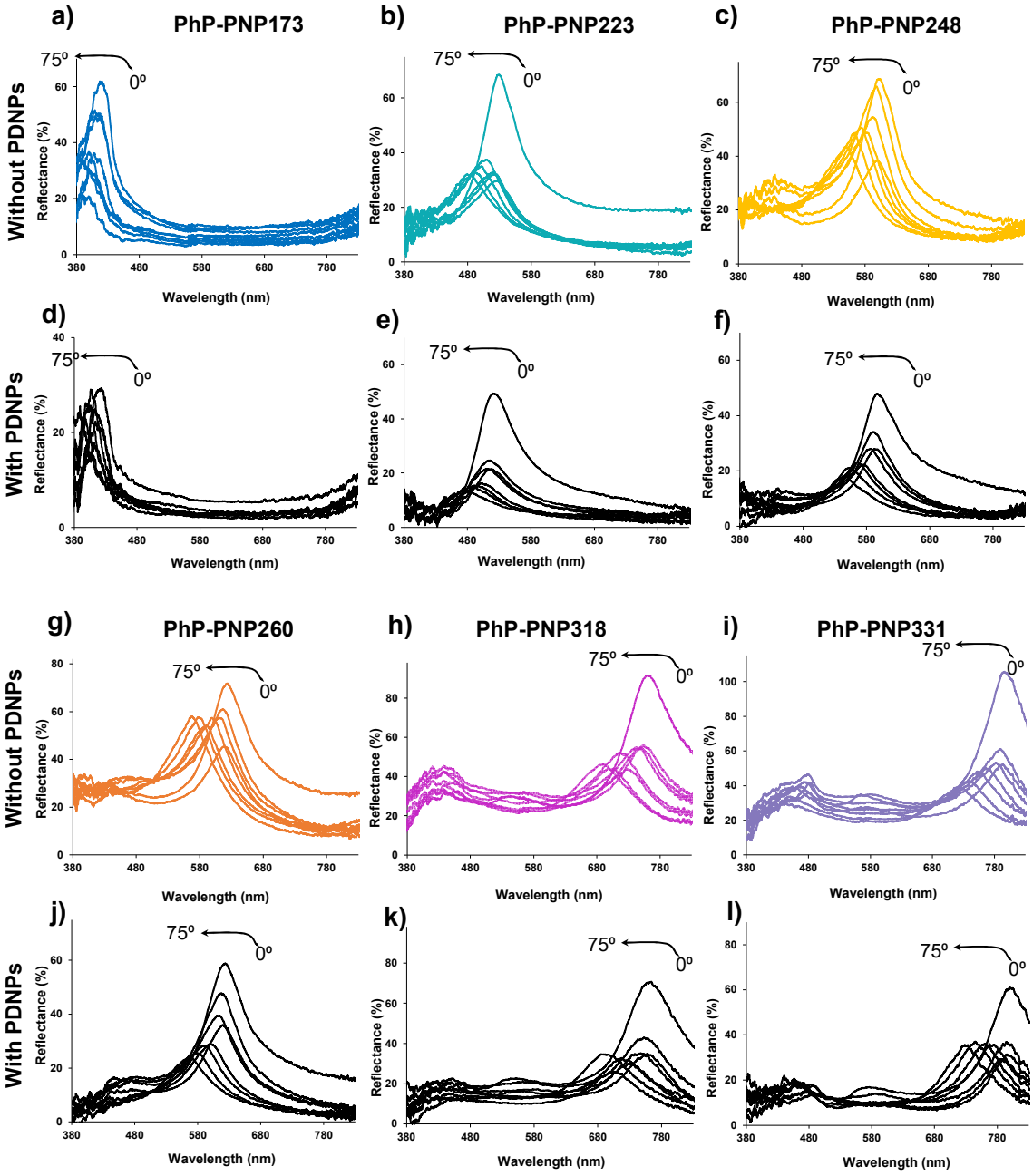

Figure A7.9: Angle resolved reflectance measurements of undoped vs doped photonic pigments for viewing angles varying from 0º to 75º. **a)** and **d)** correspond to deep blue PhP-PNP173 and PhP-PNP173-PD, respectively. **b)** and **e)** correspond to cyan PhP-PNP223 and PhP-PNP223-PD, respectively. **c)** and **f)** correspond to yellow PhP-PNP248 and PhP-PNP248-PD, respectively. **g)** and **j)** correspond to orange PhP-PNP260 and PhP-PNP260-PD, respectively. **h)** and **k)** correspond to PhP-PNP318 and PhP-PNP318-PD, respectively. **i)** and **l)** correspond to PhP-PNP331 and PhP-PNP331-PD, respectively. Absolute intensity values cannot be compared because it depends on the amount of sample measured.

8. Water-born polymer coatings with non-iridescent structural color

In this chapter we describe an efficient, simple, and environmentally friendly structural color solution for water-born polymer coatings industry. This is based on the dispersion of the spherical photonic pigments in aqueous dispersions of polymer nanoparticles to produce structurally colored water-born polymer coatings after water evaporation and film formation. These photonic pigments are highly stable in the wet paint formulation and thus were able to maintain their optical properties when encapsulated in the polymer films. This approach is an extraordinary alternative to the fade-prone conventional coloring solutions for water-born polymer coatings.

8.1. Water-born polymer coatings

Driven by environmental concerns, the demand in coatings industry for water-borne coatings continues to increase as worldwide markets switch from organic-solvent-based to water-born coatings. Water-borne coatings are greener because water is used as a diluent instead of organic solvents, thus reducing the release of volatile organic compound (VOC).[1]

Water dispersed polymer nanoparticles (i.e., latex) were found to be a good alternative to solvent-borne coatings and have been successfully used to this end.[2] They are widely applied in building and construction; automotive; corrosion protection, wood, marine or packaging.

8.1.1. Introducing color into water-born polymer coatings

The introduction of color in water-born polymer coatings is either for aesthetic reasons and market appeal or because of functional demands and is accomplished by incorporating dyes and pigments into the polymer aqueous dispersions.

In the coatings industry for coloring applications, the main components are the film forming ingredient, which are essentially polymeric materials that have the capability of forming films, and the colorants dispersed in the medium. The second imparts color and opacity to the cured films, while the first encapsulates the colorants after conversion to a solid film.[3]

The global colorant market is expected to thrive, not only due to the rising demand for colorants with the best possible performance properties but also due to the increased consumer preference towards environmentally responsible products.[3]

8.1.1.1. Dyes and pigments

Dyes and pigments have an extensive range of applications from textiles to paper, paints, coatings, plastics, construction, cosmetics, food, glass, automotive, printing inks, etc. The difference between these two colorants is that dyes are soluble in the media being colored and thus disperse at a molecular level, while pigments are insoluble and are dispersed as particles. Dyes provide bright and intense colors through electronic transitions between molecular orbitals, associated with the selective absorption of UV/Vis radiation from the chromophore group.[4,5]

On the other hand, pigments are colored, white, or black particulate organic or inorganic solids, which cannot only absorb but also scatter light. Organic and inorganic pigments properties depend on the physical characteristics of its particles, such as size and shape, and have higher physical and chemical stability in comparison to dyes.[6]

Pigments and dyes, although primarily used to impart color to polymer paints and make it attractive to the consumer can also perform other useful functions more wide-ranging than their coloring properties, which have a dramatic effect on the photostability of the polymer coating itself.[7-9] For example mechanical reinforcement or the inhibition of polymer degradation (i.e., by absorbing and/or scattering UV light).[10-12]

The main degradation process of pigments and dyes are related to photobleaching, resulting from photochemical oxidation or reduction mechanisms that originate free radicals, either by electron/energy transfer or hydrogen abstraction reactions, compromising the molecular stability and promoting degradation of both colorants and polymeric matrices.[13-16]

Polymer coatings such as paints and varnishes, especially the ones colored with organic pigments or dye molecules easily fade or change color over time or upon exposure to light and weathering, as a result of the limited photostability of the constituent pigments and dyes, that can also pose toxicity and formulation issues.[8,17] While fading requires regular repainting of goods that are intended for extended use, especially outdoors, the consequences are even more disastrous for works of art and decoration pieces, where fading or discoloration can obscure or corrupt the artist's aesthetic intentions. In addition, the waste generated during the processing and use of conventional dyes and pigments, which contain organic and inorganic harmful substances, with unfavorable influences on human health and in the environment, increased the concerns relative to the colorants industry.[18-20]

Therefore, coloration free from photobleaching or toxic materials is nowadays a central goal in the development of paints and inks.[21-24] In this sense, the structural colors exhibited by photonic pigments are one of the most promising candidates to overcome these limitations, because they offer the possibility of obtaining fade-free and nontoxic, water-based paints.[25-29]

8.1.1.2. Photonic pigments

The bright and dazzling structural colors of photonic pigments arise from interference of light scattered from inhomogeneities in the refractive index of microstructures, spaced at scales comparable to optical wavelengths. Thus, they interact with visible light in an entirely different way to conventional colorants: rather than absorbing light, they selectively reflect particular wavelengths through constructive interference.[30,31] Therefore, structural color is not susceptible to fading unless the microstructure is destroyed.[32]

Structural pigments are of interest for coloration in the near future, not just for coatings and paints industry but also for textiles or consumables, as they can be achieved with biocompatible and environmentally friendly materials.[33,34]

The photonic pigments assembled in Chapter 6 and 7, exhibit a bright macroscopic color appearance to the naked eye (Figure 8.1). They display saturated and non-iridescent structural colors, where both the periodicity and degree of order was controlled in order to obtain several hues with different color saturation.

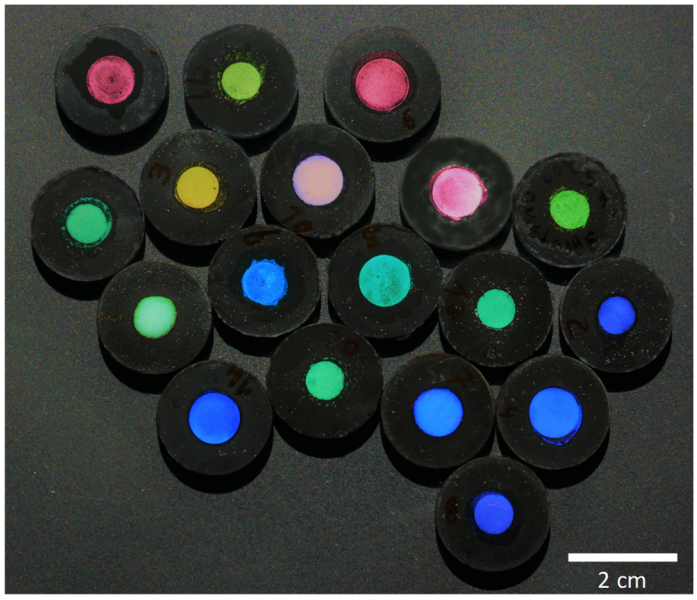

Figure 8.1: Macroscopic color appearance of the assembled spherical photonic pigments reflecting colors covering the entire visible light range.

These pigments are composed of a closed-packed arrangement of polymer nanoparticles (PNP) with a compact and stable structure due to the strong interactions between the functional groups at the PNP surface. Because we were able to precisely tune the ordered/disordered packing of PNP inside the pigment

structures, allowed us to obtain non-iridescent pigments, displaying either a uniform and matte color appearance or a vibrant and shining one.
These pigments, inspired by nature's coloration strategies, hold promise as a replacement for toxic and fade-prone absorptive colorants, most prominently in the fabrication of stable and sustainable water-born colored coating.

8.1.2. Coloration of water-born polymer coatings with spherical photonic pigments

To obtain structurally colored films, these spherical photonic pigments were added to aqueous polymer dispersions, intended for use in coatings, such as paints and varnishes. Due to the pigments inherent photostability the color of the coatings would present higher durability when compared to the traditional dye-based colored coatings. These new pigments provide fade-free, non-toxic, water-based coatings and have the potential to substitute aromatic dyes and other toxic pigments in different applications.
The different stages involved in the formation of a polymer film from a water dispersion of polymer nanoparticles and photonic pigments are shown in Figure 8.2. As water start to evaporate, film drying leads to a densely close-packed arrangement of the polymer particles and photonic pigments (stage I).[2,35,36] This is followed by particle deformation via capillary, osmotic, and surface forces, which occurs if the film is above the minimum film formation temperature (near the polymer's glass transition temperature, Tg, in the presence of water), to yield a nascent film constituted by space-filling polyhedral in close contact (stage II).
These void-free films still have weak interfaces between the particles, which are strengthened by polymer chain diffusion among adjacent particles. Diffusion occurs at temperatures above the Tg of the polymer nanoparticles, until complete healing of the interface by interdiffusion of the polymer chains and formation of entanglements across the interfaces between particles, to form a mechanically rigid film (stage III) that encapsulates the photonic pigments.[2,35,36] This results in a uniformly and structurally colored film. The degree of entanglements formed between particles determines how strong the interface is.

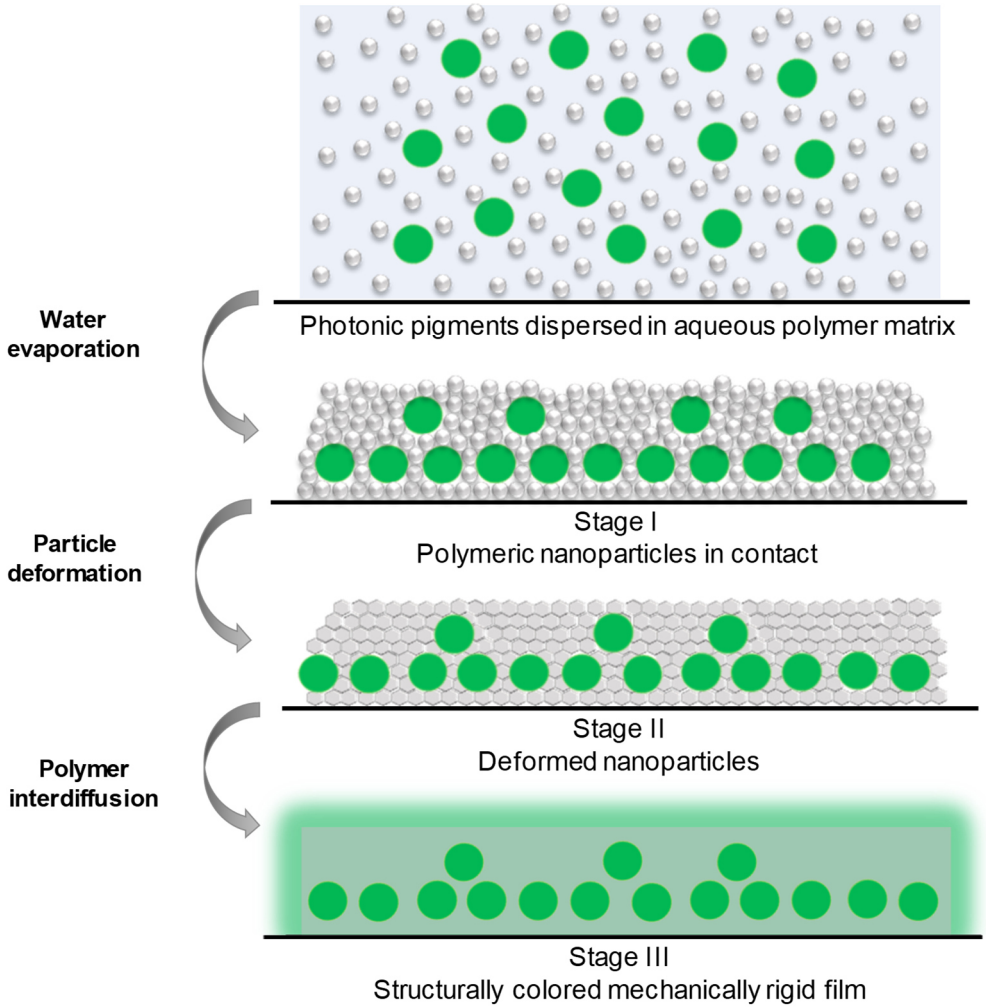

Figure 8.2: Schematic representation of the formation process of a structurally colored film from an aqueous dispersion of polymer nanoparticles (represented by the small white particles) and spherical photonic pigments (represented by the large green spheres).

In order to control other properties of the coatings such as viscosity, drying time, opacity, stability and ease of application, other compounds are added to the mixture, in small amounts (up to ~ 5% by weight), that substantially improve or modify the coating properties.[37,38]

Here, the spherical photonic pigments were incorporated in aqueous based polymer paints and applied as non-iridescent structurally colored pigments to obtain colorful and homogeneous polymer coating films, making the approach suitable for rapid implementation.

The novelty here is the use of an easily dispersible and stable dry powder composed of spherical photonic pigments without iridescence, irrespective of their ordered or disordered structure, which impart non-fading structural coloration into water-born polymer coatings.

8.2. Experimental procedure

The pigments used to introduce color into water-born polymer coatings were obtained in Chapter 6 and 7. Before being dispersed in the aqueous dispersion, photonic pigments were washed with *n*-hexane to remove the oil phase from the emulsification procedure and dried at room temperature. A dry pigment powder was obtained. The film-former of the water-born coatings are poly(butyl methacrylate) (PBMA) polymer nanoparticles because of their low glass transition temperature (Tg).

Photonic paints were produced by dispersing the photonic pigments (at a maximum solid content $\leq$ 10%, relative to the amount of aqueous polymer dispersion) in a high solid content (up to 40%) aqueous dispersion of PBMA nanoparticles.

These spherical photonic pigments are easily dispersible and stable in the aqueous polymer dispersion. When using pigments assembled without adding polydopamine nanoparticles (PDNPs), they were used as additive. Glycerol was also used as additive.

The photonic paints were homogenized by vortex mixing before applied to different substrates, such as flexible transparencies of cellulose acetate or glass coverslips. The uniform distribution of pigments in the aqueous polymer dispersion is a crucial parameter to obtain homogeneously colored water-based coatings.

Water evaporation was performed at ambient temperature and humidity conditions. The coatings obtained after the curing process resulted in structurally colored and mechanically rigid films.

8.2.1. Different compositions of the photonic paints

The optimum composition for obtaining water-born coatings colored with spherical photonic pigments, was achieved with only four different components. Different combinations and proportions were formulated (Table 8.1). The experimental procedure to obtain the structurally colored coatings is depicted in Figure 8.3. The inset show the catechol units at PDNPs surface responsible for its negative Zeta potential in aqueous media.

Table 8.1: Weight composition of the wet photonic paint with respect to the amount of aqueous polymer dispersion.

	Weight %				
	Aqueous dispersion	Undoped photonic pigment	PDNPs dispersion	Glycerol	Doped photonic pigment
Solid content (%)	10-40	-	1-5	-	-
Diameter	≤ 80 nm	45-55 µm	92 nm	-	45-55 µm
Example 1	100 %	1 - 10 %	-	-	-
Example 2	100 %	1 - 10 %	0.3 – 3 %	-	-
Example 3	100 %	1 - 10 %	-	0.1 – 3 %	-
Example 4	100 %	1 - 10 %	0.3 – 3 %	0.1 – 3 %	-
Example 5	100 %	-	-	-	1 – 10 %
Example 6	100 %	-	0.3 – 3 %	-	1 – 10 %
Example 7	100 %	-	-	0.1 – 3 %	1 – 10 %
Example 8	100 %	-	0.3 – 3 %	0.1 – 3 %	1 – 10 %

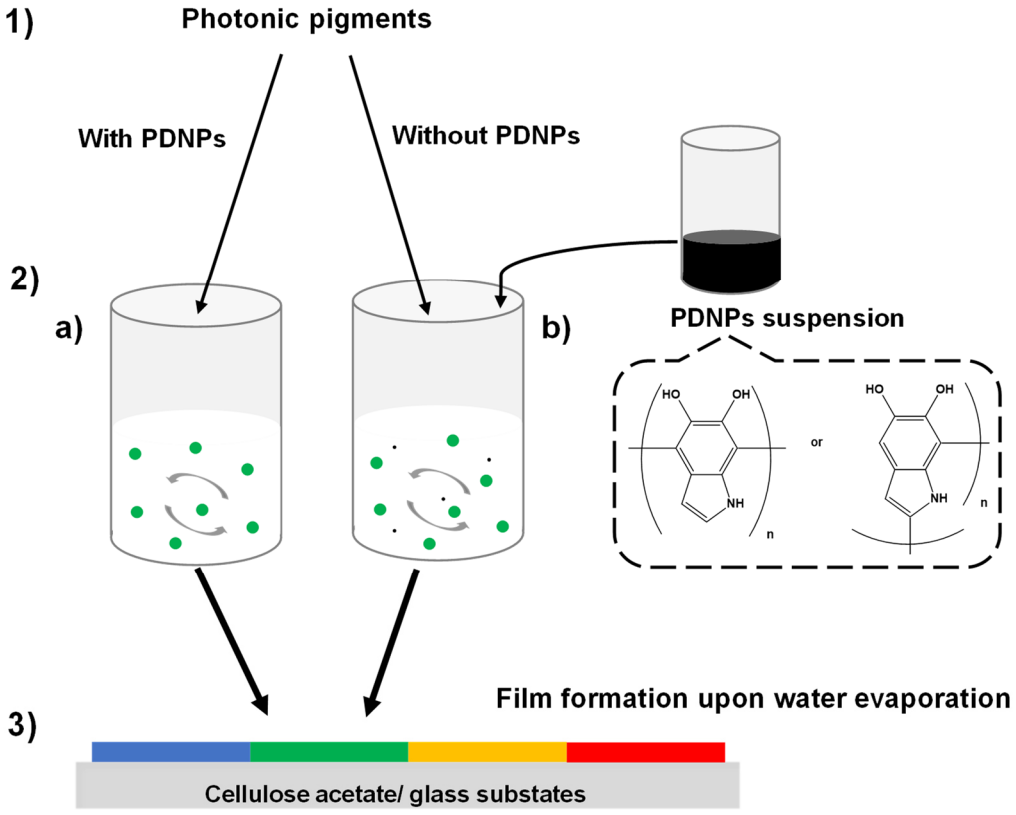

Water-born structurally colored coatings

Scheme 8.3: Experimental procedure for obtaining water-born structurally colored coatings.**1)** Photonic pigments reflecting colors from blue to red wavelengths with different hues. **2a)** The dry powder of photonic pigments doped with PDNPs is added to the aqueous polymer dispersion and orbitally stirred until complete wetting and dispersion of photonic pigments; **2b)** PDNPs are added to the aqueous polymer dispersion when using photonic pigments without PDNPs in their internal structure. **3)** Photonic paints were applied to different surfaces. After water evaporation and film formation, structurally colored coatings were obtained. The inset show the catechol units at PDNPs surface.

8.2.2. Characterization techniques

The macroscopic color appearance of the photonic pigments and water-born polymer coatings colored by them were photographed with a digital camera. Optical reflectance microscopy images of the colored films surface and from the dispersed pigments inside the polymeric films were obtained on a KERN OKM 173 microscope equipped with an ODC 832 camera at a magnification of 40x.

Angle-dependent reflectivity measurements were performed using the multi-angle probe holder under illumination at 45°, in the same conditions described in Chapter 6. CIE x, y color coordinates were obtained by converting the reflectance spectra according to the procedure described in Chapter 6.

8.3. Micro and macroscopic color appearance of the structurally colored coatings

Once the paint is applied to a substrate, water begins to evaporate and forces the film-former particles to close contact. At a certain point during drying, the particles coalesce and solidify into a homogeneous film, which encapsulates the photonic pigments and protects the surface of the substrates.

Interestingly, the difference in color between the wet and dry states of the photonic paint formulations is far greater than with conventional paints, for two main reasons: the change in average refractive index of the photonic structure and the change in light scattering from the polymer nanoparticles of the aqueous dispersion. In the wet paint, the polymer nanoparticles of the aqueous dispersion strongly scatter light, which makes the structural color to appear pale. On the contrary, in the polymer coatings, the discrete film-former nanoparticles in the wet paint have now coalesced and formed a homogeneous polymer film with a homogeneous refractive index, and therefore no longer scatter light significantly. Thus, the resulting dry paint film reflects the structural colors of the incorporated photonic pigments.

These spherical photonic pigments demonstrate excellent compatibility with the aqueous coating formulations, once they were able to retain both its structure in the aqueous medium of the wet paint, and its color in the polymer film of the dry coating, two important criteria which are difficult to address in the design of new pigment structures.[27,39]

This may be related to the surface properties of the photonic pigments, dictated by the composition of the outermost layer at the PNP surface, which is enriched with polar groups. The thin shell composed of PMMA and PAA that covers the PS core with carboxyl groups anchored on the surface, favors the formation of hydrogen bonds among PNP maintaining the integrity of the photonic structure.

Due to the broad-spectrum absorption of light, PDNPs are able to suppress the diffusely scattered light and thus increase the color saturation reflected by doped photonic pigments. However, when dispersed in the wet aqueous paint formulation, they also contribute to increase the macroscopic color saturation of the polymer coatings.[40-42]

Because polydopamine has similar catechol units to dihydroxyphenylalanine (DOPA) present in the self-produced mussel adhesive proteins, it has been confirmed to achieve strong adhesion with most substrates, through the formation of hydrogen bonds between the hydroxyl groups of the catechol units and the oxygen atoms on glass, cellulose acetate or other substrates exhibiting the same surface groups.[43-45] Thus, the addition of PDNPs to the wet paint formulation could present a synergistic effect: besides contributing to a more saturated macroscopic color appearance of the coatings could also impart adhesion properties between the photonic pigments and the film-former polymer nanoparticles and/or between the substrates and the film-former nanoparticles.

Glycerol, a natural and non-toxic trivalent alcohol mostly used as plasticizer, when added to the aqueous photonic paint formulation increase the open time of the coating, because glycerol is a slow evaporating and relatively high boiling point solvent.[46,47] In addition, also contributed to a glossier and brighter color appearance of the final coatings due to the refractive index matching with the photonic pigments structure and the final polymer coating.[38,48]

The surface of the structurally colored water-born polymer coatings was imaged by optical reflectance microscopy (Figure 8.4, upper panel). When focusing below the coating surface it was possible to observe the blue, green, yellow, and red photonic pigments evenly distributed within the polymer film (Figure 8.4, middle panel). These images reveal the structural integrity of the spherical photonic pigments inside the polymer coatings. It is important to noticed that the incorporation of photonic pigments in polymer coatings protects them against disintegration under compression forces. Applying pressure to the polymer

coatings smoothens their surface and deforms the pigments structure (Figure 8.4a). A homogeneous macroscopic color appearance of the polymer coatings is obtained (Figure 8.4, lower panel). It is also visible that the introduction of photonic pigments, responsible for imparting structural colors to the coatings, do not inhibit the coalescence and densification of the film-former nanoparticles.

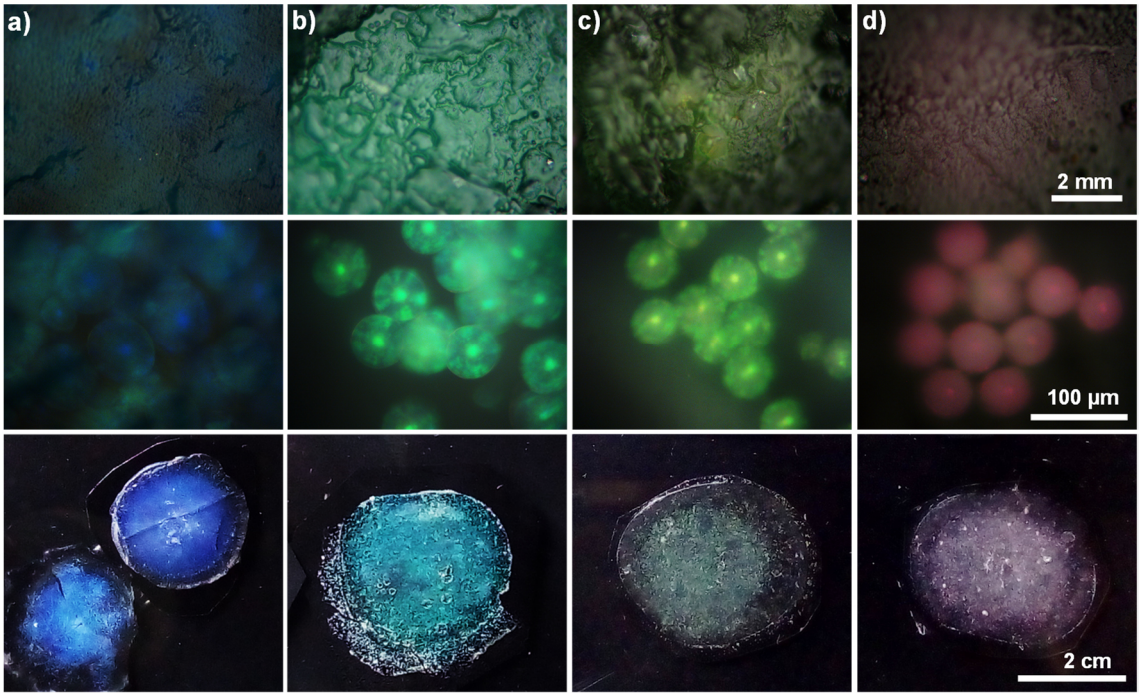

Figure 8.4: Microscopy images of structurally colored water-born polymer coatings evidencing the pigments integrity and even distribution in the polymer films. The upper panel shows the coating surface; Middle panel: shows photonic pigments inside the coatings; Lower panel: photographs showing the macroscopic color appearance of the polymer coatings. **a)** Polymer coating colored with blue pigments (PhP-PNP194) and deformed by compression; **b)** Green coating colored with PhP-PNP232; **c)** Yellow coating colored with PhP-PNP248; **d)** Red coating colored with PhP-PNP287.

The produced coatings retain the color of the original pigment powder, envisioning the applicability, scalability, and sustainability of this approach. The readiness of these photonic paints for application is demonstrated by applying them like traditional paints.

8.4. Reflectance properties and color coordinates

The angular dependence of the reflectance properties of the structurally colored water-born coatings was evaluated and compared with the properties exhibited by the photonic pigments. Angle-resolved reflectance spectra of the polymer coatings for collecting angles varying from 0° to 75°, is very similar to the ones

obtained for the pigments alone (Figure 8.5). Although incorporated in the polymer coatings, the refractive index contrast of the pigment structure ($\Delta n = \left(n_{eff}^2/n_{int}^2\right) - 1$, where n_{eff} is the effective refractive index of the photonic pigments and n_{int} is refractive index of the material filing the interstices between the PNP), do not change significantly, and thus, the wavelengths reflected by the polymer coatings is only slightly blue shifted (~ 20 nm) relatively to the pigments alone (Figure 8.5).[49,50]

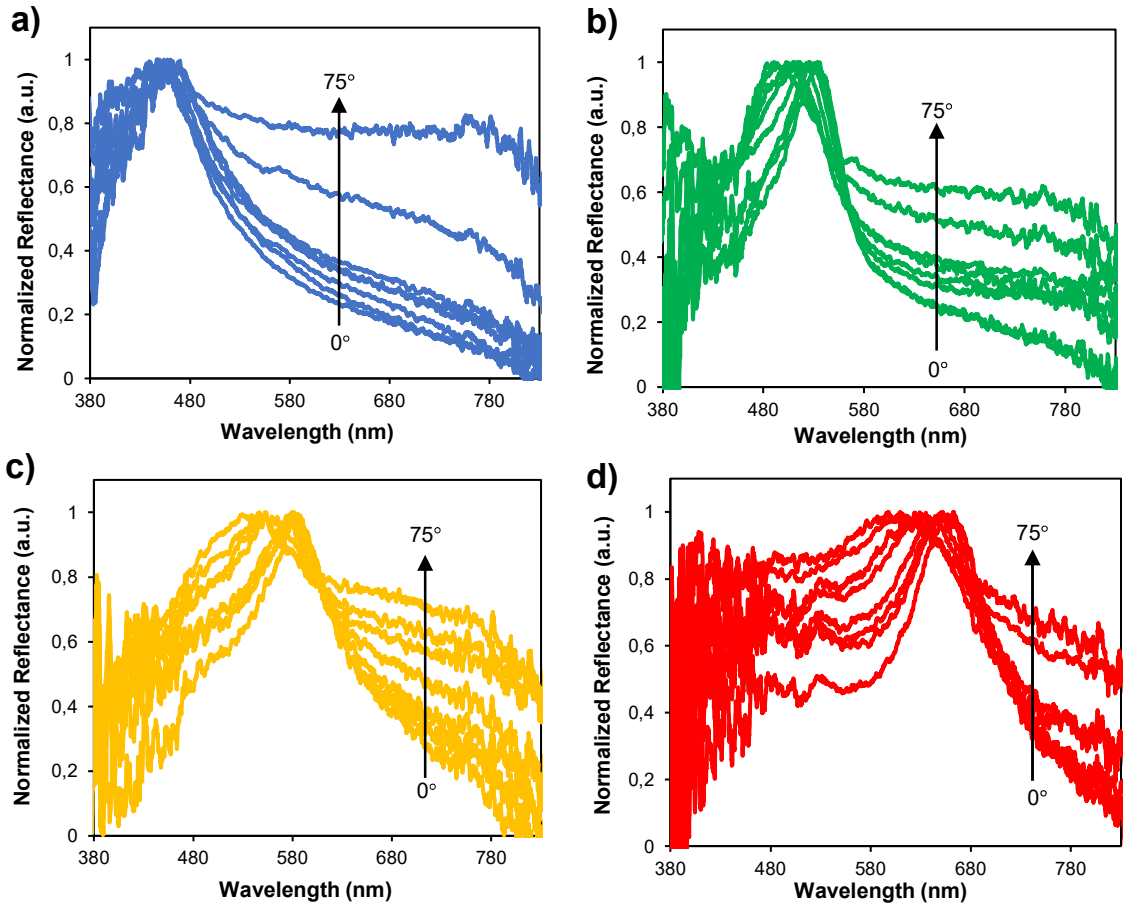

Figure 8.5: Normalized angle-resolved reflectance spectra of the structurally colored water-born polymer coatings. The spectra were collected for angles varying between 0° and 75°, under incident white light illumination at 45°. **a)** Blue coating; **b)** Green coating; **c)** Yellow coating; **d)** Red coating.

The shift in the wavelength of maximum reflectance for the blue polymer coating, colored with PhP-PNP194, correspond to 13 nm (from 460 nm at 0° to 447 nm at 75° collecting angle). This shift is much smaller than the one obtained for the photonic pigments (41 nm). For the green polymer coating, colored with PhP-PNP232, the shift corresponds to 33 nm (from 536 nm to 503 nm), a significantly lower value than the one obtained for the pigments alone (50 nm). For the yellow

coating, colored with PhP-PNP248, the shift corresponds to 36 nm (from 582 nm to 546 nm), again a significantly lower value than the one obtained for the pigments (52 nm). For the red polymer coating, colored with PhP-PNP287, a larger shift is obtained, 55 nm (from 660 nm to 605 nm). This shift, although lower, is closer to the one obtained for the pigments alone (60 nm). These results agree with the broader reflectance bands of the polymer coatings in comparison to the ones reflected by the photonic pigments. For wider viewing angles (above 55°) the reflectance spectra of the polymer coatings reflect higher diffuse scattering background across the entire visible range, that may be related with reflectance at the coating surface.[51]

The incorporation of these photonic pigments in water-born polymer coatings results in non-iridescent structurally colored films and the optical properties of the photonic pigments are maintained in the polymer coatings. In addition, the reflectance bands of the photonic pigments that falls in the ultraviolet region, arising from the diffraction of high order planes or from single-particle scattering resonances, that do not affect the perceived color, could contribute to increase the stability and lifespan of the polymer coatings, by posing some protection against UV radiation.[29,39,52]

A comparison of the reflectance spectra obtained at the backscattering angle for structurally colored blue, green, yellow, and red coatings is shown in Figure 8.6.

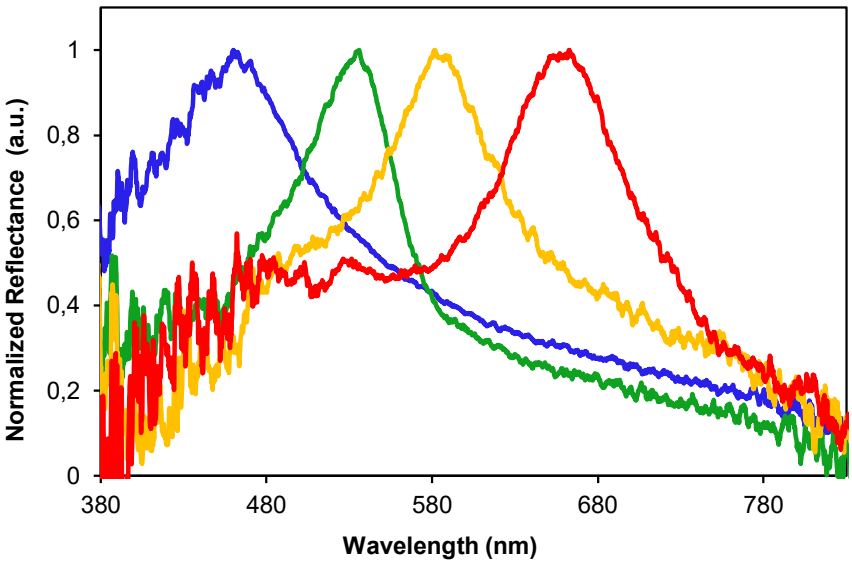

Figure 8.6: Reflectance spectra at the backscattering angle (0° relative to incident light) for structurally colored water-born polymer coatings. The wavelengths of maximum reflectance correspond to 460 nm, 530 nm, 580 nm and 660 nm for the blue, green, yellow, and red coatings, respectively.

Although broader reflectance bands with higher diffuse scattering background are obtained for the polymer coatings in comparison to the photonic pigments, when converted to x, y color coordinates, the structurally colored water-born polymer coatings reflect saturated colors, close to the coordinates of the photonic pigments (Figure 8.7).

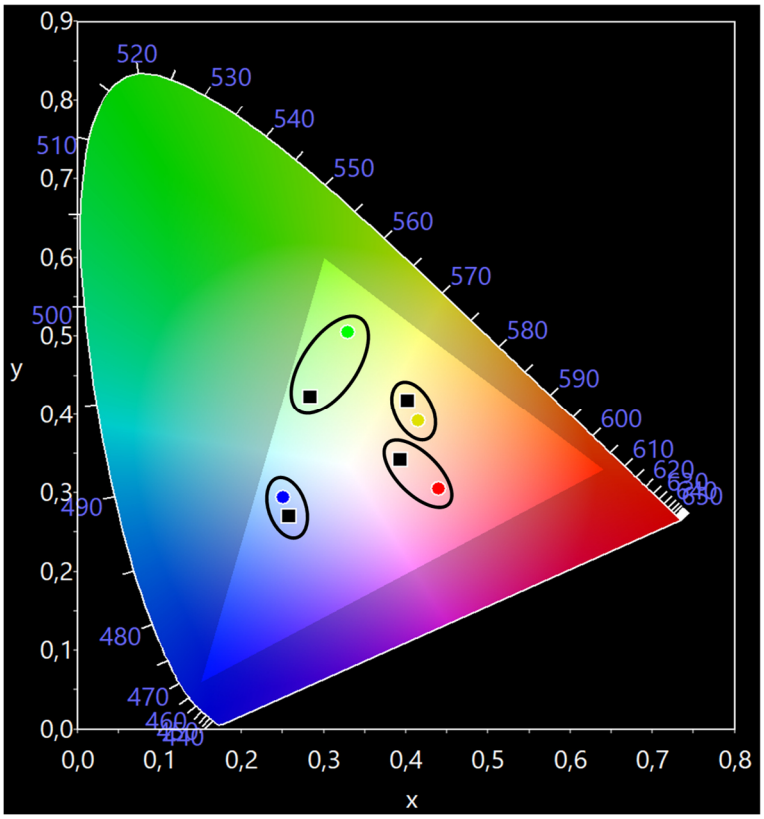

Figure 8.7: CIE chromaticity diagram comparing the saturation of the colors reflected by photonic pigments before and after being incorporated into the water-born polymer coatings. Colored circles correspond to x, y color coordinates of blue, green, yellow, and red photonic pigments. Black squares correspond to the x, y color coordinates of blue, green, yellow, and red polymer coatings. When incorporated in the water-born polymer coatings, photonic pigments impart them saturated structural coloration.

These photonic pigments are easily dispersible and stable in water and demonstrate excellent compatibility with water-born aqueous polymer coatings, retaining their structure in the wet paint formulation (without the need of additional stabilization procedures) as well as in the dried coating film.

The stability and uniformity of our spherical photonic pigments, which are able to maintain their optical properties when incorporated in the polymer films, makes this approach an extraordinary alternative to conventional pigmentary solutions for water-born polymer coatings.

8.5. Conclusions

This work has successfully demonstrated that structural color from dispersible spherical photonic pigments can be applied to realistic, water-born polymer coating formulations.

In addition to their non-fading properties, because the full variety of visible colors can be obtained with the same and especially few chemical compounds just by increasing the polymer nanoparticles diameter, these photonic pigments hold great potential for use in commercial coatings and can decrease the environmental and economic impact of colored polymer coatings.

In the future, the insights gained here will help to fulfill the huge potential of structural pigments as fade-free, nontoxic colorants for paints and coatings.

These findings should stimulate widespread application of structural pigments as colorants in not only coatings but also in a variety of industrially important materials, such as plastics, inks, or cosmetics.

8.6. References

1. Elliott, P. T. & Glass, J. E. Water-Born Coatings. in *Applied Polymer Science: 21st Century, Elsevier* 563–587 (2000).
2. Farinha, J. P. S., Piçarra, S., Baleizão, C. & Martinho, J. M. G. Smart Polymer Nanoparticles for High-Performance Water-Based Coatings, Chapter 29 in *Industrial Applications for Intelligent Polymers and Coatings, Springer* 619–626 (2016).
3. Gürses, A., Açıkyıldız, M., Güneş, K. & Gürses, M. S. Dyes and Pigments: Their Structure and Properties, Chapter 2 in *Dyes and Pigments. Briefs in Molecular Science, Green Chemistry for Sustainability, Springer* 13–31 (2016).
4. Tilley, R. J. D. Colour from Molecules, Chapter 8 in *Colour and the Optical Properties of Materials. Wiley, Second edition* 309–358 (2011).
5. Barnett, J. R., Miller, S. & Pearce, E. Colour and art: A brief history of pigments. *Opt. Laser Technol.* **38**, 445–453 (2006).
6. Gueli, A. M., Bonfiglio, G., Pasquale, S. & Troja, S. O. Effect of Particle Size on Pigments Colour. *Color Res. Appl.* **42**, 236–243 (2017).
7. Allen, N. S. Photofading and light stability of dyed and pigmented polymers. *Polym. Degrad. Stab.* **44**, 357–374 (1994).
8. Tator, K. B. Coating Deterioration. in *ASM Handbook, Protective Organic Coatings* **5B**, 462–473 (2015).

9. Hare, C. H. The Degradation of Coatings by Ultraviolet Light and Electromagnetic Radiation. *J. Prot. coatings linings - Mater. Technol.* **LU-8029**, (1992).

10. Kaul, B. L. Coloration of plastics using organic pigments. *Rev. Prog. Color.* **23**, 19–35 (1993).

11. Xin, W., Tian, N., Gong, J., Chen, Q., Qi, Y., Liu, Z., Liu, J., Jiang, Z., Chen, X. & Tao, T. Effect of nanosized carbon black on thermal stability and flame retardancy of polypropylene/carbon nanotubes nanocomposites. *Polym. Adv. Technol.* **24**, 971–977 (2013).

12. Anna, P., Bertalan, G., Marosi, G., Ravadits, I. & Maatoug, M. A. Effect of interface modification on the photo-stability of pigmented polyethylene films. *Polym. Degrad. Stab.* **73**, 463–466 (2001).

13. Haillant, B. O. The Photofading of Colored Materials. *Mater. Test. Prod. Technol. News* **39**, 1–16 (2009).

14. Ion, R.-M., Nuta, A., Sorescu, A.-A. & Iancu, L. Photochemical Degradation Processes of Painting Materials from Cultural Heritage, Chapter 9 in *Photochemistry and Photophysics - Fundamentals to Applications* 162–178 (2018).

15. Ghelardi, E., Degano, I., Perla, M., Mazurek, J., Schilling, M., Khanjian, H. & Learner, T. A multi-analytical study on the photochemical degradation of synthetic organic pigments. *Dye. Pigment.* **123**, 396–403 (2015).

16. Samain, L., Silversmit, G., Sanyova, J., Vekemans, B., Salomon, H., Gilbert, B., Grandjean, F., Long, G. J., Hermann, R. P., Vincze, L. & Strivay, D. Fading of modern Prussian blue pigments in linseed oil medium. *J. Anal. At. Spectrom.* **26**, 930–941 (2011).

17. Rehman, K., Sajid, M. & Akash, H. Prevalence of exposure of heavy metals and their impact on health consequences. *J. Cell. Biochem.* **119**, 157–184 (2018).

18. Lavanya, C., Dhankar, R., Chhikara, S. & Sheoran, S. Degradation of Toxic Dyes: A Review. *Int.J.Curr.Microbiol.App.Sci* **3**, 189–199 (2014).

19. Itayavirasuk, B. V, Unhom, S. J. & Antisaeranee, P. T. Exposure to Lead , Cadmium and Chromium among Spray Painters in Automobile Body Repair Shops. *J. Occup. Health* **47**, 518–522 (2005).

20. Bowers, L. M. R. & Sobeck, S. J. S. Impact of medium and ambient environment on the photodegradation of carmine in solution and paints. *Dye. Pigment.* **127**, 18–24 (2016).

21. Belmonte, A., Pilz, M., Nickmans, K. & Schenning, A. P. H. J. Brush-Paintable, Temperature and Light Responsive Triple Shape-Memory Photonic Coatings Based on Micrometer-Sized Cholesteric Liquid Crystal Polymer Particles. *Adv. Opt. Mater.* **8**, 2000054 (2020).

22. Xia, Y., Gao, S., He, H., Wang, X., Zeng, Z., Chen, B., Zou, N., Cao, M. & Wang, S. A New and Straightforward Strategy to Prepare an Optical Hydrogel Film with Dynamic Structural Colors. *J. Phys. Chem. C* **124**, 16083−16089 (2020).

23. Meng, F., Umair, M. M., Iqbal, K., Jin, X., Zhang, S. & Tang, B. Rapid Fabrication of Noniridescent Structural Color Coatings with High Color Visibility, Good Structural Stability, and Self-Healing Properties. *ACS Appl. Mater. Interfaces* **11**, 13022–13028 (2019).

24. Chen, G., Yi, B., Huang, Y., Liang, Q. & Shen, H. Development of bright and low angle dependence structural colors from order-disorder hierarchical photonic structure. *Dye. Pigment.* **161**, 464–469 (2019).

25. Wang, F., Zhang, X., Zhang, L., Cao, M., Lin, Y. & Zhu, J. Rapid fabrication of angle-independent structurally colored films with a superhydrophobic property. *Dye. Pigment.* **130**, 202–208 (2016).

26. Katagiri, K., Tanaka, Y., Uemura, K., Inumaru, K., Seki, T. & Takeoka, Y. Structural color coating films composed of an amorphous array of colloidal particles via electrophoretic deposition. *NPG Asia Mater.* **9**, 1–7 (2017).

27. Clough, J. M., Guimard, E., Rivet, C., Sprakel, J. & Kodger, T. E. Photonic Paints: Structural Pigments Combined with Water-Based Polymeric Film-Formers for Structurally Colored Coatings. *Adv. Opt. Mater.* **7**, 1900218 (2019).

28. Wang, X., Li, Y., Zhou, L., Chai, L., Fan, Q. & Shao, J. Structural colouration of textiles with high colour contrast based on melanin-like nanospheres. *Dye. Pigment.* **169**, 36–44 (2019).

29. Yuan, W., Zhou, N., Shi, L. & Zhang, K. Structural Coloration of Colloidal Fiber by Photonic Band Gap and Resonant Mie Scattering. *ACS Appl. Mater. Interfaces* **7**, 14064–14071 (2015).

30. Gaillou, E., Fritsch, E., Aguilar-Reyes, B., Rondeau, B., Post, J., Barreau, A. & Ostroumov, M. Common gem opal: An investigation of micro- to nano-structure. *Am. Mineral.* **93**, 1865–1873 (2008).

31. Vukusic, P. & Sambles, J. R. Photonic structures in biology. *Nature* **424**, 852–855 (2003).

32. Andrew Richard, P. 515 million years of structural colour. *J. Opt. A Pure Appl. Opt.* **2**, R15–R28 (2000).

33. Dumanli, G. A. & Savin, T. Recent advances in the biomimicry of structural colours. *Chem. Soc. Rev.* **45**, 6698–6724 (2016).

34. Goerlitzer, E. S. A., Taylor, R. N. K. & Vogel, N. Bioinspired Photonic Pigments from Colloidal Self-Assembly. *Adv. Mater.* **30**, 1706654 (2018).

35. Steward, P. A., Hearn, J. & Wilkinson, M. C. An overview of polymer latex film formation and properties. *Adv. Colloid Interface Sci.* **86**, 195–267 (2000).

36. Visschers, M., Laven, J. & van der Linde, R. Film Formation from Latex Dispersions. *J. Coatings Technol.* **73**, 49–55 (2001).

37. Mannari, V. & Patel, C. J. Introduction to paints and coatings, Chapter 1 in *Understanding Raw Materials, Vincentz Network* 19–27 (2015).

38. Brown, R. F. G. Additives in coatings - A necessary evil? in *Additives in Water-Born Coatings, RSC* 1–6 (2003).

39. Aguirre, C. I., Reguera, E. & Stein, A. Colloidal Photonic Crystal Pigments with Low Angle Dependence. *ACS Appl. Mater. Interfaces* **2**, 3257–3262 (2010).

40. Xiao, M., Li, Y., Allen, M. C., Deheyn, D. D., Yue, X., Zhao, J., Gianneschi, N. C., Shawkey, M. D. & Dhinojwala, A. Bio-Inspired Structural Colors Produced via Self-Assembly of Synthetic Melanin Nanoparticles. *ACS Nano* **9**, 5454–5460 (2015).

41. Kohri, M., Nannichi, Y., Taniguchi, T. & Kishikawa, K. Biomimetic non-iridescent structural color materials from polydopamine black particles that mimic melanin granules. *J. Mater. Chem. C* **3**, 720–724 (2015).

42. Kawamura, A., Kohri, M., Morimoto, G., Nannichi, Y. & Taniguchi, T. Full-Color Biomimetic Photonic Materials with Iridescent and Non- Iridescent Structural Colors. *Sci. Rep.* **6**, 33984 (2016).

43. Liu, Y., Shao, C., Liu, Y., Shao, C., Wang, Y., Sun, L. & Zhao, Y. Bio-Inspired Self-Adhesive Bright Non-iridescent Graphene Pigments. *Matter* **1**, 1–11 (2019).

44. Lee, H., Dellatore, S. M., Miller, W. M. & Messersmith, P. B. Mussel-Inspired Surface Chemistry for Multifunctional Coatings. *Science* **318**, 426–430 (2007).

45. Liu, P., Chen, J., Zhang, Z., Xie, Z., Du, X. & Gu, Z. Bio-inspired robust non-iridescent structural color with self-adhesive amorphous colloidal particle arrays. *Nanoscale* **10**, 3673–3679 (2018).

46. Mccreight, K. W., Stockl, R., Testa, C. & Seo, K. S. Development of Low VOC Additives to Extend the Wet Edge and Open Time of Aqueous Coatings. *Prog. Org. Coatings* **72**, 102–108 (2011).

47. Võ, U. T. & Morris, M. P. Nonvolatile, semivolatile, or volatile: Redefining volatile for volatile organic compounds. *J. Air Waste Manage. Assoc.* **64**, 661–669 (2014).

48. Zołek-tryznowska, Z., Izdebska, J. & Tryznowski, M. Branched polyglycerols as performance additives for water-based flexographic printing inks. *Prog. Org. Coatings* **78**, 334–339 (2015).

49. Bertone, J. F., Jiang, P., Hwang, K. S., Mittleman, D. M. & Colvin, V. L. Thickness Dependence of the Optical Properties of Ordered Silica-Air and Air-Polymer Photonic Crystals. *Phys. Rev. Lett.* **83**, 300–303 (1999).

50. Spahn, P., Finlayson, C. E., Etah, W. M., Snoswell, D. R. E., Baumberg, J. J. & Hellmann, G. P. Modification of the refractive-index contrast in polymer opal film. *J. Mater. Chem.* **21**, 8893–8897 (2011).

51. Hunt, R. W. G. & Pointer, M. R. Factors Affecting the Appearance of Coloured Objects in *Measuring Color, 4th Edition, Wiley* 267–292 (2011).

52. Magkiriadou, S., Park, J., Kim, Y. & Manoharan, V. N. Absence of red structural color in photonic glasses, bird feathers, and certain beetles. *Phys. Rev. E* **90**, 062302 (2014).

9. Concluding remarks and future perspectives

Spherical photonic pigments, with either crystalline or amorphous structures (SPhCs and SPhGs), were successfully obtained using a precisely controlled, reproducible, and scalable method. This was accomplished by the fine tuning of the temperature at which polymer nanoparticles, PNP, were assembled inside emulsion droplets, together with the protonation/deprotonation of the functional groups at PNP surface, and the stirring rate of the assembly process.

By increasing the temperature at which PNP, with diameters ranging from 173 nm to 331nm, were assembled inside emulsion droplets allowed the development of a palette of non-iridescent structural colors with tunable structure, reflection properties, and color appearance. In addition, the co-assembly of PNPs and the broad-spectrum absorber polydopamine nanoparticles, PDNPs, contributed to a more isotropic structure and demonstrated to be efficient at increasing color saturation.

Multi-wavelength 3D reflectance confocal microscopy, a simple, fast and non-destructive imaging technique was used for the first time to characterize the structural and optical properties of SPhCs and SPhGs. This intuitive and readily available technique provided a full three-dimensional picture of the PNPs packing inside the spherical photonic structures and gives a direct correlation between the crystalline/amorphous region distribution inside the spherical photonic pigments and their corresponding optical properties.

The PNP packing and deformation inside the photonic pigments and the strong interactions between the charged groups at PNP surface, resulted in highly stable structures and allowed their successful introduction into aqueous dispersions of polymer nanoparticles to produce structurally colored water-born polymer coatings.

These dispersible pigments exhibit bright, non-fading and low iridescent structural colors and are expected to be a valid alternative, to replace traditional coloring solutions in an efficient, simple, and environmentally friendly structural color approach for water-born polymer coatings industry.

Because these spherical structural pigments reflect bright colors covering the whole visible range, they can be used to address the challenging panchromatic structural color generation. By precisely adjusting the quantitative ratio of mixed

spherical photonic pigments, would provide a convenient way to obtain full-spectrum colors with unique patterns and properties, where the reflection bands and the observed structural colors can be varied within a specific range.

Furthermore, these structures offer new possibilities in the development of color reflective displays and overcome the poor visibility under bright sunlight of existing emissive displays.
Structural color generated interest in applications other than displays or paint technology. The development of composite materials that contain periodically arranged particles entrapped in polymer networks that allows a color change in response to a variety of stimuli such as temperature, solvent vapors, salts, health-threatening chemicals, proteins or small molecule drugs are a hot topic. They gain large interest as an alternative to electrochemical sensing because they do not require power.
To create such functional structurally colored composites, the spherical photonic structures created here can be used as templates to prepare inverse opal systems by filling the interstitial pores with monomers which are further polymerized, forming a network. Alternatively, an inorganic material precursor can be used to infiltrate in the interstices in between the particles and be solidified through a sol–gel process. The template particles are then removed and leave empty holes in the solidified matrix, resulting in an interconnected microporous structure. Inverse opals have complementary optical properties to those of the original colloidal photonic templates because the voids left by the particles are now the low-refractive-index component of the structures.

In a different approach, to tailor a dynamic photonic bandgap response, core–shell particles with different compositions can be used to explore and control the position and the width of the stop-bands. Dynamic coloration via shifting the photonic stopband or moving the photonic structure out of view could lead to added value applications such as electronic ink displays, or advanced security features in anticounterfeiting applications.

In addition, by using biocompatible materials to construct structurally colored photonic pigments and their inverse structures, they could also find applications in pharmaceutical areas, and biomedical applications.

Based on the above, various applications can be envisioned and achieved for spherical photonic structures in either displays, pigments, sensors, anticounterfeiting, catalyst supports, selective separation, drug release or cell culture microcarriers.

Despite their great commercial potential, most spherical photonic structure technologies remain in the laboratories, facing a huge gap between research results and the requirements of real-world applications. Cooperation between academia and industry is the key to take the technology out of the research laboratories. Although there is still a long way to go and numerous challenges remain in their development, these spherical photonic pigments will have a shiny future.